Semiconductor Composites for Solid-State Lighting

Zur Erlangung des akademischen Grades Doktor-Ingenieur (Dr.-Ing.)
genehmigte Dissertation von Mariel Grace Jama (geb. Dimamay), M.Sc.
aus Iligan, Philippinen

Februar 2016 - Darmstadt - D 17

TECHNISCHE
UNIVERSITÄT
DARMSTADT

UNIVERSITÉ DE
BORDEAUX

Semiconductor Composites for Solid-State Lighting

vom Fachbereich Material- und Geowissenschaften der Technischen Universität Darmstadt
zur Erlangung des Grades Doktor-Ingenieur (Dr.-Ing.)
genehmigte Dissertation von
Mariel Grace Jama (geb. Dimamay), M.Sc. aus Iligan, Philippinen

Berichter:	Prof. Dr. Wolfram Jaegermann
Mitberichter:	Prof. Dr. Georges Hadziioannou
Prüfer:	Prof. Dr. Wolfgang Ensinger
	Prof. Dr. Robert Stark

Tag der Einreichung: 02.09.2015
Tag der Prüfung: 27.10.2015

Darmstadt 2016 - D 17

Abstract

Inorganic-organic semiconductor heterostructures have been subjects of interest for solid-state lighting (SSL) in the last decades due to the potential for simultaneous utilization of the complementary favorable properties of two distinct material classes for producing light. This work proposes a hybrid composite active layer design for light emission which combines inorganic and organic semiconductors. Particular to this composite design, light-emitting organic semiconductor molecules are embedded in an ambipolar charge-transporting inorganic semiconductor matrix. The embedded molecules serve as the radiative recombination sites for charge carriers that are injected into the matrix.

Coming up with a composite layer may seem to be just a plug-and-play of different inorganic and organic semiconductor combinations. However, there are several fundamental requirements to make the concept work. Very important factor in realizing high efficiency devices are the properties of the interfaces between the different components because they often govern the physical properties of the overall structure. With this in mind, the energy level alignments at the interfaces of the candidate material combinations and the different chemical interactions taking place at such interfaces were investigated by photoelectron spectroscopy (PES). For the energy level alignment, the highest occupied molecular orbital (HOMO) and lowest unoccupied molecular orbital (LUMO) of the organic dye should be situated in between the valence and conduction bands of the inorganic semiconductor. This alignment provides the necessary energetic driving forces for electron and hole transfers from the charge-transporting inorganic matrix to the light-emitting organic molecules. The PES investigations were focused on the interface formations of these two types of materials in three deposition configurations, namely: the inorganic/organic bilayer, the composite layer and the organic/inorganic bilayer. Additionally, the interface between the inorganic and organic part has to be of high purity and electronic perfection, as otherwise defect states will destroy the coupling of the two materials. By interpreting PES data, we also determined and described the chemical composition of the interface and the resulting coupling of the two materials on the atomic scale. Furthermore, as one of the advantages of hybrid designs, energy transfer from the matrix to the dopant is another possible route for obtaining light emission from the organic dopant. Therefore, another factor to look into would be the resonance between the exciton energies of the inorganic and organic materials. With this in mind and in conjunction with available experimental methods, the room-temperature (RT) photoluminescence (PL) of the hybrid composite active layer was investigated using a high energy laser for exciting the inorganic matrix. The idea here is to exclusively excite the matrix; if there is a light emission coming from the dopant, then it could hint at two possible mechanisms: one is energy transfer and the other is charge transfer from the excited matrix to the dopant.

As one of the candidate material combinations, zinc selenide (ZnSe) and a red emitter, Ir(BPA), were investigated. Bilayer and composite thin films of ZnSe and Ir(BPA) organic light emitter were prepared *in situ* by UHV thermal evaporation technique. The measured energy band alignments for the ZnSe/Ir(BPA) bilayer and ZnSe+Ir(BPA) composite reveal that the HOMO and LUMO of the organic dye are positioned within the ZnSe bandgap. For the initial steps of ZnSe deposition on a dye film to form Ir(BPA)/ZnSe bilayers, zinc atoms were found to intercalate into the dye film leaving behind an excess of selenium at the interface that partly reacts with dye molecules. PES of the composites shows the same chemical species suggesting a similar mechanism. This mechanism leads to composite films with increased content of amorphous phases in the inorganic matrix. The PL spectra of composite films showed a relative enhancement of the emissions coming from the films with low dye concentrations as compared to the films with higher concentrations. This enhancement may hint at a charge transfer and/or an energy transfer from ZnSe to Ir(BPA). Proof of concept for the novel composite design is provided by a device that was fabricated with an active layer that is composed of alternating layer sequences of ZnSe and Ir(BPA). Weak areal emission and red intermittent sparks were visually observed from the device.

Overall, several challenges in realizing the hybrid composite active layer design were uncovered during the course of this work. From the results of the PES measurements on several material combinations, it is found that the position of the Fermi level in the pristine inorganic semiconductor and the pristine organic light emitter strongly directs the resulting energy level lineup in the bilayer and composite upon thermodynamic Fermi level equalization at the interfaces. A large interface dipole formation at the material interface can positively reinforce the desired alignment for the proposed composite design. In addition, reactive interfaces of certain compositions are formed rather than the desired abrupt material interface. This reactive interface can hinder efficient charge and energy transfers, impede charge carrier conduction and supply nonradiative recombination sites. Furthermore, alternatives for a less-chemically reactive deposition method are limited by the availability of techniques that are compatible for inorganic-organic layered and composite depositions.

Zusammenfassung

Anorganisch-organische Halbleiterheterostrukturen genossen in den letzten Jahrzehnten viel Beachtung in der Festkörperbeleuchtung, und zwar aufgrund des Potentials, sich gegenseitig ergänzende vorteilhafte Eigenschaften zweier unterschiedlicher Materialklassen simultan zu nutzen, um Licht zu erzeugen. Diese Arbeit schlägt ein Design der aktiven Schicht eines Hybridkomposits zur Lichtemission vor, welches anorganische und organische Halbleiter kombiniert. Das Besondere an diesem Kompositdesign ist, dass die lichtemittierenden organischen Halbleitermoleküle in einer ambipolaren, ladungstransportierenden anorganischen Halbleitermatrix eingebettet sind. Die eingebetteten Moleküle dienen als strahlende Rekombinationsstellen für die Ladungsträger, welche in die Matrix injiziert werden.

Eine Kompositschicht herzustellen mag zunächst nur wie ein Plug-and-Play verschiedener anorganischer und organischer Halbleiterkombinationen erscheinen. Jedoch sind zahlreiche grundlegende Bedingungen zu beachten, damit das Konzept funktioniert. Ein sehr wichtiger Faktor bei der Realisierung hocheffizienter Bauelemente, sind die Eigenschaften der Grenzflächen zwischen den verschiedenen Komponenten, da diese oft die physikalischen Eigenschaften der Gesamtstruktur bestimmen. Zu diesem Zweck wurden die Ausrichtungen der Energieniveaus an den Grenzflächen der ausgewählten Materialkombinationen und die verschiedenen, an diesen Grenzflächen stattfindenden, chemischen Wechselwirkungen mit Hilfe der Photoelektronenspektroskopie (PES) untersucht. Für die Ausrichtung der Energieniveaus sollten das höchste besetzte Orbital eines Moleküls (HOMO) und das niedrigste unbesetzte Orbital eines Moleküls (LUMO) des organischen Farbstoffs zwischen den Valenz- und Leitungsbändern des anorganischen Halbleiters liegen. Diese Ausrichtung liefert die notwendigen energetischen Triebkräfte für Elektronen- und Lochtransfers von der ladungstransportierenden anorganischen Matrix zu den lichtemittierenden organischen Molekülen. Die PES-Untersuchungen konzentrierten sich auf die Grenzflächenbildungen bei diesen zwei Typen von Materialien in drei Depositionskonfigurationen: Die anorganische/organische Doppelschicht, die Kompositschicht und die organische/anorganische Doppelschicht. Des Weiteren muss die Grenzfläche zwischen dem anorganischen und organischen Teil von hoher Reinheit und elektronischer Perfektionen sein, da andernfalls Defektzustände die Kopplung der beiden Materialien zerstören würden. Durch die Analyse der PES-Daten haben wir außerdem die chemische Zusammensetzung der Grenzfläche und die resultierende Kopplung der beiden Materialen auf atomarer Ebene bestimmt und beschrieben. Einer der Vorteile des Hybriddesigns ist außerdem, dass der Energietransfer von der Matrix zum Dotierstoff einen weiteren möglichen Weg darstellt, eine Lichtemission vom organischen Dotierstoff zu erhalten. Daher galt es auch die Resonanz zwischen den Exzitonenenergien der

anorganischen und organischen Materialien zu untersuchen. In diesem Sinne und in Verbindung mit den zur Verfügung stehenden Experimentalmethoden, wurde die Photolumineszenz (PL) bei Raumtemperatur (RT) der aktiven Schicht des Hybridkomposits untersucht, wobei ein Hochenergielaser zum Einsatz kam, um die anorganische Matrix anzuregen. Die Idee hierbei ist, ausschließlich die Matrix anzuregen. Denn falls eine Lichtemission vom Dotierstoff kommt, dann könnte es ein Hinweis auf zwei mögliche Mechanismen sein: Einen Energietransfer oder einen Ladungstransfer von der angeregten Matrix zum Dotierstoff.

Als eine der möglichen Materialkombinationen wurde Zinkselenid (ZnSe) und ein roter Emittent, Ir(BPA), untersucht. Es wurden Doppelschichten und Komposit-Dünnschichten aus ZnSe und dem organischen Lichtemittenten Ir(BPA) in situ mit Hilfe des thermischen Verdampfungsverfahrens UHF hergestellt. Die gemessenen Energiebandausrichtungen für die ZnSe/Ir(BPA)-Doppelschichten und die ZnSe+Ir(BPA)-Komposite zeigen, dass die HOMO und LUMO des organischen Farbstoffs innerhalb der Bandlücke von ZnSe positioniert sind. Während der ersten Schritte der ZnSe-Deposition auf einen Farbstofffilm, um Ir(BPA)/ZnSe Doppelschichten zu erzeugen, fügten sich Zinkatome in den Farbstofffilm ein und hinterließen dabei einen Überschuss an Selenium an der Grenzfläche, welches teilweise mit den Farbstoffmolekülen reagiert. Die PES der Komposite zeigt die selbe Spezies, was auf einen ähnlichen Mechanismus hindeutet. Dieser Mechanismus führt zu Kompositschichten mit einem erhöhten Gehalt an amorphen Phasen in der anorganischen Matrix. Die PL-Spektren der Kompositschichten zeigten bei Schichten mit niedrigen Farbstoffkonzentrationen eine relative Erhöhung der Emissionen im Gegensatz zu Schichten mit höheren Konzentrationen. Diese Erhöhung kann ein Hinweis auf einen Ladungstransfer und/oder einen Energietransfer vom ZnSe zum Ir(BPA) sein. Der Machbarkeitsnachweis für das neuartige Kompositdesign wird durch ein Bauelement erbracht, welches mit einer aktiven Schicht hergestellt wurde, die aus sich abwechselnden Schichtsequenzen von ZnSe und Ir(BPA) zusammensetzt ist. Es wurden eine schwache räumliche Emission und rote intermittierende Funken an dem Bauelement optisch sichtbar beobachtet.

Insgesamt konnten im Laufe der Arbeit mehrere Herausforderungen bei der Realisierung des Designs des Hybridkomposits mit aktiven Schichten aufgedeckt werden. Aus den Ergebnissen der PES-Messungen an den verschiedenen Materialkombinationen geht hervor, dass die Position des Ferminiveaus im unberührten anorganischen Halbleiter und dem unberührten organischen Lichtemitter stark die resultierende Energieniveau-Formation in der Doppelschicht und dem Komposit vorschreibt bei thermodynamischem Ferminiveau-Ausgleich an den Grenzflächen. Eine große Grenzflächen-Dipolbildung an der Materialgrenzfläche kann für das vorgeschlagene Kompositdesign die gewünschte Ausrichtung positiv verstärken. Zusätzlich werden anstelle der gewünschten abrupten Materialgrenzflächen reaktive Grenzflächen bestimmter Zusammensetzungen ausgebildet.

Diese reaktive Grenzfläche kann effiziente Ladungs- und Energietransfers behindern, Ladungsträgerleitung erschweren und nichtstrahlende Rekombinationsstellen liefern.

Contents

Global trends on solid-state lighting 5

Chapter 1 Introduction 12

1.1 Historical key moments of solid-state lighting 12

1.2 Motivation of this study 15

1.2.1 Brief overview of literature on organic-inorganic hybrid devices 15

1.2.2 Novel hybrid active layer approach 17

1.2.3 Interface characterization as immediate focus of research in this work 19

1.2.4 Scope and limitations of the study 20

1.3 Thesis outline 20

Chapter 2 Background of the study 23

2.1 Solid-state lighting: Light-emitting and organic light- emitting diodes 23

2.1.1 Device operation 24

2.1.2 Organic light-emitting diode architecture 26

2.2 Material: Semiconductors 27

2.2.1 Electronic structure of organic semiconductors 28

2.2.2 Electrical properties of organic solids 31

2.2.3 Photophysics of organic semiconductors 32

2.3 Donor-acceptor molecular systems 34

2.3.1 Energy transfer mechanisms 35

2.3.2 Charge carrier injection 37

2.4 Interface interactions 40

2.4.1 Conductive surface 41

2.4.2 Energy level alignment at interfaces 42

Chapter 3 Experimental methods 51

3.1 Photoelectron spectroscopy 51

3.1.1 Physical principle 51

3.1.2 Working principle 53

3.1.3 Features of the photoemission spectrum 55

3.1.4 Identification of elemental compositions and chemical states 56
3.1.5 Quantitative analysis of the core level spectra 57
3.1.6 Instrumentation and technical considerations 58
3.1.7 Ultra-high vacuum systems 60
3.2 Absorption spectroscopy and the determination of the optical bandgap in inorganic semiconductors 64
3.3 Photoluminescence spectroscopy 67
3.4 X-ray diffraction 67
3.5 Sample preparation 68

Chapter 4 Materials: ZnSe and Ir(BPA) 69
4.1 ZnSe 69
4.1.1 Deposition of ZnSe thin films 70
4.1.2 Photoelectron spectroscopy measurements of ZnSe films 72
4.1.3 Crystal structure of the films 77
4.1.4 Surface morphology of the films 81
4.1.5 Optical properties of the polycrystalline films 82
4.2 Ir(BPA) 86
4.2.1 Deposition of Ir(BPA) films 89
4.2.2 Optical properties of Ir(BPA) 89
4.2.3 Photoelectron spectroscopy measurements of Ir(BPA) films 90

Chapter 5 ZnSe and Ir(BPA): Characterization of the interface 93
5.1 Pristine layers of ZnSe and Ir(BPA) 93
5.2 Bilayer heterojunction: The ZnSe/Ir(BPA) interface 95
5.3 Bilayer heterojunction: The Ir(BPA)/ZnSe interface 102
5.4 Composite: The ZnSe+Ir(BPA) interface 108

Chapter 6 ZnSe + Ir(BPA) composite: Other characterizations 113
6.1 Raman spectroscopy of the composites 113
6.2 Crystal structure of the composites 115
6.3 Transmission electron microscopy images of composites 117
6.4 Infrared spectroscopy of the composites 120

6.5 Absorption and photoluminescence properties of the composites....121

Chapter 7 Hybrid devices for light emission....128

7.1 Phase I: Initial attempts on device design, fabrication and characterization....128

7.2 Phase II: Final attempts on device design, fabrication and characterization....133

Chapter 8 ZnO - Ir(BPA) system....139

8.1 ZnO....139

8.1.1 Deposition of ZnO thin films....140

8.1.2 Crystal structure of the ZnO film....140

8.1.3 Surface morphology of the ZnO film....141

8.1.4 Absorption spectrum and the optical bandgap of the ZnO film....143

8.1.5 Electronic structure of ZnO investigated by PES....144

8.2 ZnO/Ir(BPA) interface characterization....148

8.2.1 As-deposited ZnO/Ir(BPA) interface....148

8.2.2 Annealed ZnO/Ir(BPA) interface....152

Chapter 9 nc-TiO_2 - TSQT system....156

9.1 nc-TiO_2....156

9.1.1 nc-TiO_2 film preparation....156

9.1.2 Crystal structure of anatase nc-TiO_2....157

9.1.3 Surface morphology of the nc-TiO_2 film....158

9.1.4 Absorption spectra and the optical bandgap of nc-TiO_2....158

9.2 TSQT: monomeric squaraine-derived molecule....159

9.2.1 TSQT sample preparation....160

9.2.2 Optical properties of the TSQT molecule....160

9.3 nc-TiO_2 + TSQT composite....161

9.3.1 Energy level alignment at the internal interfaces of the nc-TiO_2 + TSQT composite....162

9.3.2 Photoluminescence of nc-TiO_2+TSQT composites....165

Chapter 10 Perspectives and outlook....169

Appendix A Vocabulary for describing the quality of solid state lighting devices....172

Appendix B Evaporation source calibration for determining deposition rates 173

Appendix C Calculations for the dopant volume percentage in a composite sample 175

Appendix D Additional J-V and I_{photo}-V data for Devices 19 and 21 180

Appendix E Additional photoelectron spectroscopy data for the nc-TiO_2 - TSQT system . 182

Bibliography 187

Acknowledgments..... 203

Global trends on solid-state lighting

Life, Science and Technology – three words that always come hand in hand on answering questions as to the premise of scientific researches. How do science and technology shape our lives and save the world?

The importance of artificial lighting to us and our society has long been established. Even though fire may have already been used as far back as 2-6 million years ago by our primeval ancestors, it is still thought of as the quintessential human invention. Artificial lighting is so integrated into our lifestyle that we barely give it notice. One of its greatest impact is on human productivity as it 'extends the day' so that we can be nearly as productive at night as during the day and it 'opens up the indoors' so that humans may be as productive indoors as outdoors.[1] Due to its importance as well as demand, technologies for its more efficient production evolved spectacularly from candles in the 18th century to gas and kerosene lamps in the 19th century and to the electrical lamps in the 20th century.

In the last two decades, the course that solid-state lighting (SSL) has been taking is revolutionizing the lighting industry.[2, 3] Light emitting diodes (LEDs), initially used mainly as small indicator lamps in electronics and toys, have become bright, efficient, and competitive as incandescent lamps. LED technology has reached a level where nearly all the lighting applications formerly provided by conventional light sources such as the incandescent and fluorescent lamps can now be provided by LED-based light sources. Thus, prompted the saying,

"*Incandescent light bulbs lit the 20th century; the 21st century will be lit by LED lamps.*" [1]

And with the latest announcement on the 2014 Nobel Prize in Physics where the works of the GaN-based blue light-emitting diode (LED) pioneers Isamu Akasaki, Hiroshi Amano and Shuji Nakamura earned the most prestigious recognition--

"*for the invention of efficient blue light-emitting diodes which has enabled bright and energy-saving white light sources,*"[4]

hopefully, the general public will learn to turn its undivided attention to solid-state lighting.

SSL is a technology that involves the use of light emitting diodes (LEDs) or organic light emitting diodes (OLEDs) for the production of general illumination lighting. Unlike the incandescent and fluorescent lamps that use filaments and gases encased in glass bulbs to create light, SSL use semiconductors that convert electricity into light. SSL branches into two major applications -- display (1) and lighting (2).

Displays are currently the largest use for LEDs: either white or red-green-blue (RGB) LEDs for backlighting liquid crystal displays (LCDs) or RGB LEDs for ultra-large video displays. White point-source LEDs are used for most backlighting that do not require very

[1] To quote the statement released by the representatives from the Royal Swedish Academy of Sciences during the awarding of the 2014 Nobel Prize in Physics.

high color quality. But for those that do require more saturated colors and a larger color gamut, RGB point-source LEDs are used. The future of LED backlighting, though, is unclear as it is tied to that of LCDs. Meanwhile, ultra-large LED video displays have the more potential for future growth. Its growth is less spectacular than backlighting but nevertheless steady.

For LED lighting, there is currently an emerging first wave of rapidly growing applications targeted at retrofitting general illumination lamps. SSL lamps are basically retrofitted into existing Edison sockets (for incandescent lamps) or troffers (for fluorescent lamps) offering simple but important performance improvements in efficiency, color rendering quality, lifetime, absence of environmental contaminants, and overall life ownership cost. With easy tailoring, SSL will eventually better serve any existing general illumination market as compared to the traditional technologies.

OLED displays have shown extensive progress in recent years. It already has made its way into the market for smart phones, game consoles, tablet computers, screen monitors and televisions. Most of the handheld devices use either the passive-matrix or active-matrix OLED display, while most of the TVs use either the RGB OLED or the 'white' OLED technology.[5] Comparing with LCDs, OLED displays promise higher efficiency, larger field of view, higher switching field, and compatibility with non-planar form factors.

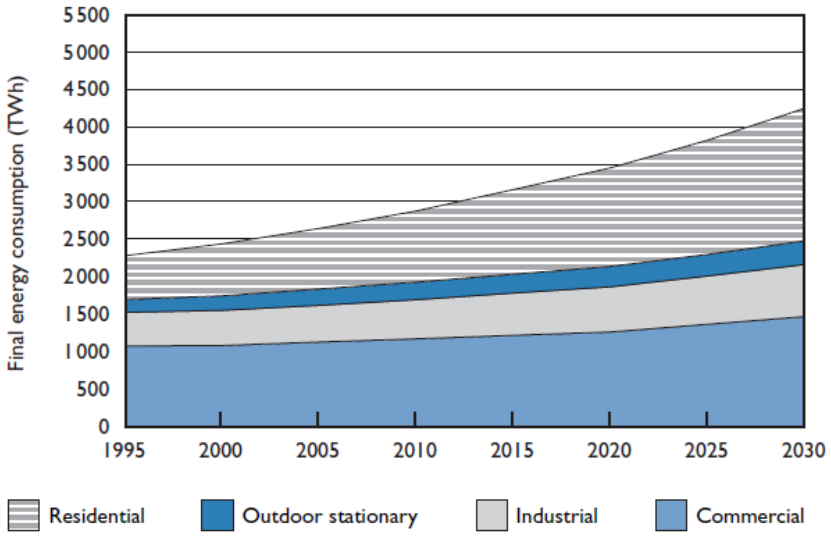

Figure 0.1: A Global lighting electricity consumption by end-use sector in 1995-2030 under the Current Policies scenario.[2]

The interest on OLED lighting is increasing since its unique characteristics allow for the alluring possibility of paper-thin flexible light sources that emit areal, warm, natural light. It can replace the small, bright spots of LEDs with sheets of light that aren't so

[2] International Energy Agency.
http://www.iea.org/Textbase/nptable/Global%20lighting%20electricity%20consumption%20by%20end-use%20sector%20in%201995-2030%20under%20the%20Current%20Policies%20scenario.pdf

piercingly bright through applications such as light tiles, partitions, and panels. But OLED lighting has yet to reach the consumer market. This is largely because OLED performance in lighting is not yet good enough.

Artificial lighting is a significant factor that contributes to the quality and productivity of human life. As a consequence, we are willing to allot huge amounts of energy to produce it. The electricity used for artificial lighting is amongst the most widespread and growing uses of energy. Lighting accounts for ~19% of total global electricity consumption, a percentage that is expected to increase with standard of living. The largest share in the consumption goes to commercial and public buildings, followed by residential lighting, industrial sector lighting and outdoor/street lighting.[6] Figure 0.1 shows the trend of the global lighting electricity consumption by the different sectors from 1995 to 2030 as reported by the International Energy Agency (IEA).

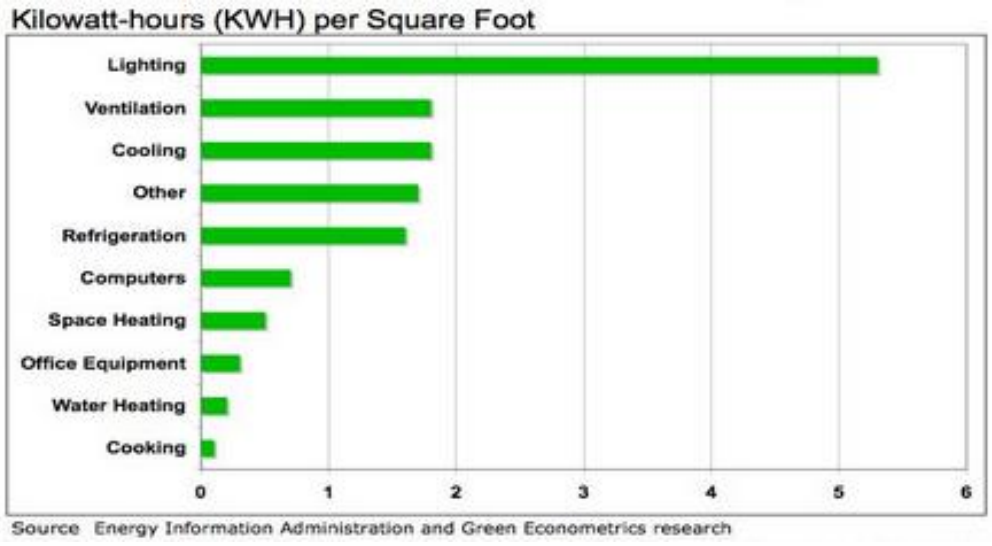

Figure 0.2: The energy intensity (in kWh/Sq. Ft.) of commercial buildings by end use.[3]

Comparing lighting to other common commercial building energy consumers, a research report from the U.S. EIA[4] concluded that lighting consumes the largest amount of electricity as measured in kilowatt-hours per square foot.[7] The data they collected, shown in Figure 0.2, reveals that lighting consumes even three times the energy consumption of air conditioning.

The electricity consumption of lighting is slightly more than that used by the nations of OECD[5] Europe for all purposes. Lighting requires as much electricity as is produced by

[3] EIA Report 2008: Electricity consumption (kWh) Intensities by End Use. http://greenecon.net/obama-energy-efficiency-and-lighting-retrofit/energy_economics.html

[4] The Energy Information Agency (EIA) is a principal agency of the U.S. Federal Statistical System responsible for collecting, analyzing and disseminating energy information.

[5] The Organization for Economic Co-operation and Development (OECD) is an international economic organization of 34 countries founded in 1961 to stimulate economic progress and world trade.

all gas-fired generation and 15% more than produced by either hydro or nuclear power. The annual cost of this service including energy, lighting equipment and labor is USD 360 billion, which is roughly 1% of global GDP. Electricity for lighting accounts for some two-thirds of this.[8]

In the white paper titled, "The Case for a National Research Program on Semiconductor Lighting," released by Sandia National Laboratories in 2000, a 3.4 % worldwide energy consumption for lighting was calculated from world data taken from the International Energy Agency together with future projections. To show some tangible numbers, the worldwide lighting cost in 1998 was about 25 quads[6] of primary fuel energy and about 2,350 TW·h of actual electricity consumed.[9] Their world data and projections are illustrated in Figure 0.3 together with U.S. data.

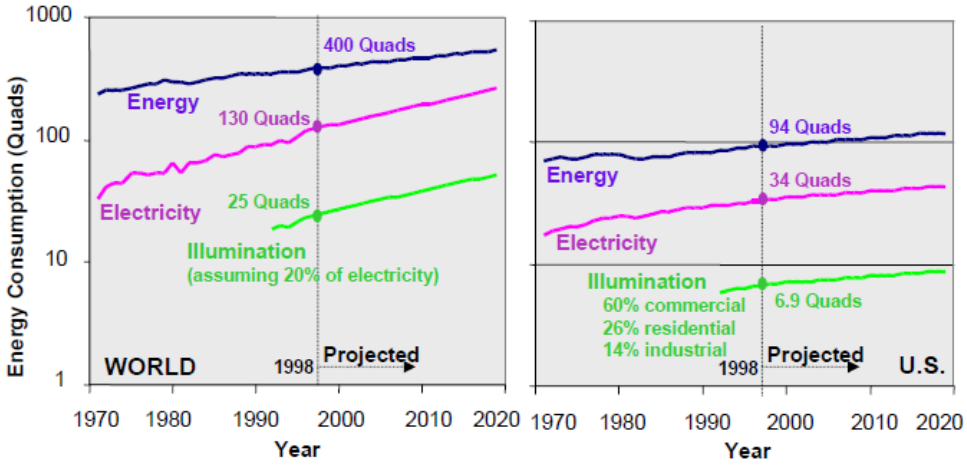

Figure 0.3: World (left) and U.S. (right) consumption of energy for use in all forms (blue),for use in electricity generation (pink) and for use in illumination (green).[9]

With a large contribution of lighting to worldwide energy consumption, it is nothing but fair that the lighting industry faces inquiries regarding energy reduction. Energy is known to be the "lifeblood of society". Its role in the global economy makes it essential in sustaining global peace and security. Its generation incurs huge direct economic and indirect environmental costs (e.g. smog and particulate emissions, acid rain, global warming, waste disposal, etc). The economic costs will increase with heightened concern on reducing the environmental costs.

As lighting consumes such a huge amount of energy, there is an equivalent amount of emitted carbon dioxide that goes with it as well. In 2006, IEA and OECD reported that the 19% of electricity consumption by lighting corresponds to a 6% of worldwide total carbon emission.[10] IEA estimated that worldwide lighting is responsible for emissions of approximately 1900 Mt CO_2 per year, roughly equivalent to 70% of the emissions from the

[6] Quad - unit of energy, short for quadrillion, 10^{15} BTU. One quad of primary energy consumed is roughly equivalent, after energy conversion and transmission losses, to 92 TW·h of electricity at the wall plug.

world's cars. 20% of these yearly emission come from the 1% of global lighting that is produced by the direct combustion of paraffin and oil lamps used by 1.6 billion people who have no access to electricity.[11] Hence, dramatically improving lighting system efficiency coupled with electrification to replace oil lamps with electric lamps would contribute in reducing the global energy consumption and controlling CO_2 emissions.

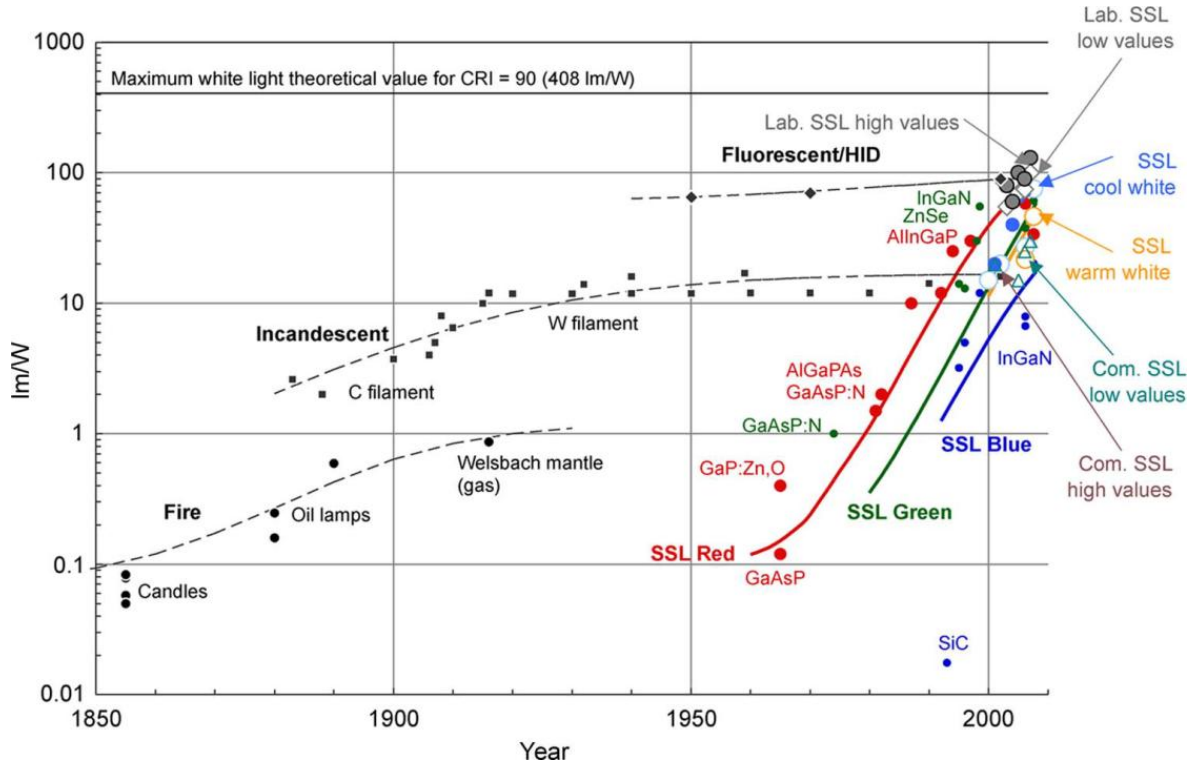

Figure 0.4: Luminous efficacies of selected lighting technologies between 1850 and 2006.[11]

SSL is an emerging technology that holds the promise of high performance features and efficiencies well beyond those of traditional artificial lighting. The evolution in the conversion efficacy of different lighting technologies since the mid-19th century is illustrated in Figure 0.4. Within the last 50 years, none of the workhorse (incandescent and fluorescent/HID) technologies have shown any significant efficiency improvements. Meanwhile, LEDs exhibit a striking steady improvement!

SSL are already known to be far more efficient than other lighting products available in the market. In the 2014 SSL Research and Development: Multi-Year Program Plan that was released by the U.S. DOE, they compared the current performance of some SSL luminaire products with conventional lighting technologies. Their table is shown in Figure 0.5. LEDs exhibit luminous efficacies that are already comparably higher to that of fluorescent lamps.[12] The efficacy of the venerable incandescent lamp actually has been approximately flat for nearly a century and is limited by the laws governing blackbody radiation. This alone immediately sets a conversion of only 5% of its power input into visible white light. The efficacy of fluorescent tubes reaches over 100 lm/W. Taking into account

also the ballast losses in a fluorescent lamp system, only up to around 28% of power input is converted to visible white light.[2, 11] In 2013, warm-white LED packages already exhibit an overall luminaire efficiency[7] of 71% under reduced operating currents.[12] LED luminous efficacy is already within the same range as that of fluorescent lamps; and depending on which LED package, the efficacy could even be way better. On average, commercial LEDs already convert around 48% of power input into visible white light; while laboratory LEDs convert even at higher percentages.[3, 11]

Product Type	Luminous Efficacy (lm/W)	CCT (K)	L_{70} (hours)
LED A19 Lamp (Warm-White)[1]	94	2700	30,000
LED PAR38 Lamp (Warm-White)[2]	78	3000	50,000
LED 6" Downlight (Warm-White)[3]	87	3500	60,000
LED Troffer 2' x 4' (Warm-White)[4]	131	3000	75,000
LED High/Low-Bay Fixture (Warm-White)[5]	119	3500	75,000
OLED Luminaire[6]	52	3500	15,000
HID (High Watt) System[7]	115	3100	15,000
Linear Fluorescent System[7]	108	4100	25,000
HID (Low Watt) System[7]	104	3000	15,000
CFL	73	2700	12,000
Halogen	20	2750	8,400
Incandescent	15	2760	1,000

Notes:
1. Based on Philips' L Prize winning A19 lamp.
2. Based on Lighting Facts database for Cree LRP38-10L-30K lamp.
3. Based on Lighting Facts database for Hubbell Lighting Prescolite LB6LEDA10L35K WH.
4. Based on Lighting Facts database for Cree CS24-40LHE-30K luminaire.
5. Based on Lighting Facts database for Cree CS18-80LHE-35K luminaire.
6. Based on Acuity Brands luminaires.
7. Includes ballast losses.

Figure 0.5: Performance of the different existing lighting technologies.[12] (Appendix A lists some definitions of technical terms regarding lighting device performance.)

Despite the many developments and product quality successes already achieved by SSL, the lighting revolution it started is yet to be won. SSL still continues to address efficacy improvement, cost reduction, and quality of light. Also, due to a required co-evolution of technical and cost innovations, markets and business models for lighting companies and

[7] The breakdown of the overall luminaire efficiency includes efficacy projection, thermal efficiency, driver efficiency, fixture/optical efficiency, and electrical efficiency (in W/W).

consumer acceptance of lighting designs that are slightly dissimilar from traditional designs, the transition from the conventional lighting to SSL is delayed. Competition with CFLs is another great delaying factor as CFLs are still ahead in price/lm.

Lighting is a global market. Nowadays, very significant demand for lighting is growing; and the more-efficient SSL devices promise to replace conventional light sources with impressive economic and environmental savings. The lighting industry, different governments and international agencies are putting in efforts to encourage the adoption of SSL by implementing policies to transform current practices, offering programs in supporting manufacturing infrastructures, and funding R&D projects to drive progress in SSL. Yet despite all these efforts to promote the use of this cost-effective lighting technology, the market still does not deliver it automatically due to several barriers that limit its deployment. End-users and key market players lack awareness of the potential for savings and the advantages of SSL product qualities. Being uninformed, they are inclined to use the technologies that they have always used. Plus, like all other emerging efficient technologies having high initial costs, users are less likely to invest on it unless they are aware of and wise enough to calculate the future savings. In residential buildings, most lighting is not installed and directly paid for by the end users, thus there are differing cost incentives for the installers and for the users. Adding to that, most of the public and private commercial organizations manage their equipment and operations budget separately and thereby create their own incentive to minimize equipment costs at the expense of higher operating costs. These and similar obstacles slow the rate at which markets learn and adopt cost-effective choices.

Steps toward a far-improved future in lighting require a united effort by every institution and every member of the population. How can we as individuals directly contribute? Embrace the wisdom around SSL and energy efficiency. ***Change a light bulb.***

Chapter 1 Introduction

Due to high efficiency, reasonable cost of ownership, controllability, light output quality, and lifetime, solid-state lighting (SSL) has the potential to become the dominant lighting technology accounting for the majority of the lighting market within the next twenty years. SSL is a type of lighting that uses semiconductor electroluminescence (EL) to produce visible light for illumination. An SSL device that uses inorganic semiconductors is a light-emitting diode (LED). A light-emitting device built with organic semiconductors is an organic light-emitting diode (OLED). In principle, the description of the SSL technology can be simplified -- electrons and holes are injected into a forward biased semiconductor *p-n* junction; when they recombine, photons are created. The resulting photons are extracted from the chip, and are then either mixed with different-colored photons from other LEDs or energy down-converted into a distribution of colors using phosphors or other down-conversion materials.

1.1 Historical key moments of solid-state lighting

Electroluminescence from inorganic semiconductors as a phenomenon was first reported in 1907 by Henry Joseph Round when he observed a light emission from a cat's-whisker[8] point contact silicon carbide crystal detector diode.[13] The first LED was created in 1927 by Oleg Losev [14], but there was no practical use made out of the discovery for several decades.[15] With the birth of semiconductor physics in the 1940-1950's, scientific developments of light emission technologies became possible. For SSL, the most influential advances are: the demonstration of GaAsP red light emission by Nick Holonyak while working with General Electric in 1962 [16], along with the similar works on GaAs of Robert Hall, Marshall Nathan, and Robert Rediker [17-19], and the demonstration of a bright GaN blue LED by Shuji Nakamura while working with Nichia Chemical Corporation in 1993 [20], along with earlier materials advances by Isamu Akasaki and Hiroshi Amano.[21, 22]

LEDs have come about with a "colorful" history. As mentioned, the first influential advancement in visible light emission was in the red. This red color dominated the early history of SSL. In 1968, the first commercial products were introduced by Monsanto as indicator lamps and by Hewlett-Packard as the first truly electronic display (a successor to the Nixie tube[9]). The initial performances of these red-emitting products were poor. The efficacy was about 0.1 lm/W. The horse race on efficacy improvement, which was prompted in the late 1980's, triggered the exploration of new materials system with higher efficacy and

[8] A cat's-whisker detector is an antique electronic component consisting of a thin wire that lightly touches a semiconducting mineral crystal to make a crude point-contact rectifier.
[9] A Nixie tube, or cold cathode display, is an electronic device for displaying numerals or other information using glow discharge.

a wider color range. AlInGaP/GaP materials emerged, covering the range of red to yellow/green. It exceeded 20 lm/W in the 620 nm red-orange part of the spectrum. The second influential breakthrough came in 1993 with the discovery of a fairly efficient blue material, GaN. Efficiency improvements followed, together with an extension of the color range from blue to green (430-530 nm).

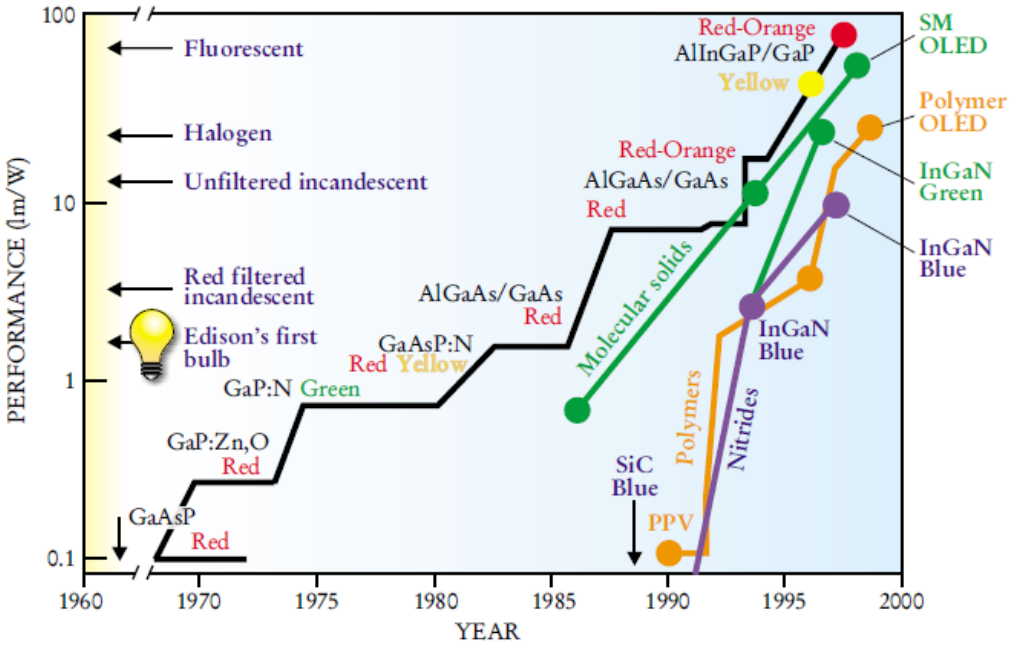

Figure 1.1: Luminous efficacy improvements of LEDs and OLEDs. The black line is a summary of three decades of work with a variety of inorganic structures. The violet line that sprouts a green branch indicates the high-performance nitride-based LEDs developed in the mid-1990s. The nearly straight green line shows the improving performance of small molecules (SM) OLEDs, while the orange line shows that of polymer OLEDs. The black arrows adjacent to the vertical axis indicate several bench-mark efficiencies of conventional lighting devices.[23]

As illustrated in Figure 1.1, the progress in the performance of LEDs was largely an outcome of the exploration and development of semiconductor materials -- first GaAsP and GaP, then AlGaAs, and finally, AlInGaP. By then, LEDs reached a point where they exhibit reasonable efficiencies that spans virtually the entire visible wavelength range. This made it possible to create white light sources from a combination of 3-6 LEDs of different colors or from a blue LED with down-conversion phosphors, enabling the penetration of LEDs into the lighting markets.

The meager beginning of EL from organic semiconductors (also called, organic dyes) goes back to 1953 when André Bernanose *et al.* [24] reported emission by applying a high AC voltage to crystalline films of acridine orange and quinacrine. In the early 1960's, Martin Pope *et al.*[25, 26] observed dark hole injection into anthracene and succeeded with obtaining EL when 400 V was applied to 10-20 μm thick single crystal anthracene devices. Following that, W. Hilfrich and W.G. Schneider [27] were able to produce double injection recombination EL at ~60 V from a 1-5 mm thick anthracene single crystal using hole and

electron injecting electrodes. By evaporating anthracene in vacuum to achieve a 0.6 μm film, P.S. Vincett *et al.* [28], who were among the first to use organic thin films, were able to lower the operating voltage to 30 V. The external quantum efficiency (EQE), however, remained very low at ~0.05%.

In a ground-breaking work, a novel structure was generated with two thin-film organic layers (~135 nm total thickness) which are independently responsible for hole and electron transport. This very first OLED device was reported by C. Tang and S. Van Slyke, while working with Eastman Kodak, in 1987.[29] The structure consisted of a vapor-deposited 8-hydroxyquinoline aluminum (Alq_3) organic small molecules as emissive layer and an aromatic diamine as hole transport layer (HTL). By adding the diamine HTL, device performance improved with an EQE of about 1% and a driving voltage of 5.5 V. Such explosive discovery marked the beginning of a rapid development of the OLED technology. By 1990, light-emitting diodes based on the conjugated polymer poly(*p*-phenylene vinylene) (PPV) as the active element was reported by J. Burroughes *et al.* [30] of the Cavendish Laboratory. They not only fabricated a luminescent polymer, they also showed it was reasonably efficient suggesting that large-area light-emitting display devices based on luminescent polymers could be developed. In 1998, the work of M.A. Baldo *et al.* [31] broke the 25% theoretical limit on the internal quantum efficiency (IQE) through the ability to harvest triplet excitons using the phosphorescent material platinum octaethylporphyrin (PtOEP) doped into Alq_3 layers. With a peak EQE of 4%, another milestone was set by Baldo since Tang's discovery. Adachi *et al.* [32] were able to push the maximum EQE to 20% with a maximum IQE of 94% in 2001. They used the phosphorescent bis(2-phenylpyridine)iridiumIII acetylacetonate [$(ppy)_2Ir(acac)$] dopant in the wide-bandgap 3-phenyl-4-(1'-naphthyl)-5-phenyl-1,2,4-triazole (TAZ) electron-transport host layer. A third class of OLED materials called dendrimers is also drawing attention in parallel with the small molecules and polymers. The use of dendrimers as the active luminophores in LEDs was first introduced by the group of J. Moore [33] in 1996. Dendrimers are branched macromolecules that consist of a core, one or more dendrons and surface groups. The different parts of the dendrimer can be selected to give the desired optoelectronic and processing properties. The first light-emitting dendrimers were fluorescent, but more recently, highly efficient phosphorescent dendrimers have been developed.[34] Green phosphorescent dendrimer OLEDs were reported in 2002 to have an EQE of up to 16% which corresponded to an IQE of 80%.[35] At the turn of the century, this overall performance demonstrated by OLEDs already allowed it to go into mainstream display and general illumination applications.

1.2 Motivation of this study

Hybrid organic-inorganic systems have also drawn much attention in the field of solid-state lighting in the last decades due to their potential in combining the favorable properties of two distinct material classes. Inorganic layers provide the potential for semiconducting properties, high charge-carrier mobility, and thermal and mechanical stability, while the organic layers offer brightness of emission, efficient light-matter coupling and structural flexibility.

1.2.1 Brief overview of literature on organic-inorganic hybrid devices

A plethora of organic-inorganic device designs that give their own unique optical and electronic properties have been presented in literature covering from active layers comprising of polymer matrices with embedded inorganic nanoparticles, heterojunctions, organic acceptor/inorganic donor structures, hybrid multilayer structure and microstructures, and so on. The hybrid devices that are mentioned here are just to name but a few.

In the 1990s, it was reported that CdSe nanocrystal clusters/(PPV [10] [36], PVK [11] [37]) polymer bilayers and blend composites can be used to make blue light emitters. TiO_2 nanoparticles blended into electroluminescent (Rhodamine 640 [38], MEH-PPV [12] [39]) organics to form solutions and dilute films exhibited laser emission with greatly reduced threshold pump powers. Insulating oxide nanoparticles (SiO_2, TiO_2) mixed into MEH-PPV resulted to increased current densities, radiances, and power efficiencies in light-emitting diode devices.[40] Organic-inorganic multilayer-structured light-emitting devices [41] which consist in most general case of alternating sequence of thin inorganic and organic layers sandwiched between two electrodes were also reported to have improved performance.

Since less than a decade ago, reports on emissions from hybrid devices showed a great influx. ZnO nanowires/PEDOT-PSS [13] [42, 43], ZnO nanorods/MEH-PPV [44], ZnO/α-NPD [14] [45], ZnO nanoparticles/TPD [15]:PMMA [16] blend [46] and PFO [17]/ZnO nanorods/PMMA [47] hybrid heterojunction or *p-n* devices exhibited EL from radiative charge recombinations in the ZnO, in the organic layers or in both. Similar multilayered devices based on ZnO nanorods/(PFO [48], PFO:TFB [18] blends [49]) junctions were also demonstrated. There are also reports on luminescence from hybrid junction LEDs composed of *n*-type GaN/InGaN multiple quantum wells and α-NPD [50] and of

[10] PPV: *p*-paraphenylene vinylene
[11] PVK: Polyvinylcarbazole
[12] MEH-PPV: Poly(2-methoxy,5-(2'-ethyl-hexyloxy)-1,4-phenylene-vinylene)
[13] PEDOT-PSS: Poly(3,4-ethylene-dioxythiophene)-poly(styrene-sulfonate)
[14] α-NPD: N,N'-diphenyl-N,N'-bis(1-naphthyl)-1,1'-biphenyl-4,4'-diamine
[15] TPD: N,N'-diphenyl-N,N'-bis(3-methylphenyl)-1,1'-biphenyl-4,4'-diamine
[16] PMMA: Poly(methyl methacrylate)
[17] PFO: Poly(9,9-dioctylfluorene)
[18] PFO-TFB: Poly(9,9-dioctyl-fluorene-co-N(4butylphenyl)-diphenylamine)

GaAs/AlGaAs single quantum well and U3[19] [51]. In order to have air-stable charge injection contacts and solution processability, metal oxides were introduced into organic optoelectronics. Several hybrid organic-inorganic lighting emitting diodes (HLEDs) based on this have been reported.[52-56]

For nanocomposite structures, large enhancements in luminescence were observed from PFO that is doped with ZnO nanoparticles [57] and from P3HT[20] that is incorporated with ZnSe quantum dots (QDs) [58]. In the case of CdSe/ZnS QDs (3.2 nm in diameter) embedded in a PFO matrix host [59], charge trapping and EL at the QDs were observed. Figure 1.2 shows their device layer structure, the corresponding energy level diagram and HR-TEM of 80 wt% QD embedded in PFO. And with the development of colloidal QDs[21], increasingly active researches that are aimed at applying these nanoparticles in optoelectronic technologies have been motivated due to their unique size-dependent optical properties. Because of the benefits of ease of processing, low cost, substrate flexibility, large area coverage and size-tunable absorption-emissions, researches on QD-polymer composites for light emission have progressed in recent years. Reported EQEs of such devices [36, 37, 60-70] increased from less than 0.01% to around 18%, approaching those of molecular OLEDs.

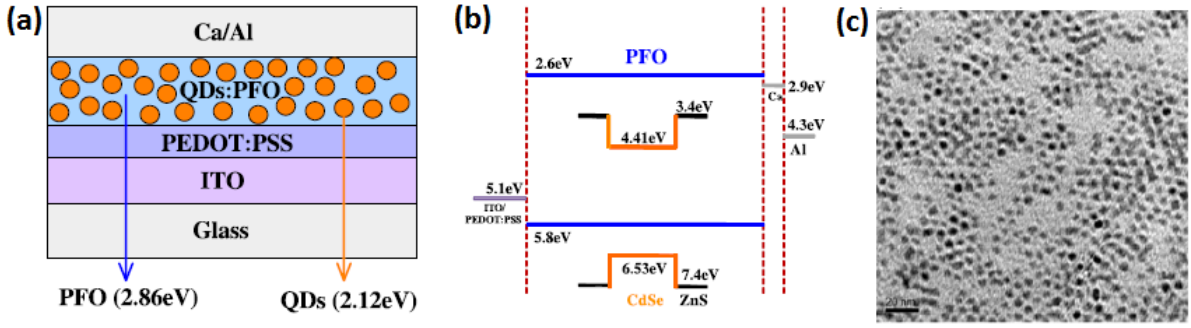

Figure 1.2: A schematic of a single layer device structure that shows CdSe/ZnS QDs embedded in a PFO layer sandwiched between ITO and Ca/Al electrodes. Arrows indicate the EL energy peaks of the QDs and PFO (a). Energy level diagram of the device, where all indicated energies are with respect to the vacuum level (b). HR-TEM of 80 wt% QD embedded in PFO (c). The figures are taken from [59].

The observed performances of the aforementioned hybrid devices are accounted to efficient energy/charge transfer from the nanoparticles to the polymer chains (or vice versa), charge trapping, increase of polymer chain separation distance, to structural effects such as change in device morphology that lead to healing of shorts and pinholes, and to increased

[19] U3: 3-[(2Z)-5-chloro-2-([(3E)-3-([5-chloro-3-(3-triethylammonium-sulfonatopropyl)-1,3-benzothiazol-3-ium-2-yl]methylene)-2,5,5-trimethylcyclohex-1-en-1-yl]methylene)-1,3-benzothiazol-3(2H)-yl]propane-1-sulfonate

[20] P3HT: Poly(3-hexylthiophene-2,5-diyl)

[21] Colloidal QDs are solution-processed nanoscale crystals comprising of a small inorganic semiconductor core (1-10 nm in diameter), often a wider-bandgap inorganic semiconductor shell, and a coating of organic passivating ligands

and more balanced charge-carrier injection and confinement effects. Other proposed mechanisms of luminescence of embedded QDs in literature are based on: (a) carrier recombination following direct charge injection, (b) radiative recombination after exciton transfer or (c) combined contribution from the afore-mentioned processes, as depicted in Figure 1.3.

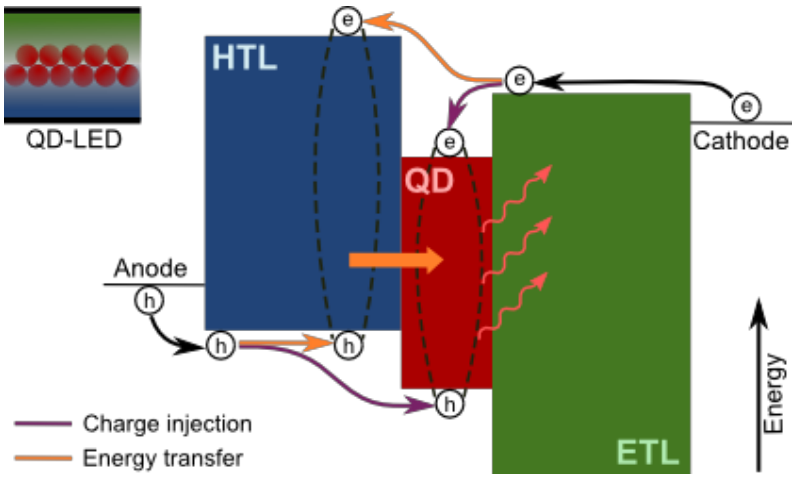

Figure 1.3: An energy band diagram of a typical QD-LED with organic electron and hole transport layers. Charge injection and energy transfer are outlined in the diagram as two possible mechanisms for QD excitation.

1.2.2 Novel hybrid active layer approach

Polymer/nanoparticle composites are increasingly being studied because of the unique optical and electrical properties they can offer. In photovoltaics for example, the incorporation of CdSe and C_{60} nanoparticles into a photoconducting organic material, such as MEH-PPV, resulted to improved photovoltaic efficiency.[71-73]

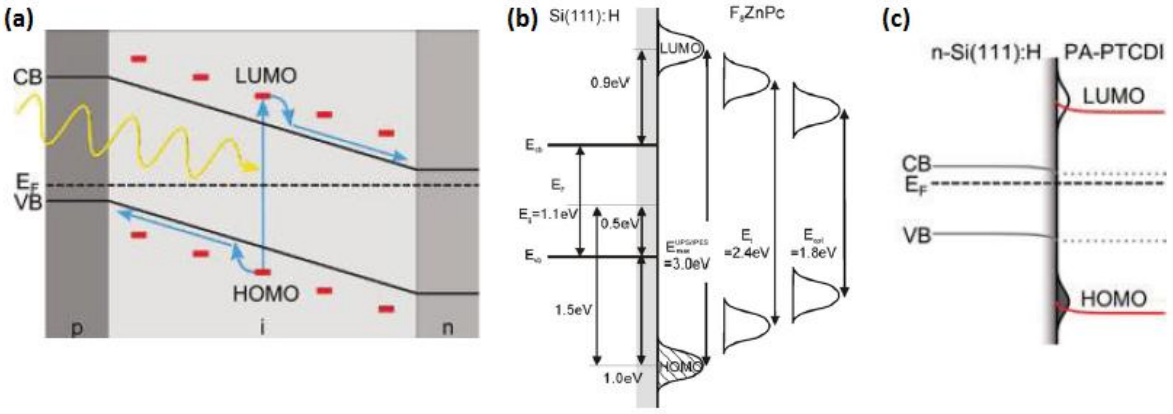

Figure 1.4: Electronic structure of the bulk composite absorber in a *p-i-n* device structure (a). Energy band diagrams of the Si(111):H/F_8ZnPc interface (b) and *n*-Si(111):H/PA-PTCDI interface (c) as determined from PES measurements. The figures are taken from [74, 75]

Previously, our group reported composites of inorganic matrices embedded with organic small molecules. These hybrid composites were comprised of Si and ZnSe matrices doped with fluorine-substituted zinc phthalocyanines [74, 76] and with perylene diimides derivatives [75]. The concept followed was bulk sensitization of inorganic semiconductors by highly absorbing organic dye molecules. From photoelectron spectroscopy (PES) measurements, energy band diagrams, as shown in Figure 1.4, were derived showing the possibility of engineering the dye molecules in a way such that the dye frontier orbitals line up symmetrically outside the energy gap of Si. This line up offers energetic driving forces for electron and hole transfer from the photo-absorbing dye to the Si matrix as required for steady state operation.

For light emission on the other hand, an organic host matrix is traditionally designed and optimized to promote energy transfer or electron and hole trapping with subsequent recombination on an organic or an inorganic dopant which can lead to efficient harvesting of excitons.[59, 64, 77, 78] From our knowledge considering the hybrid designs we encountered in literature for light emission, there has been no report yet on organic light-emitting phases that are embedded into inorganic matrices. In this work, we introduce a HLED concept where luminescent organic dye molecules are doped as radiative recombination centers into an ambipolar conductive inorganic semiconductor matrix.[79] Figure 1.5 shows the proposed composite active layer scheme where organic small molecules are embedded in an inorganic matrix. For this scheme, the HOMO and LUMO of the organic luminescent materials are nested in between the valence (VB) and conduction (CB) bands of the inorganic semiconductor.

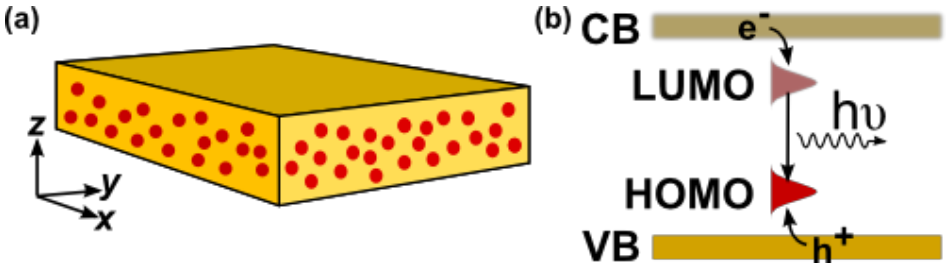

Figure 1.5: Schematic representation of the proposed bulk composite as an electroluminescent active layer for HLEDs comprising of an inorganic semiconductor matrix doped with organic small molecules (a) and the corresponding designated energy level diagram for direct electron/hole transfer from the inorganic wide bandgap semiconductor matrix to the dopants with subsequent radiative emission from the dopants (b).

In this novel approach to light emission, it is conceptualized that the inorganic semiconductor for the host matrix material must have an energy gap that is larger than that of the organic dye dopant in order to position the dye's HOMO and LUMO within the gap. Assuming that the host emissive layer is also the electron (hole) transport layer, the dye's LUMO (HOMO) must not be significantly higher (lower) in binding energy than the host CB (VB). If so, in dilute concentrations, the dopant molecules would then act as deep electron

(hole) traps that hinder transport through the device. The mechanism of dye luminescence can be any of the following: carrier recombination upon direct charge injection, recombination after energy transfer from the host matrix to the dye dopant, or a combination of any of these. With a matrix that allows ambipolar charge transport, a possible advantage with regard to the design of the device would be the elimination of additional charge transport layers.

1.2.3 Interface characterization as immediate focus of research in this work

Despite the successes achieved by HLEDs and the number of studies that demonstrate energy transfer and charge-carrier injection and trapping, there is a relative lack of quantitative understanding about the actual energy alignment at the interfaces between the organic and inorganic materials in these devices. Hybrid designs whose operations rely on efficient charge carrier transfer or injection impose a strict energy level alignment at the material interfaces. Thus, it is of critical importance to experimentally deduce the alignment of the conduction band (CB) and valence band (VB) states in the inorganic semiconductors against the highest occupied molecular orbital (HOMO) and lowest unoccupied molecular orbital (LUMO) levels in the organic semiconductors within the hybrid system. The electronic and chemical properties of the interface that is formed will govern the transfer of electrons and holes between the materials and other crucial processes in the HLED.

There are quite a number of reports in literature that highlight the importance of understanding the actual properties of interfaces in light-emitting devices. For example in the work of S. Blumstengel *et al.* [80], they were able to successfully confirm their photoluminescence (PL) transient results derived from cw and time-resolved photoluminescence (TRPL) spectroscopy from their PES-derived energy level alignment of a ZnMgO/SP6[22] interface in explaining the efficient dissociation of excitons via charge separation at the interface. I.G. Hill *et al.* [81, 82] studied the interfaces formed from depositing metal-quinolate derivatives (Gaq_3, Alq_3, $Almq_3$) on Ag by PES in order to understand the charge injection and transport processes in organic semiconductor devices. S.T. Lee *et al.* [83] and S. Olthof *et al.* [84] were able to explain the improved efficiency in a multilayer OLED through direct measurements of the electronic properties of the interfaces in the device. And for getting the desired functionality in devices, R. Schlesinger *et al.* [85] and S.Y. Kim *et al.* [86] used PES to be able to tune the energy level alignments of ZnO/F4TCNQ[23] and ITO/IrO_x/α-NPD, respectively.

Experimental approaches on determining material interactions that govern interface formations in order to quantify the electronic structure and chemical properties are

[22] 2,7-bis(biphenyl-4-yl)-2',7'-ditert-butyl-9,9'-spirobifluorene
[23] 2,3,5,6-tetrafluoro-7,7,8,8-tetracyanoquinodimethane

dominated by PES.[87] Following the general approach of the Surface Science research group, this work is aimed at obtaining knowledge of the electronic surface and interface properties of prospective organic and inorganic semiconductors for the proposed HLED concept. PES is used as the principal characterization tool coupled with the utilization of accepted clean sample preparation and deposition techniques. To determine energy band lineups at interfaces, the general procedure includes a stepwise-deposition of one material on top of another.[88] The measurement provides detailed information on the elemental composition and on the respective chemical states, binding energies and surface and interface potentials which are necessary to draw the interface energy band diagram and understand the electronic properties of the interface.

1.2.4 Scope and limitations of the study

With the proposed composite design for active layers in HLEDs, direct charge transfer from the transport host matrix to the luminescent guest dopants is critical for EL. Wide-bandgap inorganic semiconductors and luminescent organic dyes are chosen as candidate materials for study. The focus is on characterizing the organic-inorganic interfaces of different material combinations; basically aimed at finding a material combination where the HOMO and LUMO of the organic dye are nested in between the valence and conduction bands of the inorganic matrix in order to promote transfer of charge carriers. As another possible mechanism for EL is the transfer of exciton energy from the matrix to the dopant, the potential for a Förster resonance energy transfer (FRET) from the inorganic matrix to the organic dopants is also investigated through absorbance and photoluminescence measurements.

Several of the candidate materials are investigated and presented in this thesis, namely -- ZnSe, ZnO, and nc-TiO_2 for the inorganic and Ir(BPA) and TSQT monomer for the organic phases. The preparation of thin film samples of pristine materials, bilayers and composites include physical deposition via thermal evaporation of powder materials, metal organic chemical vapour deposition, spin coating, screen printing, and solution drop-casting.

1.3 Thesis outline

The thesis is organized as follows:

In Chapter 2, general descriptions of SSL device operation and design are given. The relevant properties of the materials, namely, inorganic and organic semiconductors, of which SSL technology is comprised of, together with the different optophysical properties and material interface interactions, are presented.

In Chapter 3, the different methods followed in the conducted experiments of this study are described. Since a major part of this thesis is on interface characterization, PES is described to some detailed extent.

In Chapter 4, two materials, namely, the inorganic wide bandgap semiconductor zinc selenide (ZnSe) and a commercial organic small molecule red triplet emitter Ir(BPA), are introduced. Material general descriptions and deposition methods, together with their measured properties, are presented.

In Chapter 5, results of the PES investigations on the interface formation of these two materials in three deposition configurations, namely: (1) ZnSe/Ir(BPA) heterojunction where Ir(BPA) is deposited on a ZnSe film, (2) Ir(BPA)/ZnSe heterojunction where ZnSe is deposited on an Ir(BPA) film, and (3) ZnSe+Ir(BPA) composites where ZnSe and Ir(BPA) are co-evaporated on a clean transparent conductive substrate, are presented and analyzed in detail. The band diagrams for the energy level alignment at the interfaces are derived and checked for a possible electron and hole transfer from the ZnSe to the Ir(BPA) as proposed in our novel hybrid active layer approach. The chemical compositions and descriptions of the coupling of the two materials on the atomic scale are given.

In Chapter 6, results of the additional experimental investigations that were performed on the ZnSe+Ir(BPA) composites are presented in order to give a fuller description of the characteristics of the composite material. Analyses on optical absorption and emission characterizations that were performed are presented to argue on a possible Förster energy transfer from ZnSe to Ir(BPA).

In Chapter 7, designs for hybrid devices based on the ZnSe - Ir(BPA) material system, together with details on the fabrication and results of the characterizations, are shown and discussed.

Experimental investigations were actually performed in this study on several material systems in order to find out the feasibility of an inorganic-organic semiconductor combination in implementing our proposed hybrid active layer design.

In Chapter 8, results of our investigations on a zinc oxide (ZnO) - Ir(BPA) material system are presented. A description of the ZnO film deposition method is included, together with several results from the different material characterizations that were performed. PES-derived interface band diagrams of bilayers are shown and compared against the proposed design.

In Chapter 9, results of our investigations on an anatase nanocrystalline titanium dioxide (nc-TiO_2) - TSQT material system are presented. TSQT is a laboratory-synthesized monomeric squaraine-derived molecule. The materials are described based on the experimental characterizations performed on them. The energy band diagram of the composite material is drawn according to the results obtained from PES measurements. In addition, results from photoluminescence measurements performed on composites are presented.

In Chapter 10, our final perspectives and outlook in terms of the plausibility of our hybrid active layer design for light emission are summarized. Within the chapter, the critical issues that must be overcome in order to possibly further advance the testing and application of

this design are presented. These issues basically fall within three main categories: (1) the energy level alignment at the interface, (2) chemical stability of the materials when combined and (3) the availability of methods for layered sequence and composite depositions.

Chapter 2 Background of the study

The basics of SSL technology are presented in this chapter. Theoretical concepts that describe the electronic and photophysical properties of organic semiconductors are outlined. Some details on the mechanisms of electroluminescence in donor-acceptor molecular systems are presented. And since all optoelectronic device performances are largely determined by the properties of the interfaces formed between the different layers within the devices, the principles governing interface formation are presented.

2.1 Solid-state lighting: Light-emitting and organic light-emitting diodes

LEDs are the primary SSL technology. It is a photonic device used as a light source that converts electrical energy into optical radiation. Semiconductors used in LEDs are crystals comprising of combinations of typically two or three inorganic elements. The essential elements are an electron-carrying *n*-layer and a hole-carrying *p*-layer that forms a *pn* junction. A light-emitting device built with organic semiconductors is an OLED. An OLED works much like a LED except that it features an electron injecting contact (cathode) instead of the *n*-layer and hole-injecting contact (anode) instead of the *p*-layer. LEDs can render point sources of light, while both LEDs and OLEDs can be area sources of light.

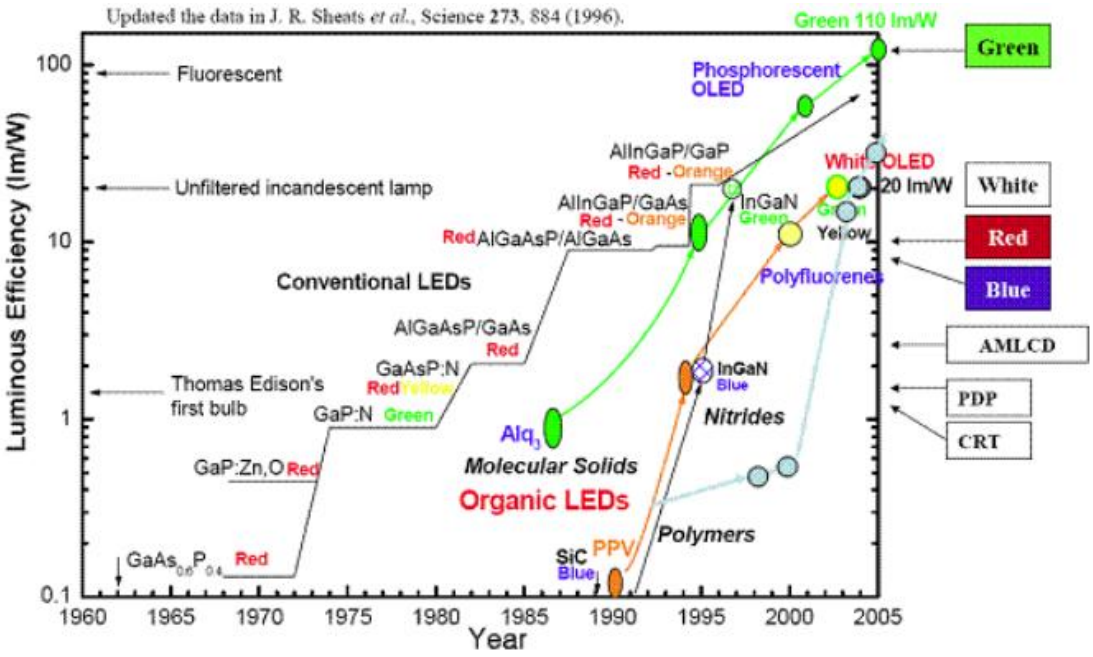

Figure 2.1: Historical progress of LED and OLED materials.[24]

[24] Figure taken from the website of Center of Super-Diamond and Advanced Films, City University of Hong Kong. http://www.cityu.edu.hk/cosdaf/oled_material.htm

Together with LEDs, research on materials for OLEDs has also been extensive. The progress in the development of materials used for LEDs and OLEDs is displayed in Figure 2.1. OLEDs have been successfully commercialized in displays and are expected to be introduced for SSL in the near future.[31, 89, 90] Phosphorescent OLEDs (PHOLEDs) have been considered as the ultimate technology because they can give internal quantum efficiencies of 100%.[31, 91, 92] Tremendous improvements in devices have been achieved using phosphorescent emissive Ir-based complexes.[91, 93-95] Most of the commercialized high-performance PHOLEDs now employ metal complex emitters incorporating metals such as iridium or platinum.

Solution and vapor deposition techniques are both being explored for OLED manufacturing. Hybrid approaches to device design are common. Vacuum-deposited OLEDs are processed by sublimation of small molecular organic materials in an ultra-high vacuum (UHV) chamber which then condense onto the substrate. Solution-processed OLEDs are prepared from polymer solutions by use of different techniques such as spin-coating, rubber stamping, doctor-blading or inkjet-printing.

2.1.1 Device operation

In order to grasp the importance of the properties of material interfaces and their impact on device performance, the basic working principle of these optoelectronic devices needs to be considered. A LED is typically a *pn*-junction (Figure 2.2) diode that emits light.

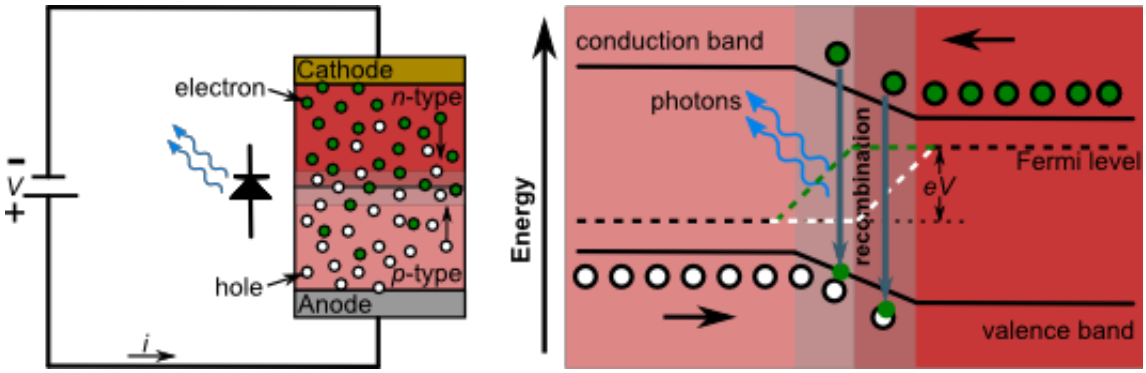

Figure 2.2: LED basic working principle. A LED operated with a forward bias leads to current flow, thereby injecting minority carriers into the region of the majority carriers. Photons are emitted during the recombination of electrons and holes.

The junction is created by putting in contact a *n*-type semiconductor and a *p*-type semiconductor; it dictates the rectifying behavior of the device as well as provides the active sites for electron and hole recombination. When a forward voltage is applied to create a flow of charge carriers into the junction, electrons would be able to meet with holes, recombine

and release energy in the form of photons.[25] This basic operation of a LED is visually outlined in Figure 2.2.

The working principle of a typical one-layer OLED is illustrated in Figure 2.3. The organic emissive layer is sandwiched between two electrodes, one of which is transparent in the visible range for the outcoupling of light. For the operation of the OLED, a voltage is applied to conduct an electric current through the emissive layer that then leads to luminescence.

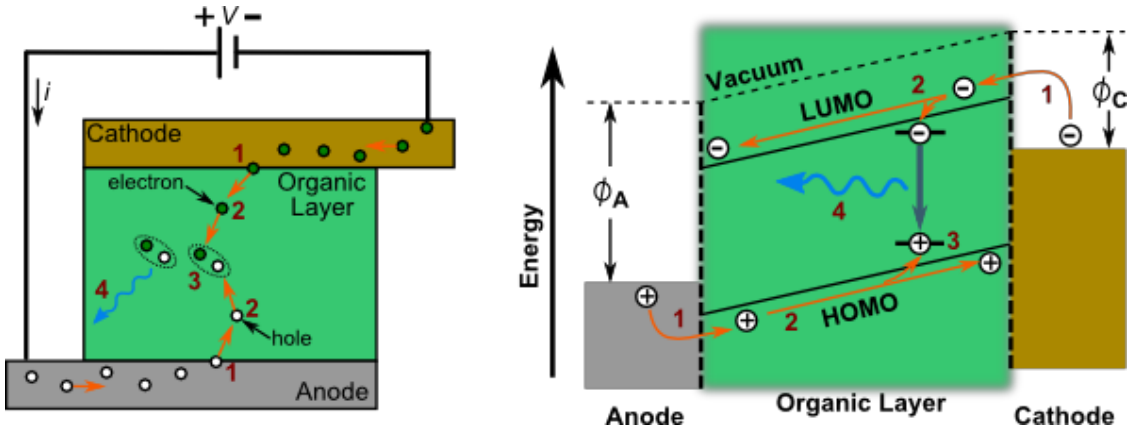

Figure 2.3: OLED basic working principle. An organic layer is sandwiched between a transparent conductive oxide as anode and a low-work function metal as cathode. Four steps of the light generation process in an OLED: (1) charge injection, (2) charge carrier transport, (3) exciton formation and (4) exciton recombination.

The light emission process in an OLED can be summarized in four basic steps:

(1) Charge injection. Free charge carriers (electrons and holes) are injected at the interface between the contact electrodes (cathode and anode) and the organic emissive layer. The contact resistances strongly depend on the electronic barrier height at the interfaces.

(2) Charge carrier transport. The injected carriers traverse the organic layer until recombination takes place. The applicable description of the charge transport ranges from a hopping mechanism for low-conducting amorphous organic films to band transport for single crystalline organic layers.

(3) Exciton formation. A localized exciton is formed when an electron and a hole becomes bound together by the electrostatic Coulomb force. These excitons are still mobile and follow the complex mechanisms dictated by quantum spin statistics on the combination and annihilation of excitonic states.[96, 97]

(4) Exciton recombination. The emission of light is the direct result of the radiative recombination of a fraction of the formed excitons. The energy of the emitted photon corresponds to the optical band gap (minus the exciton binding energy) which is governed accordingly by the molecular properties.

[25] This effect is called electroluminescence.

2.1.2 Organic light-emitting diode architecture

The architecture of OLEDs has evolved from being single-layered to multilayered as summarized in Figure 2.4.

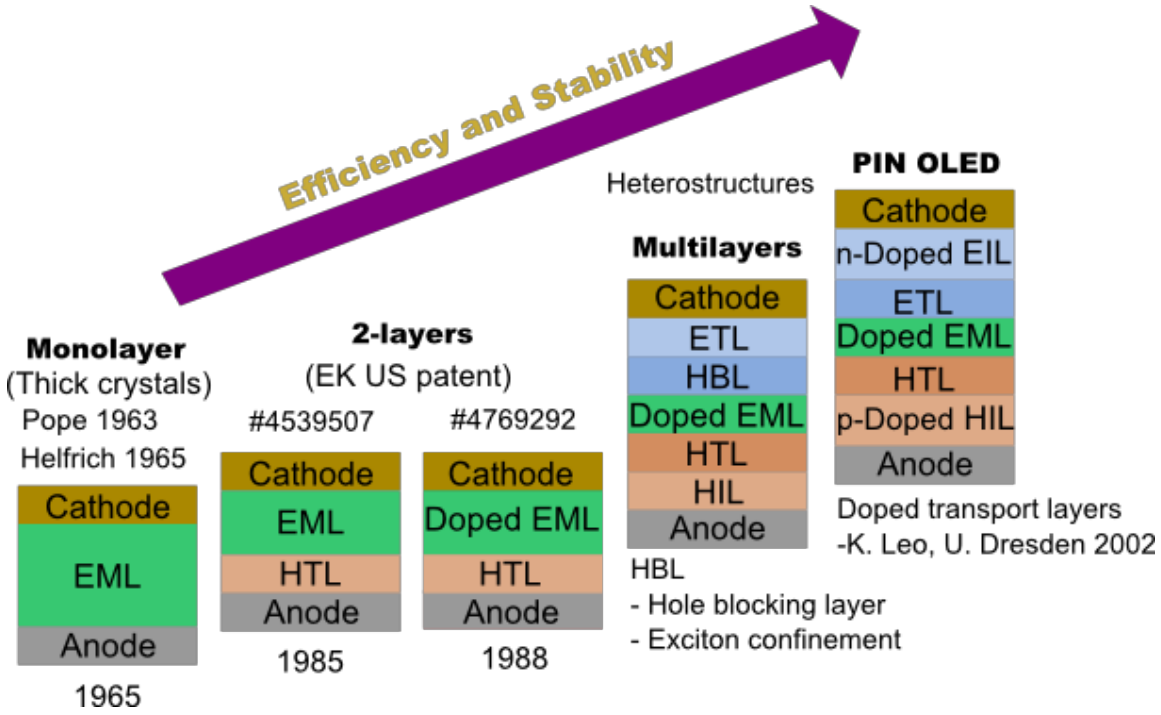

Figure 2.4: Evolution of OLED devices. (EML: emissive layer, HTL: hole transport layer, ETL: electron transport layer, HBL: hole blocking layer, HIL: hole injection layer)

A single layer OLED typically consists of a low work function cathode (e.g. Ca, Al, Ba), an organic emissive layer (EML) and a transparent anode (e.g. indium tin oxide ITO, fluorine-doped tin oxide FTO). The drawback with this design is that a balanced charge injection and carrier mobility is not observed resulting to decreased efficiencies because of exciton quenching processes close to the electrode or non-radiative recombination of charges at the electrodes. The state-of-the-art OLED has up to five layers. The aforementioned problems are addressed by incorporating hole (HTL) and electron (ETL) transport layers that sandwich the EML. The HTL and ETL provide facilitated charge injection and enhanced recombination in the emissive layer, shifting the active zone toward the middle of the OLED structure. To facilitate efficient charge injection into the transport layers, injection layers for holes (HIL) and electrons (EIL) are placed in between the transport layers and their adjacent electrodes. Despite excellent device performance, the thin EML and the complex design architecture of a multilayer OLED are, nevertheless, not desirable from the manufacturing perspective.

2.2 Material: Semiconductors

Technically, the term "semiconductor" is applied to materials that act as insulators at zero temperature according to the band theory. At such temperature, semiconductors have a fully occupied valence band (VB) and fully unoccupied conduction band (CB). Above zero temperature and well below the melting point of a solid where thermal energy can be gained by the electrons in the valence band, the solid becomes conductive. With a small gap in between these two bands, only a certain amount of energy is needed to excite the electrons from the valence to the conduction band. The electrons that are promoted to the conduction band become free from the nuclear charge of the atom and thus can move freely around the band. This free-moving electron, which is called a negative charge carrier, in this band causes electrical conductivity of the solid. When an electron leaves the valence band, the state it occupied then becomes a positive charge carrier, also called as hole.

A large number of elements and compounds exhibit semiconducting properties. These include some of the pure elements in Group 14 (e.g. Si and Ge), binary compounds of elements from Groups 13 and 15 (e.g. GaAs), Groups 12 and 16 (e.g. ZnO) and groups 14 and 16 (e.g. PbS), and within group 14 (e.g. SiC), and some ternary compounds, oxides, and alloys. Most of them are crystalline solids; while amorphous and liquid semiconductors are also known. The discovery of the dark and photoconductivity of anthracene crystals [98, 99] and the high conductivity of a perylene-iodine complex [100], which demonstrated that organic compounds can carry current, added organic solids into the list of semiconductors.

Organic semiconductors are basically organic solids of compounds that have carbon atoms as their essential structural elements. These solids can be in the form of single molecules, oligomers or polymers. Aside from consisting basically of carbon and hydrogen, nitrogen and oxygen can be contained too in these solids; while halogens can be incorporated to make them highly reactive. To add to that, a vast set of organic hybrid molecules that contain metal atoms in their molecular structures is also popular.

In comparison with purely inorganic semiconductors, the low Z[26] count and the large, complex structure of the organic semiconductors result to very low densities for these materials. This gives them unique characteristics with regard to their interaction with outer influences (e.g. stress, photons, electrons, neutrons and atoms) and also to their interactions with each other. The very difference in fundamental properties brings about challenges as well as chances for unique applications in the field of optoelectronics. Due to the weak chemical intermolecular bonds in organic semiconductors, only low processing temperatures are required to break the bonding and evaporate the materials; the final product may not be as stable as its inorganic counterpart though when it comes to, for instance, physical attributes and sensitivity to electromagnetic radiation. Encapsulation, degradation and lifetime, thus, remain as major challenges in the processing of organic

[26] Z denotes the atomic number

semiconductors. Also, these attributes dictate on the measurement method for the examination and classification of organic semiconductors, and lead to characteristic features in the measured data. The evaluation of these data can be challenging yet lenient enough for chances to extract precise and relevant information as in the case of similar inorganic semiconductors.

2.2.1 Electronic structure of organic semiconductors

The semiconducting behavior of organic solids is based on the bond forming abilities of the carbon atom. Through sp^2 hybridization [27] of carbon (shown in Figure 2.5), a bonding comprising of one strong σ bond and one weak π bond can be generated with a neighboring carbon atom. To illustrate in the simplest case of ethylene, the σ bond is formed by the head-on overlapping of one sp^2 orbital of a carbon to one sp^2 orbital of another as depicted in Figure 2.6. The π bond is formed by the overlapping of the remaining p orbitals of the two carbon atoms. The two electronic systems are distinguishable due to their orthogonality. The sp^2 orbitals form a localized, covalently bonded σ-electron system that generally becomes the backbone of molecules. The p orbitals form a π-electron system which is significantly weaker bound than the σ system due to the small overlap in the parallel orientation, but is indispensable in contributing to the semiconducting properties of organic solids as electrons are delocalized and can move freely within this bond.

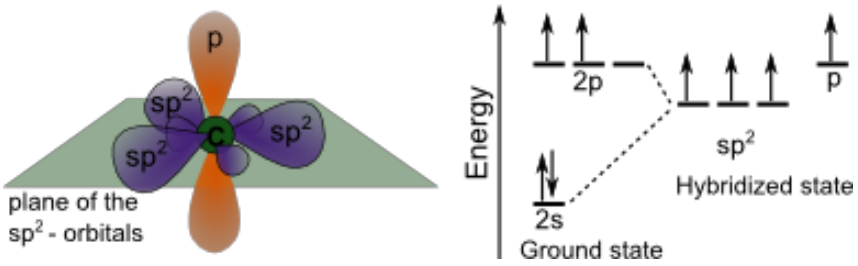

Figure 2.5: sp^2 hybridization of carbon. The combination of one s and two p orbitals from the same valence shell gives a set of three sp^2 hybridized orbitals that have equivalent energy levels but are 120° spatially apart on a single plane. The remaining p orbital lies perpendicular to this plane.

An illustration for the formation of molecular orbitals is also shown in Figure 2.6 for ethylene. The energy difference between the occupied bonding σ and unoccupied antibonding σ* orbitals is quite large and beyond the visible spectrum. But the energy difference between the occupied bonding π and the unoccupied antibonding π* orbitals is significantly smaller, leading to the strong absorption within or near the visible spectrum. Therefore, the lowest electronic excitations of conjugated molecules actually correspond to

[27] The concept of hybridization involves internal linear combination of atomic orbitals, wherein the wave functions of atomic *s* and *p* orbitals are added together to generate new hybrid wave functions. For example, if four atomic orbitals are added together, then four hybrid orbitals are formed. Each of these hybrid orbitals consists of 25% s character and 75% p character, and is described as sp^3.

the π - π* transitions with the π molecular orbital as the highest occupied molecular orbital (HOMO) and the π* molecular orbital as the lowest unoccupied molecular orbital (LUMO).

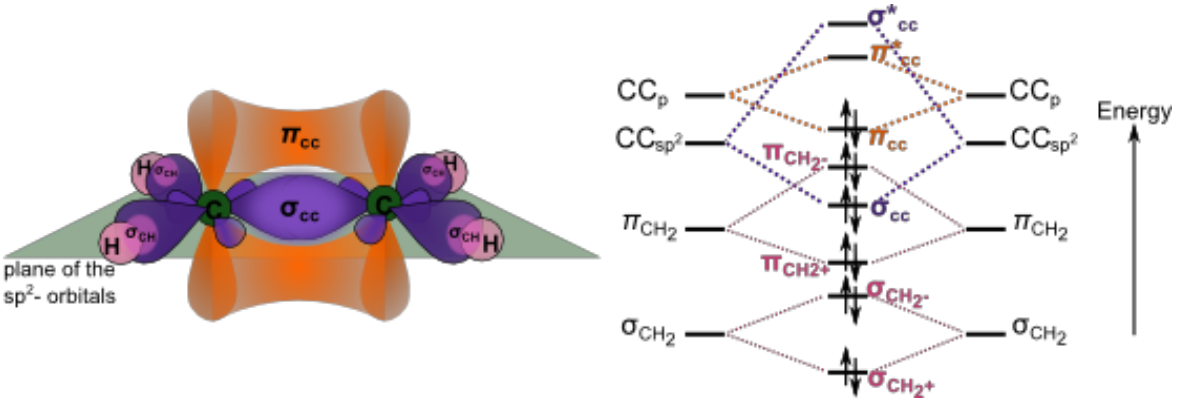

Figure 2.6: Orbital structure of ethylene (C_2H_4). End-to-end overlap of sp^2 orbitals results to a σ bond between the two carbon atoms, while side-to-side overlap of p orbitals result to a π bond.

When more carbon atoms bond to form larger molecules, the π-electron system becomes completely delocalized to form a conjugated system that often extends over the entire length of the large molecules. Two main classes of π-conjugated materials according to molecular weight can be considered: low molecular weight organic materials are usually called small molecules and high molecular weight organic materials are called polymers. The gap between occupied and empty states in these π-systems becomes smaller with increasing delocalization, leading to absorption and fluorescence in the visible. As conjugated π-systems, become larger, the energy difference for a π - π* transition becomes increasingly narrow.

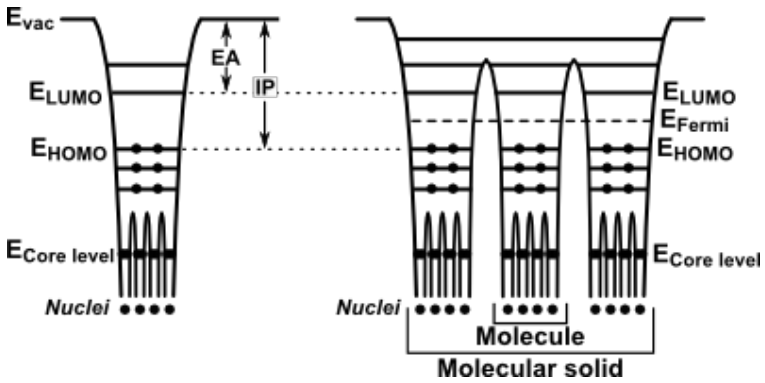

Figure 2.7: Potential well representation of the electronic structures of a molecule and a molecular solid as explained by Ishii *et al*. Figure adapted from [101].

In contrast to the strong intramolecular forces in the molecular structure, organic crystals and solid-state aggregates of molecules are held together by weak van der Waals forces. It is because of this weak interaction that an organic solid could retain the properties of the molecules that comprise it as illustrated in Figure 2.7 from the theoretical model of

Ishii *et al*. From experiments, however, energy levels have been shown to be quite different in molecules and in molecular organic solids.[102] The measured variations that organic solids exhibit relative to isolated molecules are due to polarization and relaxation processes involved in achieving stability upon the addition or removal of a charged particle and to the employed measurement method, leading to the energy level scheme shown in Figure 2.8. Electronic polarization of the surrounding molecules accounts for most of the screening of the central charge and occurs within a time scale of ~10^{-16} - 10^{-15} s. Molecular relaxation accounts for the conformational changes of the molecular ion itself due to the charge and occurs within a time scale of ~10^{-14} s. Lattice relaxation accounts for the response of the structure of the molecular solid in the immediate vicinity of the charged molecule and occurs within a time scale of ~10^{-13} - 10^{-12} s. The energetic contributions of the molecular (~0.15 eV) and lattice (~0.01 eV) relaxations are much smaller than that of the electronic polarization (~1.3 eV).[103] A charge carrier and the polarization and relaxation effects connected to it form a quasiparticle called a small polaron.

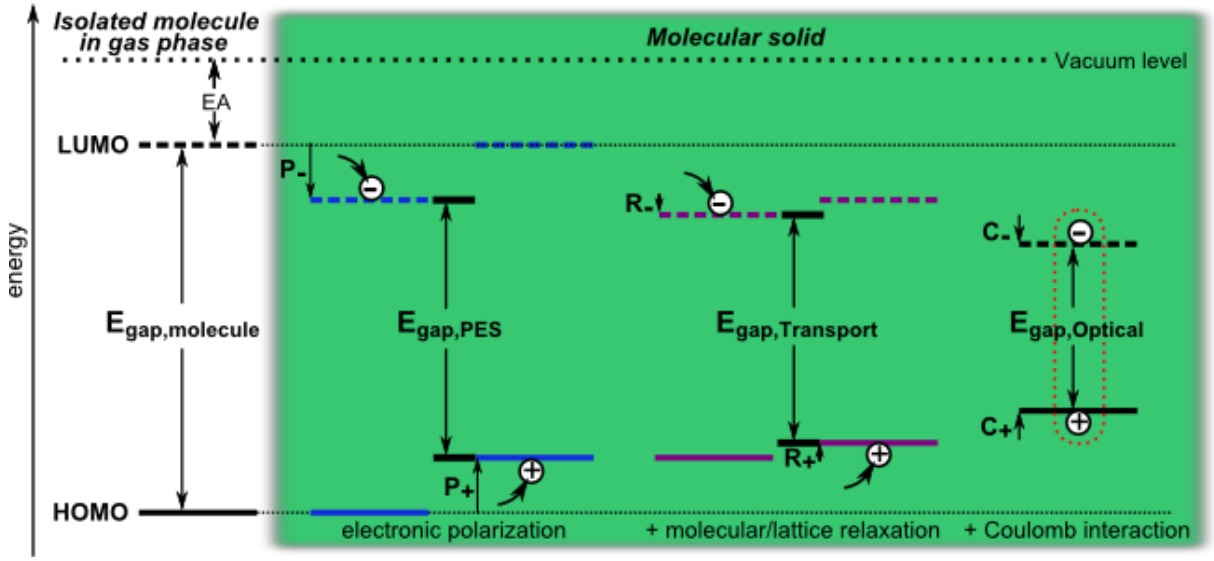

Figure 2.8: Energy levels of an isolated molecule and a molecular solid. EA denote electron affinity in the gas phase. Different energy gaps for the solid are probed by different measurement techniques. Figure adapted from [103-106].

As different measurement methods and applications involve different time scales of the processes specifically associated to them, then different energy gaps are obtained. For electroluminescence, for example, the relevant energy gap is the transport gap. In PES, the photoionization process time scale covers that of the electronic polarization.[105] In the photoconductivity technique [107, 108], the energy difference between the fully relaxed negatively and positively charge states is probed. In an optical excitation measurement, an electron-hole pair, which is simultaneously within a molecule, is created, bound together by a strong electrostatic Coulomb force. To even bring the matter further to the case for disordered or amorphous organic solids, localized variations of the polarization energies

due to different molecular environments lead to a Gaussian density of states for the distribution of transport sites as shown in Figure 2.9.

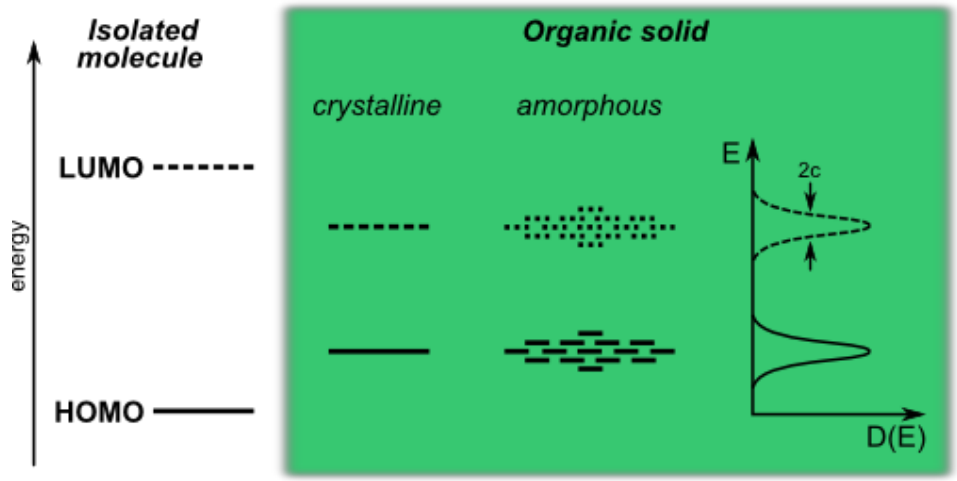

Figure 2.9: Energy level scheme for an amorphous organic solid showing a Gaussian density of states which is typically in the range of c = 80 - 120 meV. The bandwidth in molecular crystals is less than 100 meV.[104]

2.2.2 Electrical properties of organic solids

When atoms come together to form a compound, their atomic orbital energies mix to form molecular orbital energies. As more and more atoms are added, more molecular orbitals are formed. Many of these energy levels will start to be very close to, or even degenerate, in energy. These energy levels then form bands of energy. Inorganic semiconductors form broad continuous energy bands that result from at least partly delocalized electrons throughout the entire crystal lattice. This is in stark contrast to that of organic solids since there is low inter-molecular orbital overlapping between different molecules.

Consequently, charge carrier transport in organic solids becomes less efficient than in inorganic semiconductors mainly because the charge carriers lie within discrete energy levels rather than in continuous energy bands. Holes and electrons in organic solids tend to be localized over small regions facing energy barriers at the molecular boundaries rather than be delocalized over the entire lattice. Figure 2.10 presents a rudimentary illustration of the energy potential surface for charge transport in inorganic and organic semiconductors. Depending on the degree of molecular order in an organic solid, the charge carrier transport mechanism can fall between two extreme cases: band transport in those with a crystalline structure and tunneling or hopping transport in those with polycrystalline and amorphous structures. Due to the close coupling of the π-system, highly purified molecular crystals exhibit band transport at temperatures that are not too high. But since the electronic delocalization is weak, the bandwidth of these type of crystals is still small though (typically a few KT at RT, 4 - 300 meV) as compared to the 2 - 8 eV bandwidth of inorganic

semiconductors. This then translates to RT mobilities in the range of 1 - 10 $cm^2/V \cdot s$ (for comparison, mobility in crystalline silicon is ~10^3 $cm^2/V \cdot s$). However, most organic semiconductors typically form polycrystalline or amorphous films. This falls to the other extreme case where tunneling or hopping transport is exhibited, which prevalently leads to much lower mobilities (10^{-5} - 10^{-3} $cm^2/V \cdot s$).

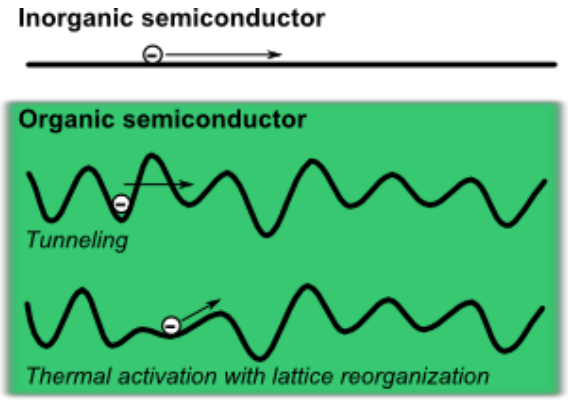

Figure 2.10: Transport of a charge carrier in organic and inorganic semiconductors. The potential energy surface for inorganic semiconductors is represented as a horizontal line because of negligible energy barriers. Due to disorder in most organic solids, adjacent molecules are differently aligned at variable distances leading to a potential energy surface as shown. Charge carriers can then only move via hopping transport which is a combination of tunneling to cover distance and thermal activation with lattice reorganization to jump up in energy.

2.2.3 Photophysics of organic semiconductors

The weak electronic delocalization in organic semiconductors leads to two important peculiarities that differ them from their inorganic counterparts. The first one is the existence of well-defined spin states (singlet and triplet) similar to that of isolated molecules that critically influences the photophysics of these materials. The second difference is the localization of an optical excitation ("exciton") on one molecule combined with a low relative dielectric constant that results to a considerably larger exciton binding energy of typically 0.5 to 1 eV.[109-112]

Spin conservation rule

In quantum mechanics, spin multiplicity indicates that a system with a total spin of zero (S = 0) has exactly one possible state, and is called a singlet state. A system with S = 1 has three possible states; and is, hence, called a triplet state. An organic molecule in its ground state has a HOMO that is filled with two electrons with opposite spins based on the Pauli exclusion principle. Such a pairing gives a total spin of zero, leading to a ground state that can only be a singlet state (S_0). An organic molecule in its excited state has an electron at an unoccupied molecular orbital that is in the n^{th} higher energetic level. If there is binding of this electron to a hole that is located at the HOMO through the attractive electrostatic Coulomb force, then an electrically neutral quasiparticle called a Frenkel exciton is formed. The Frenkel exciton can simply be put as representative of the excited state of the molecule.

Such an exciton can also be pictured as a system of two spin ½ particles that are pairing up. If the total spin of the exciton gives S = 0, then this excited state of the molecule is a singlet state (S_n); otherwise, a triplet state (T_n) if S = 1. When it comes to electronic transitions, the spin conservation rule dictates that transitions between terms of the same multiplicity are spin-allowed, while transitions between terms of different multiplicity are spin-forbidden. Thus, only singlet to singlet and triplet to triplet transitions are allowed.

Absorption, Fluorescence and Phosphorescence

Light absorption and emission processes are usually illustrated through the Jablonski diagram (Figure 2.11) where the electronic states are vertically arranged according to the relative energy level. Not all of the molecular orbitals necessarily take part in the absorption (depending on the energy of the incoming excitation) and emission processes; rather, the HOMO and LUMO are the ones that dominate. When an organic molecule absorbs a photon of proper energy, one of the two electrons in the HOMO is then promoted to the LUMO or a higher energy level. This light absorption corresponds to a transition at a time scale of ~10^{-15} s from S_0 to S_1 or a higher singlet state which is spin-allowed. For excitations to higher energy levels, a rapid (~10^{-12} s) transition and relaxation to the lowest vibrational level of S_1 takes place in addition; this process is termed internal conversion (IC).

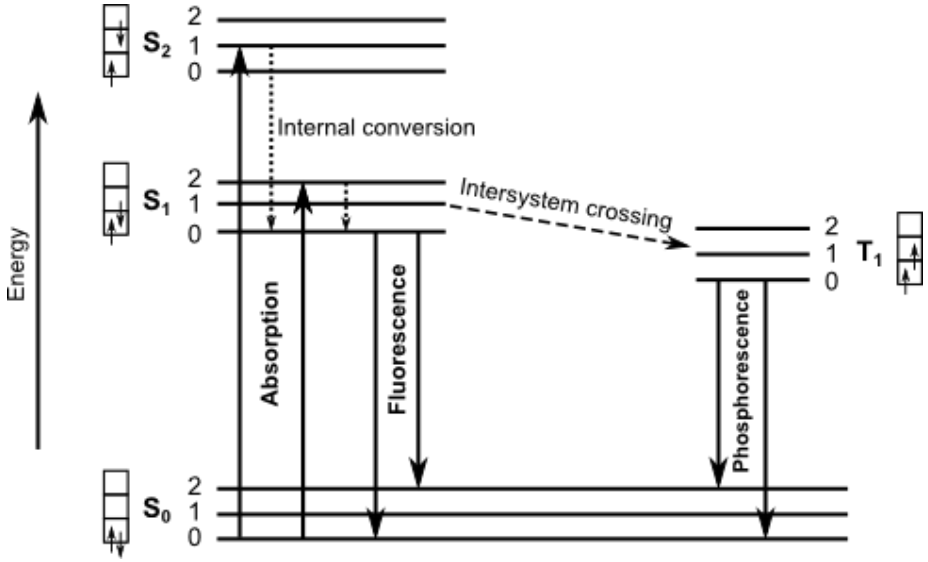

Figure 2.11: Energy level scheme of an organic molecule. (Left: singlet manifold, right: triplet manifold). The singlet ground, singlet first and second excited electronic states are depicted by S_0, S_1, and S_2, respectively. In addition, a triplet excited electronic state is also included and is depicted by T_1. The first few vibrational energy levels (depicted by 0, 1, and 2) associated with each electronic state are also included in order to take into account the motion of the nucleus relative to the molecular coordinate. Figure adapted from [104].

An electronic transition from S_1 to S_0 is also spin-allowed; this transition can occur spontaneously by the emission of a photon. The emitted light is termed fluorescence. The fluorescence lifetime, which is the average time that a molecule spends between its

excitation and its return to the ground state, for a conjugated compound is around 10^{-9} to 10^{-8} s. Fluorescence typically occurs at lower energies (longer wavelengths) than absorption. This is accounted to energy losses during the rapid thermal relaxation of S_1 from higher energy vibrational levels to the lowest and during the decay of S_1 to higher vibrational levels of S_0. The difference between the positions (in wavelength or frequency units) of the band maxima of the absorption and emission spectra is termed as Stokes shift.

Molecules in the S_1 state can also undergo a spin conversion to the first triplet state T_1. This spin conversion is referred to as intersystem crossing. Since the transition from T_1 to S_0 is spin-forbidden, the rate constants for triplet emission are several orders of magnitude smaller than those for fluorescence. The T_1 state then typically has a long lifetime of around 10^{-6} to 1 s. The light emitted from T_1 is termed phosphorescence. It is generally shifted to lower energies (longer wavelengths) relative to the fluorescence and is often too weak to be observed at room temperature. The phosphorescence quantum yield can be enhanced through the incorporation of a heavy atom into the molecule, which functions to facilitate intersystem crossing as well as generate a large spin-orbit coupling.

2.3 Donor-acceptor molecular systems

There are four routes for generating excitons in organic molecules as illustrated in Figure 2.12.

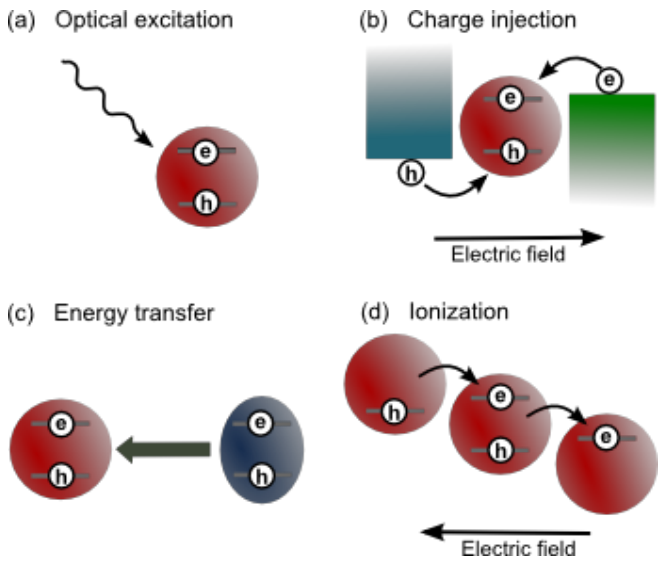

Figure 2.12: Mechanisms of excitation in organic molecules.

Through optical excitation, an exciton is formed in a molecule by absorbing a high-energy photon. In charge injection, an exciton is formed by injection of an electron and a hole from neighboring charge transporting layers. For energy transfer, an exciton is transferred to a molecule via energy transfer processes from a nearby donor molecule. In an ionization route, a large electric field ionizes an electron from one molecule to another, thereby

generating a hole. When ionization steps occur throughout a molecular organic film, the generated electrons and holes can meet on the same molecule to form excitons.

As the commonly proposed mechanisms for electroluminescence in OLED technology involve energy transfer and direct charge carrier injection, these two processes are discussed in detail within the context of donor-acceptor molecular systems. In OLEDs, a large-energy gap donor material (matrix material) is often blended with a small-energy gap acceptor material (dopant material) so that the singlet and/or triplet excitons created in the matrix can be transferred to the dopant, where they radiatively recombine.

2.3.1 Energy transfer mechanisms

Molecules in an excited state can transfer their energy to other molecules through radiative energy transfer, Förster energy transfer, or Dexter energy transfer. The trivial process of photon re-absorption, sometimes called cascade or radiative energy transfer, is relevant when large distances of typically >100 Å from the site of the excitation are involved. This is a long-range two-step mechanism,

$$D^* \rightarrow D + h\nu$$

Equation 2-1

$$h\nu + A \rightarrow A^*,$$[28]

Equation 2-2

where the emission given off by the donor (D) molecule is followed by the absorption of the released photon by the acceptor (A) molecule.

Besides the aforementioned mechanism, there are two other different single-step non-radiative energy transfer mechanisms,

$$D^* + A \rightarrow D + A^*,$$

Equation 2-3

which pertains to the classical Coulomb interaction (Förster transfer) and to the pure quantum mechanical exchange interaction (Dexter transfer) of the charge density distributions of the donor and acceptor. These two mechanisms are illustrated in Figure 2.13.

In the Förster model, Coulomb interaction occurs between the charge density distributions of the donor and acceptor. The energy transfer is mediated via a long-range resonant dipole-dipole interaction; thus, close contact is not required. The Förster radius [29] may be up to 100 Å, which is even larger than the general molecular radius. As this type of transfer is a pure dipole-dipole transition, the spin is not changed in both donor and acceptor, i.e.,

$$^1D^* + {}^1A \rightarrow {}^1D + {}^1A^* \text{ and}$$

Equation 2-4

[28] * denotes the excited state and $h\nu$ is the emitted photon.

[29] Förster radius is the distance at which the transfer efficiency of a D-A pair is 50%. At this distance, the donor emission would be decreased to half its intensity in the absence of acceptors.

$$^1D^* + {}^3A \rightarrow {}^1D + {}^3A^*.$$[30]

Equation 2-5

For energy conservation, Förster transfer requires a spectral overlap of the emission spectrum of the donor with the absorption spectrum of the acceptor. The extent of energy transfer is then determined by the distance between the donor and acceptor and the degree of spectral overlap.

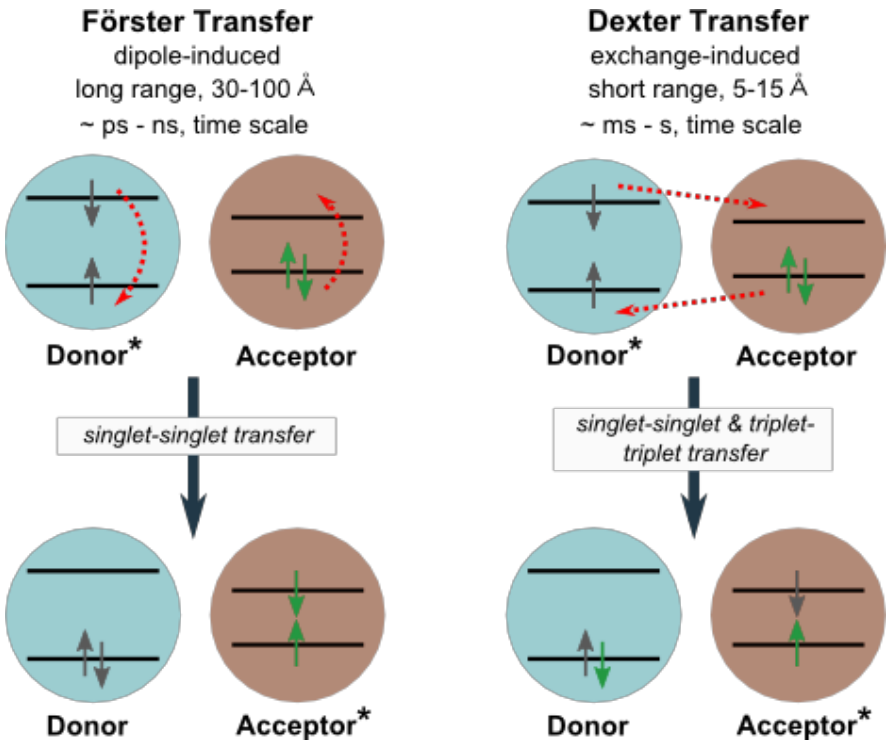

Figure 2.13: Donor-to-acceptor non-radiative energy transfers: Förster and Dexter.

In the Dexter model, exchange interaction occurs between the charge density distributions of the donor and acceptor. The energy transfer is via a short-ranged correlated two-electron exchange process; thus, it occurs typically over distances which are similar to the van der Waals distance (~5 - 15 Å). This type of transfer requires total spin conservation of the donor-acceptor system, only singlet- singlet and triplet-triplet energy transfers are allowed, i.e.,

$$^1D^* + {}^1A \rightarrow {}^1D + {}^1A^* \text{ and}$$

Equation 2-6

$$^3D^* + {}^1A \rightarrow {}^1D + {}^3A^*.$$

Equation 2-7

After transfer, the singlets on the organometallic phosphorescent acceptor molecule rapidly intersystem cross to the triplet state. Dexter transfer requires a spatial overlap of the involved donor and acceptor molecular orbitals; with the electron exchange taking place solely in the overlapping region. The extent of the exchange depends on the degree of the

[30] 1 denotes singlet state; 3 denotes triplet state

spatial overlap of the orbitals. And since this type of transfer is based on direct electron exchange, then the HOMO and LUMO of the acceptor dopant must be within the HOMO - LUMO gap of the donor matrix. The transfer efficiency will also then depend on the driving force provided by the energy difference of the HOMOs and LUMOs of the matrix and dopant.

In an amorphous film of a donor matrix that contains acceptor dopants, both Förster and Dexter transfers, in principle, can take place. The resulting energy transfer mechanism is likely to be a superposition of both modes, depending on the time and distance after the excitation. In addition, although the Förster type occurs much faster and covers a longer range, the Dexter triplet-triplet energy transfer is very important at the interfaces in OLEDs and for triplet exciton diffusion through an organic layer.

2.3.2 Charge carrier injection

In real OLED devices, high yield of excitons that are localized on the acceptor dopant is determined not only by energy transfer from the donor matrix but also by charge trapping at the dopant which will then lead to preferential exciton formation. If the HOMO (LUMO) of the dopant lies above (below) that of the matrix, a hole (electron) generated in the matrix during device operation may be trapped in the energy well that is formed at the dopant. The efficiency of hole (electron) trapping is proportional to the energy difference between the HOMO (LUMO) of the matrix and dopant. Due to this, direct charge trapping could be the prime exciton generation mechanism on the dopants. It should, however, be taken into consideration that an increased charge trapping creates a potential barrier for charge transport across the device, resulting to a significant increase in the operating voltage.

Triplet harvesting

Prior to the formation of an exciton, a trapped charge carrier has to first capture its counterpart. This capture process is spin-independent. In this manner, the spin orientation of the exciton formed will then follow spin statistics -- meaning that 25% of the formed excitons will be singlets and 75% will be triplets. This immediately sets the limit on the maximum internal efficiency of OLEDs that employ fluorescent organic emitters to only 25%. On the other hand, devices that utilize organo-transition metal complexes can compel the triplet excitons to do useful work to achieve a 100% theoretical maximum internal efficiency.

The distinct differences between organic and organo-transition metal complex emitters for OLED applications can be observed from the processes exemplified in Figure 2.14. After exciton formation and relaxations by one singlet and three triplet paths, the lowest singlet and triplet states become populated for both types of emitters.

Organic emitters exhibit a fast decaying radiative singlet ($S_1 \rightarrow S_0$) emission, i.e. fluorescence, with a ns lifetime. The efficiency of this singlet emission can reach almost 100% since the $S_1 \rightarrow T_1$ ISC rate is negligibly small compared to the fluorescence rate. ISC

times can be as long as 0.1 to 1 µs. Since the probability of a radiative $T_1 \rightarrow S_0$ transition is close to zero, the deactivation of the T_1 state occurs normally non-radiatively at ambient temperature. Therefore for the emission in organic emitters, 75% of the excitons, namely the triplet excitons, are lost to heat.

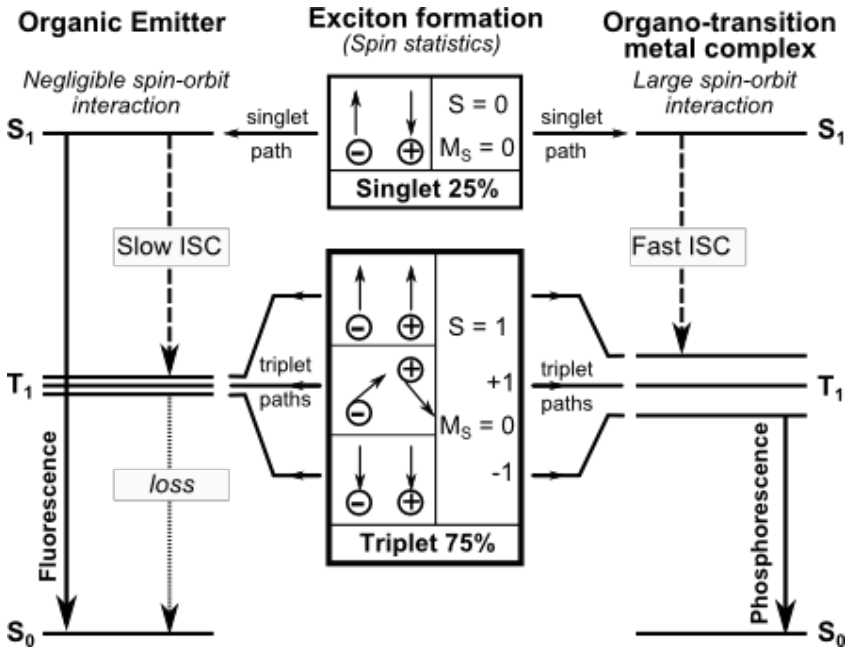

Figure 2.14: Singlet and triplet harvesting in the electroluminescence excitation processes for organic and organo-transition metal emitters. Modified from [96].

The conditions are totally different for organo-transition metal complexes due to the significant spin-orbit coupling (SOC) [31] induced by the central heavy transition metal ion. In a simplified description, SOC is a coupling between a triplet (*i.e.* spin) sub-state of an orbital to a singlet *(i.e.* orbit) state of another orbital. This then results to the radiative $T_1 \rightarrow S_0$ transition being distinctly allowed because with SOC the triplet states are no longer purely triplet. The radiative $T_1 \rightarrow S_0$ emission rate becomes large jointly with a large SOC constant, resulting to an almost 100% efficient phosphorescence even at ambient temperature. The $S_1 \rightarrow T_1$ ISC is very efficient in these complexes such that a radiative singlet emission is no longer observable. On the whole, all four possible spin orientations of the exciton are harvested and accumulated to the lowest emitting T_1 state. Thereby, the electroluminescence efficiency is higher by four times via triplet harvesting of phosphorescent triplet emitters as compared to fluorescent singlet emitters.

Basic model of exciton formation in a matrix-dopant system

The process of exciton formation as illustrated in Figure 2.15 is described particularly within the emissive layer of an OLED that is comprised of an organic matrix doped with emitter molecules. It is assumed for this model [113] that as the first step a hole gets trapped

[31] For a close look at SOC, refer to [96].

at the dopant upon injection of uncorrelated charge carriers which are statistically and spatially independent of each other.[32] Similarly, this mechanism has been proposed for $Ir(F\text{-}ppy)_3$ [33] molecules in a PVK matrix.[114]

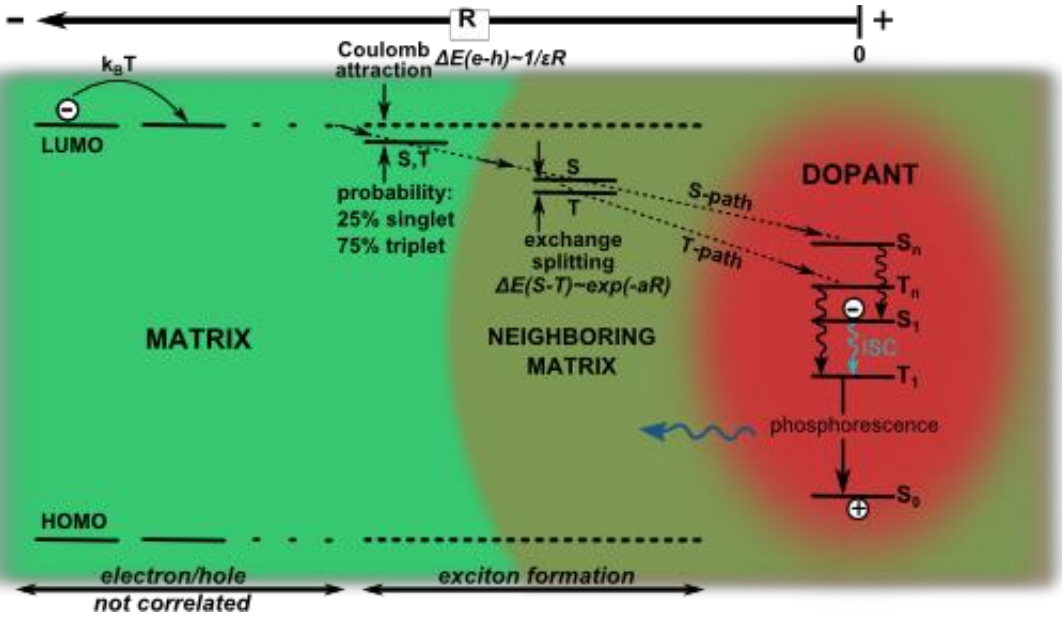

Figure 2.15: Dynamics of exciton formation in an organic matrix doped with emitter molecules. (R: electron-hole separation, a: constant depending on the respective matrix and dopant material). Adapted from [113].

Under the applied external potential, the electrons migrate independently through the matrix towards the anode. With the requirement that the Coulombic attraction must be larger than the thermal energy in order for an electron and a hole to be bonded, the maximum separation for electron-hole capture is then typically ~17 nm at room temperature. So when a migrating electron reaches at least this separation distance from the trapped hole, an electron-hole binding results. The formed exciton then takes on with equal probability any of the four possible spin states. But at such large electron-hole separations though, the energy splitting between the singlet and triplet states may be disregarded.

Driven by the attraction, the electron continues to move further towards the hole. When the electron reaches the vicinity of the nearest neighboring matrix molecules of the dopant, the wavefunctions of the electron and hole begin to overlap. This short-range exchange interaction leads to an energy splitting of the singlet and triplet states.

Finally, the electron jumps directly to the dopant which immediately results to an excited emitter. This process follows either the singlet or the triplet path depending on the initial spin orientation of the exciton. From here on, the system exhibits the behavior of a

[32] Likewise, a trapping of an electron as the first step would lead to the same model and might be relevant to other emitter molecules.
[33] fac-tris[2-(4',5'-difluorophenyl)pyridine]Ir(III)

typical excited emitter molecule (Figure 2.14) with its corresponding relaxation processes to the lowest excited states.

Charge transfer states model of exciton formation

Here, the final steps described in the basic model are slightly modified in illustrating the occurrence of the singlet and triplet paths.[96] The processes of population of an excited state of the emitter complex are described to proceed via singlet (^{1}DMCT) and triplet (^{3}DMCT) dopant-to-matrix charge transfer states as shown in Figure 2.16.

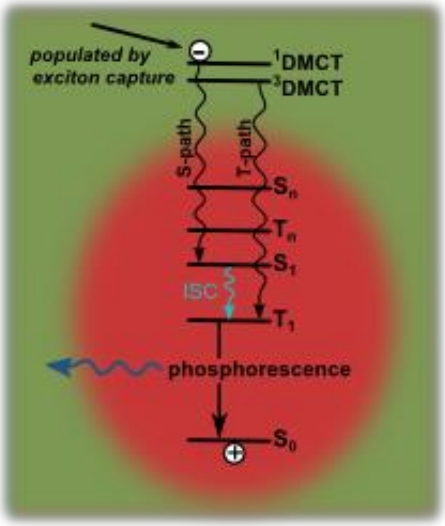

Figure 2.16: Alternative energy level scheme for the emitter dopant with its immediate surrounding matrix molecules. ^{1}DMCT and ^{3}DMCT represent dopant-to-matrix charge transfer states. Adapted from [113].

These charge transfer states are visualized as states that belong to a larger molecular unit that consists of the dopant emitter and the immediate neighboring matrix molecules. The relaxation from the ^{1}DMCT to the lower states is faster within the system of singlet states than undergoing a spin-flip first due to unfavorable ISC in the matrix. Within the dopant molecule, ISC to T_1 naturally follows upon the population of the lowest singlet state S_1. The relaxation of the ^{3}DMCT state is rather straightforward within the system of triplet states down to the lowest triplet state T_1.

2.4 Interface interactions

Several models that aim to describe the alignment of energy levels at the interfaces that conjugated organic molecules form with conductive (i.e. metal) materials and other organic molecules have already achieved certain levels of successes. And even though there is no unified model for this type of material systems, these models may be extended with caution and limitation to understand the inorganic semiconductor/organic semiconductor interface as well.

2.4.1 Conductive surface

Before proceeding to understanding interfaces, the characteristics of a conductive surface are first discussed. A conductive surface represents the outermost part of a conductive material. The Fermi level E_F divides the filled and empty states, while the work function ϕ gives the difference between the vacuum level E_{vac} and E_F. ϕ depends on the chemical potential μ of the electrons within the bulk of the material and on the change in the electrostatic potential $\varphi(z)$ from the bulk φ_{inner} through the surface towards the vacuum φ_{outer} (Figure 2.17(a)).

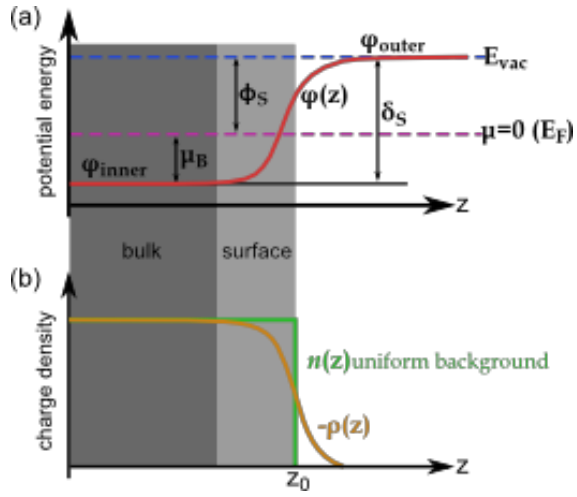

Figure 2.17: Potential energy (a) and positive and negative charge densities (b) as function of distance z through a metal/vacuum interface. Adapted from [115].

Due to a non-vanishing probability for electrons that reside outside the surface, a finite negative charge density $\rho(z)$ "spills" out into vacuum up to several Å.[116] As a consequence of overall charge neutrality, a negative charge density is missing inside the metal (Figure 2.17(b)). In addition, the jellium model describes the positive charge density created by the atomic nuclei $n(z)$ as a positive uniform background charge that shows a step-like behavior as it drops from a constant value inside the metal to zero at the surface.[116] The surface dipole δ_S is defined as the absolute change of the electron potential energy given by the difference of the inner potential energy φ_{inner}[34] and the potential energy outside of the metal φ_{outer}. The bulk chemical potential μ_B of the electrons is given by the difference between the Fermi level and the φ_{inner}.[117] Accordingly, the surface work function ϕ_S of the metal is derived as:

$$\phi_S = -\mu_B + \delta_S \,.$$

Equation 2-8

[34] φ_{inner} is usually set to zero in the jellium model.[117]

Because μ_B is a bulk property of the metal, it cannot be changed by the presence of adsorbates. But δ_S, as determined by the spill-out of electrons into vacuum, can easily be modified by adsorbates. This leads to ϕ_S that is also easily modified by adsorbates.

2.4.2 Energy level alignment at interfaces

When conductive surfaces and organic molecules come into contact, several effects occur at their interface. Generally upon contact formation, the electron density distributions change. The rearrangements of the electron density distributions are normally accompanied by changes of bond lengths; with these, structural relaxations may also take place. Depending on the strength of the electronic rearrangement, a variety of interaction regimes (Figure 2.18) ranging from weak physisorption to strong chemisorption are classified. In between these two, there are existing intermediate cases where different degrees of chemisorption occur. Within the limits of these weak and strong interaction regimes, different model theories are applied to successfully explain the implications on the properties of the interfaces in complete devices.

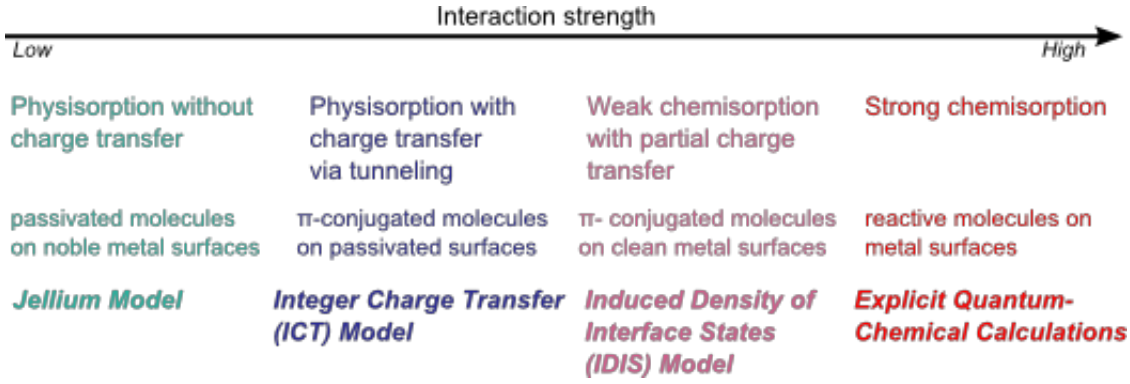

Figure 2.18: The different interaction regimes ranging from weak physisorption to strong chemisorption. (First row: interaction type, second row: example system, and third row: standard model). Adapted from [115].

Physisorption versus chemisorption

Physisorption (physical adsorption) is a process where interactions are mainly mediated by van der Waals forces. For molecules adsorbed on surfaces, this entails that the molecular and electronic structures are relatively unperturbed and that the bonding to the surface is rather weak. In reality, purely physisorbed molecules on surfaces are not found because there is always a weak electron density rearrangement (e.g. energy level broadening or "push-back" effect).

Chemisorption (chemical adsorption), on the other hand, is a process where strong interaction occurs such that, depending on the extent of electron transfer, covalent or ionic bonds are formed between the atoms or molecules and the surface. In addition, this adsorption process can strongly influence the molecular conformation.

Reorganization of surface metal electronic structure: "Push-back" effect

The closest to a real physisorption is the adsorption of unreactive molecules (e.g. Xe, TTC[35], *n*-alkane) on clean metal surfaces, because in this limiting case there is a negligible hybridization between the electronic levels of the adsorbate and the metal substrate.[101, 118-120] A sampling of the electronic system along a path perpendicular to the interface would therefore result to a sharp transition from the delocalized metal band structure to the localized orbitals of the adsorbed molecules.

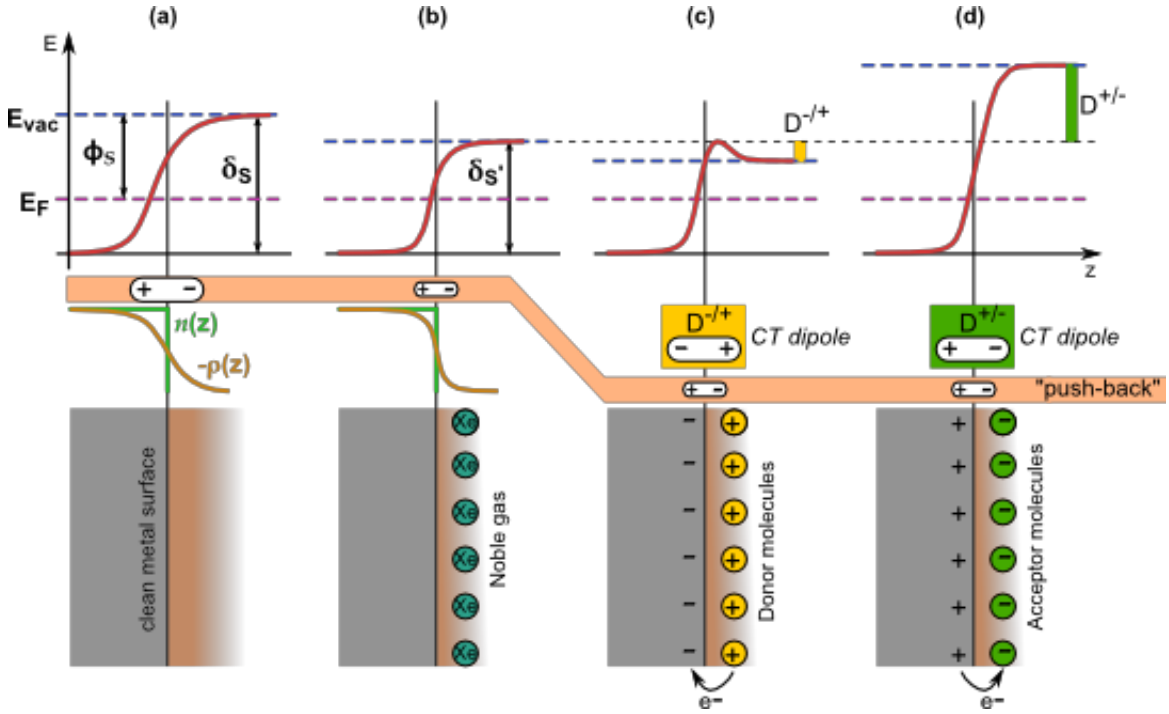

Figure 2.19: Effect of adsorbates on ϕ of metal surfaces. (a) Clean metal surface, (b) adsorption of xenon which is close to physisorption, (c) adsorption of donor molecules with net electron transfer to the metal, and (d) adsorption of acceptor molecules with net electron transfer to the adsorbate. The change in the electron tail upon physisorption of Xe is demonstrated in (a) and (b).[101] Together with the push-back effect, additional changes in the work function from induced charge transfer CT dipoles at a chemisorptive interface upon deposition of donor and acceptor molecules are shown in (c) and (d).[121-127]

Despite the negligible interaction, a pronounced influence on the work function of the joint system is observed. The work function is lowered significantly upon adsorption [118, 121, 125, 127-130] due to the Coulomb repulsion between the electron density of the molecule and the surface electrons that locally "pushes" the tail of the electron wave function (Figure 2.17) back into the metal, effectively decreasing δ_S and ϕ. An illustration is provided in Figure 2.19 (a)-(b); note that there is no creation of a new dipole but only a change in the existing δ_S. This push-back effect (also known as pillow effect) has been found to be a general phenomenon occurring upon physisorptive and chemisorptive adsorption of atoms or molecules on clean metal surfaces as illustrated in Figure 2.19 (a)-(d), with a magnitude

[35] Tetratetra-contane

that is dependent on the substrate's δ_S, the adsorption distance and effective surface coverage.[101, 119, 131]

Vacuum level alignment

In the limiting case of vacuum-level alignment where surface dipole effects are not taken into account (Schottky Mott limit[36]) in a metal-semiconductor junction, the injection barriers ϕ_B for electrons and holes are directly calculated from separately determined material parameters, namely, electron affinity *EA* and ionization potential *IP* of the semiconductor and ϕ_S of the metal (Figure 2.20(a)).

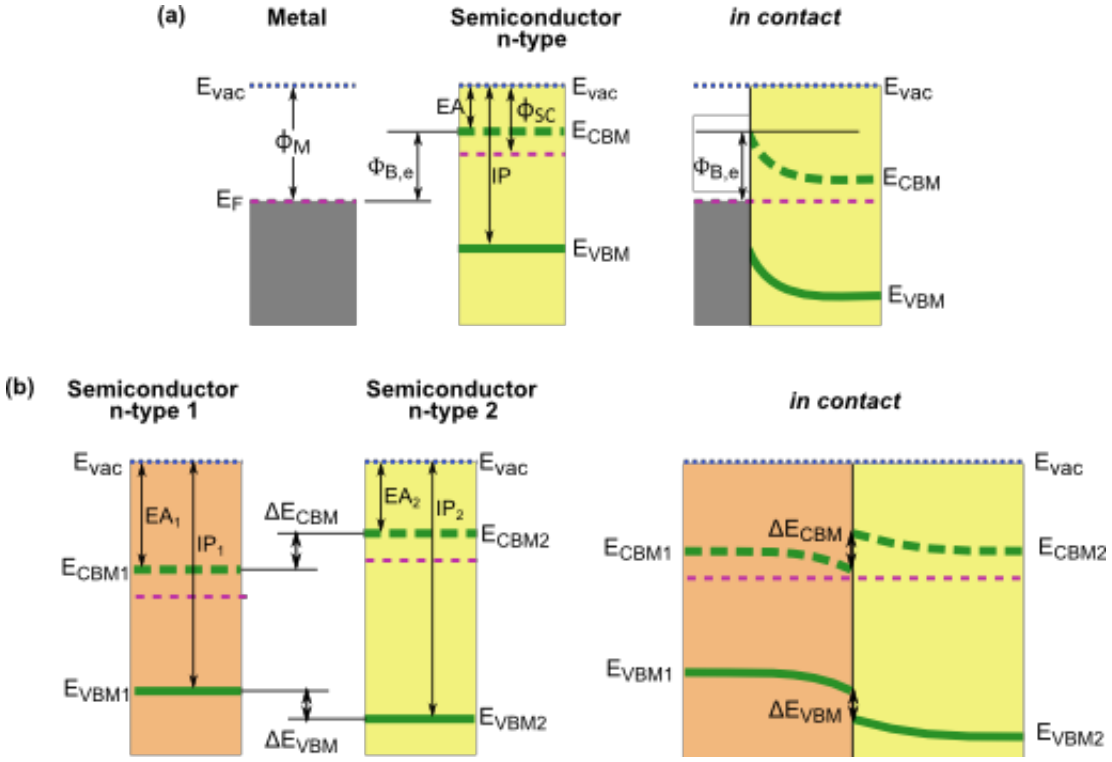

Figure 2.20: (a) Schottky-Mott model that describes the construction of the metal-semiconductor junction energy band diagram. (b) Anderson's rule that describes the construction of the heterojunction between two semiconductor materials.

The barriers in this model are formed by aligning the vacuum levels first and then matching the Fermi levels. The exchange of charges upon contact follows the principle of charge neutrality. Due to the high density of charge carriers in a metal, the exchanged charge is shielded within about 0.1 Å. On the other hand, due to the limited number of free charge carriers in a semiconductor, an extended space charge region (band bending) is created.

Although the Schottky-Mott model correctly predicts the existence of band bending in the semiconductor, it gives grossly incorrect predictions for the Schottky barrier heights in most real interfaces. So as it turns out, vacuum-level alignment is rather the exception than the rule. This is particularly relevant for interfaces formed with clean surfaces because an

[36] The interface is essentially free of gap states.

interface dipole δ_I results in almost every case from the "push back" of electron density alone into the metal by the semiconductor.[101, 131]

To describe the heterojunction between two semiconductor materials, the Anderson's rule (also known as the electron affinity rule) was derived from the same thought experiment of bringing together two materials in vacuum as with the Schottky-Mott model.[132, 133] With the same principle, a common vacuum level is first assumed to obtain the bands' alignment at the junction followed by a common Fermi level as illustrated in Figure 2.20(b). The band offsets at the junction are directly obtained from the differences in the EAs and IPs of the two semiconductors:

$$\Delta E_{CBM} = EA_1 - EA_2$$

Equation 2-9

$$\Delta E_{VBM} = IP_1 - IP_2$$

Equation 2-10

In contrast to the metal-semiconductor junction, space charge regions are formed on both sides of the semiconductor heterojunction due to reduced densities of free charge carriers. The shape of the band bending in the two semiconductors can be obtained through Poisson's equation. Heuristic application of the Anderson's rule found success in specific systems such as the 60:40 rule used for the GaAs/AlGaAs system.[134]

Fermi level pinning in physisorptive junctions

By the time that the vacuum level alignment model was disproved by several early experimental evidences, the very first Fermi level pinning model was introduced. This initial model assumes that intrinsic surface states at the inorganic semiconductor energy gap are pinning the metal Fermi level.[135] Actually, on a side note, models that have been developed later are basically extensive derivations of these two primary models.

Fermi level pinning is generally observed in many material systems where the interaction between the conductive substrate and the subsequently deposited organic molecules is not strong. It must be noted for such interactions described here that the hybridization between molecular and substrate levels and the overlap of the electronic orbitals are negligible. In addition for this case of passivated interfaces, the push back effect does not happen due to saturation by the presence of the molecules at the interface to the substrate.

There are several cases where vacuum level alignment can actually be observed for interfaces between metal substrates and conjugated organic molecules within a given range of the substrate's work function ϕ_{Sub} as shown in Figure 2.21(a). In these cases where the Fermi level of the substrate is found anywhere between the HOMO-LUMO gap of the organic molecules, no driving force is existent for spontaneous charge carrier transfer from the metal to the molecular layer or vice versa. The work function of the joint system is then basically given by the work function of the metal substrate. On a separate note -- since this system representation does not include a full description of the Fermi level in the organic

molecule itself, an alignment as shown in Figure 2.21(d) via a Fermi level movement in the organic material farther than the interface is also suggested.[136]

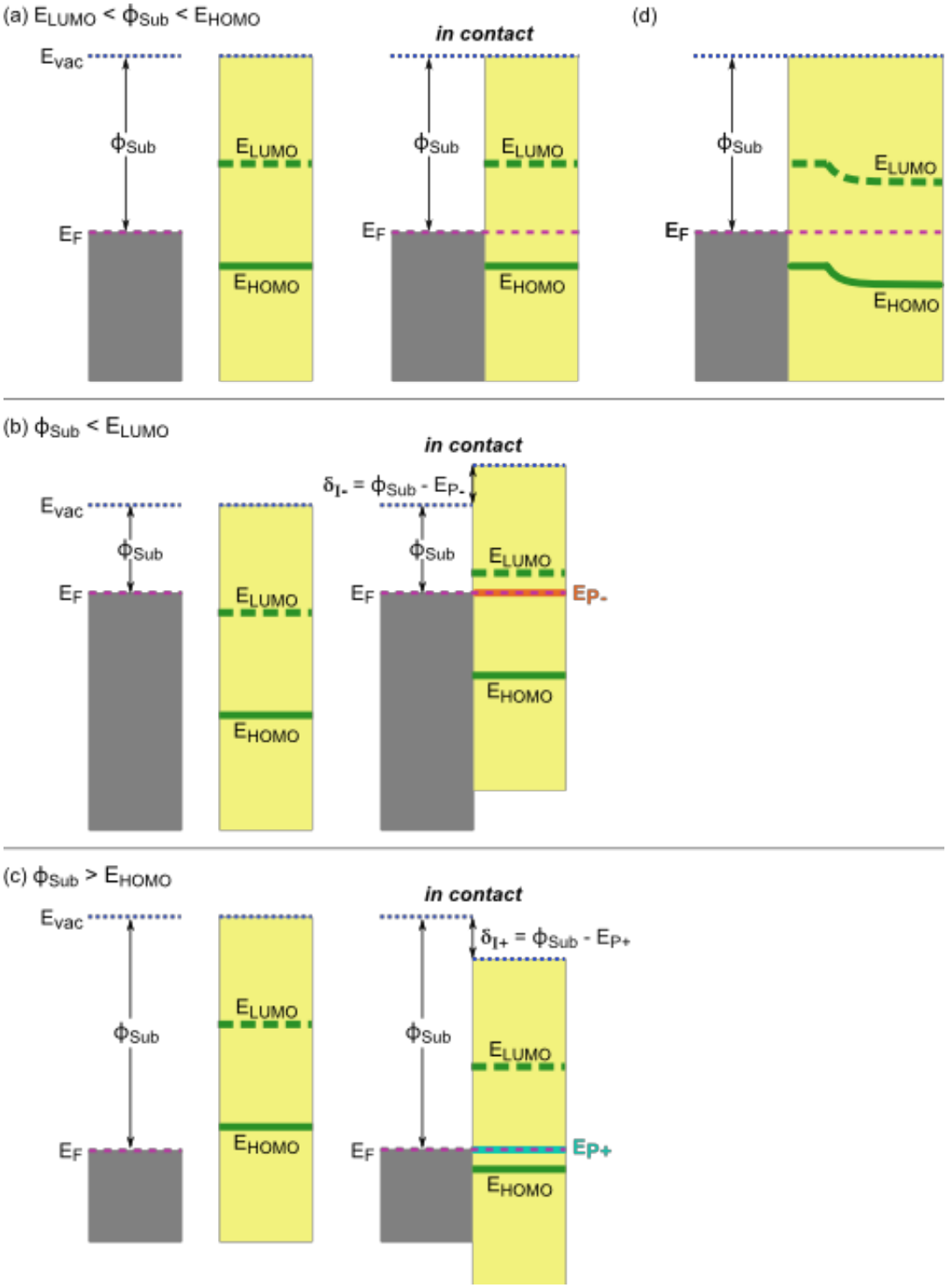

Figure 2.21: Schematic energy level diagrams of the two pinning regimes of the Fermi level: (b) if the Fermi level of the substrate is above the LUMO of the organic molecules, then a pinning of a molecular level P- (a charged polaron state) at the Fermi level occurs, and (c) if the Fermi level is below the HOMO, then a pinning of a molecular level P+ (a charged polaron state) at the Fermi level occurs. (a) For the case where the substrate's Fermi level is located between the HOMO-LUMO gap, no pinning takes place. (d) An extended model of the vacuum level alignment that considers movement of the Fermi level in the organic material at distances that are relatively far from the interface.

However, if the Fermi level of the substrate is not within the HOMO-LUMO gap of the organic molecules, then charge transfer[37] and pinning of molecular levels at the Fermi level will occur. This situation is depicted in Figure 2.21(b) and Figure 2.21(c). Due to the potential gradient in the case where $\phi_{Sub} < E_{LUMO}$, electrons are transferred from the metal to the unoccupied states in the molecules. The LUMO is then being raised to the Fermi level of the substrate while equilibrium is being accomplished. While charging, the molecules relax into a molecular level -- the charged polaron state P-, which is comparable to an anion that forms a polaron in the organic layer. This stabilized state is at a larger binding energy position that is fixed with respect to the LUMO. The process continues until the created dipole δ_{I-} layer finally shifts the polaronic state to the Fermi level. In the final relaxed state of this system, a pinning of the molecular level *P*- at the Fermi level occurs as depicted in Figure 2.21(b). When $\phi_{Sub} > E_{HOMO}$, the potential gradient promotes electron transfer from the molecules to the metal until the HOMO of the molecules is at the Fermi level of the substrate. A polaronic *P*+ state of a stabilized hole with a smaller binding energy than the HOMO is formed. For the final relaxed state of this system, a pinning of the molecular level *P*+ at the Fermi level occurs and an interface dipole δ_{I+} is created as depicted in Figure 2.21(c). There are several models that aim to explain the existence of this pinning behavior-- the prominent ones are the integer charge transfer model for metal/organic and organic/organic interfaces [115, 137] and the tail gap state model for metal/organic interfaces [138, 139].

Alignment in heterojunctions formed by chemisorption

When the interaction strength between the substrate and molecules is increased, partial charge transfer and/or formation of covalent or ionic bonds takes place. Such interaction gives rise to a slight hybridization of the molecular orbitals and the metal continuum states. Bond formation is usually observed in the interfaces of molecules and reactive metals.[131] On the other hand, charge transfer is generally observed in weakly interacting interfaces of strong acceptor or donor molecules and conductive substrates. In the case of strong electron donors, the electrons are transferred from the molecules to the substrate (Figure 2.19(c)). It is speculated in some models that as the molecular orbitals lose electron density, all molecular orbitals should shift towards the Fermi level.[122, 123] The work function is usually decreased beyond the typical values of the push-back effect as the charge transfer (CT) dipole $D^{-/+}$ points in the direction that is illustrated in Figure 2.19(c).[121, 124, 126] In the case of strong electron acceptors, the transfer of electrons is directed from the metal to the molecules (Figure 2.19(d)). Such a transfer leads to a

[37] This charge transfer from the substrate to the organic layer and vice versa can happen by coherent or thermally activated hopping processes.

partially filled metal-molecule hybrid state[38] that is located just below the Fermi level in the chemisorbed layer.[140, 141] The work function in this case is usually increased due to a CT dipole $D^{+/-}$ pointing away from the metal that is established across the interface.[125] The change in the work function induced by $D^{+/-}$ may be affected by the decrease in value brought by the push-back effect as illustrated in Figure 2.19(d).

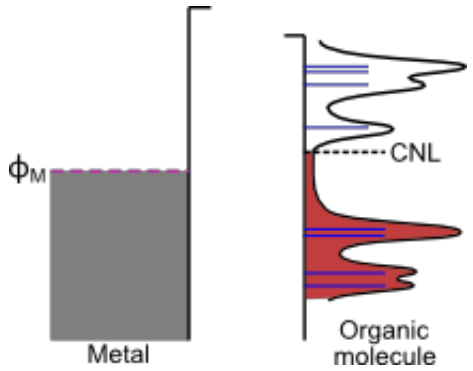

Figure 2.22: At weakly interacting metal/organic interfaces, charge transfer tends to align the organic CNL and metal work function. This gives rise to an induced dipole at the interface and to the partial pinning of the Femi level in the organic energy gap.

The most intensively developed model that covers weak chemisorption with partial charge transfer in both metal/organic [142-144] and organic/organic interfaces [125, 126, 144] is the induced density of interface states (IDIS) model, which was originally a model developed for metal/inorganic and inorganic-inorganic interfaces to explain the band offsets and the Schottky barrier formation associated to the energy level alignment.[145] This model describes weak interacting interfaces based on the concept of induced density of states (DOS) and charge neutrality level (CNL). The interaction between the metal and the organic material gives rise to a shift and broadening of the molecular levels, turning the initial discrete distribution of molecular states into a continuum DOS as illustrated in Figure 2.22. The former energy gap becomes "filled" by induced DOS, which is precisely the IDIS. The CNL position is such that the integrated IDIS up to the CNL yields the number of electrons of the isolated molecule. In thermodynamic equilibrium, the CNL aligns with the metal work function or the CNL of another organic material. If the CNL is higher than the metal work function, then electrons will be transferred from the organic molecules to the metal. This gives rise to an electrostatic dipole at the interface that shifts the relative positions of the materials in the direction of aligning the CNL and metal work function. The degree of alignment is determined by the screening at the interface. Thus, the IDIS is central to the alignment as it acts as the buffer for charge exchange, pinning the interface Fermi level either strongly or weakly near the CNL.

[38] This hybrid state is derived from the former LUMO of the neutral molecule and is usually mainly located on the molecule. Thus merits the charge transfer process to a simple filling of the former LUMO.

Internal interface charge transfer model

In the work of Mayer *et al*. [146, 147], the internal interface charge transfer model was proposed to describe the mechanism of the doping induced variations of the matrix Fermi level in phase mixed matrix:dopant composites (Figure 2.23(a)). The foundation of this model lies on the assumption that the Fermi levels of two mixed phases align at their internal interfaces; it takes into account that such Fermi level equalization is achieved by interface dipole formation and charge transfer between the matrix and dopant clusters.

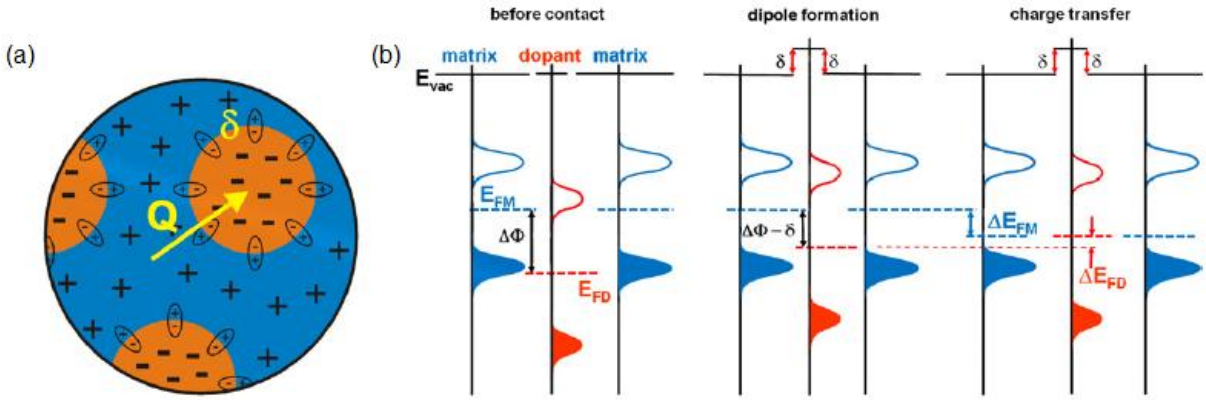

Figure 2.23: (a) Sketch of a composite material comprising of an organic matrix (in blue) and clusters of dopant molecules (in orange). p-type doping is also illustrated. (b) Development of the energy band diagram according to the internal interface charge transfer model. Taken from [146].

The alignment process of the model is described in Figure 2.23(b) in the case of *p*-type doping of an organic matrix by clusters of a metal oxide. The figure shows the energy levels of the matrix (with the small work function) and the dopant (with the large work function). The initial Fermi level difference $\Delta\Phi$ is given by the difference in the individual work functions of the materials. When the two materials are joined, a dipole δ is formed at the internal interface, thereby reducing $\Delta\Phi$. At the same time, spontaneous electron transfer from the matrix to the dopant takes place, which advances further the Fermi level equalization. If the absolute shift is given by $\Delta\Phi$, then the following equation holds:

$$\Delta E_{FM} + \Delta E_{FD} = \Delta\Phi - \delta \, .$$

Equation 2-11

The exchange of charge consequently creates extended space charge regions, with the degree of band bending depending on the density of states. But in the case of dopant clusters whose dimensions are much smaller than the extension of the space charge region, band bending in the clusters is neglected. If the dipole at the internal interfaces of a composite is the same as that at the interface of a bilayer, then

$$\Delta E_{FM} = eV_{BB,M}$$

Equation 2-12

$$\Delta E_{FD} = eV_{BB,D} \, .$$

Equation 2-13

With the assumptions and simplifications considered in this model, the energy level alignment in matrix-dopant composites can be estimated from matrix/dopant bilayer interfaces.

Chapter 3 Experimental methods

This chapter introduces the experimental methods employed in this work. Descriptions of the characterization and sample preparation techniques are given. For recognition, photoelectron spectroscopy (PES) is the main characterization method employed in this work. PES dominates all experimental approaches in studying the formation of interfaces. In addition, experimental parameters and details of the data evaluation are outlined.

3.1 Photoelectron spectroscopy

Photoelectron spectroscopy (PES) is a quantitative spectroscopic technique that utilizes photoionization and analysis of the kinetic energy distribution of the emitted photoelectrons for the determination of the electronic structure, elemental composition, chemical state and bonding interactions of materials. It differs from conventional spectroscopic methods as it detects electrons rather than photons. PES is an indispensable powerful experimental technique employed in the study of surfaces and interfaces due to its high surface sensitivity. Traditionally, this technique is subdivided according to the source of exciting radiation into x-ray photoelectron spectroscopy (XPS) and ultraviolet photoelectron spectroscopy (UPS). With the development of synchrotron radiation sources, high resolution synchrotron-induced photoelectron spectroscopy (SXPS) studies can be carried out with radiation spanning a much wider and more complete energy range (~5 - 5000 eV). SXPS is not generally used in relation to photoelectron studies due to the expense, complexity and limited availability of such sources. In this section the basics of PES are explained. Detailed descriptions are found in references [148-153].

3.1.1 Physical principle

PES is basically a photon-in/electron-out process. Such photoemission process can be described in a three-step model: (1) photoexcitation of an electron in the solid, (2) traveling of the excited electron to the surface of the solid and (3) the escape of the electron from the solid into the vacuum through the surface. (Elaborate and detailed physical descriptions are given in references [153-158].) Through these three steps, the kinetic energy distribution curve of photoemitted electrons (or photoelectrons) (e.g. Figure 3.2)

$$I(E_{kin},\omega) = I_P(E_{kin},\omega) + I_S(E_{kin},\omega)$$

Equation 3-1

consisting of the primary distribution $I_P(E_{kin},\omega)$ of electrons without any inelastic collisions and the secondary distribution $I_S(E_{kin},\omega)$ of electrons with energy losses from one or more collisions, can be obtained. The primary distribution of electrons without energy loss marks

the crucial part of the PES spectrum for the analysis of the electronic structure of the solid surface. It is a product of three factors

$$I_P(E_{kin},\omega) = P(E_{kin},\omega) \times T(E_{kin}) \times D(E_{kin},\omega)$$

Equation 3-2

which are determined individually in the three-step process. $P(E_{kin},\omega)$ is the distribution of photoexcited electrons, $T(E_{kin})$ is the transmission function and $D(E_{kin},\omega)$ is the escape function.

In the first step, photons are absorbed and the excitation of electrons takes place. This photoexcitation of electrons depends on the probability of transition from an electron's initial state to the final state which is obtained from Fermi's golden rule. For the resulting dipole moment of an electronic transition to be non-vanishing, energy and momentum conservation must be met. To detect an electron at a certain kinetic energy, E_{kin}, the energy of the final state must be equal to E_{kin} and that E_{kin} must be large enough to overcome the work function of the solid. This step gives $P(E_{kin},\omega)$.

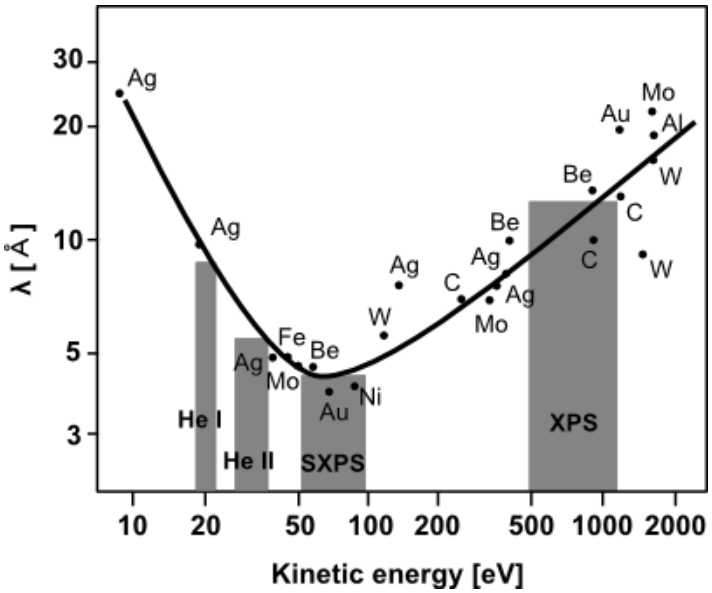

Figure 3.1: The inelastic mean free path λ of emitted photoelectrons as a function of their kinetic energies E_{kin}. Typical kinetic energy ranges resulting from specific photon sources are indicated.

Once transitions have taken place, the propagation of the excited electrons to the surface of the solid is considered as the second step. Some of these electrons undergo one or more inelastic scattering processes on their way to the surface, losing a part of their energy and all information about their initial state. These inelastically scattered electrons contribute to the secondary electron, $I_S(E_{kin},\omega)$, background in the photoemission spectrum if their energy at the surface is large enough to overcome the work function of the solid. The probability that an electron reaches the surface without inelastic scattering is described by the mean-fee electron path $\lambda(E_{kin})$, which can be derived from the universal mean-free path curve shown in Figure 3.1.[159, 160] From this step, the propagation is described simply by a

transmission function $T(E_{kin})$ which is proportional to $\lambda(E_{kin})$. Since the mean free paths of the electrons are dependent on their kinetic energies, the information depths within the sample for analysis can be tuned by choosing the appropriate photon source energies. This is the step that makes PES a surface sensitive technique. In addition, electrons emitted from different orbitals have different binding energies as well as resulting kinetic energies. As a consequence, the surface sensitivities of these electrons are different for a fixed excitation energy.

As every electron state of a solid can be described by a Bloch electron wave, the final state of the emitted electron can be viewed as a wave scattered by a surface-atom potential. In the third step, the transmission of an electron into the vacuum through the surface requires conservation of its wave vector component that is parallel to the surface. The wave vector component that is directed towards the surface is not conserved during the transmission and can be obtained from the energy conservation. The escape of an electron into vacuum is only possible for those electrons with a component of the linear momentum that is normal to the surface and with sufficient E_{kin} to surmount the potential barrier. This step gives $D(E_{kin},\omega)$.

3.1.2 Working principle

The working principle of PES is based on the well-known photoelectric effect.[161, 162] Here, electrons of a sample are excited by an incident monochromatic light beam with energy $h\nu$ (illustration shown in Figure 3.2). Considering that the energy of the photon is transferred completely to an electron and that it is sufficient to overcome the binding energy E_B of the electron in its respective electron state relative to the Fermi level and the work function of the sample ϕ_{sample}, then the electron leaves the surface into the vacuum with a kinetic energy E_{kin} of

$$E_{kin} = h\nu - E_B - \phi_{sample} .$$

Equation 3-3

However, in an actual PES system, the sample is in electrical contact with the spectrometer. The contact aligns the Fermi levels of the spectrometer and the sample, which in turn builds up a contact potential $\Delta\Phi$ due to the difference in the work functions of the spectrometer $\phi_{spectrometer}$ and the sample ϕ_{sample} :

$$\Delta\Phi = \phi_{spectrometer} - \phi_{sample} .$$

Equation 3-4

This contact potential will either accelerate or slow down the electrons depending on the relative values of $\phi_{spectrometer}$ and ϕ_{sample} to each other. Considering the $\Delta\Phi$, the kinetic energy of the detected photoelectrons are modified in the spectrometer to:

$$E_{kin} = h\nu - E_B - \phi_{sample} - \Delta\Phi$$
$$= h\nu - E_B - \phi_{sample} - (\phi_{spectrometer} - \phi_{sample})$$
$$= h\nu - E_B - \phi_{spectrometer},$$

Equation 3-5

which is clearly independent of the work function of the sample. Since the binding energy of the electrons at the Fermi level is zero by definition, then an energy calibration using a metal standard is possible where $\phi_{spectrometer}$ is determined and necessary system adjustments are then made so that the zero point of the binding energy spectrum corresponds to the Fermi level.

A typical kinetic energy distribution curve obtained in a PES experiment is shown in Figure 3.2, where the number of counted photoelectrons is plotted against their kinetic energy. The electrons with the largest E_{kin} originate from the highest occupied state of the sample (i.e. E_F for a metal and HOMO for an organic solid). The reference level is commonly a E_F because it is aligned between the sample and the spectrometer. Going further to increased E_B in the spectrum, broad peaks or structured features of photoelectrons coming from the valence region of the sample with slightly smaller E_{kin} than the HOMO are observed next. To first order approximation (i.e. without accounting for cross-section and selection rule effects), PES yields the density of occupied levels of a solid. The valence region photoelectrons may then be related to the valence bands of extended systems (e.g. covalent or van der Waals crystals, polymers) or to the various σ- and π-type orbitals of organic molecules. The measured core level photoelectrons at increasingly smaller E_{kin} originate from excited deep lying localized atomic orbitals that are well-shielded by the valence electrons. At very low kinetic energies, the majority of the contribution to the total spectrum come from the secondary photoelectrons. The sharp lowest E_{kin} cutoff in the spectrum, which is also called secondary electron (SE) cutoff, is a direct measure of the local vacuum level E_{vac} position (in front of the sample as in contrast to the vacuum level at infinity ϕ_∞ [101, 163]) as electrons have just enough energy to overcome ϕ_{sample}, and then leave the sample in the limit $E_{kin} \rightarrow 0$ eV. At a given excitation energy, applying Equation 3-3 to the SE cutoff gives

$$\phi_{sample} = h\nu - E_{B,SEcutoff}.$$

Equation 3-6

In the actual PES measurement, to resolve photoelectrons with the lowest E_{kin} at the region around the SE cutoff, a constant negative potential Φ_{bias} (typically a few eV) is normally applied to the sample. Φ_{bias} provides the necessary extra kinetic energy for such photoelectrons to reach the spectrometer. This rigidly shifts the whole spectrum to higher E_{kin} by the constant value of Φ_{bias}, thereby, ensuring that all photoelectrons are detected. Equation 3-6 is then modified to

$$\phi_{sample} = h\nu - E'_{B,SEcutoff} - \Phi_{bias}$$

Equation 3-7

where $E'_{B,SEcutoff}$ is the new binding energy position measured with the applied potential.

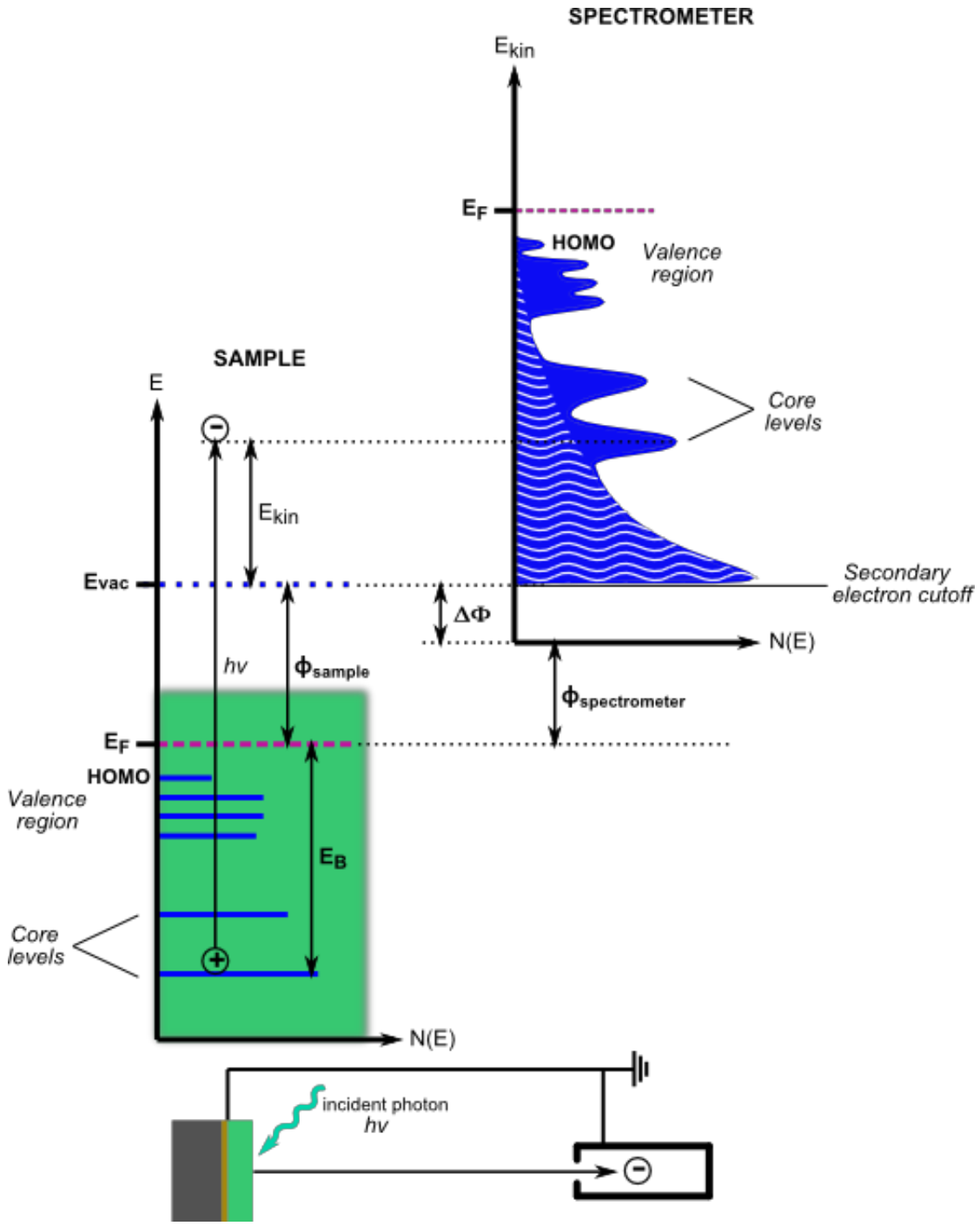

Figure 3.2: Schematic diagram of the energy levels in a sample and the corresponding kinetic energy E_{kin} distribution curve of photoelectrons as detected by the spectrometer. The number of photoelectrons increases strongly with decreasing E_{kin} and then drops drastically at E_{kin}=0. The E_{kin} distribution of the primary (represented by the solid blue curve) and secondary (represented by the curve with wave patterns) photoelectrons are superimposed.

3.1.3 Features of the photoemission spectrum

The spectrum obtained from a PES measurement is generally displayed as a plot of the photoemission intensity versus the electron binding energy with a fixed, small energy

interval. The position on the kinetic energy scale that is equal to the difference in the photon excitation energy and the spectrometer work function corresponds to a binding energy of 0 eV with the Fermi level as the reference (Equation 3-3). So typically, a linear binding energy scale with 0 at that point is used.[164]

As can be seen from a survey spectrum (e.g. Figure 3.2), the peaks that are well-defined are due to electrons that have not suffered an inelastic energy loss through the sample. These peaks could correspond to any of the following: core level, Auger, or satellite photoelectron emissions. The inelastically scattered electrons increase the level of the background at binding energies higher than the peak energy. This background is nearly continuous because the energy loss processes are random and multiple.

For chemical state identification, quantitative analysis of compositions and peak deconvolution or other mathematical manipulations of the data, detailed spectra are obtained in order to get precise peak positions and accurate registration of lineshapes. For such kind of detailed spectra, it is necessary to calibrate the binding energy scale throughout the data-gathering process in order to ensure the accuracy of the data. The best way to calibrate is to record the Fermi edge and the suitable photoemission lines from metal standards such as gold (Au $4f_{7/2}$, 84 eV), silver (Ag $3d_{5/2}$, 368.29 eV) and copper (Cu 2p, 932.67 eV). The obtained binding energies are then compared to the standard values in order to establish the linearity of the energy scale and its position. A calibrated spectrum is then obtained by shifting the binding energy values according to the measured shift in the Fermi level and core level positions of the metal standards.

Aside from the calibration of the binding energy scale, the removal of the background contribution of the inelastically scattered photoelectrons to the detailed spectrum is also necessary. In most cases, a Shirley function is utilized for the subtraction of the background since it widely gives physically reasonable results. In other cases, a Tougaard, linear, or polynomial function might also be applied.

3.1.4 Identification of elemental compositions and chemical states

The composition of elements in a sample is determined from the core level peaks that are present in the photoemission spectra, since no two elements have the same set of electronic binding energies. Generally, the measured survey spectra are directly compared to reference spectra and tables [164], which contain all the emissions of the different electronic orbitals of each element, in order to have an overview of all identifiable emissions. The set of binding energy positions for the different core level peaks is unique for different elements with their respective orbitals. The type of electronic orbital dictates the line shape of the core level emission peak. All orbitals except the *s*-orbital give rise to doublets with two possible states having different binding energies. This is known as the spin-orbit splitting. Uniquely, the *p*-, *d*- and *f*-orbitals give peaks with specific area ratios based on the degeneracy of each spin state. The ratio for *p* lines is about 1:2, *d* lines 2:3 and *f* lines 3:4.

These ratios and the energy difference of the spin-orbit split emissions contribute to the explicit identification of the core level emissions.

Different chemical bonds and environments induce different changes in the photoemission lines. This is called a 'chemical shift'. The electronegativity of the surrounding atoms, to which bonds are formed, dictate the binding energy positions of core line emissions due to the relative electron density seen by the detected atom. Oxidation states of elements are distinguished according to their binding energies. In general, a shift of a core level emission toward a higher binding energy indicates an oxidation, while a shift to a lower binding energy indicates a reduction of the corresponding element.

3.1.5 Quantitative analysis of the core level spectra

Stoichiometry of the elemental composition

Aside from elemental composition, the XPS core level spectra provide information as to the relative concentrations of elements in a sample. Granted that the cross section of a certain element is independent of its electronic configuration and thus constant for a given beam energy and experimental geometry, quantitative evaluation of the core level spectra is possible from the area of the photoemission lines.[155] As a consequence, the integrated peak area, A_X, of the most intense core level emission from element X is proportional to the number of atoms in the analyzed volume. Specifically, the integrated peak area of an element in the compounds is a function of the cross section, the detection efficiency and transmission function of the spectrometer, the incident photon flux and the density of the elements in a certain volume (n_X).[155] For a practical analysis, however, all these factors, except for n_x, are summarized in the so-called atomic sensitivity factor (ASF):

$$A_x = n_x \cdot ASF_x.$$

Equation 3-8

Specifically, the ASF incorporates the analyzer parameters such as the transmission function and spectrometer sensitivity and the sample parameters such as the inelastic mean free path of the photoelectrons and the ionization cross section. Ideally, ASFs should be determined from a sample with a well-known stoichiometric ratio of the elements using the experimental setup that is being used for the experiments. Because this ideality is but only seldom possible, ASF values for special geometries, certain types of analyzers and light sources are tabulated[39] for a large number of elements. In this work, two lists were taken into consideration: one for analyzers from Physical Electronics [164] and the other one for analyzers from Escalab. The percentage C_x of a specific element in a homogeneous sample can then be given by

[39] Uses of this tabulated ASFs have shown a reproducibility in quantification for well-known components of about 10%.[155]

$$C_x = \frac{n_x}{\sum_i n_i} = \frac{\frac{A_x}{ASF_x}}{\sum_i \frac{A_i}{ASF_i}}$$

Equation 3-9

Assessment of the coverage and thickness of adsorbates and thin films by XPS

The attenuation of a substrate core level photoemission upon coverage by an overlayer of adsorbate can be utilized to estimate the thickness of the adsorbate film. Since the Beer-Lambert law also applies to the damping of a substrate's core level (A) photoemission intensity, the following relation holds for its intensity before (I_A^0) and intensity after (I_A') the deposition of the adsorbate under the assumption of a homogeneous substrate coverage:

$$\frac{I_A'}{I_A^0} = exp\left(-\frac{d}{\lambda(E_A)}\right)$$

Equation 3-10

where d is the thickness of the adsorbate film and $\lambda(E_A)$ is the IMFP of the photoelectron emitted from A in the overlayer. Likewise, it is also possible to obtain the adsorbate film thickness from the increase in its core level (B) photoemission intensity from the following relation:

$$\frac{I_B'}{I_B^\infty} = 1 - exp\left(-\frac{d}{\lambda(E_B)}\right)$$

Equation 3-11

where I_B' is the integrated intensity of the core level B when the film thickness is d, I_B^∞ is the integrated intensity at the complete coverage of the substrate by the adsorbate, and $\lambda(E_B)$ is the IMFP of the photoelectron emitted from B in the film adsorbate itself. These two relations can easily be applied in determining the film thickness only if the substrate emission is still present. Film thicknesses can also be estimated from pre-determined deposition rates; this is normally applied when the adsorbate film is thick with the absence of a substrate emission.

3.1.6 Instrumentation and technical considerations

The basic assembly of a photoemission spectrometer is displayed in Figure 3.3. The photon source emits a monochromatic beam of photons that is directed onto the sample. The photoelectrons that are emitted from the surface of the sample upon excitation are then focused by a set of electronic lenses to the entrance slit S_1 of the hemispherical analyzer (HSA). This lens system also facilitates the kinetic energy retardation of the photoelectrons. Here, the retarding voltage is varied to change the kinetic energy of the photoelectrons reaching the analyzer while measuring a spectrum.

After passing through S_1, the photoelectrons with kinetic energies matching the pass energy are allowed to traverse the HSA by moving from S_1 through the central trajectory between the inner and outer hemispheres to the exit slit S_2. Hence, an energy dispersive

analysis is possible. The transmission through the HSA and the spectral resolution strongly depends on this pass energy. Since the HSA is a capacitor with a constant radial electric field between the inner and the outer hemispheres, the photoelectrons are deflected by the field into elliptical trajectories between the hemispheres. The detection of the photoelectrons is done by multi-channel detectors. These detectors are basically channeltrons that enhance the individual electron signal through a cascade process.

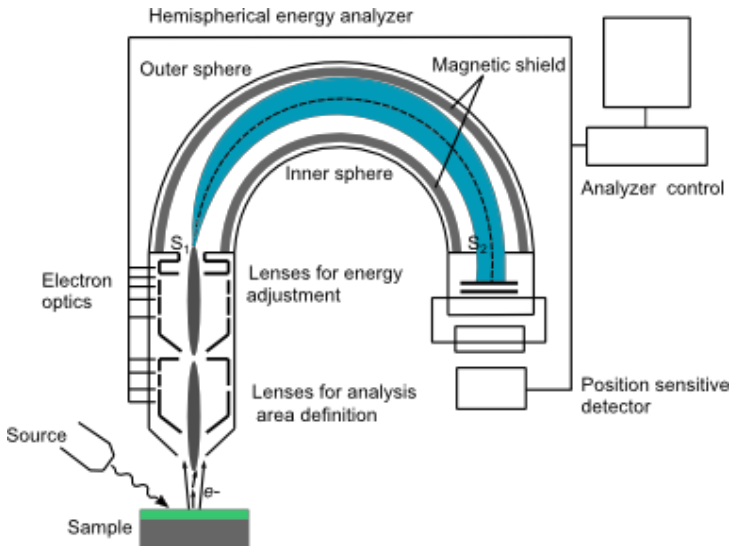

Figure 3.3: The working principle of a state-of-the-art photoelectron spectrometer with a hemispherical analyzer (HSA). Photoelectrons are generated through the irradiation of the sample with a monochromated electromagnetic radiation. They are directed to the detector above the sample, passing through the HSA which selects the kinetic energy of the detected electrons. The photoelectrons are eventually detected by a position sensitive detector. Adapted from a website.[40]

Performing PES experiments with high precision, an ultra-high vacuum (UHV) environment is required for two reasons. First, due to the high surface sensitivity of the technique, a surface layer of adsorbates would deteriorate a measurement at a non-UHV condition. Second, the deflection of the emitted photoelectrons traveling from the sample surface to the detector needs to minimized. All PES measurements in this thesis were performed at vacuum pressures in the lower 10^{-9} - 10^{-10} mbar regime.

PES is popularly the choice for surface, interface and thin film studies because $\lambda(E_{kin})$ in solids is rather short: up to a few tens of Å for XPS and 2-10 Å for UPS.[160] The whole PES setup can yield the core level spectra in the energy range of X-rays and the valence band spectra in the energy range of ultraviolet photons. It should be noted that PES is generally a surface averaging technique, because the analyzed sample spot size is usually in the range of μm^2 or even mm^2. In addition, sample charging and photo-degradation need to be avoided to obtain reliable data as these are particularly setback issues for organic materials. Photoelectrons leave the sample positively ionized, and charge neutrality must, thereby, be

[40] Website: J.D. Grunwaldt. Surface analysis (xps, iss, etc.). http://www.baiker.ethz.ch/members/grunwaldt/Surface_Analysis_XPS_PartI.pdf.

re-established through current from the substrate. The photoionization of the sample surface may lead to a positive charge build-up because of the low conductivity of many organic materials and to subsequent chemical reactions between positively charged molecules.[165] Sample illumination with visible light can be employed to efficiently remove eventual charging because it generates mobile charges via internal photoemission at the interface with the substrate.[166, 167]

3.1.7 Ultra-high vacuum systems

The study of the chemical and electronic properties of material surfaces and interfaces by means of photoemission spectroscopy is typically carried out in an ultrahigh vacuum (UHV) condition where the pressure of the analysis system is below 10^{-7} Pa. The UHV condition guarantees lossless transport of the emitted photoelectrons to the detector. Since PES is a surface-sensitive technique that can measure the elemental composition at the parts per thousand range, a high vacuum is critical to keep the surfaces of samples free of adsorbates during the experiment. For samples that are prepared in an ambient atmospheric environment, their surfaces are easily covered by adsorbates, resulting to photoemission contributions coming from adventitious carbons, hydrocarbons, oxygen and water. Such contaminations also modify the chemical and electronic structure of the surface.

There are several pre-treatments for the removal of adsorbates prior to a PES analysis. For substrates that are prepared externally, the cleaning treatment can involve ultrasonic agitations with acetone, ethanol, and isopropyl alcohol in sequence. For oxide surfaces, a moderate heating at 400-600°C in oxygen tend to be very useful.[168] For materials that are sensitive to oxidation and degradation at high temperatures (*e.g.* organic materials), heat treatments are waived. Ar-ion sputtering is another pre-treatment where the surface layers are removed by an incident beam of Ar ions. However, ion bombardment leads to the breaking of chemical bonds, thereby, destroying the crystallinity and forming defects. Furthermore, sputtering leads to changes in the composition of the surface due to the preferential sputtering of certain elements over others (*i.e.* different sputtering rates for different atomic weights).[169, 170] Ozone (O_3) surface activation can also be applied in the removal of residual carbon contaminations.[171]

In performing PES, a system that allows in-situ analysis after a sample deposition without breaking vacuum offers a great advantage as it warrants a contamination-free surface in the absence of air exposure. Such an integrated type of system was provided by the DAISY-MAT, DAISY-SOL, HEISY-ORG and SoLiAS for the different film depositions and surface/interface analysis that was carried out in this work.

Darmstadt Integrated Systems

The Darmstadt Integrated System for Materials Research (DAISY-MAT), shown in Figure 3.4, is an UHV system composed of a section for different deposition techniques contained in individual chambers that are all attached to a single distribution chamber and a section for surface analysis equipped with a Physical Electronics Phi 5700 surface analysis unit. The base pressure of the system at the time of this work was in the range between 10^{-7} - 10^{-8} Pa. The design of the integrated system allows samples to be transferred from the deposition chambers to the analysis chamber with the safety of not getting exposed to air for reliable *in-situ* XPS and UPS measurements. For this work, the physical vapor (PV) deposition chamber was used for material evaporation to obtain thin films and the measurements of the film characteristics were carried out afterwards in the surface analysis chamber.

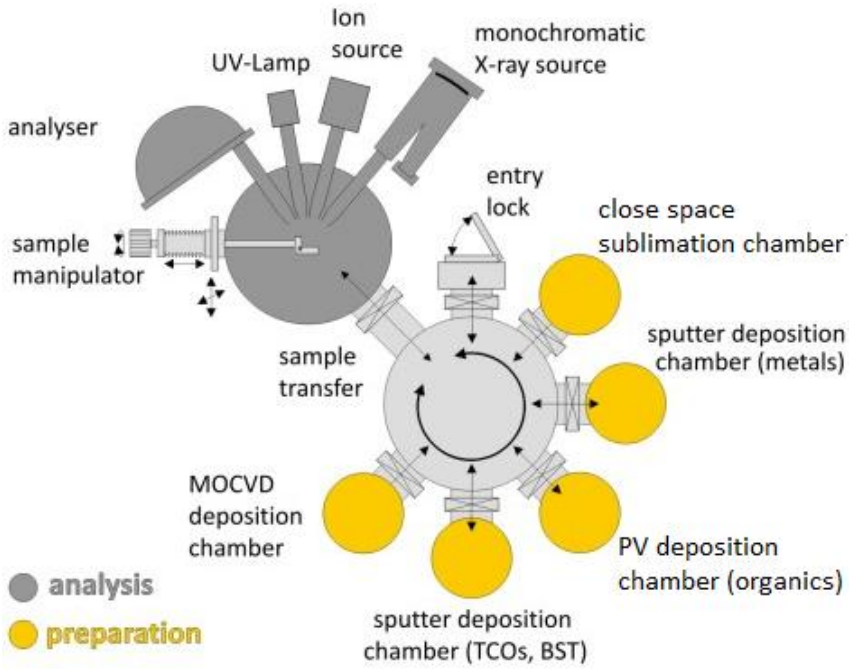

Figure 3.4: Layout of the DAISY-MAT in Darmstadt. Different dedicated deposition chambers are all attached to a single distribution chamber that is connected to the analysis chamber for *in-situ* XPS and UPS measurements. Adapted from the Surface Science website.[41]

Another integrated UHV system in Darmstadt dedicated for solar cell research is the DAISY-SOL. The schematic layout of the system is shown in Figure 3.5. The analysis chamber in the DAISY-SOL is equipped with a VG Escalab 250 surface analysis unit. In this work, the chemical vapor deposition (CVD) and the physical vapor deposition (PVD) chambers were used for thin film preparations.

[41] http://www.mawi.tu-darmstadt.de/of/of/methoden/daisy_mat/index.en.jsp

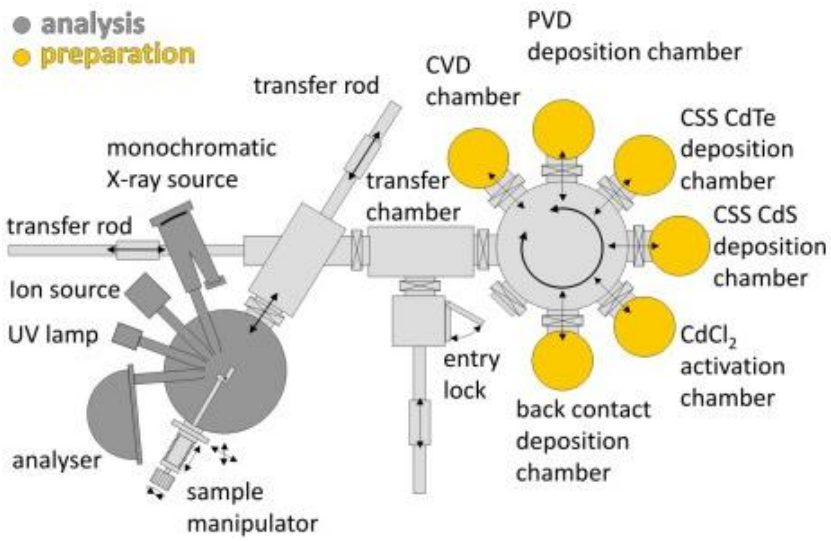

Figure 3.5: Layout of the DAISY-SOL in Darmstadt. Different dedicated deposition chambers are all attached to a single distribution chamber that is connected to the analysis chamber for *in-situ* XPS and UPS measurements. Taken from the Surface Science website.[42]

Clustertool

The clustertool at the InnovationLab in Heidelberg is a huge integrated system for sample preparation and characterization for the joint research activities of the TU Braunschweig, the University of Heidelberg, and the TU Darmstadt. The layout of the system is shown in Figure 3.6.

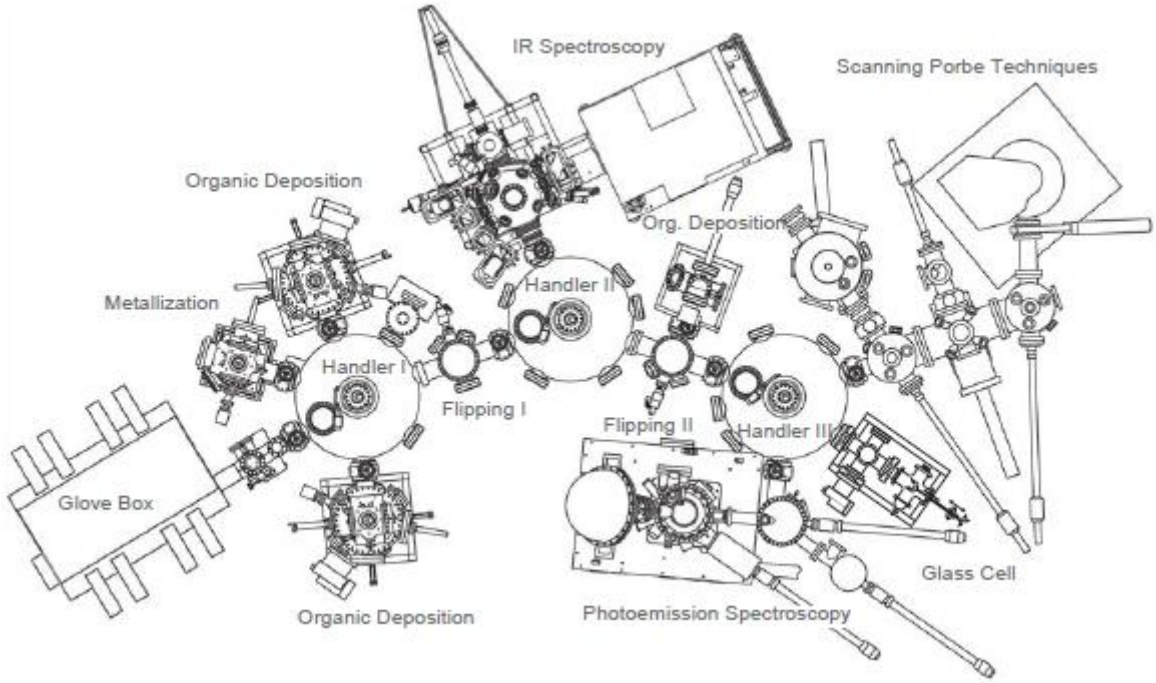

Figure 3.6: Layout of the integrated system Clustertool of the Analytics Competence Center at the InnovationLab in Heidelberg. Taken from [105].

[42] http://www.mawi.tu-darmstadt.de/of/of/methoden/daisysol/index.en.jsp

It has a glovebox for solution-based depositions in an inert atmosphere, and it is attached to the UHV system via a loadlock. It has several chambers for vacuum depositions, three distribution chambers that are interconnected to each other and three analysis chambers dedicated to infrared spectroscopy, PES and scanning probe techniques. For this work, the buffer chamber and glass cell combination that is built close to the PES unit was utilized. This combination is specifically a design developed by the Surface Science division for a solution-based deposition technique for organics that is suitable (*i.e.* no exposure to air) for PES analysis. Here, the glass cell is continuously rinsed with pure argon (argon 5.0 or 6.0) and the buffer chamber is also flooded with pure argon during sample transfers. Additional details on the glass cell together with the drop-casting deposition method performed in this cell are presented in Chapter 9.

SoLiAS

The solid-liquid interface analysis system (SoLiAS) is an integrated system that is specially dedicated to wet chemical experiments and solid interface experiments. It is stationed at the Berlin synchrotron radiation source, BESSY II. The general layout of the system, which is divided into three levels, is shown in Figure 3.7. The analysis chamber is in the first level. It is equipped with a Phoibos 150 hemispherical analyzer (SPECS) and a nine-channel detector. The second level provides the possibilities for UHV sample preparations. Sputter cleaning of substrates and deposition by thermal evaporation are performed in this level. The third level contains the equipment for organic molecule and solvent adsorption experiments. It also contains a buffer chamber and glass cell combination for the solution-based deposition technique, drop-casting.

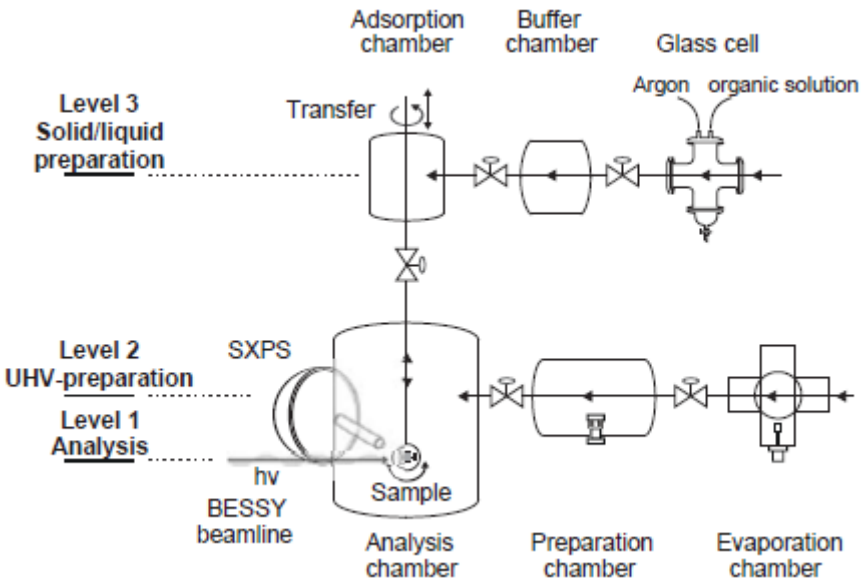

Figure 3.7: Layout of the SoLiAs at BESSY II in Berlin. Taken from [105].

The SoLiAS provides opportunities for synchrotron-induced photoemission spectroscopy (SXPS) measurements. The synchrotron light has excellent properties like a small divergence and source size, a linear and circular polarization, a pulsed time structure and a high brilliance, flux and stability. A big advantage of SXPS is that the excitation energy of the radiation source can be varied. This enables the information depth to be tuned and maintained upon consideration of the dependence of the IMFP of photoelectrons on their kinetic energies (Figure 3.1) in order to get the highest surface sensitivity.

In this study, all the X-ray photoelectron spectroscopy (XPS) measurements were performed using a monochromatized Al Kα ($h\nu$ = 1486.6 eV) radiation source providing a spectral resolution of approximately 0.4 eV as determined from the Gaussian broadening (full width at half maximum) of a sputter-cleaned Ag sample's Fermi edge at room temperature. While in some cases core level binding energy values are given with 10 meV precision to track relative changes, the absolute positions should be rounded to the next 100 meV digit. The ultraviolet photoelectron spectroscopy (UPS) measurements were all done in normal emission with He I excitation ($h\nu$ = 21.22 eV) from a gas discharge lamp. The binding energies are given with respect to the Fermi energy of the metallic sample holder as was derived using the Ag sample. Binding energy positions are determined from the spectra after Shirley background subtraction and spectral fitting analysis using Voigt profiles consisting of a convolution of Gaussian and Lorentzian lineshapes.

3.2 Absorption spectroscopy and the determination of the optical bandgap in inorganic semiconductors

Absorption refers to the physical process of absorbing light. The absorptions of atoms and molecules generally lie within the ultraviolet to the visible region; thus the term "UV-Vis absorption". The absorption spectrum is obtained by recording the absorbance as a function of the wavelength (or frequency) of the incident light.

Inorganic semiconductors are transparent to photons whose energies lie below their bandgap and are strongly absorbing for photons whose energies exceed the bandgap energy. In the case of organic semiconductors, many molecules absorb ultraviolet or visible light depending on the electronic orbitals that are involved. Their absorption spectra generally show a number of absorption bands corresponding to the structural units of the molecule.

In an absorption measurement, the absorbance actually records the attenuation of the transmitted radiant power in a material. Because of absorption, the amount of light that is transmitted through a material diminishes as it travels through the material. For inorganic semiconductors, the bandgap may be determined from the transmission of light of various wavelengths. The intensity of the light that is transmitted through the semiconductor, I_T, follows the Beer-Lambert law, and is given by

$$I_T = I_O e^{-\alpha d}$$

Equation 3-12

where α is the absorption coefficient and d is the thickness of the semiconductor material. I_O is the intensity of the incident light. The absorption coefficient strongly depends on the wavelength of the incident light, and it can be in the range of 10^5 cm^{-1} for photons whose energies are larger than the bandgap of the semiconductor. Defining transmittance, T, as:

$$T = \frac{I_T}{I_O}$$

Equation 3-13

the absorption coefficient can, thus, be directly determined from the measurement.

For a large number of inorganic semiconductors in both crystalline and amorphous forms, the dependence of the absorption coefficient upon the photon energy $h\nu$ for optically induced transitions takes the form

$$\alpha h\nu = A(h\nu - E_g)^m$$

Equation 3-14

where E_g is the energy gap, A is a constant and $m = \frac{1}{2}$ for an allowed direct energy gap and $m = \frac{3}{2}$ for a forbidden direct energy gap. Plotting the graph of $(\alpha h\nu)^2$ versus $h\nu$ gives an approximate value of E_g by taking the intercept of the extrapolation to the zero absorption with the photon energy axis, i.e. $(\alpha h\nu)^2 \rightarrow 0$.[172-177]

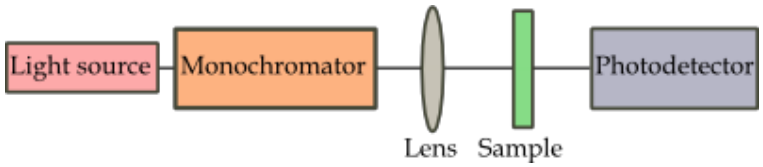

Figure 3.8: Basic components in an optical absorption measurement setup.

A basic experimental setup for absorption spectroscopy is given by the schematic diagram in Figure 3.8. The transmission spectrum of a semiconductor may be observed with the use of a monochromator and a photodetector. Light from a source that passes through the monochromator will be reflected at different angles for different wavelengths by a grating placed inside the monochromator. By rotating the grating it is possible to tune the wavelength of the incident light through the exit slit of the monochromator for the recording at the photodetector of the transmitted light intensity through the sample as a function of the wavelength.

Determination of the film thickness from the transmission spectrum

Generally there are several techniques that can be employed to determine the thickness of a film deposited on a transparent substrate, e.g. profiling stylus, cross-section SEM, or various interferometric techniques. A straightforward analysis, as developed by Swanepoel [178], is based on the use of the extremes of the interference fringes present in a transmission spectrum (a sample spectrum is shown in Figure 3.9). Here, a widely used

envelope method had been developed for transmittance measurements to evaluate the refractive index, film thickness, extinction coefficient, and absorption coefficient with accuracies better than 1% given that the thickness is uniform.[178, 179]

In this work, film thicknesses, d_{film}, were also calculated from the interference pattern in the measured transmission spectra using the following formula from Swanepoel's method:

$$d_{film} = \frac{\lambda_1 \lambda_2}{2(\lambda_1 n_2 - \lambda_2 n_1)}$$

Equation 3-15

where n_1 and n_2 are the refractive indices at two adjacent maxima (or minima) at λ_1 and λ_2. Using the envelope curves for T_{max} (T_M) and T_{min} (T_m) as shown in Figure 3.9,

$$N = 2n_s \frac{T_M - T_m}{T_M T_m} + \frac{{n_s}^2 + 1}{2}$$

Equation 3-16

the refractive index can be calculated,

$$n = [N + (N^2 - {n_s}^2)^{1/2}]^{1/2}$$

Equation 3-17

For this work, however, the values for the refractive indices (as a function of the wavelength) needed to be known for the calculation of film thicknesses. Refractive indices were then taken from a database [43] because our substrates were combinations of transparent conducting oxides and glass.

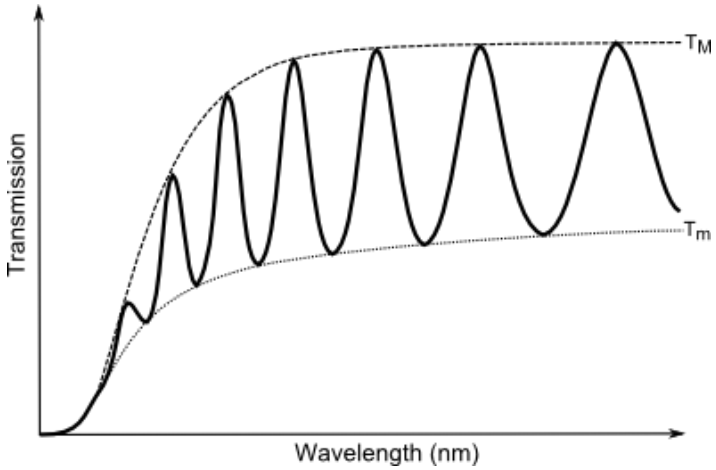

Figure 3.9: A sample transmission spectrum to illustrate the interference fringes that can be found from uniform thin films grown on transparent substrates. T_M and T_m, which are continuous functions of the wavelength, represent the envelopes for the maxima and minima of the interference fringes.

[43] Refractive index database. RefractiveIndex.INFO
http://refractiveindex.info/?shelf=main&book=ZnSe&page=Connolly

3.3 Photoluminescence spectroscopy

Photoluminescence (PL) is a process that is complementary to absorption: the electron-hole pair that is created when a photon is absorbed by a semiconductor may undergo a radiative recombination where a photon is re-emitted with a lower energy and random phase, polarization and direction. A prompt emission that occurs within 10^{-9} - 10^{-8} s after excitation is called a fluorescence; while an emission that occurs within 10^{-6} - 1 s is called a phosphorescence (refer to Chapter 2.2.3). In this work, the PL spectra were obtained using a Labram HR800 Horiba spectrometer fitted with a 150 grooves/mm grating. The spectrometer was equipped with an air-cooled Andor CCD detector. The samples were illuminated with different laser sources operating at different wavelengths depending on the material requirements for excitation. PL spectra of liquid solutions of organic dyes were also obtained using a Varian Cary Ellipse spectrophotometer, which is equipped with a Xe-arc lamp as the excitation source. All the PL measurements were performed at room temperature.

3.4 X-ray diffraction

X-ray diffraction (XRD) is an analytical technique that is primarily used to identify crystal phases and provide information on unit cell dimensions. XRD is based on the constructive interference of monochromatic X-rays in a crystalline material. These X-rays are generated by a cathode ray tube and then filtered to produce monochromatic radiation. They are collimated to concentrate toward the sample. The interaction of the incident rays with a given sample produces a unique constructive interference of diffracted rays when the conditions satisfy Bragg's law:

$$n\lambda = 2d \sin\theta$$

Equation 3 -18

where n is an integer, λ is the wavelength of the X-ray, d is the spacing between the planes in the atomic lattice and θ is the angle between the incident X-rays and the planes. The diffracted rays are detected, counted and processed. By scanning the sample through a range of 2θ angles, all the possible diffraction directions of the sample atomic lattices are gathered. The conversions of the positions of the diffraction peaks to d-spacings lead to the identification of the sample as d is a unique parameter. The lattice spacing, d, is calculated from the Bragg's formula:

$$d = \frac{\lambda}{2 \sin\theta}$$

Equation 3-19

where λ is the wavelength of the X-ray source (Cu Kα radiation) and θ is the Bragg diffraction angle. The lattice parameter is calculated using the formula (e.g. for cubic lattices):

$$\frac{1}{d^2} = \frac{h^2 + k^2 + l^2}{a^2}$$

Equation 3-20

where h, k and l are the Miller indices of the lattice plane. The average crystallite size is estimated using the Scherrer formula [180]:

$$\tau = \frac{K\lambda}{\beta \cos\theta}$$

Equation 3-21

where K is the shape factor that was taken to be 0.94 and β is the full width at half maximum of the peak.

In this work, XRD patterns of the thin films were obtained using a monochromatic Cu K$\alpha_{1,2}$-source (Philips X'Pert Pro MPD, 1.5406 Å). The XRD measurement for a nanocrystalline film was performed with a Seifert PTS 3003 diffractometer using a Cu anode and an X-ray mirror on the primary side. On the secondary side, a long Soller slit and a graphite monochromator were used to separate the Cu Kα line.

3.5 Sample preparation

Film samples were prepared through different techniques depending on the sample requirements of the employed characterization methods. These techniques included physical vapor deposition, metalorganic chemical vapor deposition, spin-coating, doctor-blading and drop-casting. Details of the different sample preparations are discussed together with the description of the materials used in this study in the succeeding chapters.

Chapter 4 Materials: ZnSe and Ir(BPA)

The hybrid system described in the previous chapter consists of an electron- and hole-conducting inorganic semiconductor matrix and a luminescent organic semiconductor dopant. Zinc selenide (ZnSe), which is a wide bandgap semiconductor, is looked into as a candidate for the matrix material. And Ir(BPA), a red triplet light-emitter, is the candidate for the dopant material. In this chapter, the properties of ZnSe and Ir(BPA) for this part of the work are presented. Since the main focus is on the investigation of the interfacial electronic and chemical properties of the two materials put in contact with each other, descriptions of the electronic properties derived from PES of the individual materials are given. The crystal structures, optical properties and morphologies of the materials are described here as well.

4.1 ZnSe

ZnSe is a widely-known solid compound which is comprised of zinc (Zn) and selenium (Se). And because Zn and Se belong to groups 12 and 16 of the periodic table, respectively, ZnSe is classified to belong to the II-VI semiconductor group. ZnSe is a clear yellow polycrystalline material that transmits in the 0.5 - 15 μm range. It has a high melting point at ~ 1500°C and a density of 5.27 g/cm^3. ZnSe is a intrinsic semiconductor material with a large bulk band gap of 2.82 eV (440 nm), high refractive index, low absorption at the infrared spectral region and good transmission at the visible wavelengths. It, therefore, has a vast potential use in thin film devices and infrared components, and as windows and lenses. It is also non-hygroscopic and chemically stable; thereby making it a good capping layer for many organic semiconductor devices.[181-183]

Particular interest is on ZnSe because of its intense UV blue luminescent properties.[184-192] The very first blue-green laser diodes that were fabricated from wide-gap II-VI semiconductors by M.A. Haase *et al* of the 3M Company emitted coherent light at 490nm from a ZnSe-based single quantum-well structure under pulsed current injection at 77 K.[193] It was a real breakthrough because until its discovery researchers were hard-pressed in coaxing semiconductors to emit even a little blue light.

Light-emitting devices require high mobilities of charge carriers. Gallium arsenide (GaAs) from the III-V family of semiconductors, for example, which is largely used for infrared LEDs and laser diodes, exhibit an electron mobility of ~ 5000 cm^2/V·s in *n*-type GaAs and a hole mobility[44] of ~ 300 cm^2/V·s in *p*-type GaAs at normal room-temperature (RT) operation (300 K).[194] ZnSe from the II-VI group of semiconductors, on the other hand, is not particularly popular in terms of mobility.[194] At 300 K, its electron and hole

[44] Hole mobilities are lower than electron mobilities due to the large effective mass of holes as compared to that of electrons in most semiconductors.

mobilities are 500 $cm^2/V{\cdot}s$ and 30 $cm^2/V{\cdot}s$, respectively. The highest mobility on record is about 12000 $cm^2/V{\cdot}s$, but at 50 K, from ZnSe crystals grown by the vapor-phase growth technique.[195] Still overall, the carrier mobilities in inorganic semiconductor materials are higher than their molecular and polymer organic LED materials counterparts, where the carrier hopping is the dominant conduction mechanism. ZnSe could, therefore, still be a viable material candidate. In terms of an actual device, a ZnSe *p-n* diode exhibited RT electroluminescence at 467 nm (blue) with a turn on voltage of 5.70 V.[189] This *p*-ZnSe had a RT mobility of only 102 $cm^2/V{\cdot}s$.

The preparation technique for the ZnSe films greatly dictates the conducting quality of the films. Reports on ZnSe thin films obtained by the thermal evaporation technique indicate that the films show high resistivity.[196] A possible route to obtain high conductivity ZnSe films would be to co-evaporate ZnSe with Ga and excess Zn followed by annealing in Zn vapor.[197] The as-deposited ZnSe film without the co-evaporation and annealing exhibited a high resistivity of 5×10^8 Ω·cm despite an excellent optical quality (i.e. a sharp absorption edge) and a highly polycrystalline structure.

4.1.1 Deposition of ZnSe thin films

ZnSe thin films can be prepared by a variety of techniques like vacuum thermal evaporation [76, 173-175, 198-205], molecular beam epitaxy [204, 206-217], atomic layer epitaxy [218, 219], r.f. magnetron sputtering [220], spray pyrolysis [176], chemical bath (CBD) [221, 222] and chemical vapor deposition [223-225]. Definitely, the method of deposition influences film properties.[226] In this work, the ZnSe films were obtained by thermal evaporation. In general, thermal evaporation is very common due to its simplicity, low cost, reproducibility, high deposition rate and scalability to deposit onto large area substrates. Moreover, the films that are produced with this method are highly adherent and uniform. It is one of the best techniques for the synthesis of polycrystalline films.

Among the various techniques for preparing ZnSe films, thermal evaporation is relatively simple, yet a very useful method to prepare thin films in a more simple and convenient way. As a variant of the physical vapor deposition (PVD), it basically involves the evaporation of source materials in a vacuum chamber followed by the condensation of the vaporized form onto various substrate surfaces to get the desired film material. For our type of study, this method offers the possibility of a step-wise deposition for bilayer systems as well as a co-deposition for mixed (or composite) systems.

In this work, thin films of ZnSe were obtained by the thermal evaporation of ZnSe crushed crystals that are stuffed into the alumina crucible of our home-made temperature-controlled Knudsen-type cell shown in Figure 4.1. When ZnSe evaporates, a congruent vaporization produces a Zn and Se_2 flux.[198] The high temperatures for evaporation of ZnSe are achieved in this home-made cell through resistive heating of the tantalum wire that is wrapped around the crucible. The evaporation temperature is monitored through a

thermocouple that is in contact to the crucible. The ZnSe bulk crystals (with approximately a 2 - 7 mm maximum dimension) were purchased from Chempur and used as received. As substrates, commercial 120 nm thick tin-doped indium oxide (ITO) films on glass and plain quartz glass were used depending on which characterization technique the samples were going to be used for.

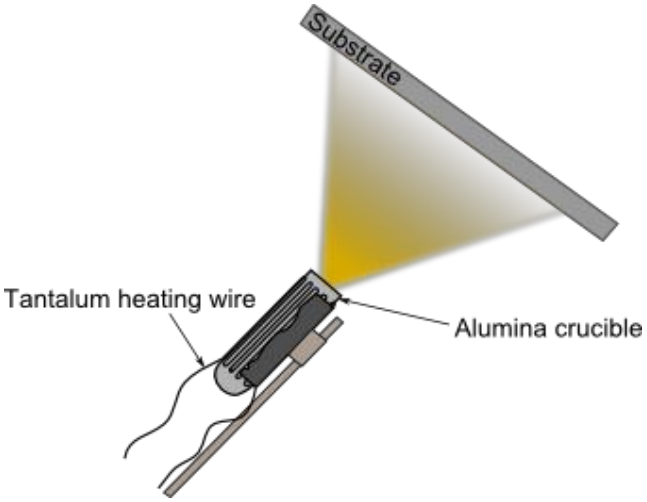

Figure 4.1: Thermal evaporation deposition technique. The home-made Knudsen type cell is basically composed of an alumina crucible that is wrapped with a tantalum wire for resistive heating.

Procedure-wise, after filling a source crucible with ZnSe crystals and prior to any further depositions and measurements, source calibrations are normally performed in order to determine the deposition parameters (*e.g.* source current, voltage and temperature) and their corresponding deposition rates. The calibration proceeds through quantitative determination of the attenuation of the intensity of a substrate emission line. Ex-situ cleaning of the substrates is also necessary prior to introducing them into the vacuum system. The substrate cleaning procedure is comprised of ultrasonic agitations with acetone, ethanol and isopropyl alcohol in sequence and argon ion sputtering.

Commonly known, the microstructure and optical properties of a thin film depend very much on the conditions upon which the deposition has been carried out as well as to postproduction process such as annealing. Through depositing on heated substrates or post-deposition annealing, the properties of deposited thin films could be tailored to some extent. From several reports in literature and depending on the deposition technique, these steps could be necessary to obtain crystalline structures, improve certain optoelectronic properties and eliminate residues of the deposition precursors on the sample.[176, 198, 214, 216, 227-229] In one particular study on ZnSe films obtained through thermal evaporation [199], the as-grown films and the films grown on heated substrates do not show substantial differences on all aspects. The differences are only found once these films undergo post-deposition annealing at temperatures ranging from 200 - 400°C. The most obvious is on the morphologies of the films. While both exhibit an increase in grain size upon annealing, the

change in their initial faceted structure to a more rounded structure is only exhibited by the as-grown film.

Heat treatments were briefly performed in this work in order to substantiate their effect on the electronic, structure and optical qualities of our own ZnSe films. Based on our hybrid design concept, any heat treatment for ZnSe must be carefully considered to avoid thermal degradation and re-evaporation of the organic counterpart. This entails that heating treatments should not go over 200°C to avoid affecting the organic material.

4.1.2 Photoelectron spectroscopy measurements of ZnSe films

A 11.2 nm thick ZnSe film was deposited on an ITO glass substrate. The source temperature for the evaporation of ZnSe was 737°C, with a deposition rate of 56 Å/min. This rate was obtained from a ZnSe source calibration experiment where the attenuation of the intensity of the substrate In3d emission was used. The calculation required the IMFP of the emitted In3d photoelectrons in the ZnSe layer, which was obtained from the NIST electron inelastic-mean-free-path database. Details can be found in Appendix B.

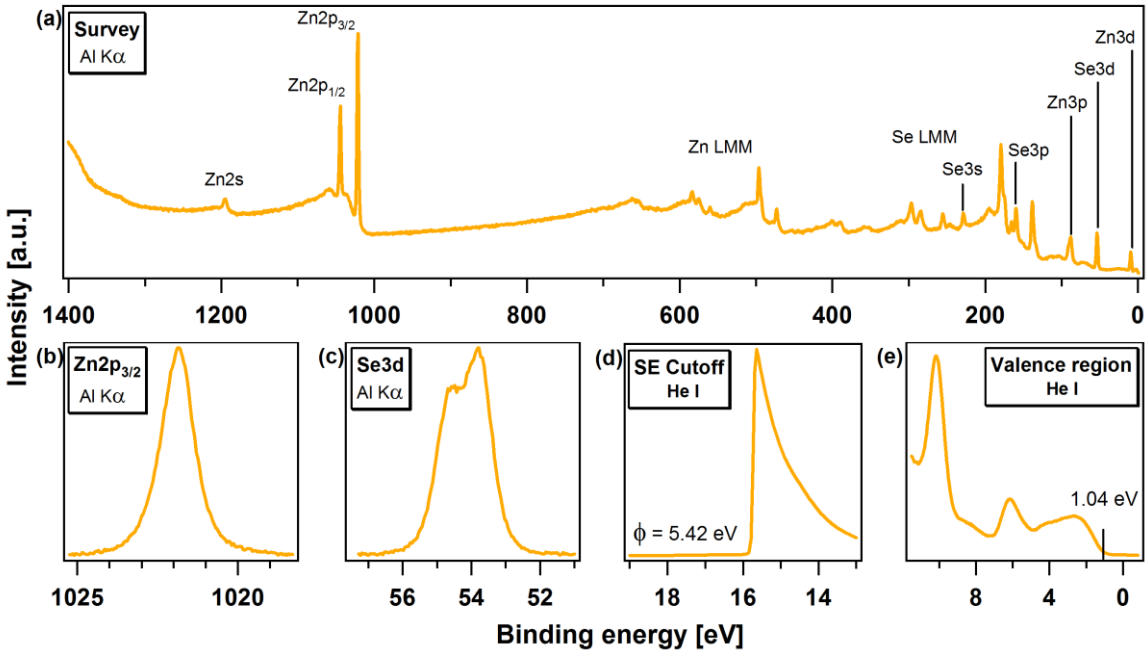

Figure 4.2: (a) A survey spectrum showing all the peak photoemissions that are representative of the elemental composition of a ZnSe film deposited on ITO glass substrate. Detailed spectra of (b) $Zn2p_{3/2}$ and (c) Se3d emissions. (d) The SE cutoff where ϕ is determined to be 5.42 eV. (e) The valence region where the VBM is at 1.04 eV from the Fermi level.

The XPS survey and detailed spectra together with the UPS SE cutoff and valence region spectra taken from the film are shown in Figure 4.2. The evaporation and PES measurements were performed *in situ* using the DAISY-MAT in Darmstadt. In the XPS survey spectrum, all ZnSe characteristic emissions are designated. With no traces of

contamination and substrate photoemissions found, a clean deposition and a thick enough film with the absence of pinholes are indicated, respectively.

The most intense photoemission lines representative of the elements present in the compound (i.e. Zn and Se) come from the $Zn2p_{3/2}$ and Se3d core levels. The detailed spectra of these core levels are shown in Figure 4.2 (b)-(c). The expected doublet structure of the 3d orbital is clearly exhibited in the Se3d detail spectrum. After performing Shirley background subtraction and spectral fitting, the binding energy of $Zn2p_{3/2}$ is determined to be ~ 1022 eV and the Se3d binding energy ~ 54 eV. The $Zn2p_{3/2}$/Se3d intensity ratio normalized to the respective ASFs of $Zn2p_{3/2}$ and Se3d is 1.07. This almost a 1:1 Zn to Se ratio at the surface.[217]

With a He I excitation (UV, $h\nu = 21.22$ eV), the SE cutoff and the valence region spectra are obtained and displayed in Figure 4.2(d)-(e). The lineshape of the valence region is confirmed in literature.[198, 204, 230] The onset of photoemission at the lowest binding energy end of the spectrum is taken to be the position of the valence band maximum (VBM). Using a linear fit of the leading edge and then taking the intersection of the fitted line to zero intensity with the binding energy axis, the VBM is obtained to be at 1.04 eV from the Fermi level position (at 0 eV on the binding energy scale). The sudden drop of photoemission at the high binding energy end is taken to be the SE cutoff. A similar linear extrapolation yields the binding energy position of the SE cutoff. Using Equation 3-6, the work function ϕ of the ZnSe film is calculated to be 5.42 eV. From ϕ and VBM, the ionization potential is then 6.46 eV which corresponds well with literature.[231, 232]

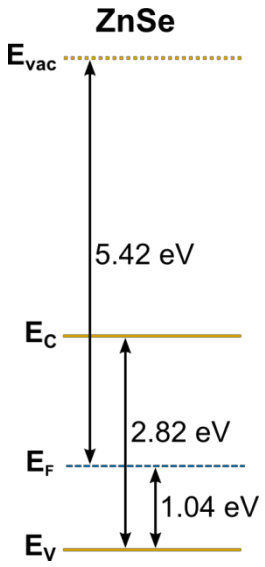

Figure 4.3: Energy levels of ZnSe as deduced from the UPS measurement: $\phi = 5.42$ eV and VBM at 1.04 eV. The energy gap is taken from transmittance measurements (found in the succeeding sections).

ZnSe is a semiconductor with a bulk direct energy gap value of 2.82 eV at 300 K for both the zincblende and wurtzite crystal structures. This value is listed at The

Semiconductors-Information Website.[45] Depending on the form (e.g. bulk, film, nanocrystals) and other relevant attributes (e.g. thickness, doping, morphology, size, impurities, final sample composition), the values presented in literature are somewhere between 2.13 eV - 3.22 eV range. There is a group who measured PES-IPES on their MBE-deposited ZnSe(001) films.[233] From their measurements, a PES bandgap of 2.80 eV was deduced from the VBM onset in PES and CBM onset in IPES. From our transmittance measurements (Figure 4.10), the deduced optical gap for our ZnSe film is 2.82 eV. Taking the energy gap to be 2.82 eV, the electronic structure of this pristine ZnSe film is drawn in Figure 4.3. The ZnSe film is slightly *p*-doped. The PES measured ionization potential for the ZnSe film coincides well with other literature reports.[204, 230, 232]

Effect of heat treatments on the occluded Se^0 in ZnSe films

Thermally evaporated ZnSe films measured with XRD, transmittance, FTIR, Raman and PL experiments demonstrated that even at RT deposition the obtained ZnSe thin films have better quality than films deposited elsewhere on heated substrates.[174] However, heat treatments are popular due to certain necessities and preconditions as aforementioned. There are already several reports in literature on the heat treatment effects on the structural and optical properties of ZnSe films deposited by thermal evaporation; here, the effect of heat treatment on occluded Se^0 in these films is instead studied as it has not been investigated in detail yet. In one report, it was concluded that annealing resulted in the evaporation of occluded Se^0 in CBD films.[221] They accounted the reddish/orange tint of their as-grown CBD films to the occluded Se^0. Upon annealing, the color of their films turned to the characteristic yellow tint of ZnSe. A similar observation of the reddish/orange color was actually found for some of our ZnSe films.

An XPS (with excitation using a Mg $K\alpha_{1,2}$ line at 1253.6 eV) study of the Se3d peak for Se in different selenium compounds reported the binding energy to be 55.5 eV for pure Se and 54.7 eV for ZnSe.[234] This places the Se3d binding energy position of elemental Se^0 at a higher value than that of Se^{2-} in ZnSe. From literature, the excess of Se^0 on the growing surface was observed in the PES measurements on a ZnSe film deposited on GaAs by MBE and on SnO_2 substrates by CBD.[206, 221] From the PES measurements on our as-grown ZnSe films using a freshly-filled evaporation source, photoemission from Se^0 is also observed (Figure 4.4 A). However, the film exhibited no hint at all of a reddish/orange tint in this case. Upon continued deposition, and as the ZnSe source aged after several succeeding depositions, the tint of the film products shifted from the characteristic yellow to the reddish/orange. This is indicative of a high Se^0 content in the films produced from the aged source. For a clear observation of the effect on excess Se^0, heat treatments were performed on these films from the aged source. In this study, two heat treatments were considered: one was a deposition on a heated substrate where the temperature of the

[45] http://www.semiconductors.co.uk/propiivi5410.htm

substrate was held at 170°C and the other one was an *in situ* post-deposition annealing of as-grown films with two annealing temperatures, 125°C and 210°C. Note again that though higher temperatures (300 - 500°C) are more popular in literature as such temperatures result to rather drastic improvements in grain size, the heating temperatures in this study had to be maintained below 200°C as higher temperatures will affect the organic counterpart based on our hybrid design concept if heating is ever to be implemented.

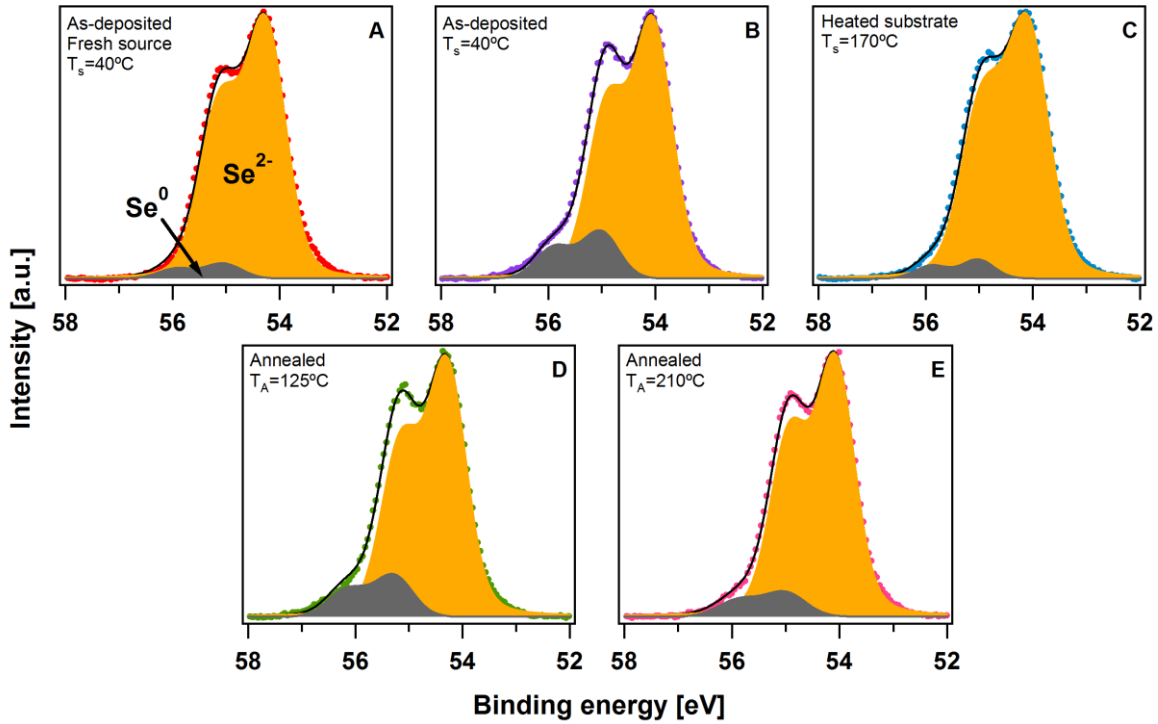

Figure 4.4: Spectral fits of the Se3d emission (A: As-grown film deposited from freshly-filled source, B: As-grown film deposited from aged source, C: Film deposited on heated substrate from aged source, C-D: Annealed as-grown films deposited from aged source).

The Se3d emission spectra, which were obtained through XPS with an Al Kα radiation source, of our ZnSe films are summarized in Figure 4.4. Due to radiative heating and the duration of the deposition (120 mins), the ambient temperature at the substrate for the as-deposited films went up to a steady 40°C. Spectral fittings were performed on all spectra using two Voigt doublet profiles: one doublet is assigned to the Se^{2-} species and the other doublet to Se^0 species. The spin-orbit splitting of the Se3d peaks was taken to be 0.86 eV [164] as compared to a literature where 0.85 was used.[207] The ratio of 2:3 (for d core lines) was considered for the doublet intensities.

For a freshly-filled source, the amount of occluded Se^0 in the as-deposited film is minimal as shown in Figure 4.4 A. As the source aged upon a continuous series of depositions, the amount of occluded Se^0 in the film product is increased and is evidenced by the large amount of Se^0 observed in the Se3d spectrum as shown in Figure 4.4 B. All heating treatments on films produced from the aged source resulted to a reduction of the Se^0 content

as can be observed in Figure 4.4 C-E. As deduced from the fitted spectra, post-deposition annealing at 125°C results only to a small Se^0 reduction. Deposition on a substrate, which was heated to 170°C, showed the largest reduction. Meanwhile, annealing of a sample from the same batch at an even higher temperature, 210°C, did not show much improvement as compared to the heated substrate at 170°C.

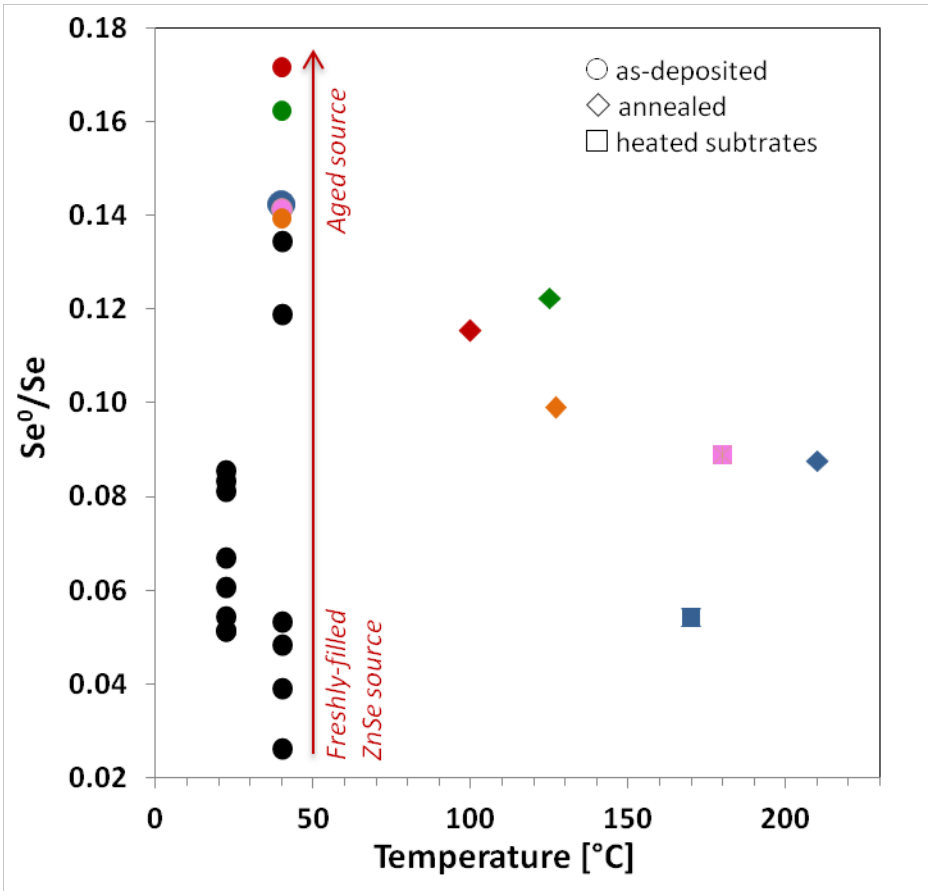

Figure 4.5: Se^0-to-Se ratio as a function of deposition temperature. The colors of the data points indicate the same batch of samples in the case of the heated substrate treatment and the same samples in the case of the post-deposition annealed treatment. Meanwhile, the shapes indicate the heat treatment performed on the samples. All heat treatments resulted to a reduced Se^0. The deposition on a heated substrate exhibited the largest reduction of Se^0.

A plot of the ratio of the integrated intensities, which are normalized to the atomic sensitivity factor for Se3d, of the occluded Se^0 to the total Se for ZnSe films deposited from a singly filled evaporation source is shown in Figure 4.5. For the as-deposited films (represented by the circle data points in the graph), two deposition temperatures are registered. These are primarily due to the deposition times. For film depositions involving a long deposition time[46], radiative heating becomes significant. The temperature of the

[46] Long deposition times (e.g. 2 - 6 hrs) were needed to obtain ZnSe film samples that are thick enough for XRD and optical transmittance measurements.

substrate reaches a steady 40°C. For short deposition times[47], the recorded temperature of the sample is around the ambient temperature of 22°C. For a freshly filled source, the amount of Se^0 in the as-deposited films is minimal. As the source aged over time, the amount of Se^0 steadily increased. Again, all heat treatments led to the reduction of Se^0 in the films. Interestingly, it seems apparent that a heat treatment is not really necessary concerning the amount of the occluded amorphous Se^0 in the films as long as the source is freshly filled.

4.1.3 Crystal structure of the films

ZnSe crystallizes into two possible crystal classes: cubic (zincblende) and hexagonal (wurtzite). Depending on the deposition procedure, either zincblende or wurtzite is obtained. Deposition of ZnSe by thermal evaporation commonly leads to films that are single-phase (*i.e.* cubic) polycrystalline with a zincblende structure.[173-175, 199, 201] The same cubic zincblende structure is found for ZnSe films grown by MBE.[209, 210]

Zincblende is based on a face-centered cubic (fcc) lattice of anions. For ZnSe zincblende structure, there are 4 Zn ions and 4 Se ions in a unit cell. This structure is shown in Figure 4.6. Each Zn atom is surrounded by 4 equidistant Se atoms at the corners of a regular tetrahedron; similarly, each Se atom is surrounded tetrahedrally by 4 Zn atoms. All the Zn-Se bonds lie parallel to a given body diagonal of the cube point in the same direction. This structure is the same as that of diamond (with all C atoms instead of Zn and Se atoms). The zincblende structure has no center of symmetry.

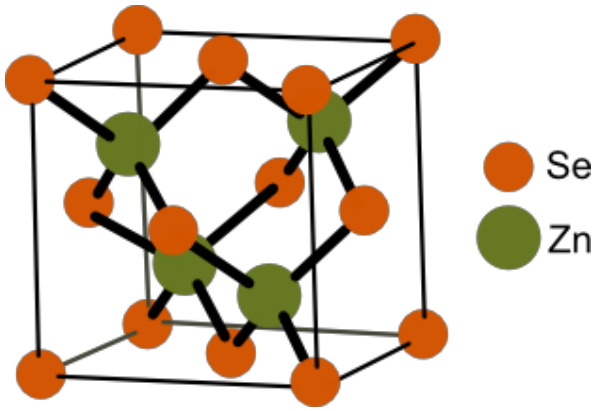

Figure 4.6: Zincblende crystal structure of ZnSe.

The crystalline structure of a RT deposited ZnSe 35 nm thin film on ITO glass substrate was determined from the X-ray diffraction pattern shown in Figure 4.7. The XRD pattern clearly exhibited reflections corresponding to the (111) and (220) diffraction planes of cubic ZnSe. These indicate that our ZnSe film, even at RT deposition, has a single phase and

[47] Short deposition times (5 - 10 mins) were enough to obtain ZnSe film samples which are fully closed (i.e. substrate photoemissions are not observed) yet thin enough so as to avoid surface charging effects for a reliable PES data set in studying the electronic structure of the ZnSe films.

is polycrystalline, which is in good agreement with previous studies.[173, 174, 177, 235] With a thin ZnSe film, peaks and a broad background from 2θ=15°-40° that correspond to the ITO on amorphous glass substrate are expected to be present in the pattern.

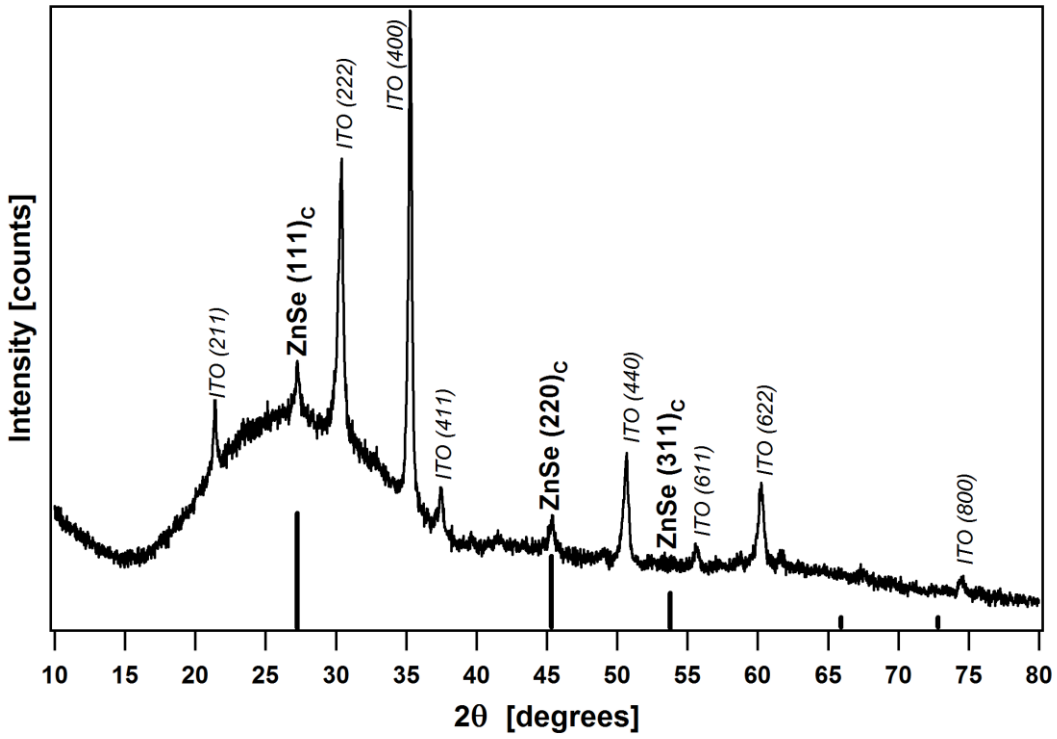

Figure 4.7: X-ray diffraction pattern of a ZnSe film deposited on ITO on glass substrate at RT along with bar markings on the *x*-axis for the bulk.

Effect of heat treatments on the crystal structure of ZnSe films

The XRD patterns from the heat-treated ZnSe films together with the patterns from the as-deposited and pulverized source pellets are shown in Figure 4.8. From the XRD patterns, the reflections that correspond to the cubic ZnSe can be identified.[173, 175, 176, 201, 220, 227, 229, 236] Notably, a highly preferred orientation along the (111) plane, which is the close-packing direction of the zincblende structure, is exhibited by all the films. It is generally found in literature that annealing of thermally-deposited ZnSe film leads to an increase in the degree of orientation of crystallites along the (111) plane, thereby increasing the (111) reflection peak height, as well as to an increase in crystallinity, thereby decreasing the peak heights from other reflections.[173, 175, 199, 205] Our results, however, are not conclusive to the effects of the heat treatments on the crystallinity of our films.

The thicknesses of the films as indicated in the figure were determined by a Dektak profilometer. The proportion of the intensity contributions coming from the ITO glass substrate as well as the peak intensities of the (111) reflection corroborates with the relative thicknesses of the films measured by the profilometer.

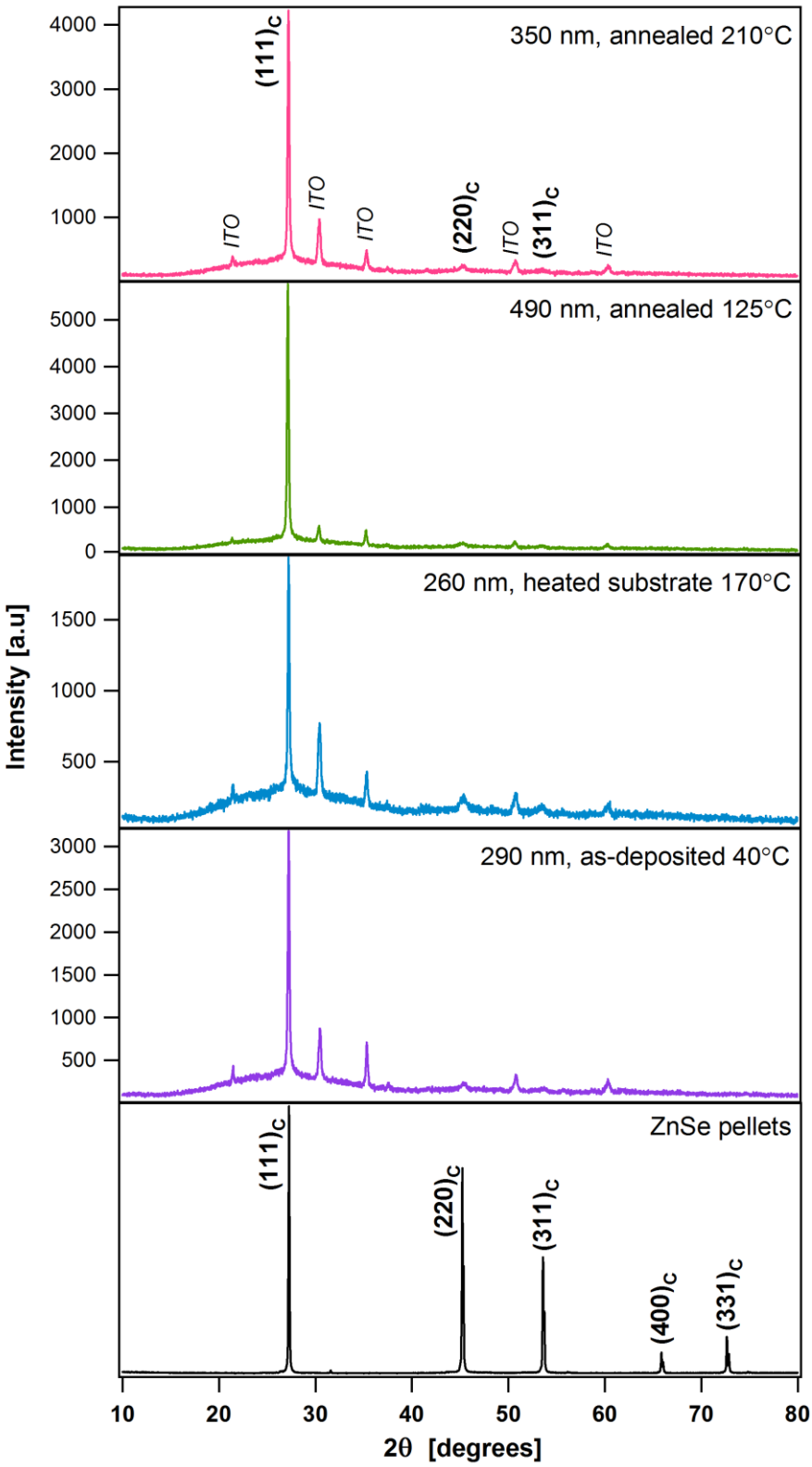

Figure 4.8: XRD patterns from as-deposited, heated-substrate and annealed ZnSe thin films together with the pattern from pulverized ZnSe pellets.

That is, the XRD pattern from the film sample with the heated substrate, which is the thinnest, showed the most intense contributions from ITO and glass. On the other extreme

end, the thickest sample which was annealed at 125°C showed the least intensity contributions from the substrate. Oddly, although all of the film samples were deposited under the same deposition parameters from the same aged source, they possess different thicknesses. This could be due to differences in the sticking coefficient and to effects brought about by the annealing. Comparing the XRD patterns shown in Figure 4.7 and Figure 4.8, the thicker films exhibit better crystallinity, which is in agreement with a study where the (111) reflection peak was reported to have intensified as the thickness of the samples increased together with the damping of other reflections.[201]

On a side note, it might be expected that the films from the aged source would overall be less crystalline because of the large amount of amorphous Se^0 in the films as observed from the PES measurements. However, comparing the XRD pattern of the as-deposited film in Figure 4.8 to the XRD patterns of the heat-treated films which have less Se^0 phases, no conclusions can be drawn. This is accounted to the differences[48] in the final film thicknesses and the low heating temperatures set in this study as compared to the reports found in literature. Also, PES being a highly surface-sensitive technique, while XRD being more a bulk technique, could be another reason. The excess Se^0 measured in PES is probably found mostly on the surface and not in the bulk of the film.

The calculated structural parameters for the (111) peak such as the lattice spacing *d*, lattice parameter *a*, and grain size τ are summarized in Table 4.1. The calculated lattice parameters of the films coincide well to the standard for bulk ZnSe at 300 K, which is 0.5668 nm. The grain size is only slightly larger in the heat-treated films as compared to the as-deposited film similar to a report found in literature.[199] Markedly, comparing to two reports in literature where their grain sizes only ranges from 20 - 28 nm for RT deposition,[173, 177] the grain size of our as-deposited film is better and is actually already almost in the same range as their 225 nm and 500 nm thick films annealed at 300°C, whose grain sizes range from 45 - 47 nm. In the case of heated substrates, a study showed that the grain size of their films deposited at a substrate temperature of 200°C was only 17 nm.[205]

Sample	2θ (°)	d (Å)	a (Å)	τ (nm)
As-deposited, T=40°C	27.24	3.274	5.670	42.72
Heated substrate, T=170°C	27.24	3.274	5.670	44.97
Annealed, T=125°C	27.16	3.283	5.687	47.46
Annealed, T=210°C	27.22	3.276	5.674	44.97

Table 4.1: The structural parameters for the (111) peak of the ZnSe films under different heating treatments (d: lattice spacing, a: lattice parameter, τ: grain size).

[48] If the film thickness is not constant for all the films under different deposition conditions, it would not be possible to narrow down any change in the XRD pattern in terms of peak intensity in order to conclude on the presence of a possibly more crystalline phase than amorphous phase.

In terms of the implications of heat treatments on the electronic property of the ZnSe films, the greater impact would be on the improvement of the conductivity brought about by the increase in grain sizes due to the merging of grains upon annealing.[222] In other words, for annealed films, there would be less grain boundaries that impose resistance to the flow of charge carriers. In terms of the electronic energy levels, there was a study [198] that reported no change in the valence band discontinuity at the ZnSe/GaAs interface for the as-grown and crystallized at 300°C ZnSe. They account this to the fact that RT deposition of ZnSe already leads to well-ordered polycrystalline films.

4.1.4 Surface morphology of the films

The deposited ZnSe thin films were uniform, pinhole-free and well-adherent to the ITO glass substrate. The morphologies of the films were investigated by atomic force microscopy (AFM) analysis. Surface images of the different heat-treated ZnSe films, as displayed in Figure 4.9, show a rough surface with rounded microstructures and an inhomogeneous grain size distribution in agreement with literature.[173, 174, 221, 225]

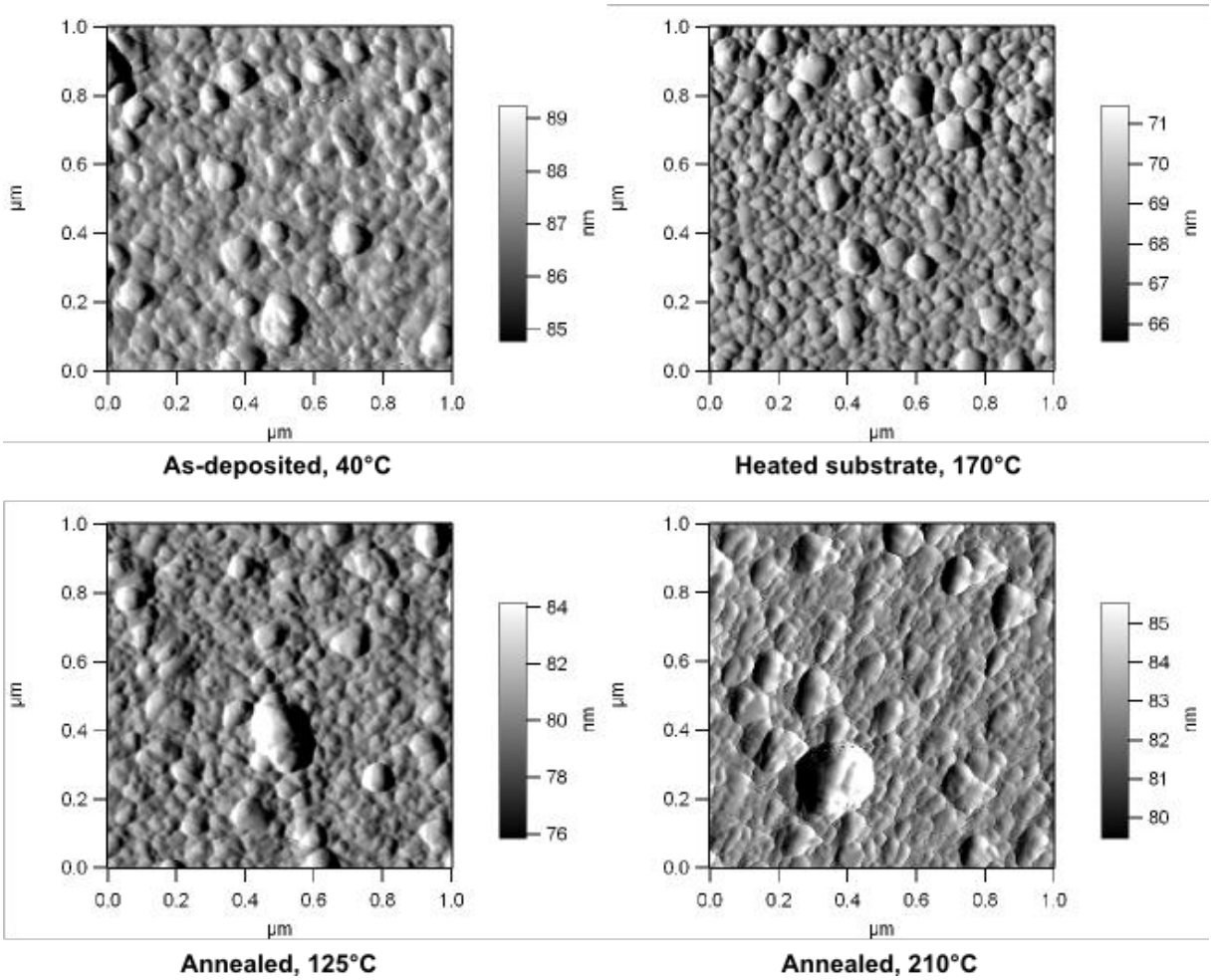

Figure 4.9: AFM image of a thermally-evaporated ZnSe film deposited on ITO glass substrate at room temperature.

The apparent grain size ranges from 30 nm to 130 nm. No voided boundaries that separate the grains were found on the films. The ITO substrate possibly contributed to the rough topography of our films; this is in agreement to a paper where the roughness of their commercial SnO_2 substrates were transmitted to their ZnSe films giving rise to more irregular surfaces as compared to their films deposited on glass substrates.[221]

Comparing our films to each other based on the AFM images, the heat-treated films do not show any significant differences from the as-deposited film. An increased grain size and improved surface smoothness could have been expected, as was reported.[173, 199, 221] But again, the grains of their as-deposited films were only half the size of the grains of our as-deposited films.

4.1.5 Optical properties of the polycrystalline films

ZnSe has a wide optical energy bandgap (~2.7 eV), high refractive index, low optical absorption in the visible and infrared spectral region. Thermally deposited ZnSe films typically exhibit good optical transmission with a sharp cutoff in the absorption edge.

Transmittance measurements and the optical energy gap of ZnSe

The optical properties of ZnSe films were studied by transmission measurements at room temperature in the spectral range from 300 nm to 900 nm. The transmission spectrum of a ZnSe film deposited on an ITO glass substrate is shown in Figure 4.10. The oscillatory pattern seen below the bandgap (i.e. at longer wavelengths) of ZnSe is due to thin film interference as expected for a film/substrate system, and it carries with it information on the film thickness (the calculated value is 410 nm).

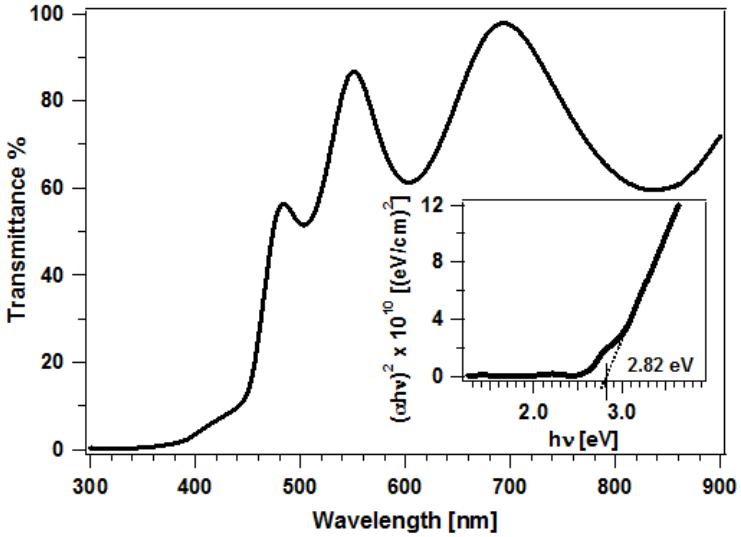

Figure 4.10: Optical transmission of the 440 nm ZnSe film deposited from a freshly-filled source. The inset shows the two direct transitions of ZnSe. The 2.82 eV is the ZnSe energy gap for the allowed direct transition.

Above the bandgap (i.e. at shorter wavelengths), no interference occurs due to the high absorption coefficient of ZnSe in this region. Absorption coefficients have been evaluated using the percentage transmittance data and the ZnSe film thickness. The plot of $(\alpha h\nu)^2$ versus $h\nu$ is then obtained and shown in the inset of Figure 4.10. From the graph, the optical band gap is found to be 2.82 eV.

In addition, there are actually two linear regions that can be found on the $(\alpha h\nu)^2$ versus $h\nu$ graph for this ZnSe film which give two different band gap energy values: namely, 2.61 eV and 2.82 eV. Reports in literature account these to the existence of two direct transitions detected in ZnSe thin films.[174, 175, 199, 235] The first linear region is associated to a forbidden direct transition, while the second to an allowed direct transition.[174, 175, 235] The two transitions are accounted to spin-orbit interaction that causes a splitting of the valence band at k=0 of ZnSe.[237-239]

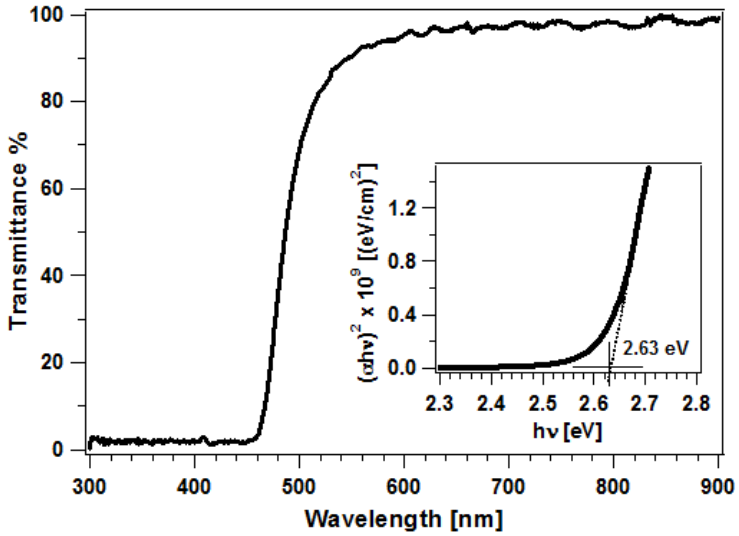

Figure 4.11: Optical transmittance of a 950 nm ZnSe film deposited on a quartz substrate. The inset shows an energy gap of 2.63 eV for the film.

Figure 4.11 shows the optical transmission spectrum of a 950 nm thick ZnSe film deposited on a quartz substrate. Absorption coefficients have also been evaluated using the percentage transmittance data and the ZnSe film thickness. The plot of $(\alpha h\nu)^2$ versus $h\nu$ is shown in the inset of the figure. The film possesses an optical band gap of 2.63 eV. For stoichiometric ZnSe single crystals at RT, an optical band gap of 2.67 eV has been reported in literature.[226] Differences in the experimental values of the ZnSe band gap are due to the different deposition methods, post-deposition treatments, substrates used, and resulting film thicknesses.[176, 177, 199, 201, 226, 235, 240] Moreover, only one transition is observed. This could be accounted to the thicker film in this case, comparable to literature results.[173, 175, 239]

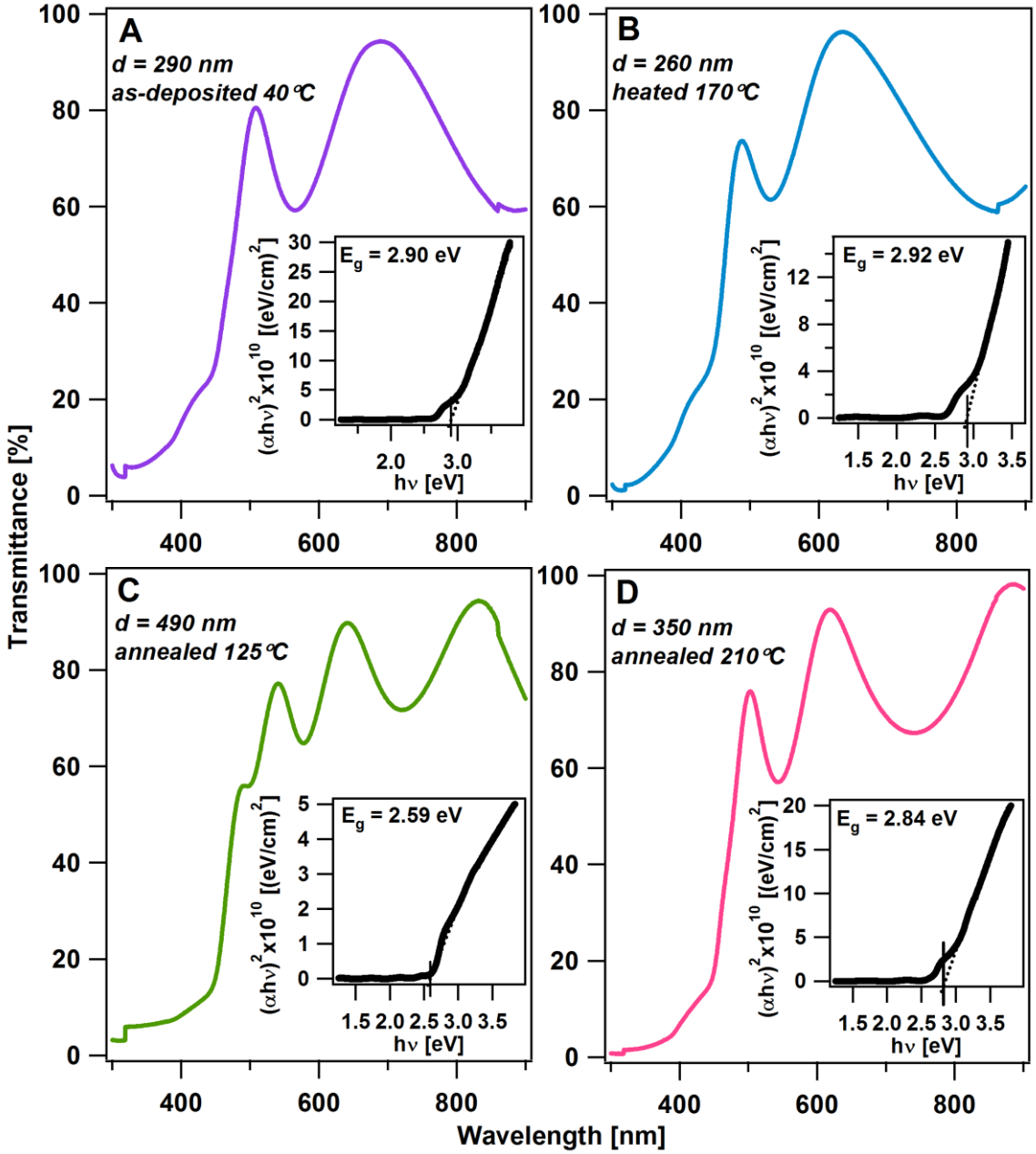

Figure 4.12: Transmittance spectra of ZnSe films on ITO glass substrates under different sample treatments. Deposition parameters of the source and the deposition time were maintained constant for each case. (A) As-deposited sample with a substrate temperature at 40°C due to radiant heating from the source, (B) Sample with the substrate heated at 170°C during the deposition, (C) Sample with post-annealing at 125°C and (D) sample with post-annealing at 210°C.

Literature presents several studies that demonstrate the effect of heat treatments on the optical properties of ZnSe films.[173, 199, 221, 222, 235, 241] From these studies, several factors are suggested to influence the optical properties of ZnSe. From a study on CBD films, annealing at 300°C of as-grown Se^0-rich ZnSe films lead to a higher transparency of the films to visible light owing to the loss of the amorphous Se^0 occluded in the films.[221] The presence of Se^0 was confirmed by XPS. The optical energy gap for their as-grown films was observed to be at 2.13 eV, which is nearer to the optical energy gap of amorphous Se^0 at

1.90 eV. For their annealed films, the energy gap shifts to higher values at around 3.14 eV, between the gap of ZnSe (2.82 eV) and ZnO (3.40 eV). Apparently, their annealing step led to CBD films which are characteristic to ZnSe and then to ZnO. From the observed change in the energy gap, it can be deduced that Se^0 greatly contributes to the optical properties of ZnSe films. Meanwhile, two studies [199, 222] report that the optical band gap decreases with increased annealing temperature arising from the increase in grain size (*i.e.* decreasing quantum size effect). For the films that are initially deposited on a heated substrate and then annealed, the opposite trend was observed. The authors account this to stoichiometric changes and formation of discontinuities in the film with high temperature annealing.[199] For ZnSe films deposited on substrates heated at different temperatures, it was observed that the bandgap is decreased when the substrate temperature during the deposition is increased.[235]

In this study, the transmission spectra of heat-treated ZnSe layers were obtained and are shown in Figure 4.12. Plots of the $(\alpha h\nu)^2$ versus the photon energy, $h\nu$, are shown in the insets of each of the transmission spectra in the figure. The derived energy bandgaps range from 2.59 - 2.92 eV. A bandgap value greater than 3 eV is also commonly found in literature for ZnSe.[175, 238, 239, 242] The general trend observed here is that the thinner the film the larger the bandgap. No apparent dependence on the heat treatment can be concluded as the films have very different thicknesses (notably, film thickness also influences the optical characteristics of ZnSe [175, 201]). Whether the observed change of spectral properties result from defect-related band edge tails of bulk ZnSe or of Se^0/ZnSe phase mixtures cannot be concluded from our data.

Description	Thickness /nm (Dektak stylus profiler)	Thickness /nm (Transmittance data)	$E_{g,optical}$ /eV
As-deposited, at ambient T = 40°C	290	297	2.90
Heated substrate at T = 170°C	260	276	2.92
Post-deposition annealing at T = 125°C	490	510	2.59
Post-deposition annealing at T = 200°C	350	350	2.84

Table 4.2: The thicknesses of the films obtained through a profilometer and through calculations from the interference pattern in the transmittance spectra. The optical energy gap of our films are increased with decreased film thickness. No dependence on the heat treatment can be deduced from the data.

The transmission spectra of the films also exhibit interference fringes. Using a method from literature described in Chapter 3.2, the film thickness were derived and are tabulated in Table 4.2. The average thicknesses of the films as indicated in Figure 4.12 and

also tabulated in the table were determined using a surface-profiling stylus. The thickness profiles were taken from the edges of the films, and then the average thicknesses were then calculated. The thicknesses obtained from the profilometer and from the transmission spectra agrees well with each other, thereby confirming the validity of the applied method.

In addition, it is interesting to note that the measured average thicknesses of the films differ in each case even though the deposition parameters for the evaporation source were kept constant. This might have to do with changes [49] taking place within the source itself as it aged from continuous use over time leading to changes in the deposition rates. Since selenium evaporates at ~150°C [207], a re-evaporation of Se^0 present in the film deposited on the heated substrate and a desorption of Se^0 from the annealed films would have contributed to the final thicknesses of the films.

4.2 Ir(BPA)

Ir complexes are organo-transition-metal compounds that exhibit phosphorescent light emission from the lowest triplet states to the singlet ground states. These d^6 metal complexes are quasi-octahedral compounds of iridium ions coordinated by organic ligands. State-of-the-art OLEDs employ emissive layers that are doped with phosphorescent organic dyes, and Ir complexes are the most popular in efficient electrophosphorescent OLEDs.[243-247] These Ir complex organic dyes remain to be the most effective phosphorescent emitters because of their abilities in achieving maximum internal quantum efficiency of nearly 100% and high external quantum efficiency in devices.[32, 248-252] Big factors that contribute to the outstanding performance of Ir complexes are the extensive possibilities in tailoring the ligand structures to obtain unique metal-ligand based luminescence for color tuning in the visible and near-infrared range [243-246, 253-256] and their relatively short phosphorescent lifetime to avoid saturation of emissive sites that leads to triplet-triplet (T-T) annihilation during device operation at high currents [96, 243, 245, 247, 250, 254]. The reported emission decay times of Ir complexes at ambient temperature are within the range of 0.1 - 5 μs.

A molecular orbital (MO) diagram of an organo-transition-metal complex with a quasi-octahedral geometry is shown in Figure 4.13, together with the possible electronic transitions and their nomenclature. These transition metal complexes are characterized by partially filled *d* orbitals that are split into a triply degenerate occupied level (d_1, d_2, d_3) and a doubly degenerate unoccupied level (d_1*, d_2*). The splitting arises because the two e_g orbitals are directed toward the six ligands and the three t_{2g} orbitals point between the ligands. The

[49] Visually, the remaining ZnSe pellets inside the crucible of an aged source show traces of grayish tint over a dull yellow as compared to the bright yellow of fresh ZnSe pellets. Also, metallic gray particulates can be found mixed with the ZnSe pellets. The grayish tint found over the ZnSe pellets and the gray metallic particulates could possibly be aggregates of Zn atoms. Zn, for a fact, has a lower vapor pressure than Se. And so, it is less volatile. After a succession of depositions, as the rates of evaporation of Zn and Se are dissimilar, the possibility of having an excess of Zn left in the source is highly likely to happen.

lowest excited states are derived from promoting an electron to one of the unoccupied orbitals. The excited state classification is determined by the original and final orbitals. This leads to three types of excited states: metal-centered *d*-*d* states, ligand-centered (LC) π-π* states, and charge transfer (CT) *d*-π* or π-*d* states.

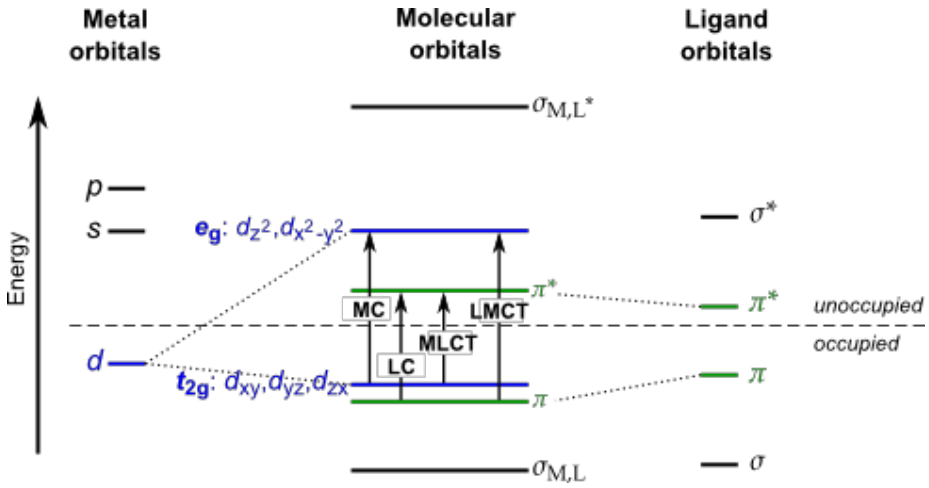

Figure 4.13: Schematic diagram of selected molecular orbitals (MOs) for a quasi-octahedral organo-transition metal complex. The octahedral crystal field of the ligands splits the five degenerate *d* orbitals into a triply degenerate t_{2g} level (d_{xy}, d_{zy}, d_{zx}) and a doubly degenerate e_g level (d_{z^2}, $d_{x^2-y^2}$). Recall that there are always four possible excited states (one singlet state and three triplet substates) for each electronic transition from the ground state. Combined adaptation from [257] and [258].

The lowest ligand excited states are π-π* states derived from promoting a π electron to a π* level. There are triplets and singlets, and the triplet is always below its analogous singlet state. This type of transitions are largely localized on the organic ligands and are spectroscopically very similar to those of the free ligand. Similarly, singlet and triplet *d*-*d* excited states arise from promoting a bonding t_{2g} electron to an e_g level. Transitions to *d*-*d* states are formally forbidden, even for the spin-allowed singlet-singlet transitions. *d*-*d* transitions are, thereby, characterized by long radiative lifetimes and high susceptibility to environmental quenching. Consequently, luminescence yields become negligible. CT states involve both the organic ligand and the metal. Metal-to-ligand (*d*-π*) charge transfer (MLCT) involves promoting an electron from a metal orbital to a ligand orbital, thereby, reducing the ligand and oxidizing the metal. Promoting an electron the other way around gives a ligand-to-metal (π-*d*) charger transfer (LMCT) excited states. CT transitions tend to be more strongly allowed than *d*-*d* transitions. They have shorter radiative lifetimes and are less susceptible to intramolecular and environmental quenching. The molar extinction coefficient[50] of spin-allowed transitions are large, making the CT states easier to pump optically. The long lifetime of this excited state is due to the fact that it is a triplet and that the structure of this kind of molecule allows for charge separation.

[50] Molar extinction coefficient is a measure of the strength of a chemical species in attenuating light at a given wavelength.

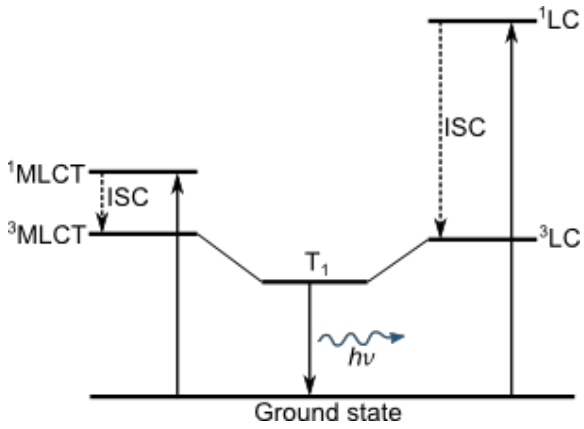

Figure 4.14: Narrow energetic distance and overlap between ^{3}MLCT and ^{3}LC states result in a mixed lowest excited triplet state T_1. Adapted from [255].

Generally, there are two basic types of electronic states in Ir(III) complexes that would compete for the LUMO, which is the only light-emitting state in a condensed matter: (1) ligand-centered triplet state, ^{3}LC ($^3\pi$-π^*), and (2) metal-to-ligand charge transfer triplet state, ^{3}MLCT (^3d-π^*). Due to the narrow energetic distance and degree of overlap between these two states, a mixed lowest excited triplet state T_1 is formed as illustrated in Figure 4.14. The "mixing" of these two triplet states is popularly suggested to be a two-step mechanism. It consists of configurational mixing (configuration interaction, CI)[51] of the ^{3}LC substates with the ^{3}MLCT substrates, and then a subsequent direct spin-orbit coupling (SOC) of the latter ones with ^{1}MLCT states.[259-261] Alternatively, the hybridization of the transition metal *d*-orbitals with the ligand π-orbitals as deduced by molecular orbital theory may be used to describe the mixing of the different excited states.[262]

Designing highly bright luminophores entails a high quantum yield and molar extinction coefficient and a low degree of oxygen quenching (necessary to keep a high luminescence in the oxygen-rich natural environment). Ir complexes satisfy such challenging conditions.[263, 264] The Ir(III) complex that was investigated in this study is the red emitter *bis-(1-(4'-tert.-butyl-phenyl)-isoquinoline)-1,3-pentanedionate-iridium complex* [Ir(4-tBupiq)$_2$(acac) or, shortly, Ir(BPA)]. The chemical structure of the Ir(BPA) dye is shown in Figure 4.15 together with a photograph of the powder under a UV lamp illumination. The dye exhibits an intense red luminescence even when left in ambient environment at RT over a long period of time. The dye was purchased in sublimed grade from Sensient Imaging Technologies GmbH and was used as received. This product is actually a prototype developed by the company. The product specifications of Ir(BPA) are listed in Table 4.3.

[51] Configuration interaction is a post-Hartree-Fock linear variational method. It is based on electron-electron interaction. CI-induced mixing can occur only between states of equal spin multiplicity.

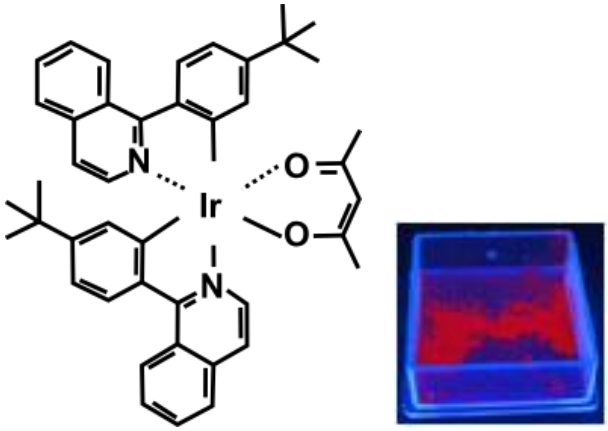

Figure 4.15: Molecular structure of Ir(BPA). The central metal atom, iridium, is coordinated by conjugated organic ligands. Photograph: Ir(BPA) powder under UV lamp illumination displaying a bright red luminescence even at RT and ambient atmosphere.

	Ir(BPA)
Chemical formula	$C_{43}H_{43}IrN_2O_2$
Molar mass	812 g/mol
Melting point	347.6°C (DSC peak)
Density	~1.8 g/cm^3 [253]

Table 4.3: Ir(BPA) product specifications.

4.2.1 Deposition of Ir(BPA) films

Small molecule organic semiconductors are quite often insoluble. To obtain thin films of these materials, vacuum sublimation is typically required. In this work, thin films of Ir(BPA) were obtained by the thermal evaporation of Ir(BPA) dye powder stuffed into the alumina crucible of our home-made temperature-controlled Knudsen-type cell (similar to the one shown in Figure 4.1). The evaporation temperature is monitored through a thermo-couple that is in contact to the crucible. Throughout the thermal evaporation process, no glass transition was observed. The dye always stayed intact in its original powder form and color.

4.2.2 Optical properties of Ir(BPA)

The photophysical properties of Ir(BPA) dispersed in toluene are shown in Figure 4.16. A spectroscopic panorama is observed for the absorption spectrum of the dye as is typical to Ir complexes. The intense bands appearing at the ultraviolet part of the spectrum below ~380 nm can be assigned to the spin-allowed π-π* transitions of the ^{1}LC states centered at the cyclometallating (1-(4'-tert.-butyl-phenyl)-isoquinoline) ligands. Maxima are observed at 309 nm, 351 nm and 366 nm (shoulder). The absorption bands extending into the visible region between 380 nm and 520 nm can be assigned to the overlapping spin-allowed *d*-π* transitions of the ^{1}MLCT band with maxima at 396 nm (shoulder), 419 nm (shoulder), 439 nm (shoulder) and 491 nm. A striking feature for this

complex is the strong intensity of a peak in the ^{1}MLCT band at around 491 nm (2.52 eV). The weaker absorption tail at wavelengths longer than 520 nm involves mainly spin-forbidden transitions of the ^{3}MLCT band with maxima at 532 nm, 564 nm (shoulder) and 607 nm (shoulder). These assignments should not be taken too strictly since the LC and MLCT states are usually mixed.[96, 243, 245, 247, 253, 256]

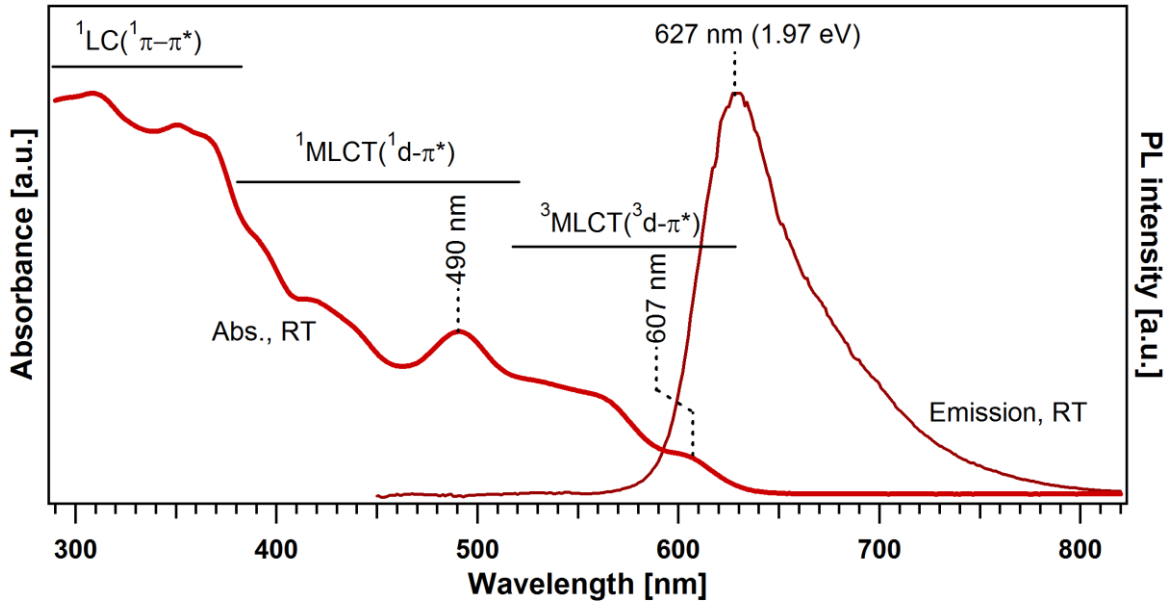

Figure 4.16: Room-temperature UV-Vis absorption spectrum of Ir(BPA) dispersed in toluene. A spectroscopic panorama is observed accounting to the several probable excitations of the dye.

At ambient RT, Ir(BPA) is highly emissive. The broad and unstructured deep-red emission shown in the figure has a maximum at 627 nm. The emission band overlaps with the lowest energy absorption peak at 607 nm. These bands are assigned to the electronic $S_0 \leftrightarrow T_1$ transitions, which exhibit a Stokes shift of about 20 nm.

For the electronic properties of organo-transition metal complexes, it seems suitable to discuss then on the basis of HOMO-LUMO excitations. However, this can be misleading because such a simple model does not comprise singlet or triplet states. And if these states are deduced just from the HOMO-LUMO excitation, it might occur that the resulting triplet does not represent the one of the lowest energy. Since the Ir(BPA) is a triplet emitter, its light emission definitely corresponds to a transition from the lowest triplet excited state to the singlet ground state. In this work, the gap of this transition is taken to be the energy gap in drawing a simplified energy band diagram for Ir(BPA).

4.2.3 Photoelectron spectroscopy measurements of Ir(BPA) films

A nominal 15.2 nm thick Ir(BPA) film was deposited on an ITO glass substrate. The source temperature for the evaporation of the dye was 207°C, with a deposition rate of 15.2 Å/min. The XPS survey and detailed spectra taken from the film are shown in Figure 4.17. The evaporation and PES measurements were performed *in situ* using the

DAISY-MAT in Darmstadt. In the XPS survey spectrum, all Ir(BPA) characteristic emissions are designated. With no traces of contamination and substrate photoemissions found, a clean deposition and a thick enough film with the absence of pinholes are indicated, respectively.

The most intense photoemission lines representative of the elements present in the compound (i.e. C, Ir, O and N) come from the C1s, Ir4f, O1s and N1s core levels. Detailed spectra of these emissions are shown in the figure. The stability of the dye during the deposition was confirmed by the absence of chemically shifted dye emissions and by the correct stoichiometry of the dye constituents' (Ir, C, O, and N) core line spectral contributions. The expected doublet structure of the 4f orbital is clearly exhibited by the Ir4f emission from the dye. After performing Shirley background subtraction and spectral fitting, the binding energy of Ir4f is determined to be ~ 61.56 eV with a spin-orbit splitting of 2.98 eV, which coincides well with the values listed in the XPS handbook.[164]

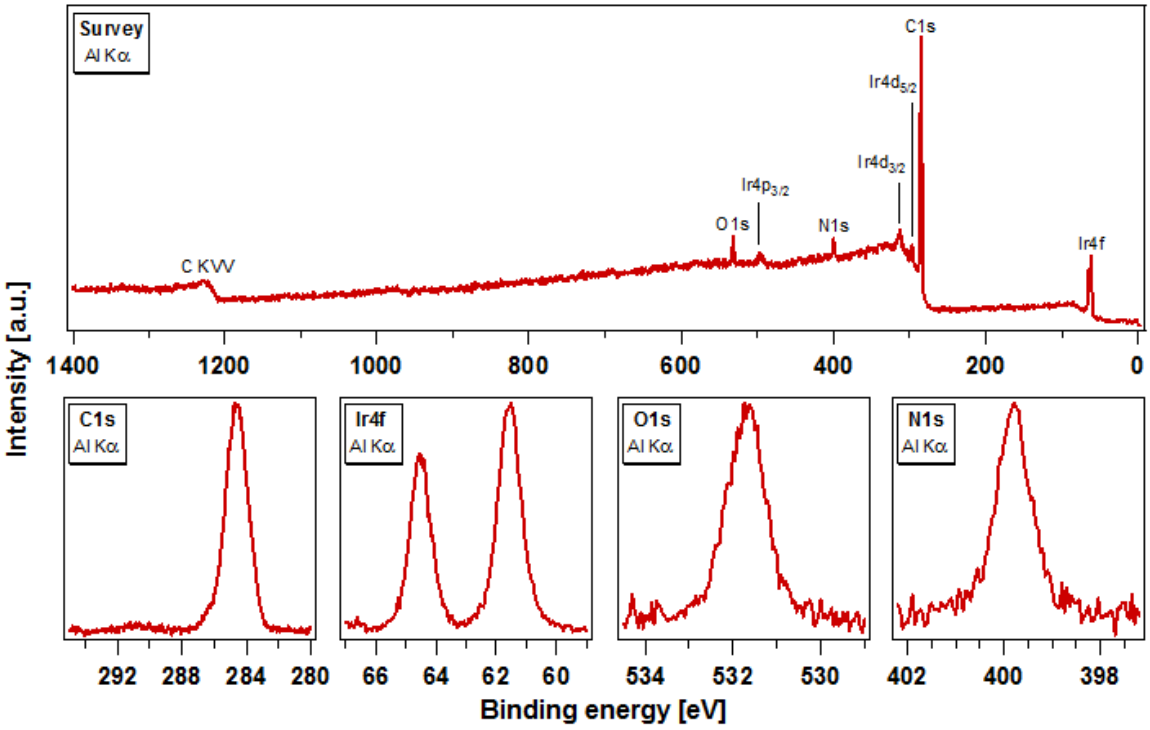

Figure 4.17: Survey spectrum showing all the peak photoemissions that are representative of the elemental composition of an Ir(BPA) film deposited on ITO glass substrate. Detailed spectra of the C1s, Ir4f, O1s and N1s emissions confirm the stability of the dye during the deposition through the absence of chemically shifted dye emissions.

The SE cutoff and the valence region spectra for the Ir(BPA) film under a He I excitation are displayed in Figure 4.18. The onset of photoemission at the lowest binding energy end of the spectrum is taken to be the position of the HOMO with respect to the Fermi level at 0 eV on the binding energy scale. Using a linear fit of the leading edge and then taking the intersection of the fitted line to the zero intensity with the binding energy

axis, the HOMO is obtained to be at 1.09 eV from the Fermi level position. A similar linear extrapolation yields the binding energy position of the SE cutoff. The work function ϕ of the Ir(BPA) film is calculated to be 3.96 eV. From the HOMO position and ϕ values, the ionization potential is then 5.05 eV which corresponds well with literature.[243, 246, 247, 254]

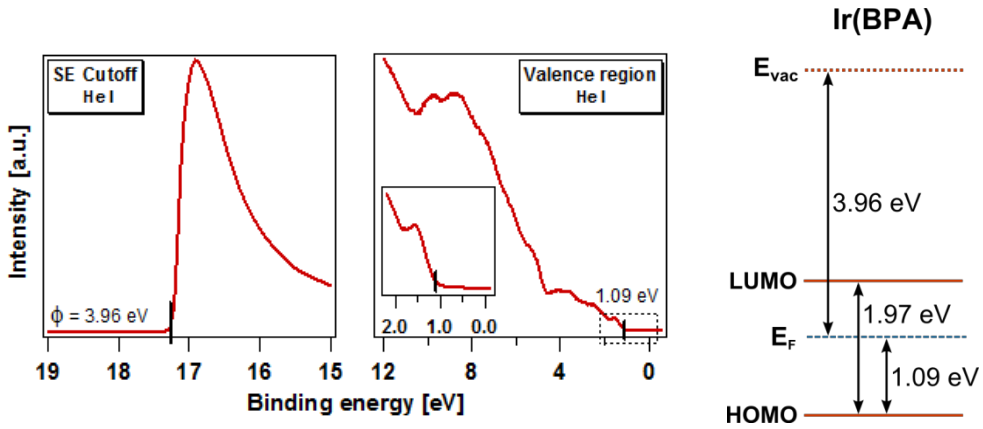

Figure 4.18: The SE cutoff where ϕ is determined to be 3.96 eV and the valence region where the HOMO is at 1.09 eV from the Fermi level. The inset shows in greater detail the HOMO onset of the dye. Energy levels of Ir(BPA) as deduced from the UPS measurement. The energy gap of 1.97 eV is taken from the optical measurement.

The electronic structure of pristine Ir(BPA) is drawn in Figure 4.18. From the peak of the photoluminescence (Figure 4.16), the optical energy gap for Ir(BPA) is approximated to be 1.97 eV and is the value used in the diagram of the electronic structure. A gap of this value is within the reported range for red Ir complex emitters.[265] Moreover, we have been using the optical gap to get at least an estimate of the energy level lineups; but to be frankly accurate, it has to be considered that the HOMO-LUMO gap measured by PES differs from the optical gap and the transport gap (which is the relevant gap for the charge transfer in our composite emissive layer design) (Figure 2.8).

Chapter 5 ZnSe and Ir(BPA): Characterization of the interface

There are only a few investigations of the interfaces of inorganic-organic materials in spite of the obvious importance for understanding the chemistry and controlling the electronic properties of heterojunctions and contacts. The deposition of ZnSe and Ir(BPA) by thermal evaporation is possible as presented in the previous chapter. The electronic and chemical structure of the ZnSe and Ir(BPA) interface obtained through a classical UHV interface experiment are presented. Three deposition configurations are considered, namely: (1) ZnSe/Ir(BPA) heterojunction where Ir(BPA) is deposited on a ZnSe film, (2) Ir(BPA)/ZnSe heterojunction where ZnSe is deposited on an Ir(BPA) film and (3) ZnSe+Ir(BPA) composites where ZnSe and Ir(BPA) are co-evaporated on a clean substrate. Energy band diagrams of the ZnSe/Ir(BPA) bilayer and the composite are derived as well as the chemical composition and description of the coupling of the two materials on the atomic scale. The sample depositions and PES experiments were all performed at the DAISY-MAT.

5.1 Pristine layers of ZnSe and Ir(BPA)

A ~170 Å thick film of ZnSe was deposited on an ITO substrate. The source temperature for the evaporation of ZnSe was 736°C, with a deposition rate of 56 Å/min.

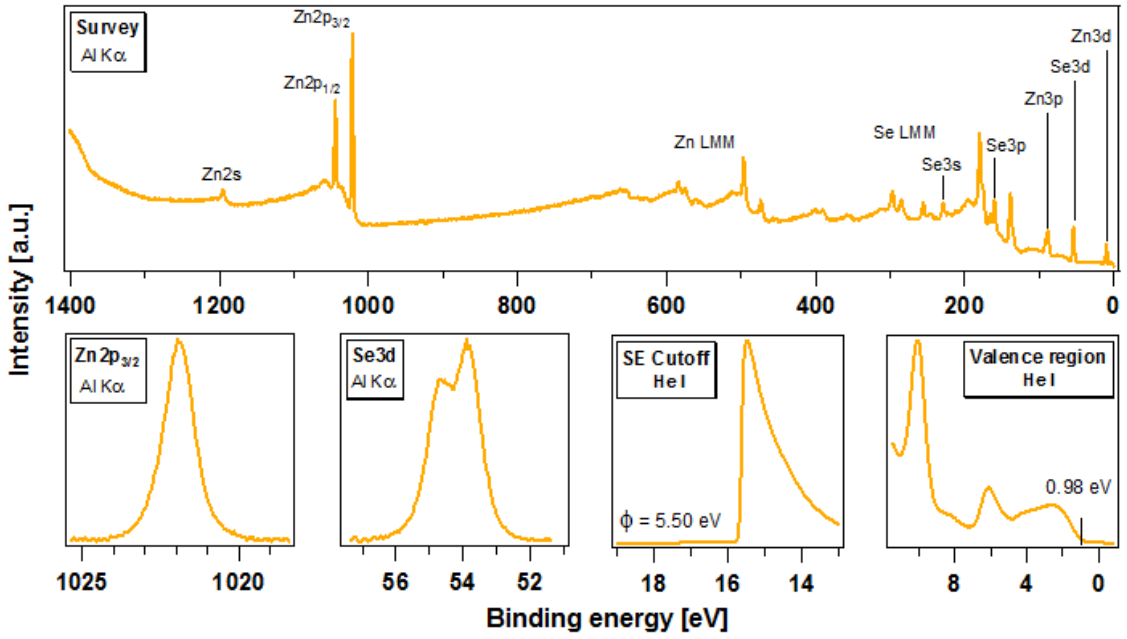

Figure 5.1: Survey spectrum, $Zn2p_{3/2}$ and Se3d detailed spectra, SE cutoff and valence region spectra of the ZnSe layer. No contamination is evident. The features found in the valence band spectrum are representative of that of ZnSe.

The survey, Zn2p$_{3/2}$, Se3d, SE cutoff and valence region spectra for the ZnSe layer are shown in Figure 5.1. No surface contamination is evident as O1s emission is absent in the survey. To conclude about surface contamination from a C1s emission would be indefinite due to the presence of a peak from a Se LMM Auger line at the same binding energy region. From the He I UPS measurement, ZnSe has a work function of 5.50 eV and a valence band onset at 0.98 eV.

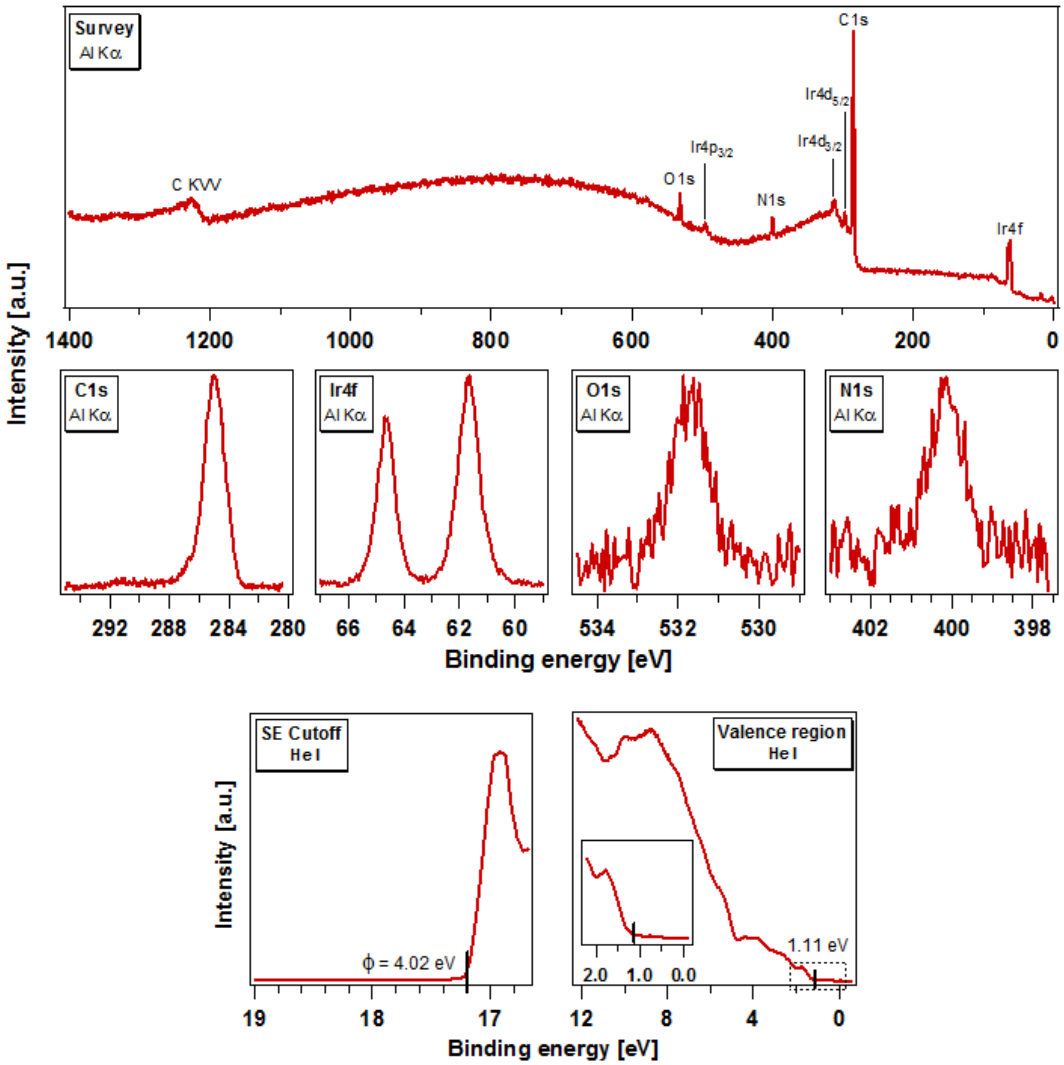

Figure 5.2: Survey spectrum, core levels (C1s, Ir4f, O1s, N1s) detailed spectra, SE cutoff and valence band spectra of the Ir(BPA) layer. The O1s and N1s emission spectra do not have good signal-to-noise ratio due to low atomic sensitivities.

The PE spectra of the finally closed 165 Å thick film of Ir(BPA) deposited for 651 s on ZnSe in the interface experiment is shown in Figure 5.2. To calculate the thickness of the Ir(BPA) layer, the decrease in the intensity of the Zn2p$_{3/2}$ emission and the mean evaporation rate of 15 Å/min of the Ir(BPA) were considered. In the survey spectrum, the higher intensity of the Ir4f emission as compared to those of O1s and N1s emissions is due to the

large ASF for Ir4f. From the He I UPS measurement, Ir(BPA) has a work function of 4.02 eV and a HOMO onset at 1.11 eV.

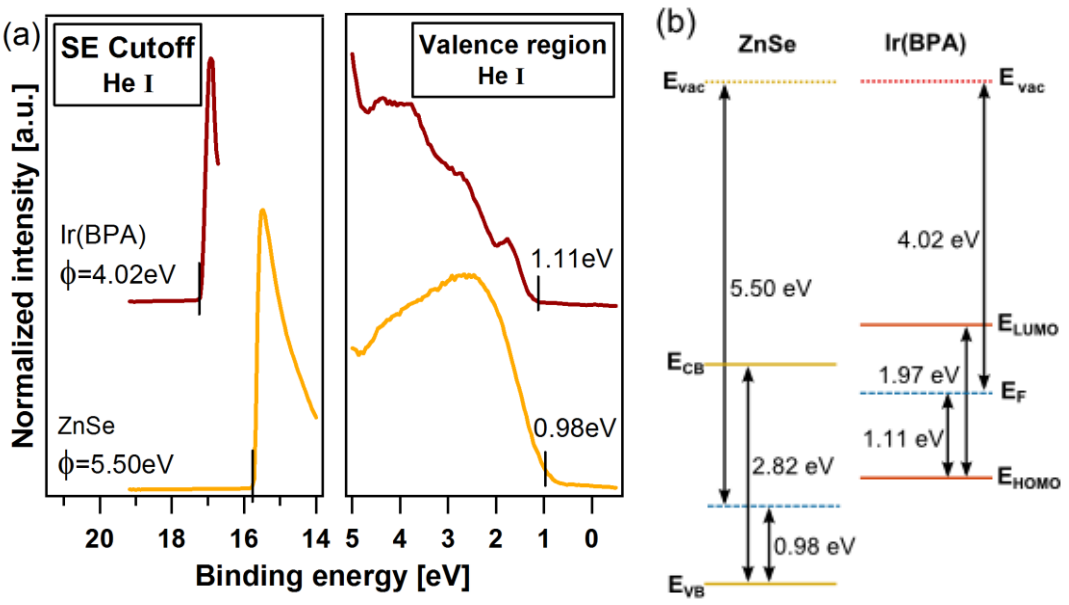

Figure 5.3: (a) SE cutoff and valence region spectra of pristine ZnSe and pristine Ir(BPA). The work function (ϕ) and VBM/HOMO onset values are indicated. (b) A schematic diagram of the relative energy levels of ZnSe and Ir(BPA). Aligning the vacuum levels of the two materials before contact reveals that the energy level alignment is not as needed for carrier injection as described in Figure 1.5.

The UP spectra for pristine ZnSe and Ir(BPA) are compiled together in Figure 5.3(a) showing the work functions and valence band onsets. Energy band gaps of 2.82 eV for ZnSe and 1.97 eV for the dye (comparable to values reported in literature [177, 199, 211, 243-245, 254, 266]) is deduced from the optical transmittance and photoluminescence measurements as presented in the previous chapter. The electronic structures of ZnSe and Ir(BPA) before contact are compared in Figure 5.3(b) using an Anderson lineup where the vacuum levels of the two materials are aligned. As seen from the vacuum level alignment, the LUMO of the dye is at around 0.5 eV above the conduction band of ZnSe. Looking at the isolated materials, the electron transfer from the conduction band of ZnSe to the dye LUMO would not be energetically favorable.

5.2 Bilayer heterojunction: The ZnSe/Ir(BPA) interface

Characterizations of electronic interface properties by PES are normally carried out by a classical in situ ultra-high vacuum interface experiments. In an interface experiment, the overlayer material is deposited stepwise on another until the overlayer is completely closed. After each deposition step, the PES measurements are performed to obtain the spectra of the core line emissions of the materials, valence band, and secondary electron (SE) cutoff. To obtain the characteristics of the ZnSe/Ir(BPA) heterojunction, Ir(BPA) was stepwise-deposited onto the fully-closed 170 Å thick ZnSe film. The stability of the dye

during the deposition was confirmed by the absence of chemically shifted dye emissions that could indicate degradation upon thermal evaporation and by the correct stoichiometry of the dye constituents' - Ir, C, O and N - core line spectral contributions.

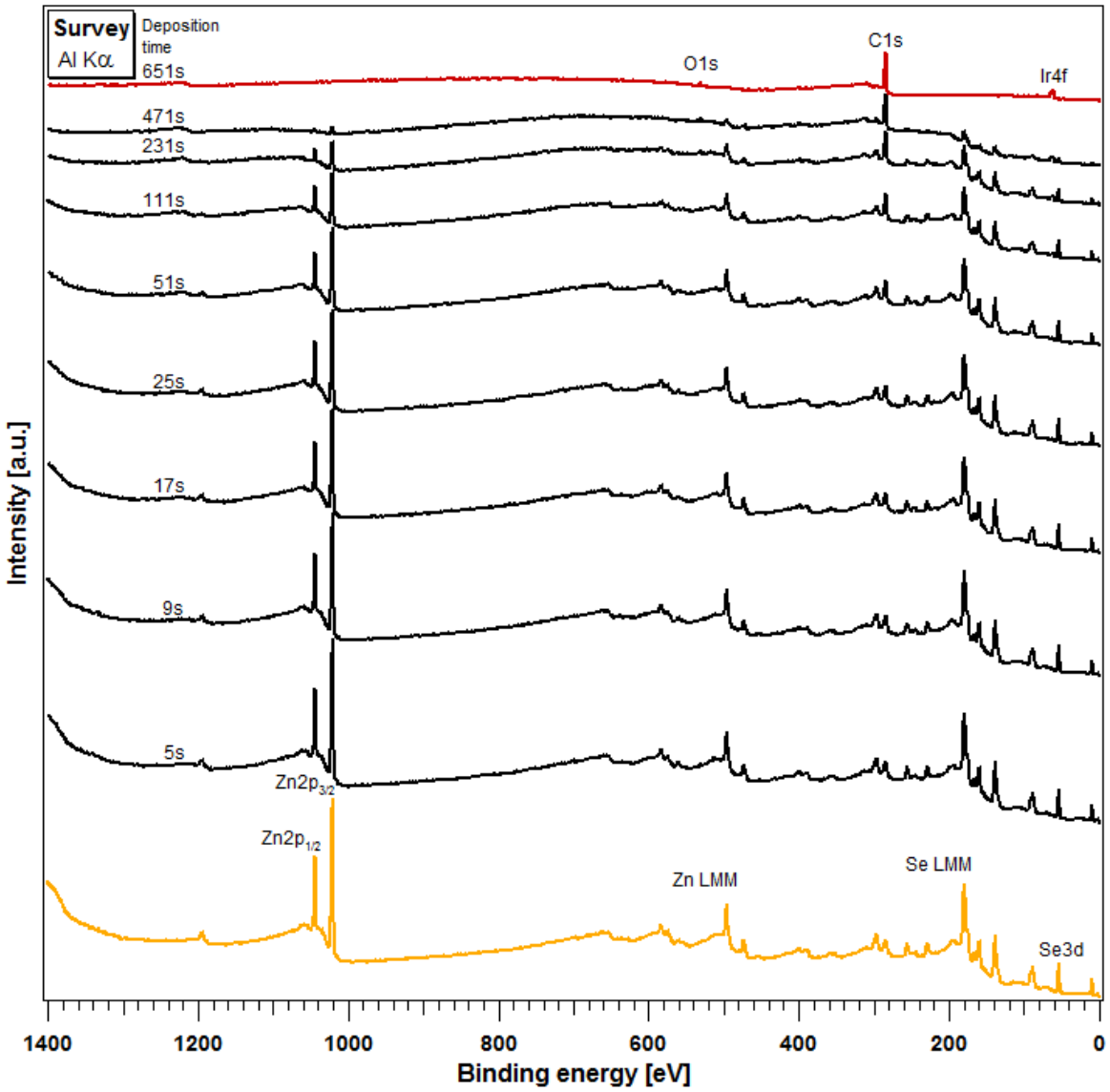

Figure 5.4: Survey spectra of ZnSe and the step-wise deposited Ir(BPA) in the interface experiment for a ZnSe/Ir(BPA) bilayer. The total times for each of the Ir(BPA) deposition steps are indicated.

The obtained survey spectra starting from the pristine ZnSe followed by the Ir(BPA) overlayer in sequential deposition steps are shown in Figure 5.4. The total deposition times of Ir(BPA) for each of the deposition steps are indicated in the figure. With increasing Ir(BPA) deposition, the evolutions of the ZnSe and Ir(BPA) intense core lines are clearly observed. No photoelectron emissions from other elements are present in the survey spectra, indicating a clean and homogeneous sample preparation.

The core level spectra of the most intense photoemission lines are shown in Figure 5.5 for increasing Ir(BPA) deposition time. No changes in the lineshapes of the core

line emissions of both the ZnSe substrate and Ir dye overlayer are observed. The $Zn2p_{3/2}$ and Se3d emissions in Figure 5.5(a) show no shifts of their binding energy positions during the course of the step-wise Ir(BPA) deposition. This indicates a Fermi level pinning in ZnSe. The $Zn2p_{3/2}$ and Se3d emissions exhibit a gradual damping in intensity. The more rapid damping of the $Zn2p_{3/2}$ emissions as compared to Se3d emissions corresponds to the higher kinetic energy, i.e. lower surface sensitivity, of the emitted Se3d as compared to the $Zn2p_{3/2}$ electrons.

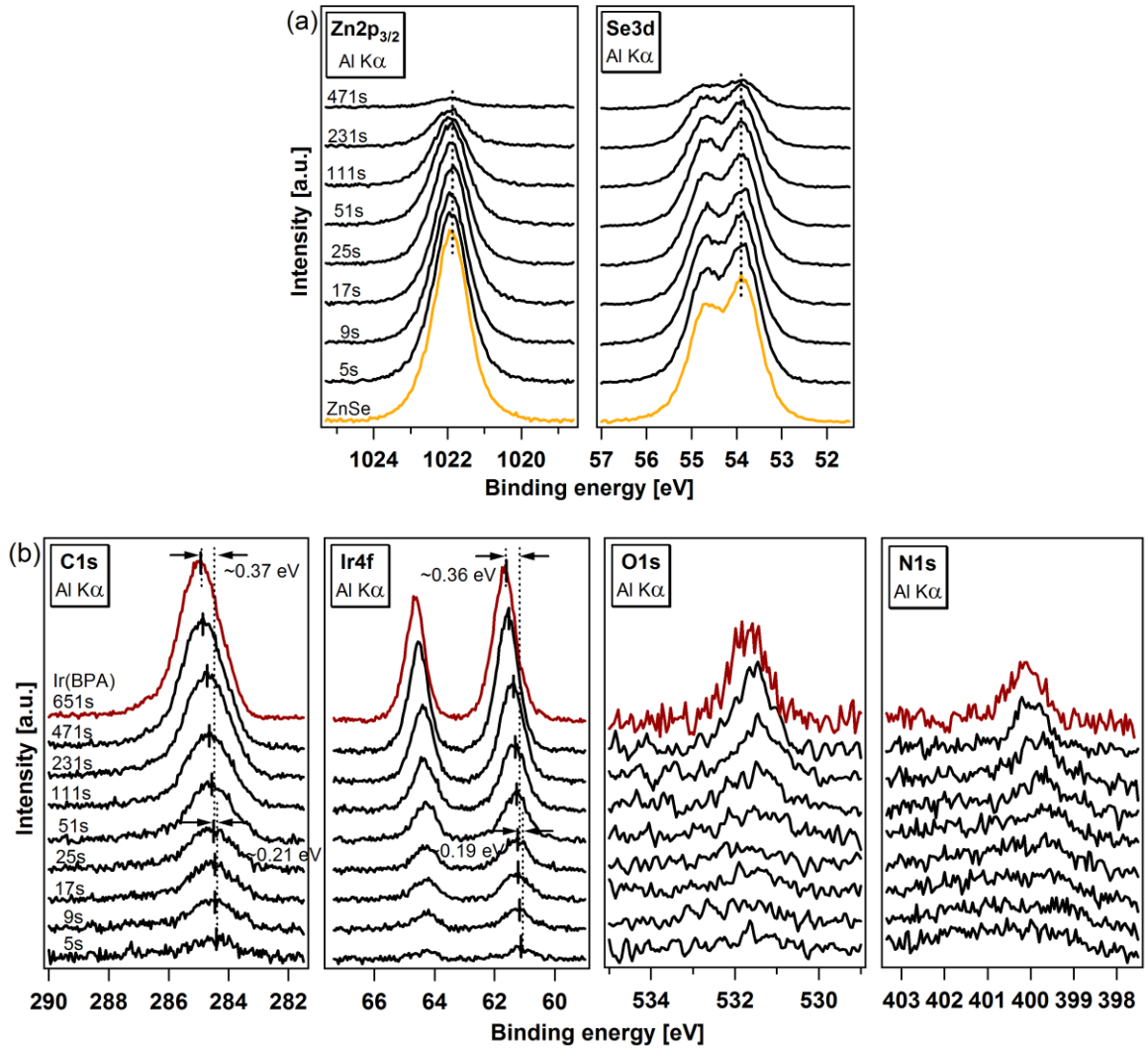

Figure 5.5: $Zn2p_{3/2}$ and Se3d core level emission spectra of the ZnSe substrate (a) for the increasing depositions of the Ir(BPA) overlayer. C1s, Ir4f, O1s and N1s core level emission spectra of the step-wise deposited Ir(BPA) (b) (for C1s, the difference spectra are shown from which the Se LMM Auger emission has been removed). The Ir(BPA) deposition times are indicated. With increasing coverage, the Ir(BPA) core line emissions shift to higher binding energies by ~0.20 eV from 5 s to 25 s and by ~0.37 eV from 25 s to 651 s, while the $Zn2p_{3/2}$ and Se3d binding energies remain constant.

Due to overlapping C1s and Se LMM Auger emissions within the same binding energy region, the calculated difference spectra are shown in Figure 5.5(b) for C1s emissions of Ir(BPA) from which the Se LMM Auger emissions of ZnSe have been removed. At the first

deposition step, the C1s and Ir4f emissions of the dye can already be resolved as opposed to the O1s and N1s emissions. From the chemical structure of Ir(BPA), there are only 2 O atoms and 2 N atoms in each dye molecule. Because of this low atomic percentage coupled with the small photoelectric cross-section for the O1s and N1s orbitals, the O1s and N1s emissions are not distinctly resolved at low Ir(BPA) coverages.

Looking at the C1s and Ir4f emissions, shifts of the binding energy positions are observed. There is a shift of ~0.37 eV to higher binding energies of the dye core levels from the 25 s deposition until the closed dye layer at 651 s. There is also a ~0.20 eV shift to higher binding energies from the 5 s to the 25 s deposition.

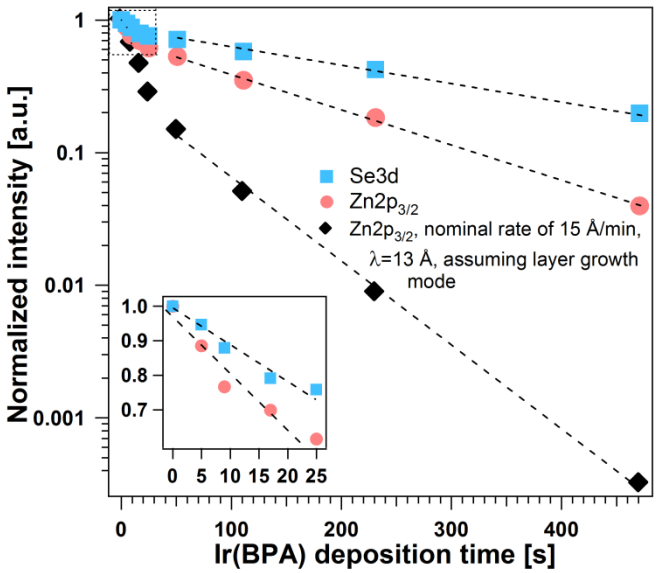

Figure 5.6: Normalized integrated $Zn2p_{3/2}$ and Se3d emission intensities versus Ir(BPA) deposition time. Below 25 s the damping increases linearly (shown in the inset), indicating growth of a monolayer. Above 25 s the damping is exponential, indicating layer-by-layer or island growth. In addition, the calculated damping of $Zn2p_{3/2}$ emission is shown for a layer-by-layer growth considering a nominal deposition rate of 15 Å/min and a photoelectron escape depth of 13 Å.

The attenuations of the $Zn2p_{3/2}$ and Se3d emission intensities with increasing Ir(BPA) deposition time are plotted in Figure 5.6 on a logarithmic scale; in addition, the first deposition steps are on the inset in a linear scale. Two regions are clearly distinguished--below and above ~25 s with a linear and an exponential damping, respectively. The initial linear damping is a clear indication of monolayer growth of the dye. Above 25 s, the damping increases exponentially. Assuming a constant sticking coefficient for Ir(BPA), this exponential damping of the substrate $Zn2p_{3/2}$ emission is too slow to account to a layer-by-layer dye growth when compared to the calculated damping of the $Zn2p_{3/2}$ emission (also shown in Figure 5.6) where an escape depth (λ) of 13 Å was assumed. The slower damping indicates that dye islands are formed instead. Thus, the dye first grows a monolayer with a molecular thickness of approximately 7 Å, and then proceeds to grow in islands. The

thickness coincides well with literature reported diameter values of 7 - 9 Å for other Ir complexes with a similar structure to Ir(BPA).[253, 267]

The spectra of the UPS measurements of the interface displaying the secondary electron cutoff, the valence states region including Zn3d core line and the difference spectra of the lower valence states of which the ZnSe emission has been removed are compiled in Figure 5.7. A 0.37 eV binding energy shift starting from the 25 s deposition until the closed dye layer at the 651 s deposition is exhibited by the SE cutoff and by the prominent valence feature at 8.8 eV binding energy and HOMO onset of the dye. However, the SE cutoff displays a strong shift of the vacuum level from the ZnSe substrate to the 25 s deposition (low dye coverages) that is in stark contrast to the rather gradual shift of the Ir dye valence region and the core line emissions.

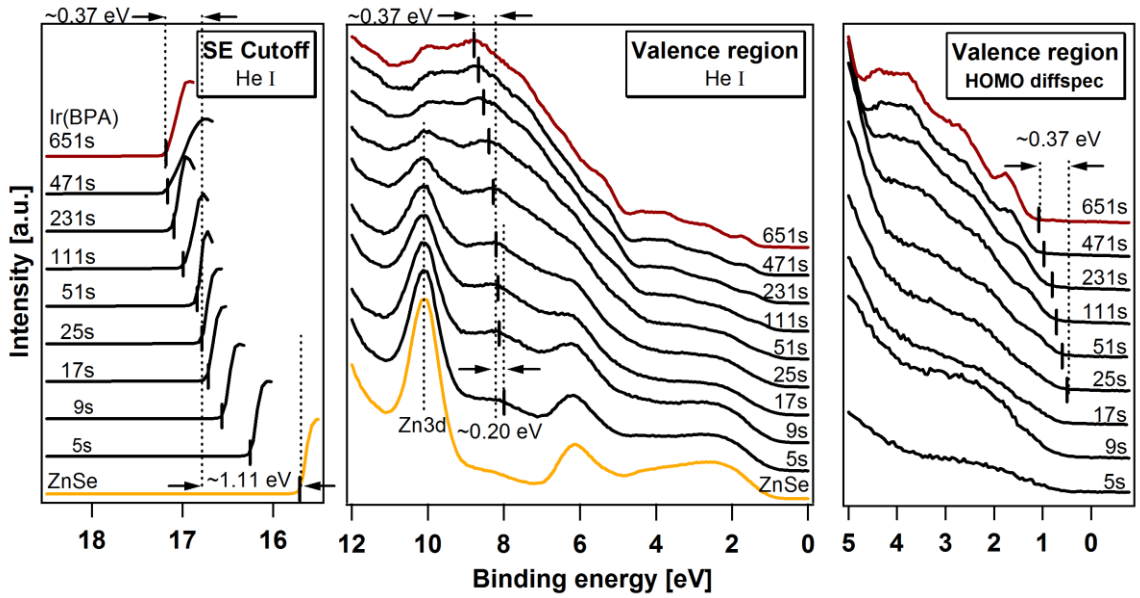

Figure 5.7: Secondary electron cutoff and valence region spectra during the stepwise deposition of Ir(BPA) on ZnSe. The Ir(BPA) deposition times are indicated. A distinct Ir(BPA) valence feature at ~8.80 eV is marked in the valence spectra. During monolayer growth, φ decreases strongly by about 1.11 eV while the dye features shift by 0.20 eV to lower binding energy. Then the SE and the dye features shift by an additional 0.37 eV.

The changes of ϕ and the shifts of the dye HOMO and core level lines are summarized in Figure 5.8. During the initial monolayer growth, ϕ changes steeply by 1.11 eV from the ZnSe substrate to the dye monolayer, while the Ir dye core lines and the valence feature that is at around 8.80 eV binding energy display a rather gradual shift of 0.20 eV. Approaching the saturated fully closed dye layer at the 651 s deposition starting from the dye monolayer at the 25 s deposition , a further binding energy change of 0.37 eV for ϕ, dye core levels, valence feature at around 8.80 eV, and HOMO onset is observed. Two regions are classified. During the initial monolayer growth (region I in Figure 5.8), the change of the dye orbitals binding energies cannot be caused by the formation of a space charge region. Instead we correlate the initial binding energy shifts to the formation of a

coverage-dependent interface dipole between the ZnSe substrate and the dye monolayer. In addition the dye molecules induce a strong dipole towards the vacuum, where the larger part of ϕ change occurs. During the island growth on top of the dye monolayer (region II in Figure 5.8), the shift in binding energy is interpreted as band bending in the 3-dimensional dye islands. This band bending leads to the additional change of ϕ by the same magnitude.

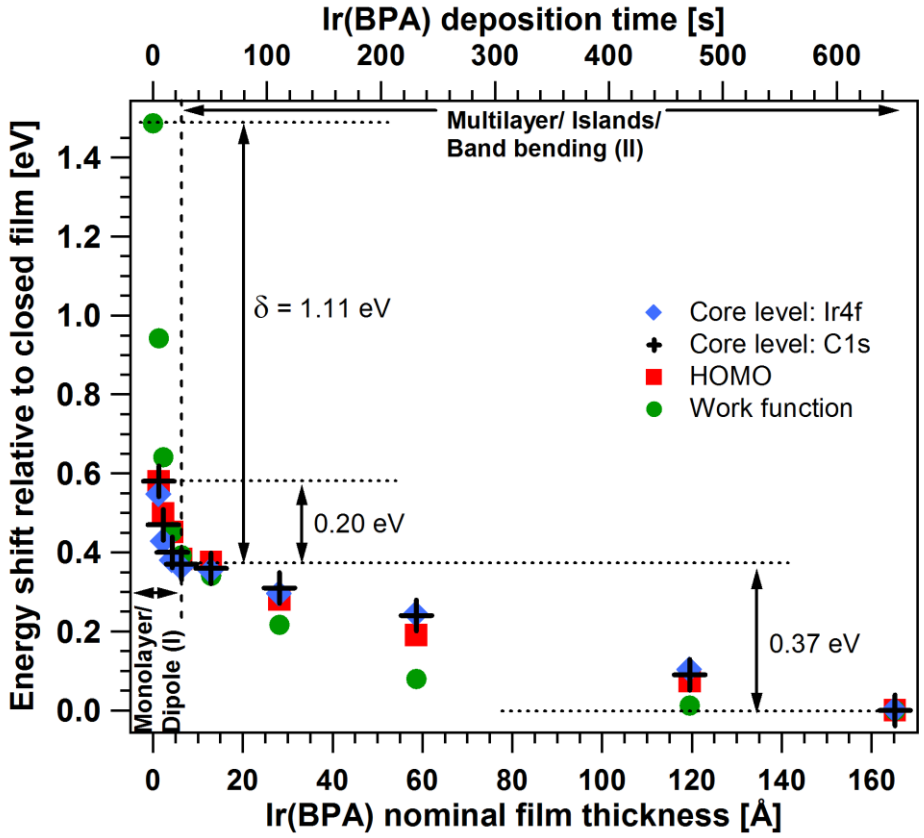

Figure 5.8: Relative binding energy shifts of the Ir4f and C1s emissions, as well as of the HOMO and ϕ plotted versus increasing Ir(BPA) nominal film thickness calculated from the experimentally derived deposition rate of the dye. The corresponding deposition time scale is given on the top axis. Two regions are discriminated by a vertical dashed line, namely: (I) Ir(BPA) monolayer formation accompanied with a presence of a 1.11 eV interface dipole as manifested by the large shift of ϕ in contrast to the slight shift of the dye emissions, and (II) Ir(BPA) multilayer/island formation accompanied with a 0.37 eV band bending as manifested by the parallel shift of the dye emissions and ϕ.

The electronic characteristics of the ZnSe/Ir(BPA) heterojunction derived from the interface experiment, which include a constant Fermi level in ZnSe, an interface dipole and a band bending in the Ir(BPA) layer, are summarized in the energy band diagram shown in Figure 5.9. The 1.48 eV difference in the Fermi level position represented by ϕ of ZnSe and Ir(BPA) (Figure 5.3) is adjusted by a 1.11 eV large interface dipole [268] and a 0.37 eV band bending in the Ir(BPA) overlayer. In the diagram, a thin reactive interface layer is drawn to point out that there is a chemical interaction taking place between the monolayer dye molecules (as evidenced by the strong spectral change of dye HOMO region in the 5 s to 25 s deposition steps shown in Figure 5.7) and the ZnSe substrate. Since the molecules in the dye

monolayer do not show any evidence of degradation (the lineshapes of the dye's core lines in the 5 s to 25 s deposition steps do not differ from that of the pristine Ir(BPA)), it can be concluded that the chemical interaction does not affect the formation of an abrupt material ZnSe/Ir(BPA) heterojunction. The drawn energy band diagram is, therefore, representative of the abrupt ZnSe/Ir(BPA) material interface.

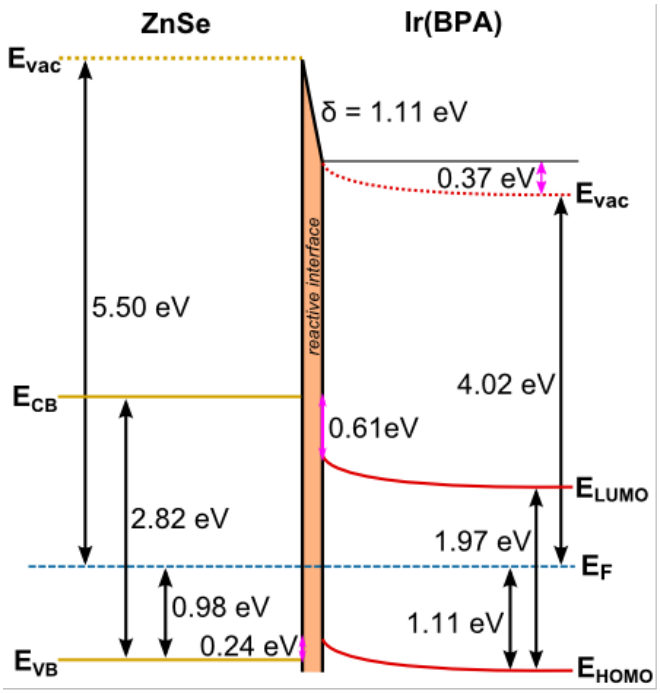

Figure 5.9: Interface band diagram of the ZnSe/Ir(BPA) heterojunction including a large interface dipole of 1.11 eV and band bending in the emitter of 0.37 eV.

Due to a large interface dipole, an energy level alignment where the dye's HOMO and LUMO are situated in between the valence and conduction bands of ZnSe can be achieved, even though the electron affinity of the pristine dye layer is 0.50 eV smaller than that of the pristine ZnSe. While for organic dopant - organic host OLED systems, where the vacuum-level alignment seems to hold [83, 269], photoemission studies have demonstrated the formation of an interfacial electric dipole layer for inorganic/organic interfaces.[268, 270, 271] which is also measured for our system. As possible origins of the induced interface dipole, the formation of charge transfer complexes at the interface [268, 271, 272], orientation of molecular dipoles [273, 274], charge redistribution at the interface [127], and polarization of the interface molecules [81] have been discussed in literature. With the shifts induced by the interface dipole leading to band offsets of 0.61 eV for electrons and 0.24 eV for holes, electron as well as hole transfer from the ZnSe layer to the Ir(BPA) layer is, therefore, energetically favorable. In addition, the resulting alignment may have turned out to be ideal for charge carrier transfer from the ZnSe to the Ir(BPA), but the presence of the reactive dye monolayer at the interface could, in the end, have some potential drawbacks which can lead to reduced efficiency in the charge carrier transfer.

5.3 Bilayer heterojunction: The Ir(BPA)/ZnSe interface

To approach the more complex ZnSe+Ir(BPA) co-deposition configuration, the reversed deposition sequence to obtain an Ir(BPA)/ZnSe interface was also investigated. An Ir(BPA) film with a ~150 Å nominal thickness was prepared on an ITO glass substrate and characterized. The thickness of the film was obtained from the 15.26 Å/min mean evaporation rate of Ir(BPA). This rate was obtained from an Ir(BPA) source calibration experiment where the intensity decrease of the In3d emission was used. To proceed with the interface experiment, ZnSe was then step-wise evaporated onto the dye film. At this point, it is necessary to take into consideration that ZnSe evaporates via congruent vaporization to produce a Zn and Se_2 flux.[198]

The survey spectra starting from the pristine Ir(BPA) followed by the increasing ZnSe overlayer in sequential deposition steps are shown in Figure 5.10. The total deposition times of ZnSe for each of the deposition steps are indicated in the figure. With increasing ZnSe deposition, the evolutions of the Ir(BPA) and ZnSe core lines are clearly observed. No photoelectron emissions from other elements are present in the survey spectra, indicating a clean and homogeneous sample preparation.

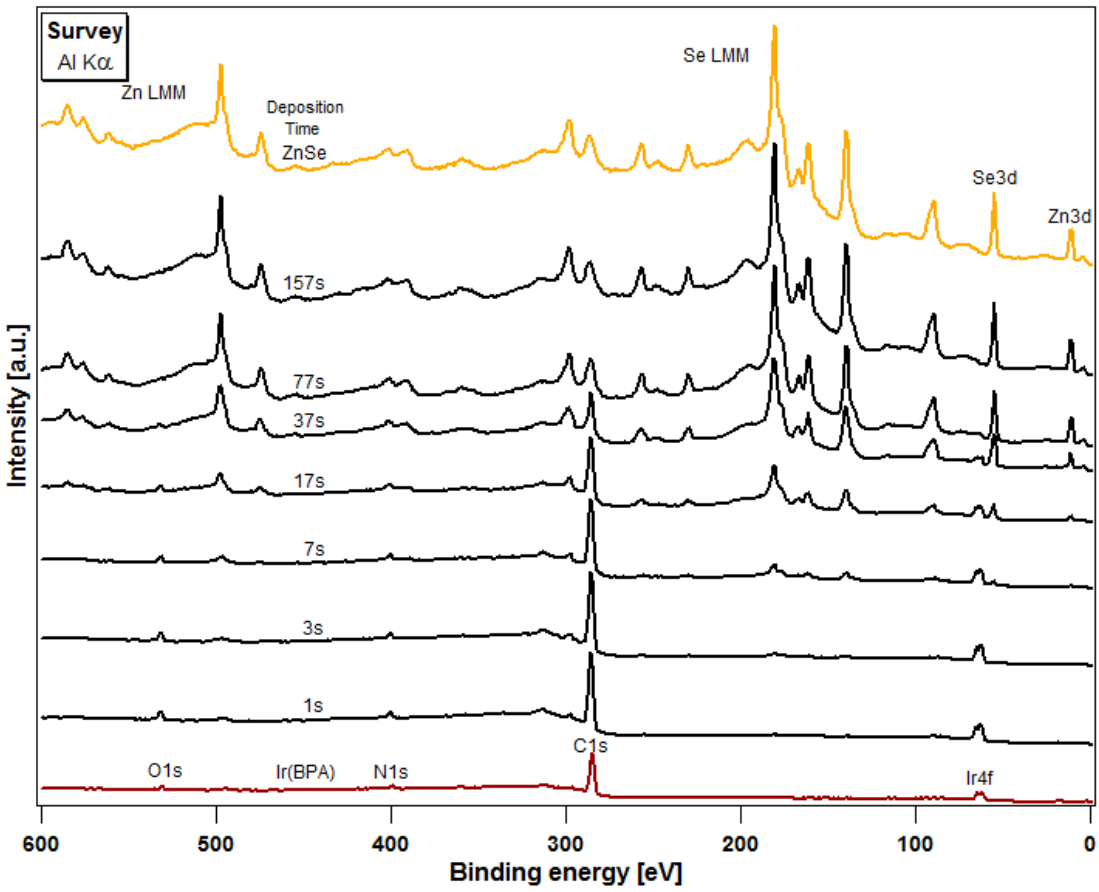

Figure 5.10: Survey spectra of Ir(BPA) and the step-wise deposited Ir(BPA) in the interface experiment for a ZnSe/Ir(BPA) bilayer. The total times for each of the Ir(BPA) deposition steps are indicated.

The UP spectra of the SE cutoffs and valence region from the subsequent PES measurements in the interface experiment are shown in Figure 5.11. From the SE cutoff, it is seen that ϕ decreases initially. But starting from the 37 s deposition, a second SE cutoff structure from a phase with a large ϕ appears and then dominates for the longer ZnSe deposition times. Also at the 37 s deposition, a clear emission of the Zn3d core line and the characteristic feature of the ZnSe valence band spectrum start to develop; whereas for the initial depositions, notably only dye-related valence features are observed. The second SE cutoff structure is attributed to ZnSe photoemission since the shift of its binding energy position follows the same trend that is observed for Zn3d during the 37 s to the 317 s depositions in the valence region spectra.

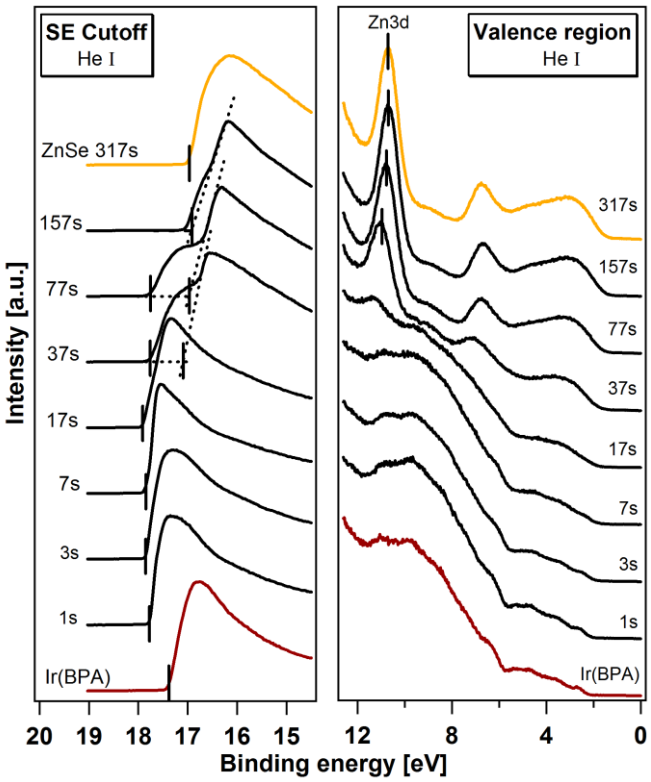

Figure 5.11: Photoemission spectra of the secondary electron cutoff and the valence region for ZnSe deposition onto the Ir(BPA) layer. The ZnSe deposition times are indicated. At the 37 s deposition step, the SE cutoff starts to exhibit a double edge structure and the valence region shows a sudden increase of Zn3d and the appearance of ZnSe valence features.

The corresponding core line emission spectra for the increasing ZnSe deposition times are plotted in Figure 5.12 for both the Ir(BPA) substrate and ZnSe overlayer. In the C1s spectral region in Figure 5.12(a), a transition is observed from the carbon contribution of Ir(BPA) to the Se LMM Auger electron emission of ZnSe as the ZnSe coverage increased. For the C1s and Ir4f emissions of the dye, there were no shifts of the binding energy positions. The $Zn2p_{3/2}$ and Se3d emissions are shown in Figure 5.12(b). For the Se3d emission, a transition

from a broad to a sharper emission that shows resolved $Se3d_{3/2}$ and $Se3d_{5/2}$ contributions is observed.

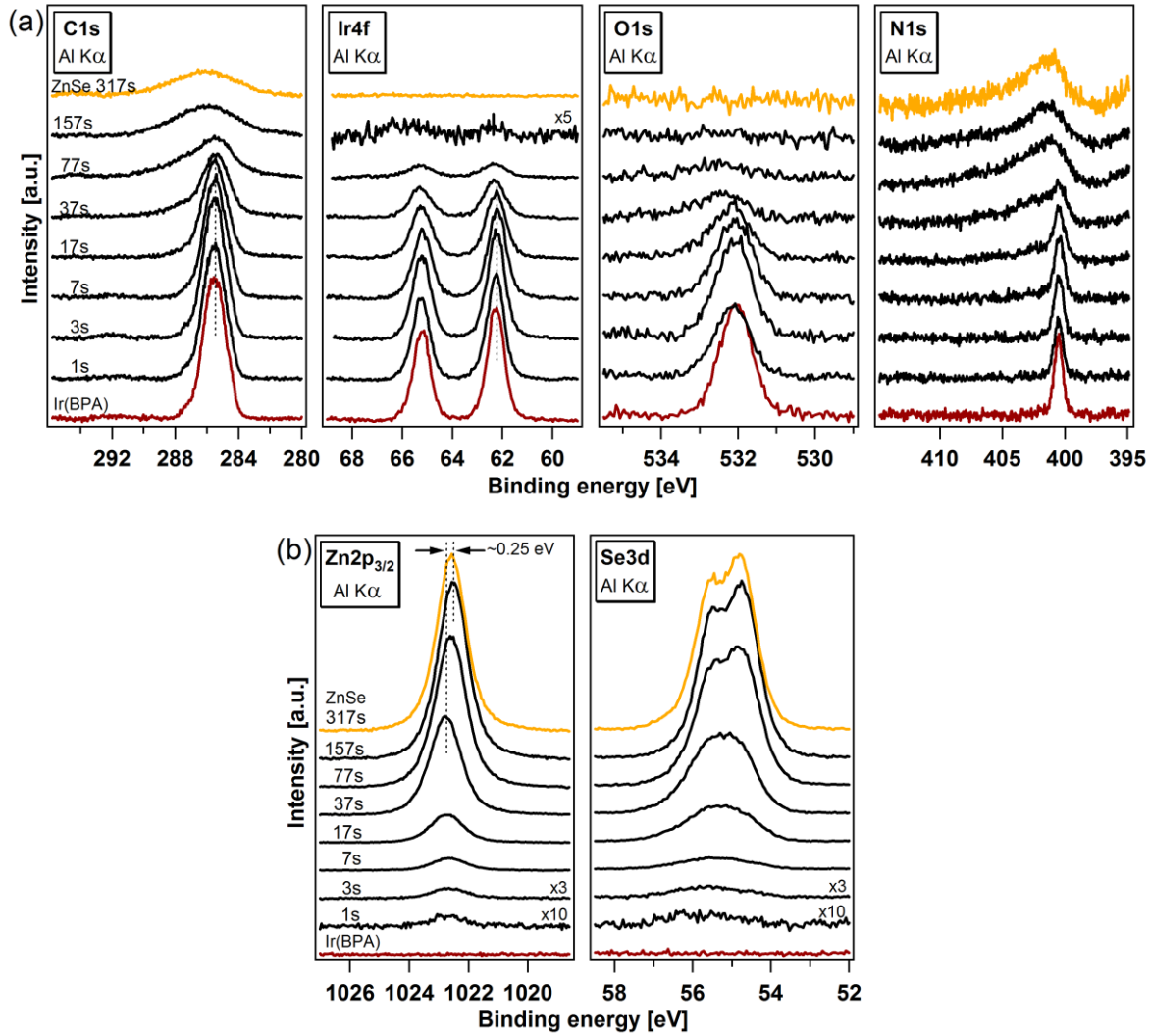

Figure 5.12: Ir(BPA) C1s, Ir4f, O1s and N1s emission spectra (a), ZnSe $Zn2p_{3/2}$ and Se3d emission spectra (b) during the stepwise deposition of ZnSe on an Ir(BPA) film. The ZnSe deposition times are indicated. While the dye's C1s and Ir4f binding energies remain constant with increasing overlayer coverage, the $Zn2p_{3/2}$ and Se3d emissions shift to lower binding energies approaching that of pristine ZnSe.

The high surface-sensitive UPS analysis do not show the Zn3d emission during the initial 1 s to 7 s deposition steps in Figure 5.11. On the other hand, the less surface-sensitive XPS core level analysis (Figure 5.12(b)) show a weak $Zn2p_{3/2}$ emission during these deposition steps which eventually becomes disproportionately strong by the 37 s deposition step. These observations lead to the interpretation that Zn atoms intercalate during the initial deposition steps into the Ir(BPA) layer; and from the 37 s deposition onward, ZnSe starts to distinctly grow in patches that finally form a closed film.

A plot of the photoelectron intensity ratio of the Se3d emission to the $Zn2p_{3/2}$ emission as a function of the deposition time is shown in Figure 5.13. In the figure, the ratio is high at the initial stages of growth. It reaches a maximum at the 17 s deposition before it

drastically drops at the 37 s deposition. Afterward, the ratio saturates to the value of the thick ZnSe film at 317 s deposition. As it appears, there is an excess of Se at the growth front and after several more depositions the growing surface changes to the stoichiometry of the thick ZnSe. This actually supports the intercalation of Zn atoms as deduced from the UPS and XPS measurements. On an additional note from literature where ZnSe is step-wise deposited on GaAs (111) by MBE coupled with XPS and RHEED measurements after each deposition step, it is reported that ZnSe growth proceeds in the biatomic layer-by-layer mode with an excess Se^0 at the growth front.[206] Initially, the photoelectron intensity ratios of Se/Zn indicates an excess of Se^0 giving off a (1x1) RHEED pattern. After a few bilayers of ZnSe, the growing surface changes to a stoichiometric (2x2) structure.

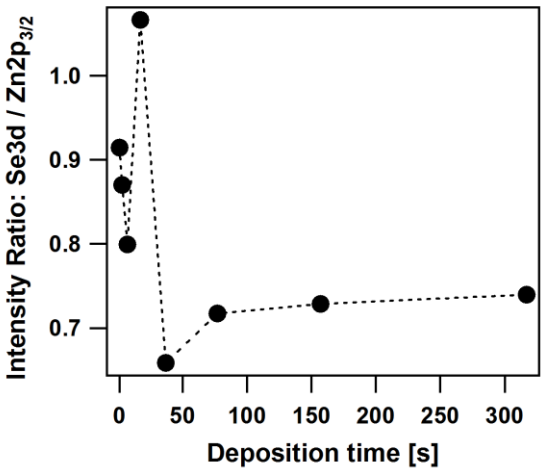

Figure 5.13: Photoelectron intensity ratios of the Se3d and $Zn2p_{3/2}$ emissions plotted as a function of the deposition time.

From the initial deposition steps to the final deposition where the ZnSe coverage is fully closed, a transition from a broadened Se3d emission to an emission with well-resolved Se3d spin-orbit splitting is observed in Figure 5.12(b). Following in detail this evolution of the Se3d emission, spectral fitting analyses were performed as displayed in Figure 5.14(a). The intensities are normalized in the graph for a better visual comparison. A good fit of the Se3d emission is obtained using three Voigt profiles which are attributed to excess selenium Se^0, Se^{2-} corresponding to ZnSe and a more reduced Se species. For the initial ZnSe evaporation steps, the Se^0 and reduced Se species are more intense than the Se^{2-} species of ZnSe. This correlates to the intercalating Zn atoms as such results to a few Zn atoms left at the interface to bond with the selenium atoms in forming ZnSe. And by the 37 s deposition step, the Se^{2-} emission from ZnSe starts to dominate the overall spectra.

The overlaying spectra of the Ir4f and O1s emissions of Ir(BPA) that is normalized in intensity are displayed in Figure 5.14(b). A component at a higher binding energy position is present in both core line emissions. This indicates a chemical reaction between the dye and

selenium at the interface at which electrons are exchanged resulting to reduced selenium and oxidized dye species.

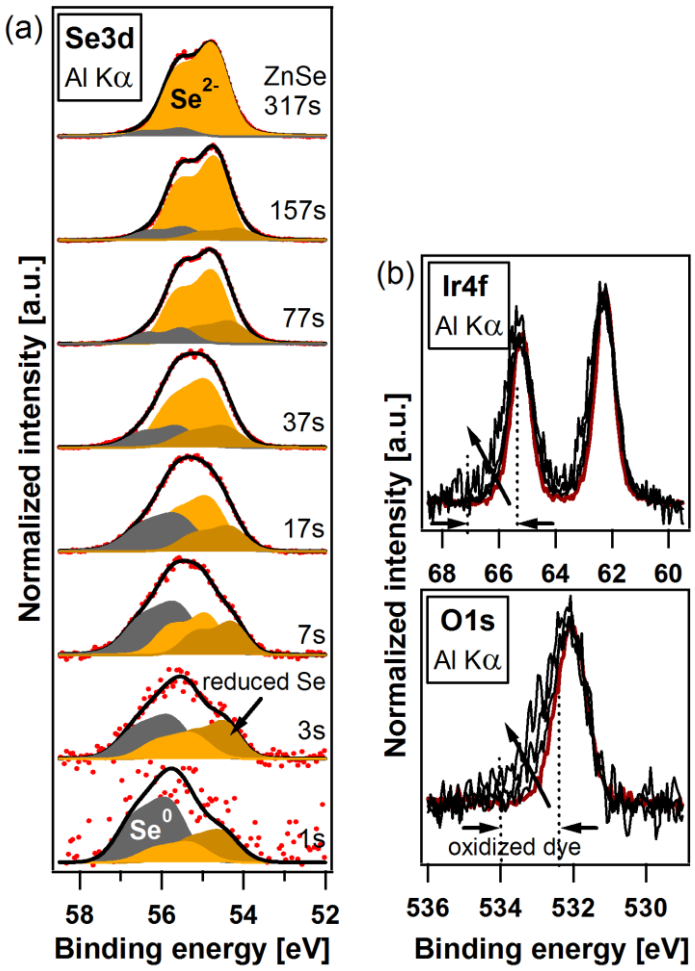

Figure 5.14: Peak fitted Se3d photoemission spectra (a). Good fitting is obtained with three contributions assigned to elemental Se0, Se2- in ZnSe and a more reduced component. (b) Normalized Ir4f and O1s emissions for 0 s, 17 s, 37 s and 77 s ZnSe evaporation show formation of high binding energy components.

The electronic characteristics of the Ir(BPA)/ZnSe heterojunction approximated from the interface experiment is shown in Figure 5.15. A thick reactive layer is drawn at the interface because the deposition of ZnSe onto the Ir(BPA) layer results to the intercalation of Zn atoms into the immediate Ir(BPA) layer, the formation of a mixed phase region comprising of ZnSe, Se^0 and reduced Se, and the oxidation of Ir(BPA) molecules. For the energy levels of the Ir(BPA) layer, only the ZnSe deposition steps leading up to 17 s are considered. The Ir(BPA) layers corresponding to depositions longer than this already showed clear evidence of the presence of oxidized dye molecules (Figure 5.14(b)). In the dye core level spectra, no binding energy shift is observed. From the UPS measurement of the pristine Ir(BPA) layer (Figure 5.11), the HOMO is positioned farther from the Fermi level.

This is accounted to the thick Ir(BPA) layer.[52] For the energy levels of the ZnSe overlayer, only the deposition steps starting from 37 s are considered. A shift of ~0.25 eV to lower binding energies is observed from the ZnSe core levels. This is accounted to a band bending in the ZnSe layer.

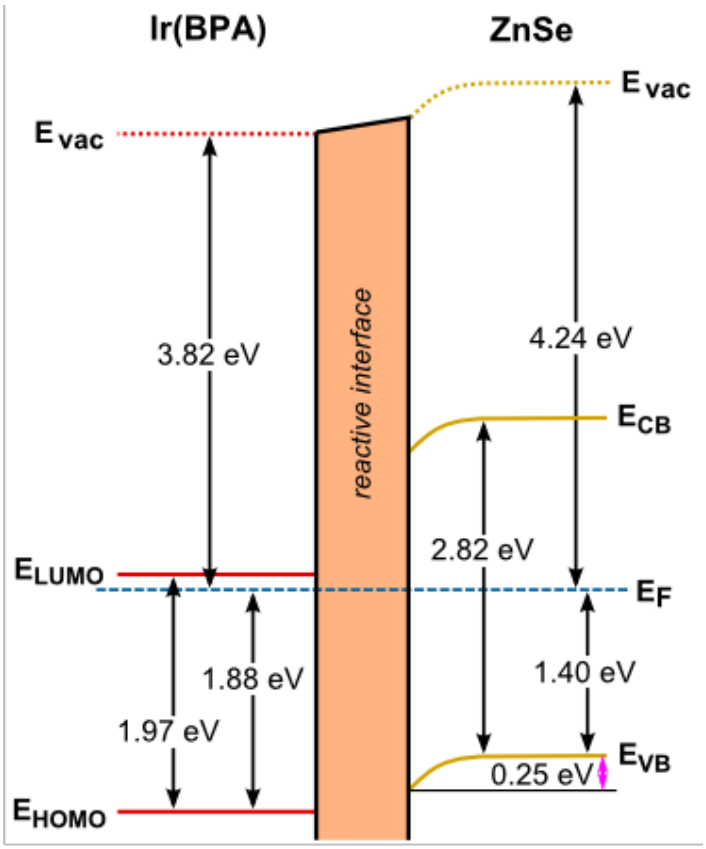

Figure 5.15: Energy band alignment for the Ir(BPA)/ZnSe heterojunction where only depositions up to 17 s is considered for the Ir(BPA) layer and depositions starting from 37 s is considered for the ZnSe layer. The deposition of ZnSe on top of Ir(BPA) leads to an interface region where the two materials are reactive (i.e. intercalation of Zn atoms into the immediate Ir(BPA) layer; formation of mixed phases of ZnSe, Se^0 and reduced Se; oxidation of Ir(BPA) molecules).

Overall, it turns out that our deposited Ir(BPA)/ZnSe heterojunction does not mirror the ZnSe/Ir(BPA) heterojunction presented in section 5.2. This is due to the formation of a thick reactive interface layer, which contains a gradient of intermediate material phases, brought about by the strong chemical interaction induced by the dye that affects the ZnSe deposition kinetics taking place right at their interface. So expectedly, it should be duly noted that the above energy band diagram is not representative of the actual abrupt Ir(BPA)/ZnSe material

[52] PES experiments have shown that once the Ir(BPA) film thickness exceeds ~120 Å nominally, saturated charging and probable X-ray effects on the dye become apparent. Exposure to X-ray coupled with charging for "thick" Ir(BPA) films seems to permanently alter the electronic characteristics of the dye but not affecting its chemical integrity (as no evidences of chemically shifted core level components and changes in the core level intensities were found).

interface; and therefore, it should not be expected to mirror the energy band diagram of the ZnSe/Ir(BPA) interface.

5.4 Composite: The ZnSe+Ir(BPA) interface

ZnSe nanocrystals embedded in a polymer polymethylmethacrylate (PMMA) matrix and ZnSe quantum dots in a polymer poly(3-hexylthiophene-2,5-diyl) (P3HT) matrix have been reported.[58, 275, 276] Their samples were prepared by colloidal solutions, and films were then obtained through the spin-coating technique. Without an experimental setup for sample preparation and characterization that offers a clean and contamination-free environment, the study of the interfacial electronic and chemical properties between the materials comprising the composite would not be possible.

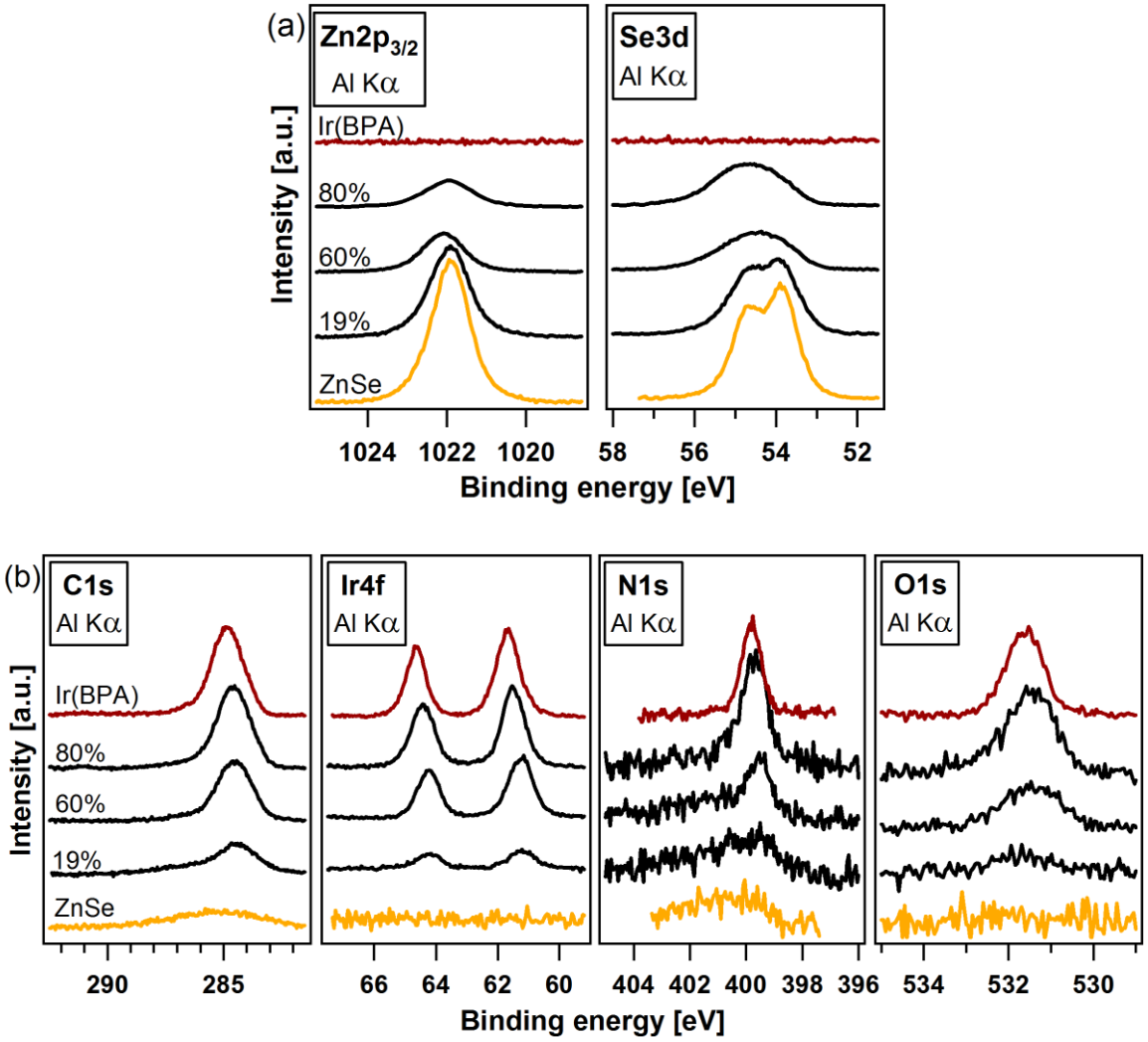

Figure 5.16: $Zn2p_{3/2}$ and Se3d core level emission spectra (a), C1s, Ir4f, O1s and N1s core level emission spectra of Ir(BPA) (b). The dye volume percentages are indicated. The spectra of pristine ZnSe and Ir(BPA) are added. The Se3d spectra show a gradual broadening with increased dye concentration.

In this study, composite sample preparations and characterizations were all performed in UHV. ZnSe + Ir(BPA) composite films were obtained by co-deposition of ZnSe and Ir(BPA). This was done by simultaneous evaporations of ZnSe and the dye, and targeted onto an ITO glass substrate. The achievement of a closed composite film is indicated by the absence of the ITO substrate core lines. Dye volume percentage compositions of the films were estimated from the intensities of the core line emissions by considering atomic orbital specific sensitivities and the spatial volumes of ZnSe and Ir(BPA) (Appendix C).

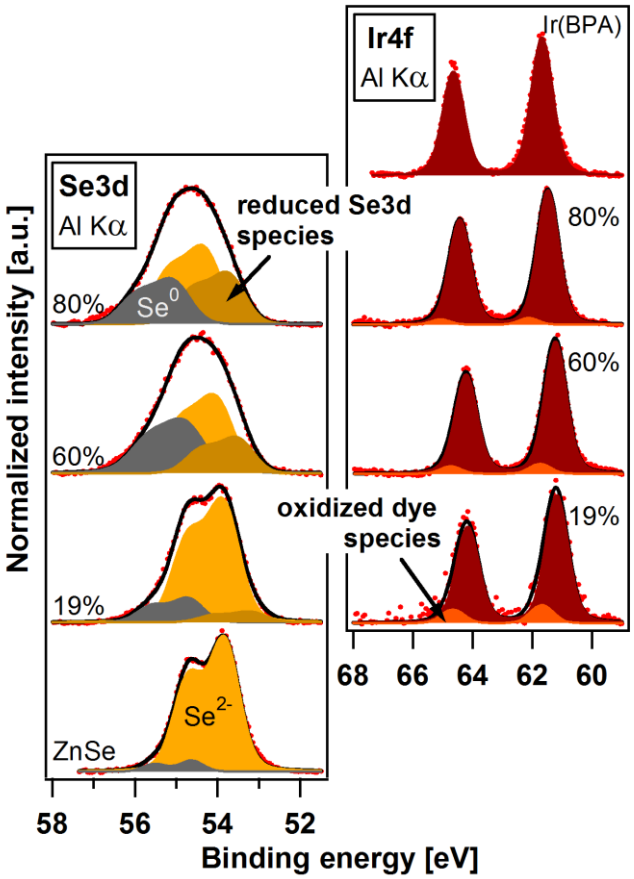

Figure 5.17: Curve fitting analysis for Se3d and Ir4f core level emission spectra. Se3d fit reveals the presence of three species contributing to the emission: Se^{2-}, Se^{0} and reduced Se. Ir4f fit shows presence of oxidized dye species.

The different core line emission spectra of three composites together with pristine ZnSe and pristine Ir(BPA) are shown in Figure 5.16. For the $Zn2p_{3/2}$ spectra of the composites in Figure 5.16(a), no changes in the lineshapes are observed. The Se3d spectra show a gradual broadening as the amount of dye is increased. The change of the Se3d line shape observed for the composites is similar to the changes observed in the initial stages of overlayer growth of ZnSe on Ir(BPA) (Figure 5.12(b)) in the Ir(BPA)/ZnSe interface experiment. In the C1s spectral region (difference spectra was not obtained here) shown in Figure 5.16(b) for the composites, the Se LMM emission overlaps with the C1s emission of Ir(BPA). For the 19% composite, the C1s and Ir4f binding energy positions are shifted to a

lower value by 0.49 eV relative to that of the pristine dye; this shifted position then gradually approaches that of the pristine dye with increasing dye content in the composites.

For the inspection of the observed trend in the Se3d emission, peak fitting analyses of the spectra were also performed together with the Ir4f spectra of the dye. Figure 5.17 displays the spectral fits. Good fits are obtained using the same components that were used for the Ir(BPA)/ZnSe interface (Figure 5.14). For the pristine ZnSe film, the analysis of the Se3d doublet reveals that 95% of the total Se compounds are from ZnSe, and the remaining 5% are from small amounts of occluded bulk selenium, Se^0.[207, 221] The orange-red pigmentation acquired by our ZnSe films with slightly larger Se^0 content (from other pristine ZnSe film depositions and XPS measurements not shown here) is attributed to the presence of Se^0.[221] The Se^{2-} species of the ZnSe phase in the composites shift toward higher binding energy positions at large dye concentration in agreement to our internal interface charge transfer doping model, which assumes Fermi level alignment at internal interfaces of the phase separated composite constituents by charge transfer and dipolar effects.[146] The composite films exhibit additional species corresponding to reduced selenium at lower binding energies and oxidized Ir4f species at higher binding energies. The reduced selenium species in the composite chemically correspond to the oxidized dye species in the Ir4f emission, similar to our findings on the Ir(BPA)/ZnSe interface.

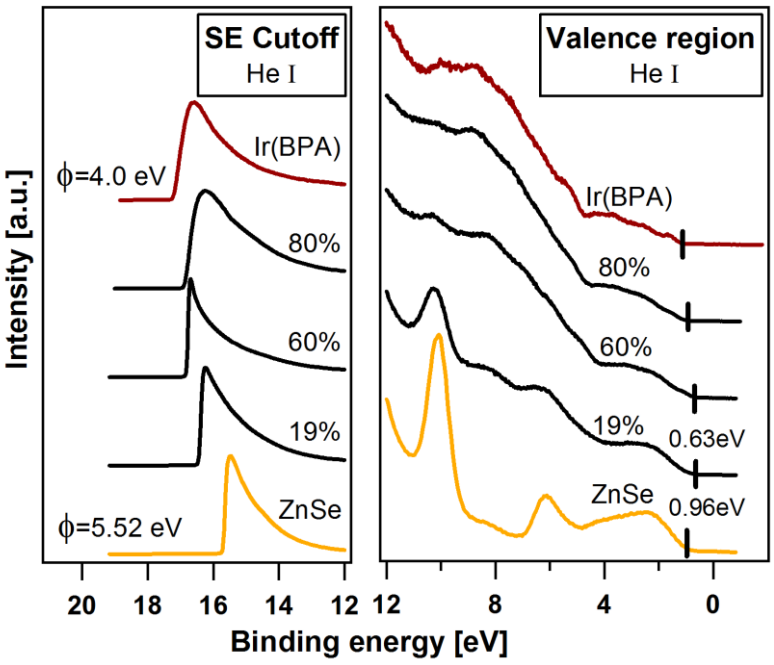

Figure 5.18: Secondary electron cutoff and valence band spectra of the composites. The values of ϕ and HOMO/VBM onsets of ZnSe and 19% composite are indicated. The HOMO onset is shifted to a lower binding energy position as compared to that of pristine Ir(BPA).

The SE cutoff and valence region of the composites are shown in Figure 5.18. With increasing dye concentrations, the Zn3d emission and the valence features of ZnSe disappear in the spectra similar to that of the Ir(BPA)/ZnSe interface (Figure 5.11). The

HOMO onset is shifted to a lower binding energy by 0.48 eV in the 19% composite relative to the pristine dye, and gradually shifts to the pristine dye position.

In order to draw a picture of the energy level alignment in a ZnSe+Ir(BPA) bulk composite design which is proposed in this study for HLED active layer applications, we considered the composite with 19% dye concentration since the amount of ZnSe in this case is significantly large relative to the amount of Se^0 and the reduced selenium/oxidized dye species within the bulk of the composite film. From the $Zn2p_{3/2}$ and Se3d emissions of this composite, no shifts in binding energies were observed with respect to that of pristine ZnSe. This indicates Fermi level pinning within the ZnSe matrix as similarly observed in the ZnSe/Ir(BPA) heterojunction. With the absence of shifts in the ZnSe phase of the 19% composite, we take the pristine ZnSe values of 5.52 eV and 0.96 eV for ϕ and the position of the valence band maximum, respectively. The HOMO onset of the dye in the composite was determined by linear extrapolation to be at 0.63 eV below the Fermi level. To evaluate ϕ of the dye and the interface dipole in the composite, we considered the band energy approximation as given by the internal interface charge transfer doping model.[146] The ionization potential of the dye is 5.13 eV, derived from the ZnSe/Ir(BPA) interface experiment (Figure 5.9). With the HOMO of the dye at 0.63 eV from the Fermi level of the composite, the calculated hypothetical value of ϕ inside the ZnSe matrix would be 4.50 eV.

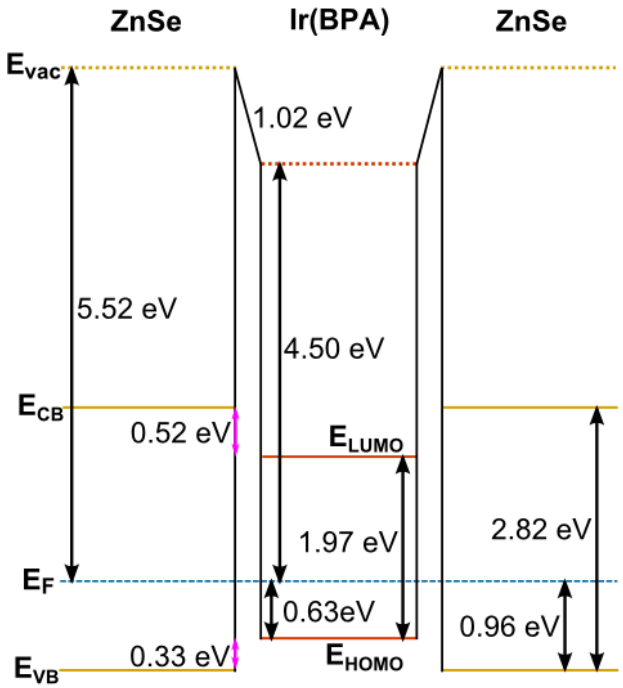

Figure 5.19: Energy band alignment at the internal interfaces of the 19% ZnSe+Ir(BPA) composite. This band diagram displays the dye frontier orbitals being sandwiched by the ZnSe energy levels. The difference in the measured ϕ of the pristine ZnSe and the calculated ϕ of the dye in the composite is assigned to a 1.02 eV interface dipole that leads to the measured lineup.

The energy band diagram is displayed in Figure 5.19. A 1.02 eV interface dipole that shifts down the energy levels of the dye leading to band offsets of 0.52 eV for electrons and

0.33 eV for holes is deduced. With this alignment of the energy levels within the composite, charge carrier transfer from the ZnSe matrix to the dye dopant is energetically favorable. ZnSe and Ir(BPA) are, therefore, suitable for the matrix-dopant combination in the emissive layer design proposed by this study.

Results from both the composites and the reverse Ir(BPA)/ZnSe interface experiments complement each other. Because of the nature of thermally evaporating ZnSe, the co-deposition and reverse deposition affects the formation of ZnSe at the interfaces it forms with Ir(BPA). Upon reaching the substrate, a number of Zn atoms intercalate into the much larger dye molecule aggregates, leaving behind excess Se^0 at the surface. Adding to that, selenium interacts with the dye molecules as indicated by the presence of reduced selenium and oxidized dye species. These mechanisms compete against ZnSe formation at the interface leading to a gradient of mixed amorphous and polycrystalline [177, 198, 199, 230] phases rather than the desired distinctly abrupt material interface between the dye and polycrystalline ZnSe.

Chapter 6 ZnSe + Ir(BPA) composite: Other characterizations

From PES measurements, the chemical integrity of Ir(BPA) in a co-deposition with ZnSe was confirmed from the correct stoichiometry of the dye constituents. And by other experimental techniques outlined in this chapter, this was even further confirmed. Though the co-deposition does not affect the dye characteristics, it does affect the formation of ZnSe as was observed in the PES measurements. Excess Se^0 is formed together with intercalated Zn atoms, leading to amorphous phases mixed with ZnSe in the matrix. The increased amorphousness with increased Ir(BPA) content in the composites can readily be observed as presented below.

6.1 Raman spectroscopy of the composites

Raman spectroscopy was briefly performed on pristine ZnSe, Ir(BPA) and their composites deposited on quartz glass substrates. The spectra were recorded using a Labram HR800 spectrometer fitted with a 600 grooves/mm grating and 100 µm aperture. The spectrometer was equipped with an air-cooled Andor CCD detector. A Spectra Physics krypton-ion laser source operating at a wavelength of 752.45 nm was used to illuminate the samples. The spectra were obtained using a back-scattering geometry with a resolution of ~2 cm^{-1}.

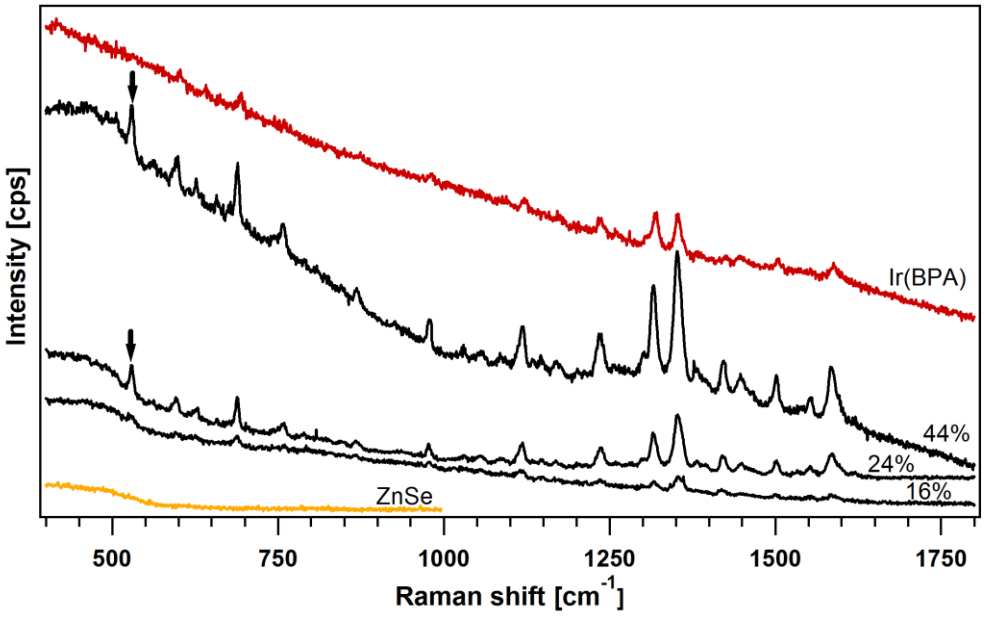

Figure 6.1: Raman spectra of ZnSe + Ir(BPA) composite films deposited on quartz glass substrates together with pristine ZnSe film and Ir(BPA) powder. The dye volume percentages are indicated. The vibrational modes of the dye molecules are also present in the composites. Arrows point at an additional vibrational mode at 529.5 cm^{-1} that is unique to the composites.

The Raman spectra of the pristine and composite films in the range 400 - 1800 cm^{-1} are shown in Figure 6.1. All the Raman features associated with the Ir(BPA) powder are present in the composite films. Interestingly in the composites, the intensities of the Raman lines are increased. In addition, the relative intensities are modified in the composites. These differences are assigned to the different chemical environment and anisotropic behavior of the molecule.[76, 277] Raman peaks from iridium - ligand vibrational modes in Ir(III) complexes are typically found at wavenumbers < ~450 cm^{-1}; peaks at wavenumbers higher than this value are from ligand vibrational modes.[278, 279] However in this case, no distinct peaks were found below 450 cm^{-1}, which is possibly due to the highly intense overlapping background signal coming from the strong luminescence of Ir(BPA). The Raman peaks found in the spectra all correspond to the different ligand vibrational modes except for the peak located at 529.5 cm^{-1}, which is exclusively found only in the composites. We tentatively assign this to a vibrational mode coming from the chemical bond of the dye with selenium.[280, 281] This assignment coincides with the electron exchange that led to the reduced selenium and oxidized dye species in the composites as found in the PES of the composites (Chapter 5.4).

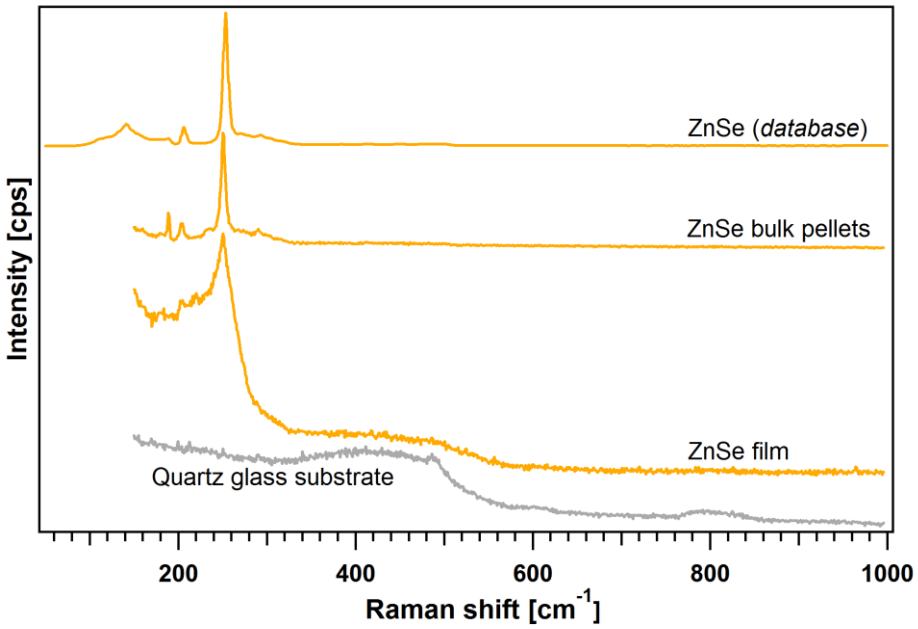

Figure 6.2: Raman spectra of ZnSe from a film deposited on a quartz glass substrate, the bulk source pellets and the database. The spectrum obtained for a bare quartz glass substrate is also included.

Moreover, the Raman spectrum of a ZnSe film deposited on a quartz glass substrate, together with the spectra from the database and from the bulk source pellets, are plotted in Figure 6.2. The broadened and increased background signal in the spectra of the ZnSe film comes from the contributions of the substrate and the Se^0 phases [282-285] present in the film. When ZnSe is co-deposited with the Ir(BPA) dye to obtain the composites, the relative amount of Se^0 is increased together with increased Ir(BPA) concentration as observed in the

PES measurements. This increased Se^0 trend is also evident in the Raman spectra of the composites from the increased intensity and broadened structure in the wavenumber range 200 - 280 cm^{-1} as shown in Figure 6.3.

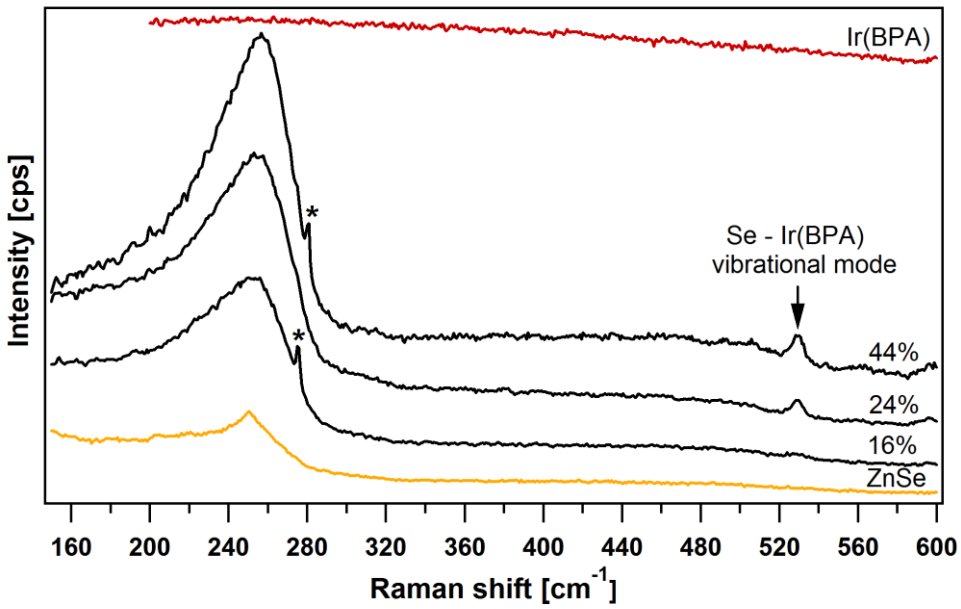

Figure 6.3: Raman spectra of the composite films in the wavenumber range 150 - 600 cm^{-1}.

In general, selenium exists in the amorphous, trigonal and monoclinic forms. The trigonal form consists of helical chain molecules, whereas, the monoclinic form consists of Se_8 ring molecules. The structure of the amorphous selenium is not clear; it may consist of the ring molecules or the chain mixed with ring molecules.[283, 285] These three forms have bond-stretching vibrational modes that altogether contribute to a broad frequency band in the 200 - 280 cm^{-1} range.[284, 285] Additionally, there is a sharp peak (marked by an asterisk) in the spectra of the 16% and 44% composites that is shifted to a higher frequency with increased Ir(BPA) concentration. No vibrational mode from selenium nor ZnSe can be assigned to these peaks.

6.2 Crystal structure of the composites

The crystalline structures of composites deposited on quartz substrates containing 23% and 51% volume of Ir(BPA) were determined from the X-ray diffraction patterns shown in Figure 6.4 together with that of a pristine ZnSe film deposited on an ITO glass substrate. XRD reflections from ITO and a broad background from around 15° to 40° from the glass substrate are observed in the XRD pattern of the pristine ZnSe film sample. The broad, smooth background seen on the pattern for the composites are expected and are accounted to contributions from the amorphous substrate, Se^0 phases, and Ir(BPA). The XRD patterns of the 23% and 51% composites, however, still exhibit 3 major broad peaks at 27.2°, 45.1°, and 53.3° that correspond well to the (111), (220) and (311) reflections of the cubic zincblende

phase of ZnSe. These Bragg reflections are well matched with the literature values (refer to Chapter 4.1.3).

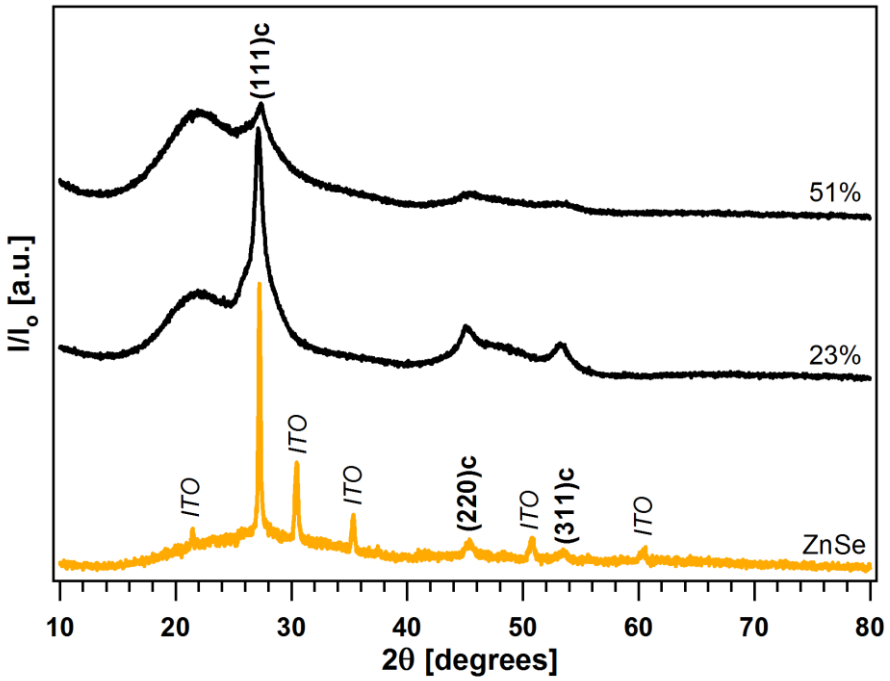

Figure 6.4: X-ray diffraction patterns of ZnSe film deposited on ITO on glass substrate at room temperature.

The presence of the reflections from polycrystalline ZnSe in the XRD pattern of the composites gives evidence that polycrystalline ZnSe phases are still formed even in a co-deposition with Ir(BPA). An intact crystallinity for ZnSe in the composite is important in the design for the composite emissive layer proposed by this study since the ZnSe is supposed to be the matrix for the transport of electrons and holes from the electrodes to the Ir(BPA) emitter dopants. In a possible practical application of the proposed hybrid concept into devices, the extent of the dye doping may not necessarily be as high as 20%, nor even 10%. For such low doping levels, there would be fewer amorphous phases and the crystallinity of the ZnSe phases would be higher. Annealing at around ~150°C to remove the Se^0 phases in the composites could also lead to further improvement.

6.3 Transmission electron microscopy images of composites

Transmission electron microscopy (TEM) was employed to investigate the morphological structure of ZnSe + Ir(BPA) composites. The TEM analyses were carried out using a Hitachi H7650 microscope in high contrast mode. The nominal thickness (as estimated from the individual deposition rates of ZnSe and Ir(BPA) determined from calibration experiments) of the composite films deposited on carbon-coated Cu grids is within ~500 - 600 nm.

In some matrix-dopant systems, it has been found that the morphology of dopant aggregates changes with doping concentration. The aggregates take on spherical shapes at low doping concentrations. As the concentration is increased, the aggregates tend to coalesce to grow into forms in the shapes of dendrites or needles.[250, 286]

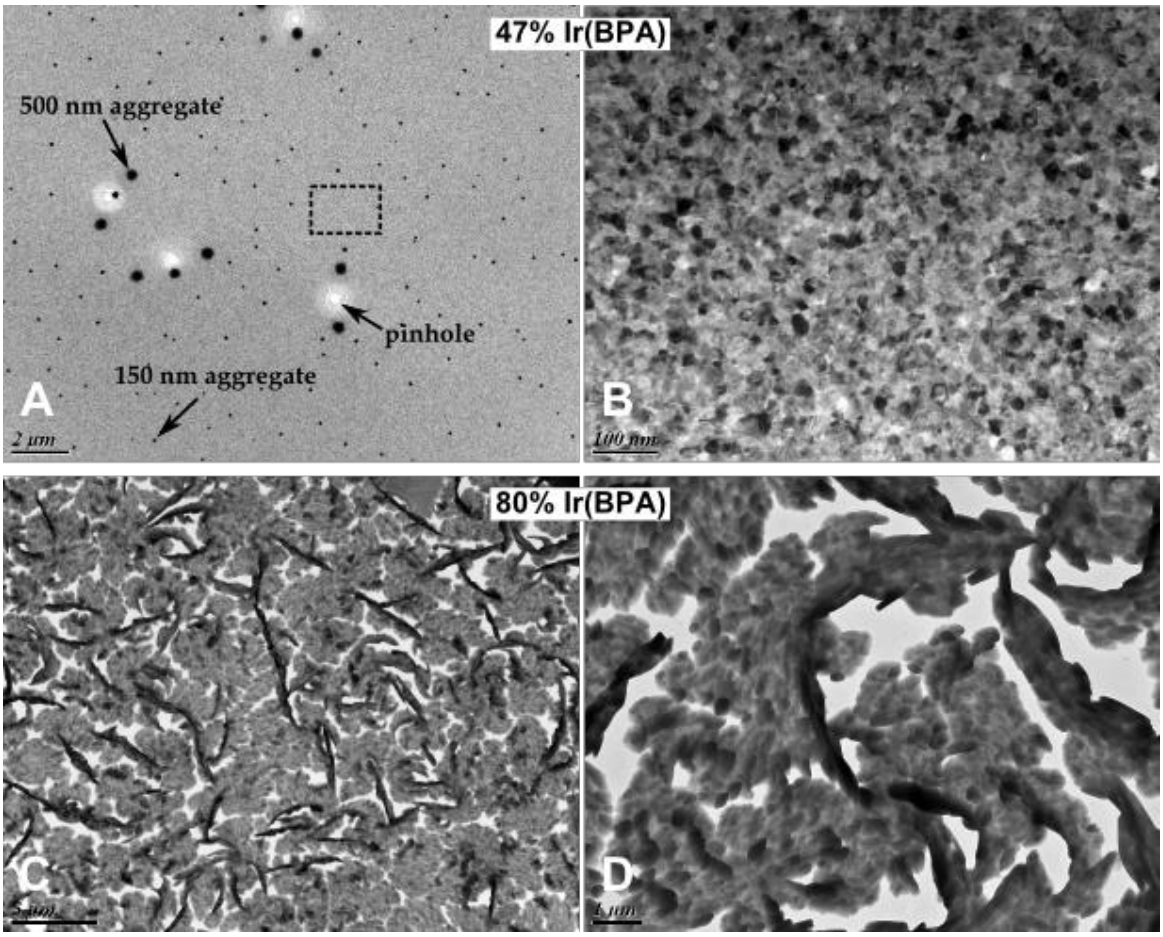

Figure 6.5: TEM images of ZnSe + Ir(BPA) two composite films with dye volume percentages of 47% (A, B) and 80% (C, D) under different magnifications. Apparently, the aggregation of the dye increases with increased amount of dye concentration in the composite film.

The TEM images of two composite films under varied magnifications are displayed in Figure 6.5. Since the iridium atom has the largest electron scattering cross-section amongst all the atoms in the composite, the dark spots are highly likely to be Ir(BPA) aggregates (note that the molecule has a small diameter of around < ~10 Å). At high doping

concentrations, the assumption of a homogeneous dispersion of single Ir(BPA) molecules in a ZnSe matrix is not valid. The TEM images clearly provide evidence of aggregate formation of Ir(BPA) in ZnSe. For the composite with the lower dye concentration of 47%, the aggregates are majorly homogenously distributed (as seen on the dashed-squared area in Figure 6.5A, which is Figure 6.5B), with sparsely scattered larger aggregates with diameters of ~150 nm and ~500 nm. For the ZnSe + Ir(BPA) composite, clearly the Ir(BPA) aggregates take on a dendrite formation at high concentrations as evident from the TEM images in Figure 6.5C and Figure 6.5D. Based on the amount of pinholes present in the 80% composite, this type of aggregate formation exerts a lot of strain on the film structure as the dye coalesce into large dendrites.

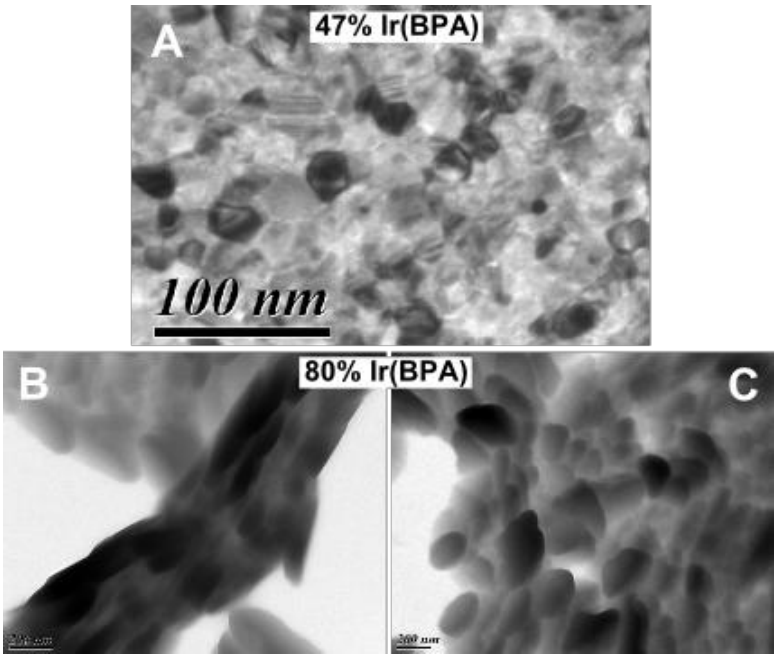

Figure 6.6: TEM images of the composites under higher magnification.

Figure 6.6 displays an enlarged TEM image of the 47% composite and TEM images of the 80% composite under a higher magnification. At a low dye concentration (Figure 6.6A), the mixing is rather more homogeneous. From the high magnification image of a dendrite (Figure 6.6B), it looks like it is comprised of bundles of needle aggregates of the dye. Other parts of the film (Figure 6.6C) exhibit the formation of ZnSe (Figure 4.9) mixed with aggregates of the dye.

The inhomogeneity in the distribution of Ir(BPA) due to large aggregate formation throughout the entire 80% composite film was also observed in the XPS measurements. The Ir4f and Se3d emissions measured at different parts of the sample are shown in Figure 6.7. Variations in the measured intensity ratio of the dye and ZnSe core level emissions were observed at different parts of the sample. The given dye volume percentage of 80% is the average taken from the different parts of the sample.

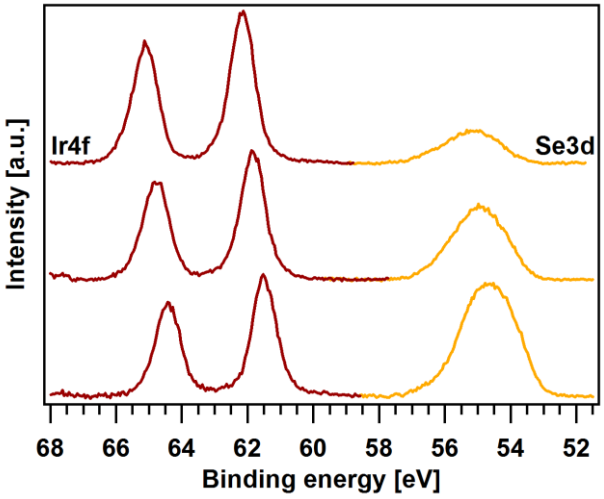

Figure 6.7: Ir4f and Se3d emissions of the 80% composite measured at different parts of the sample. Variations in the intensity ratio of the Ir4f and Se3d emissions confirms the inhomogeneity observed in the ZnSe and Ir(BPA) distribution from the TEM images.

In matrix-dopant systems, it is known that aggregates prohibit a sufficient close contact for exciton transfers between the donor and acceptor materials.[250, 287, 288] The obvious formation of aggregates in our composites with large dye content will pose a negative effect on the energy transfer from the ZnSe matrix to the Ir(BPA) molecules. Thus, it will become necessary to take the precaution of considering only small concentrations of Ir(BPA) in the composite hybrid design.

6.4 Infrared spectroscopy of the composites

Infrared (IR) spectroscopy was used to identify the Ir(BPA) molecules in the composite films. The IR experiments in this work were performed using a Fourier transform infrared (FTIR) spectroscope operated in attenuated total reflection (ATR) mode.

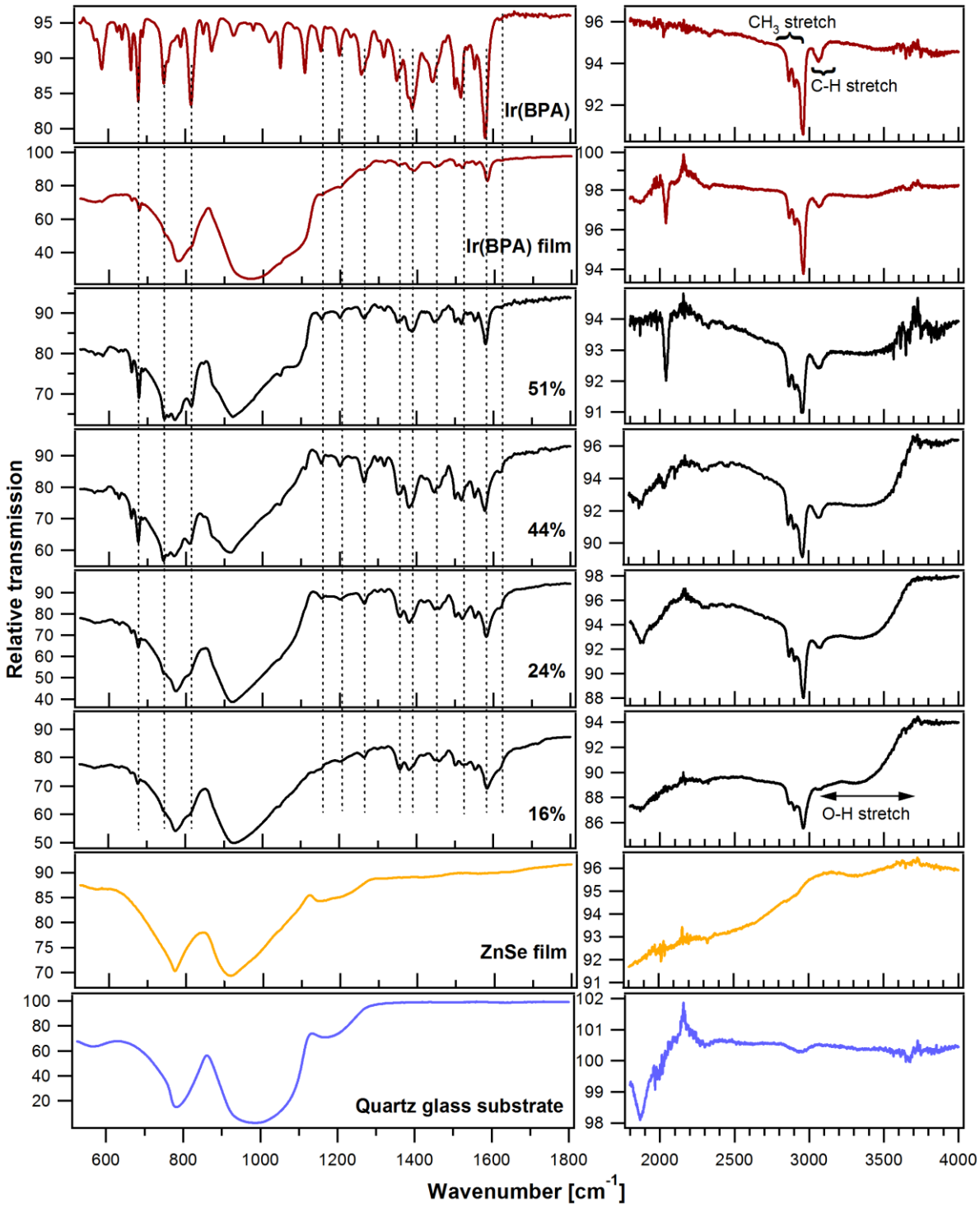

Figure 6.8: IR spectra of the composites together with the pristine dye in film and powder, ZnSe film and the quartz glass substrate.

Figure 6.8 shows the IR spectra of several composites with different Ir(BPA) concentrations together with pristine Ir(BPA), ZnSe and the quartz glass substrate. If there is degradation through defragmentation of the dye molecule or changes in the chemical structure, then there should be differences in the manifested vibrational modes in their IR spectra. In addition, any changes in the chemical composition of the composites as compared to the pristine Ir(BPA) and ZnSe should also appear in the spectra.

The composite films clearly exhibit the vibrational modes of the dye within the frequency range of 2850 - 3100 cm^{-1}. The modes within 2850 - 3000 cm^{-1} originates from the methyl group of the tert-butyl-phenyl in the ligands of the dye. Modes of the dye in the lower frequency range of 500 - 1650 cm^{-1} also appear in the spectra of the composites. At frequencies < 1200 cm^{-1}, strong broad background contributions dominate the spectra. A broad and weak O-H stretching band (3300 - 3400 cm^{-1}) was observed from all film samples. This just indicates a weak water absorption during sample storage.

6.5 Absorption and photoluminescence properties of the composites

The onset of dye absorption is at ~640 nm (Figure 4.16). At the long wavelength range, the absorption corresponds to the ^3d-π* transitions. The absorbance gradually increases towards the UV range, which corresponds to the ligand-centered π-π* transitions. The transmission spectra of three composite films with 25, 44 and 51 dye volume percentages deposited on quartz substrates are shown in Figure 6.9 together with the spectra of the pristine ZnSe and Ir(BPA) films. The transmittance of the composites appears to be a superposition of the transmittance of ZnSe and Ir(BPA). Fringes are also present in the spectra due to thin-film interference.

As was described in Chapter 2, the electroluminescence of composite devices (i.e., matrix-dopant systems) is speculated to be driven by direct charge injection, energy transfer, or both. In the case of a direct charge injection, an electron and a hole are injected from the charge transporting layers into the dopant molecules, forming an exciton that subsequently recombines to emit a photon. For the ZnSe+Ir(BPA) composite, the possibility of a direct charge injection from the charge transporting ZnSe matrix to the light-emitting Ir(BPA) molecule dopants was proven from the PES-derived alignment of the valence and conduction bands of ZnSe to the HOMO and LUMO of Ir(BPA). For a possible energy transfer, particularly Förster transfer, the most direct approach to experimentally validate is the spectral overlap of the ZnSe emission spectrum and the Ir(BPA) absorption spectrum. Figure 6.10 shows the PL spectrum of a ZnSe pellet under 325 nm HeCd laser excitation superimposed to the absorption spectrum of Ir(BPA) molecules dispersed in toluene. The ZnSe emission has a full spectral overlap with the absorption of ^{1}MLCT of Ir(BPA). The presence of a spectral overlap between the ZnSe emission and Ir(BPA) absorption shown in the figure strongly suggests the possibility of a Förster energy transfer.

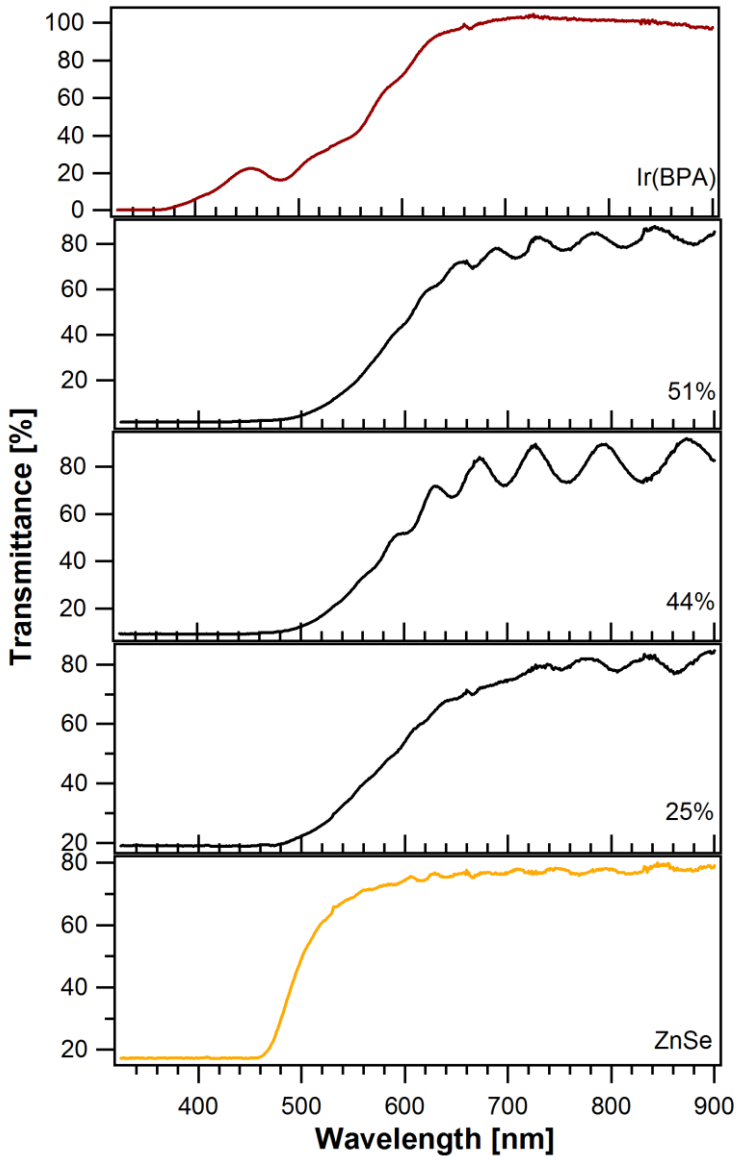

Figure 6.9: Transmittance spectra of ZnSe + Ir(BPA) composite films together with pristine ZnSe and Ir(BPA) films all deposited on quartz glass substrates.

For a composite system (*e.g.* polymer matrix + organic small molecule dopants and polymer matrix + inorganic nanoparticle dopants), reports in literature elucidate energy transfers through observed exciton dynamics from time-resolved luminescence spectroscopy techniques.[51, 57, 250, 289-291] In the absence of available transient techniques at low temperatures, we employed a direct measurement of the photoluminescence of our hybrid composite system at room-temperature using two different excitation sources instead. Such a method, in general, will not be able to conclude on Dexter energy transfer due to competing nonradiative processes[53] which include triplet diffusion to defect sites followed by dissipative transitions. And since zinc selenide is basically not a triplet emitter, its

[53] Reducing the temperature slows the rate of phonon-assisted decay and triplet diffusion.

fluorescence generally happens faster than intersystem crossing, which means an electron would fluoresce before it proceeds to occupy a triplet state through thermal relaxation.

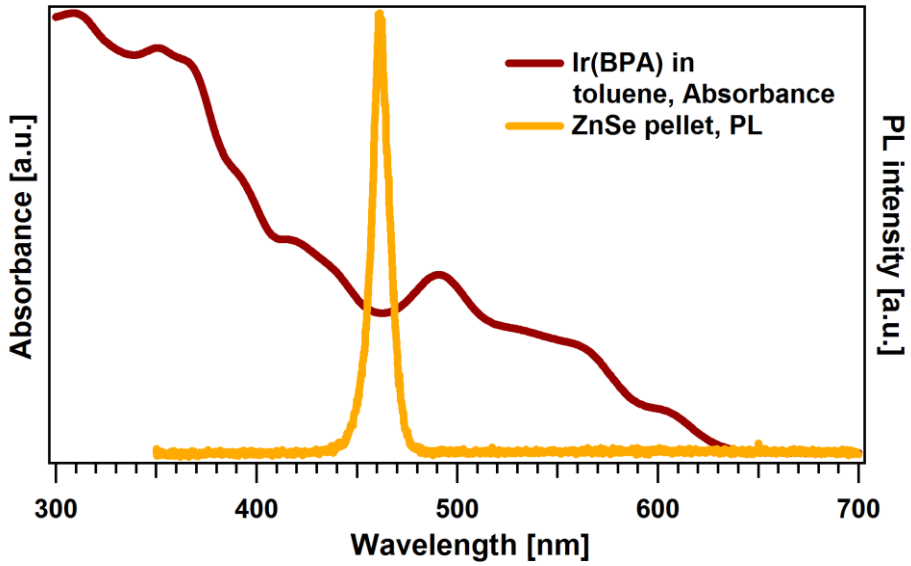

Figure 6.10: Photoluminescence spectrum of a ZnSe pellet shown together with the absorption spectrum of Ir(BPA) molecules dispersed in toluene to demonstrate the total spectral overlap, which indicates the likelihood of resonant exciton energy transfer from ZnSe to Ir(BPA) molecules.

Additionally, in the case for ZnSe, the possibility of a Dexter energy transfer to Ir(BPA) is negligible because the phosphorescent emission of ZnSe (only observed at very low T) is at ~635 nm [292], which would mean that the T_1 of ZnSe is positioned below the T_1 of Ir(BPA). On the other hand, with the sufficient spectral overlap of the donor (ZnSe) emission and acceptor (Ir(BPA)) absorption (Chapter 2.3.1) as shown in Figure 6.10, the long-range competing mechanism of Förster energy transfer would typically predominate. After Förster transfer from ZnSe to Ir(BPA), the resulting singlets on Ir(BPA) are expected to rapidly intersystem cross to the emitting triplet state. Based on some literature reports, Förster transfer at room temperature has actually been observed in hybrid composite systems comprising of polymer matrices doped with inorganic nanoparticles (*e.g.* ZnSe and ZnO).[57, 58] They demonstrated enhancement of the polymer matrices' photoluminescence through energy transfer from the excited inorganic dopants.

For our PL measurements, the idea of using two excitation laser sources is to discriminate the excitations of the Ir(BPA) dye dopants and the ZnSe matrix as illustrated in Figure 6.11. The site of exciton formation upon excitation is controlled to be either on the guest dopants or on the host matrix. By using a green laser for excitation, where ZnSe is transparent, we are able to excite only the Ir(BPA) molecules and observe its emission from the composites. By using a short wavelength laser, we are able to excite ZnSe since it exhibits an optical absorption band at <460 nm. Ideally, if Ir(BPA) has no absorption in the UV range, any emission coming from the Ir(BPA) molecules in the composites can then be easily accounted exclusively to Förster energy transfer from the excited ZnSe matrix. However,

Ir(BPA) does absorb at 325 nm, but the resulting dye PL emission intensity is lower than when excited at 514 nm as shown in Figure 6.12.

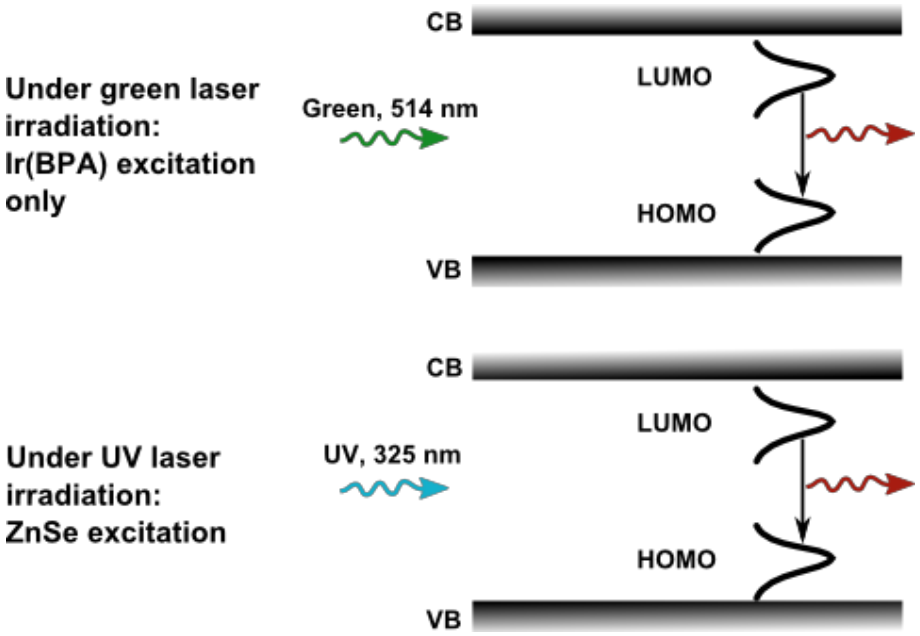

Figure 6.11: Photoluminescence measurement technique employed in this study. Using a green laser for excitation, only the Ir(BPA) molecules in the composites are excited; thereby, only the emission of Ir(BPA) would then be observed. Under UV laser irradiation, the ZnSe matrix can be excited. If the dye does not absorb in the UV region, then any emission coming from the dye can be accounted to a Förster energy transfer from ZnSe to the dye.

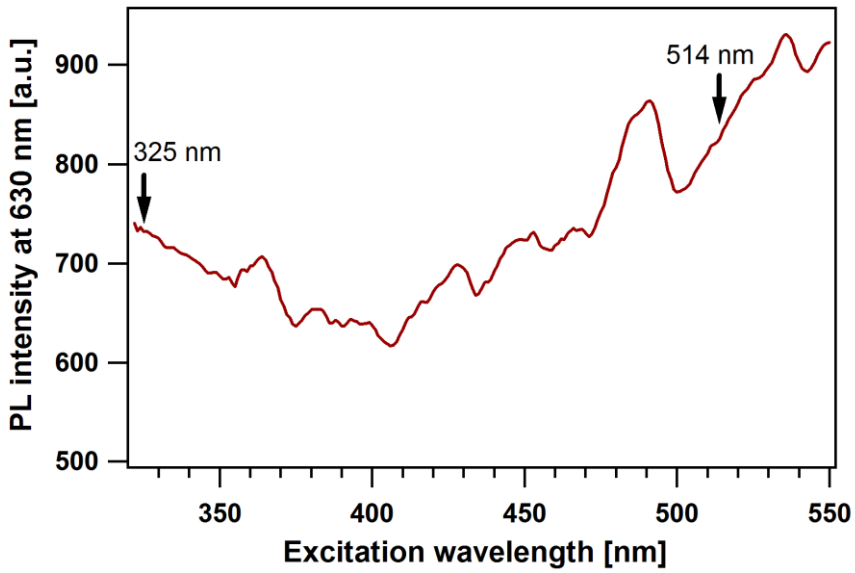

Figure 6.12: Excitation spectra of Ir(BPA) at 630 nm emission wavelength. The PL intensity of the dye under a 325 nm excitation is lower than under a 514 nm excitation.

For the photoluminescence measurements of the ZnSe+Ir(BPA) composite films, the same Raman setup as used before was utilized but with modifications to detect photoluminescence. The spectrometer was fitted with a 150 grooves/mm grating. An argon-

ion laser emitting at a wavelength of 514 nm (green) and a HeCd laser emitting at a wavelength of 325 nm (UV) were used to illuminate the film samples for excitation. Figure 6.13 shows the photoluminescence spectra obtained from thick composite films (~8 - 10 µm as compared to ~180 - 250 nm thick samples for the PES measurements) deposited on quartz glass substrates under the two laser excitations. In addition to the ZnSe+Ir(BPA) composites of 1%, 3%, 42%, 62% and 73% dye content, the spectra of pristine ZnSe and Ir(BPA) films as well as of dye molecules dissolved in toluene are displayed for comparison. The intense red luminescence of the dye is observed from all of the composite samples indicating chemical integrity of the dye molecules when co-deposited with ZnSe.

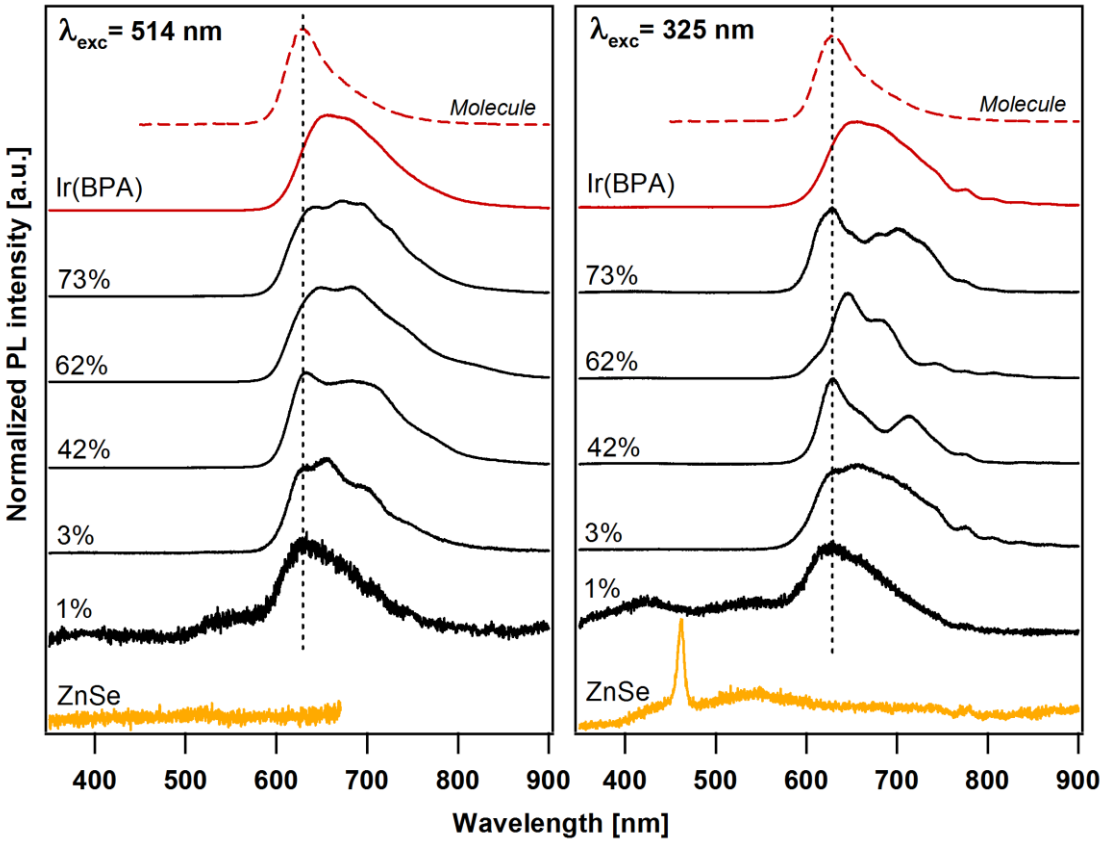

Figure 6.13: Room-temperature photoluminescence spectra of ZnSe+Ir(BPA) composite thick films deposited on quartz substrates under 514 nm (green laser) and 325 nm (UV laser) excitation together with the spectra of pristine ZnSe (bottommost) and dye (second from the top) films and dye molecules in toluene solution (topmost). All spectra are normalized to the maximum PL intensity. The dye content percentages as indicated are obtained from the integrated PL intensities of the composites relative to that of the pristine dye film. The strong red luminescence of the pristine dye is observed from all of the composite films. At 325 nm excitation, the composite films exhibit no luminescence from ZnSe.

Compared to the luminescence from dispersed molecules in toluene which has a maximum at 627 nm, the PL of the pristine dye film is red-shifted to a maximum peak at 657 nm and at 653 nm under the green and UV laser excitations, respectively. This red-shifted luminescence is generally accounted to pi-stacking.[293-295] The appearance of an additional luminescence maximum at around 627 nm for the composite films is an

indication of the presence of dispersed single molecules in the ZnSe matrix.[296] Hence, we can conclude that the PL of the composites is a superposition of contributions from singly dispersed molecules and dye molecule aggregates. The changes in the spectral lineshapes toward the longer wavelength region of the PL of the composites are attributed to contributions from optophysical and chemical interactions with the matrix environment, modified structures of the solid composite system and aggregations of the molecules in varying degrees depending on the dye content.[294, 296, 297]

With the 325 nm UV excitation, the pristine ZnSe film exhibits a PL emission at RT that peaks at ~462 nm, similar to other reports.[174, 298, 299] This sharp peak corresponds to the strong excitonic band-edge PL of ZnSe.[219, 299, 300] However, this emission is not found in the PL spectra of the composites. The absence of the ZnSe matrix PL emission could indicate an efficient Förster energy transfer to Ir(BPA), which contributes to the eventual red emission of the dye in the composites. However, any solid conclusion on energy transfer cannot be made as we cannot discriminate whether the red emission of the dye is solely from the energy transfer or from dye excitation or from both.

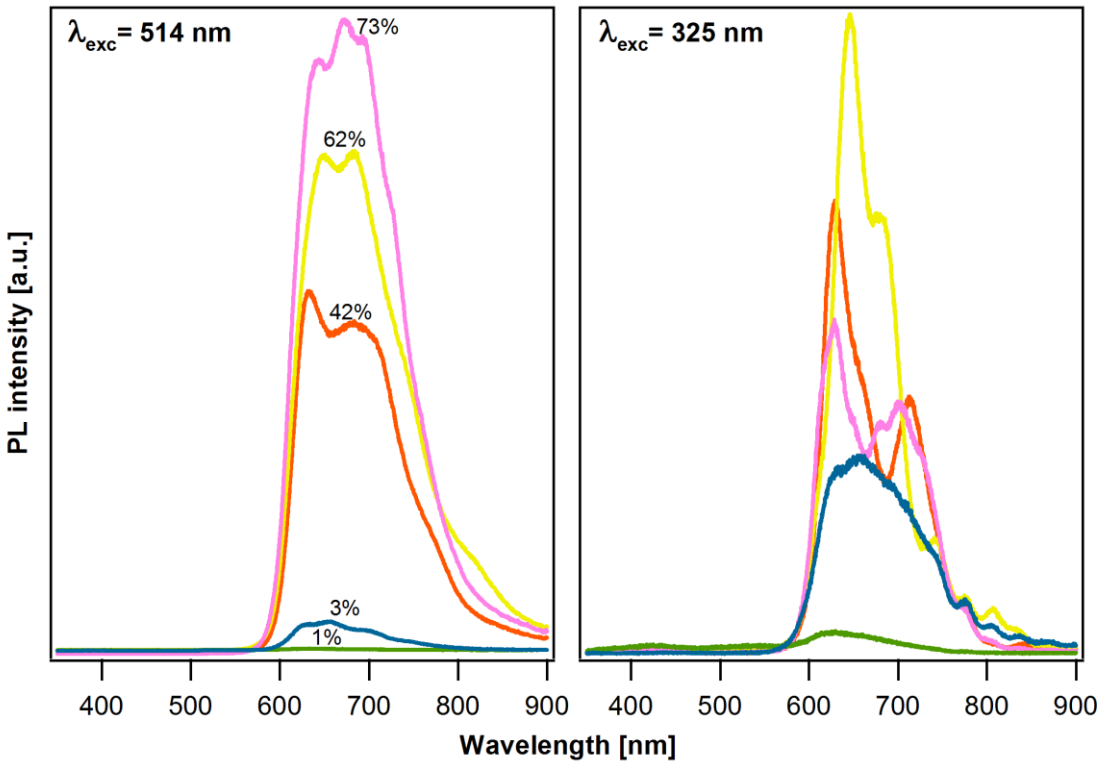

Figure 6.14: Superimposed PL spectra of the composites under the 514 nm and 325 nm laser excitation. Under the 325 nm UV laser excitation, the luminescence of the dye in the 1% and 3% composites is enhanced relative to the luminescence of the composites with the large dye content.

Figure 6.14 shows the superimposed PL spectra of the composite films under the two excitations. Comparing the PL intensities of the composites for the 514 nm and 325 nm excitations, the increase in PL intensity of the 1% and 3% composites for 325 nm excitation

relative to that of the composites with the larger dye volume percentages could possibly indicate enhancement of the dye luminescence due to the energy transfer from the excited ZnSe matrix to the embedded dye molecules. A similar relative luminescence enhancement was used to argue for a Förster resonance energy transfer at RT in P3HT + ZnSe QDs [58] and polyfluorene + ZnO nanoparticles [57] composites. The large difference in the relative intensities of the 3% and 42% composites for the 514 nm and 325 nm excitations is due to inhibited Förster energy transfer from ZnSe to Ir(BPA) in the 42% composite. As expected, any luminescence enhancement by energy transfer for composites with large dye content is impeded due to the formation of dye aggregates (confirmed from the TEM measurements, Figure 6.5). In addition, we could not expect Dexter transfer from ZnSe to Ir(BPA) due to the reactive interface (Figure 5.9), which would either hinder an efficient electron transfer or contribute to a non-radiative recombination. As this intermediate phase remains unclear in its chemical composition based on the first results obtained in this study, a quantification is not yet possible.

Chapter 7 Hybrid devices for light emission

With the experimental evidences that are described in Chapters 5 and 6, an electroluminescence (EL) from Ir(BPA) could be possible through direct charge injection or by Förster energy transfer from ZnSe to Ir(BPA). These two mechanisms could result in an EL spectrum that consists entirely of Ir(BPA) luminescence. The lineup of the HOMO and LUMO of Ir(BPA) versus the valence and conduction bands of ZnSe offers energetic driving forces for direct electron and hole transfer from ZnSe to the light-emitting Ir(BPA) as required for steady-state operation. The spectral overlap of the emission of ZnSe against the absorption of Ir(BPA) gives evidence for a possible Förster energy transfer. And as was deduced from photoluminescence measurements, efficient energy transfer can be observed in composites with low dye concentrations.

7.1 Phase I: Initial attempts on device design, fabrication and characterization

The simplest design for an organic electroluminescent device consists of an active emitter layer sandwiched between two electrode materials of dissimilar work function. When a sufficient bias is applied to the electrodes, charge carriers are injected into the active layer. These charge carriers will recombine within the active emissive layer (EML) to form excitons. The excitons may then undergo a radiative decay that gives off visible radiation or may excite other emitter molecules in the layer. The active region may be made up of organic small molecules, molecularly doped polymers or pure polymeric systems. In this study particularly, the active region is a hybrid structure composed of inorganic and organic semiconductors.

In addition to the active layer, electron (ETL) and hole (HTL) transporting layers may be inserted for a balanced transport of charges in the emitting layer. This added layers become necessary because most organic materials transport holes preferentially which causes imbalanced carrier injection in an organic EL device. Holes, in most cases, have higher mobility than electrons in organic materials. For the simplest EL device design, this shifts the recombination zone of holes and electrons close to the cathode where excitons are easily quenched.

Other layers that are commonly added as well for a state-of-the-art design are injection layers. Effective injection of charge carriers from the electrical contacts to the device is necessary to achieve a low operating voltage, which influences directly the efficiency and stability of the device. Carrier injections from the electrodes are dependent on the energy barrier heights at the interfaces between the electrodes and organic layers.[301, 302] In most OLEDs, the barrier height for holes is relatively lower than that for electrons; therefore, the injection of holes are more easy than of electrons. To achieve a balanced and effective

injection of electrons, it is common to use low work-function metals (e.g. Li, Ca, Mg). Such metals, however, are not stable in air and in some cases are reactive with and diffusing into organic materials. This eventually leads to the deterioration of the device.

In our proposed design, the active layer is a hybrid inorganic-organic EML where the inorganic matrix is responsible for charge transport and the organic dopant for light emission within the EML. For this phase of the study, though, an alternating sequence of ZnSe and Ir(BPA) layers was employed because of the challenges encountered in controlling the dye concentration during a co-deposition with ZnSe. Specifically, a nominal 5 nm thick Ir(BPA) layer that is sandwiched by thicker ZnSe layers was utilized.

The substrates used during this initial phase were unpatterned commercial ITO glass substrates where the thickness of the ITO film is 150 nm. The ITO layer serves as the anode for the device. A standard cleaning procedure with liquid solvents (acetone, ethanol, methanol and distilled water) was employed for the substrates, followed by an ozone treatment. A 45 nm layer of poly(3,4-ethylenedioxythiophene) : polystyrene sulfonate (PEDOT:PSS) was then spin-coated, covering the ITO.

On a side note, it has become a common practice to cover the ITO with a layer of the conductive polymer composite PEDOT:PSS. This was found to improve the device efficiency, lifetime and operating voltage in OLEDs.[303, 304] There are several reasons for the observed improvement. First, the thin (typically ~50 nm) layer of PEDOT:PSS smoothens the rough ITO surface; this prevents filamentary current injection leading to high local fields and short circuits in the device. Second, it is a barrier that prevents diffusion of oxygen and migration of indium from the ITO into the semiconductor. Third, it improves hole injection (as the work function of the PEDOT:PSS matches better the HOMO of the semiconductor) due to a better electronic interaction between the active layer and the anode by increasing the open circuit voltage (as PEDOT:PSS has a higher work function than ITO). Actually in this initial phase, several devices were also fabricated without the PEDOT:PSS layer. Most of our devices that do not have the PEDOT:PSS layer showed short circuits, while the others exhibited very high resistance.

For electron blocking [305] as well as hole transport [187], an N,N'-bis-(1-naphthalenyl)-N,N'-bis-phenyl-(1,1'-biphenyl)-4,4'-diamine (α-NPD) layer with a nominal thickness of 50 nm was deposited on top of the cured (at 110°C) PEDOT:PSS layer by thermal evaporation. In a literature report, α-NPD was found to be useful as a hole transporting layer together with ZnSe as the electron transporting and light-emitting layer in a blue LED hybrid structure.[187]

The alternating layers of ZnSe and Ir(BPA) for the EML were then deposited using our standard conditions. The ZnSe layers were designed to be thicker than the Ir(BPA) as ZnSe acts as the charge transporting layer to the light-emitting Ir(BPA). With regards to the light-emission from Ir(BPA), the thicker ZnSe layers will not pose a problem since ZnSe is highly transparent to the red spectral region of light. In a report on white light-emitting

diodes, the roles of ZnSe, which is sandwiched between organic layers, include ETL, HTL and EML.[306] Additionally, ZnSe can also act as a protective film to the chemically and physically delicate underlying organic films.[181]

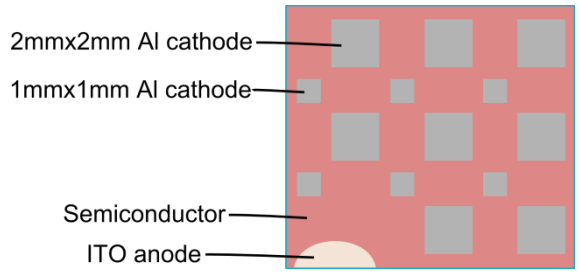

Figure 7.1: Top-view schematic picture of a sandwich-type electrode geometry for devices: the bottom-most is a glass substrate covered entirely with unpatterned ITO layer as the anode, the various semiconductor films are on top of the ITO layer, and the top-most is comprised of 8 2mm *x* 2mm and 6 1mm *x* 1mm aluminum cathode pads. This, in total, yields 14 devices with identical cross-sectional structures.

As a final step, a 150 nm layer of Al was deposited to serve as the cathode, similar to light-emitting hybrid structures with ZnSe layers [187, 306]. Al is a logical choice over Au (whose work function is around 5.1 eV) because it would result to a lower energy barrier at the ZnSe/metal interface, improving electron injection into the device. The Al electrodes were evaporated through a shadow mask, which is comprised of cut-out square patterns of sizes 2 mm x 2 mm and 1 mm x 1 mm, in an orthogonal direction to the center of the substrate. The final geometry of the device looks like the top-view schematic shown in Figure 7.1. The active area is defined by the overlap of the ITO and Al electrodes. For this geometry then, there are 14 devices in total. Contacts to each of the electrodes are made by pressing probe needles.

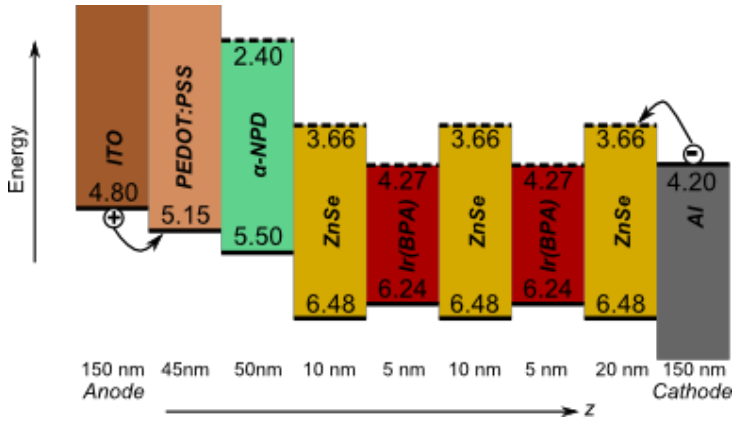

Figure 7.2: Schematic diagram of Device 2 structure together with a suggested energy-band diagram. The active layer is composed of alternating 3 ZnSe and 2 Ir(BPA) layers.

Figure 7.2 shows a schematic of the cross-section structure of a device, namely, Device 2. The EML of this device is comprised of 3 layers of ZnSe and 2 layers of Ir(BPA)

that gives an overall thickness of 50 nm. The topmost ZnSe layer was designed to be thicker since it is also to serve as a protective layer as well as to ensure that the recombination zone of the injected charge carriers is within the EML. The alignment of the energy levels between ZnSe and Ir(BPA) in the diagram was taken from the energy level lineup obtained by the PES measurements on the composites; while the alignment with the rest of the device layers were taken from literature values of the work functions of the isolated materials.

The *J*-V characteristics of two devices (labeled as Device 2C and Device 2D) from Device 2, which were generated using a two-point electrical measurement technique with probe needles, are displayed in Figure 7.3(a). The measured currents are considerably smaller than those reported in literature for a typical polymer [307] and a hybrid [45] LED, indicating a very high electrical resistance in the device.

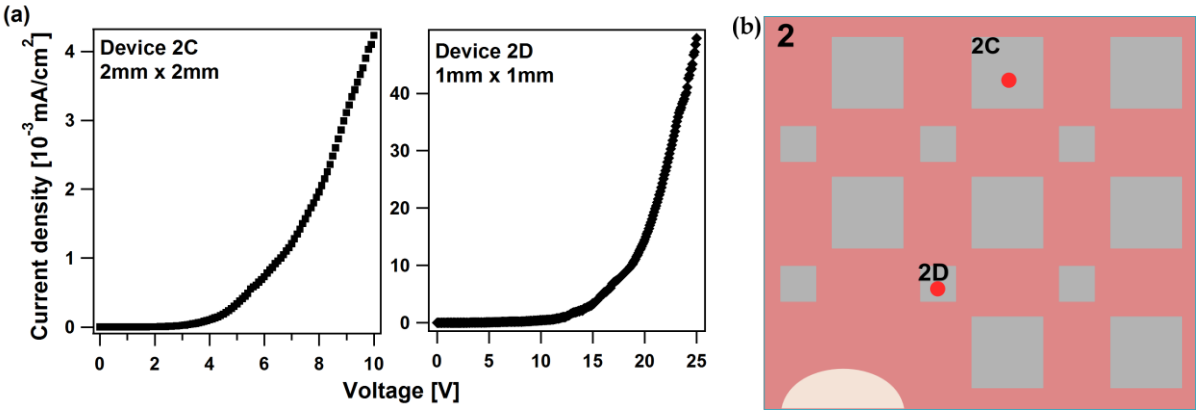

Figure 7.3: (a) Current-voltage characteristics of Device 2C (2mm x 2mm) and 2D (1mm x 1mm). (b) Top view schematic picture of Device 2 showing devices with two sizes: 2mm x 2mm and 1mm x 1mm. Device 2C and 2D emitted red sparks at the vicinity where the probe needle comes into contact with the Al cathode pad. Note that the viewpoint for luminescence is through the transparent glass backside and not through the opaque Al cathode; the red dots on the figure are just for illustration of the observed red sparks.

When the device was brought to a darkroom, a momentary spark of red EL at the vicinity of the point of contact at the cathode pad by the probe needle was observed by naked eye upon highly increased current injection, as roughly illustrated in Figure 7.3(b). A steady and lasting EL was not observed, thereby, forfeiting all possibilities of obtaining the EL spectrum. The observed red sparks could only come from the Ir(BPA) layers since the other semiconductor layers of the device do not emit in this spectral region (i.e., α-NPD emits strong PL and EL at ~430 nm [45] and PEDOT:PSS exhibits weak PL peaks at 380 nm, 416 nm, ~460 nm, and ~505 nm [308, 309]).

Figure 7.4 is a schematic of the cross-section structure of another device, namely Device 3. The EML of this device consists of two layers of ZnSe that sandwiches a single layer of Ir(BPA). The overall thickness of the EML is nominally 30 nm, which is thinner than the 50 nm thick EML of Device 2.

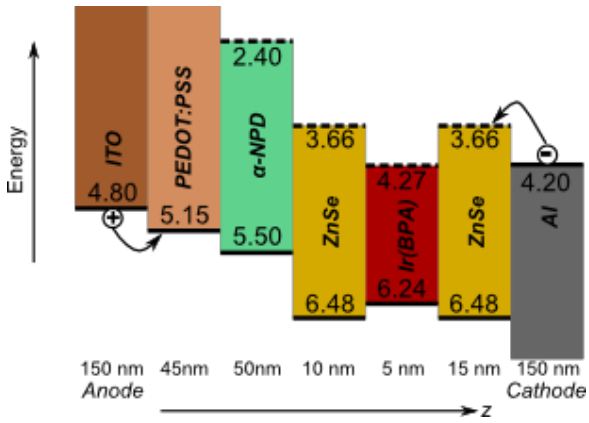

Figure 7.4: Schematic diagram of Device 3 structure together with a suggested energy-band diagram. The active layer is composed of alternating 2 ZnSe and 1 Ir(BPA) layers.

For Device 3, the electrical properties are remarkably improved compared to Device 2 as evidenced by the increased current densities shown in Figure 7.5(a). These *J*-V characteristics of Device 3E and Device 3F are comparable to those reported.[45, 307] Similar to Device 2, red sparks were also observed from the devices (Figure 7.5(b)) around the points of contact of the needle probe to the Al cathode pad.

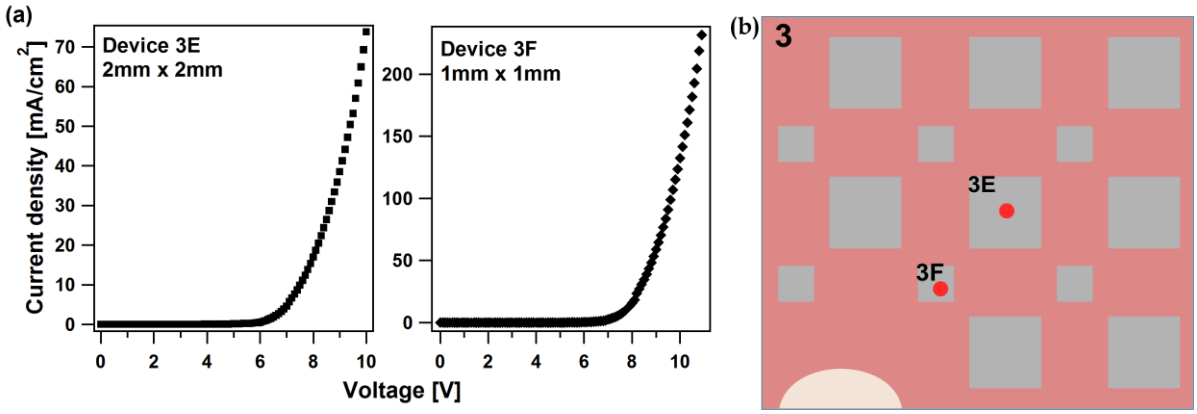

Figure 7.5: (a) Current-voltage characteristics of Device 3E (2mm x 2mm) and 3F (1mm x 1mm). (b) Top view schematic picture of Device 3 showing devices with two sizes: 2mm x 2mm and 1mm x 1mm. Device 3E and 3F emitted red sparks at the vicinity where the probe needle comes into contact with the Al cathode pad. Note that the viewpoint for luminescence is through the transparent glass backside and not through the opaque Al cathode; the red dots on the figure are just for illustration of the observed red sparks.

The better electrical characteristics of Device 3 as compared to Device 2 can be accounted to the thinner EML, which has a smaller amount of the non-conductive Ir(BPA) dye. Also, the lower number of alternating layers reduces the number of Ir(BPA)/ZnSe interfaces. As was determined in the PES measurement of the Ir(BPA)/ZnSe interface, a reactive interface, which also contains an amorphous Se^0 phase, is present at the phase boundary. This phase has an electrical conductivity that is negligible in the dark, but can be of some value when exposed to visible light. Intercalation of Zn atoms into the Ir(BPA) layer

was also deduced from the interface experiment. The intercalated Zn atoms pose potential non-radiative recombination sites for the injected charge carriers.

7.2 Phase II: Final attempts on device design, fabrication and characterization

A different approach on device fabrication, which is partially based on a protocol developed by the TUD - Electronic Materials research group, was followed in this phase of the study. Polished glass substrates with an OLED-grade, patterned ITO were utilized. The thickness of the ITO is 150 nm. The top-view geometry of this substrate is shown in Figure 7.6.

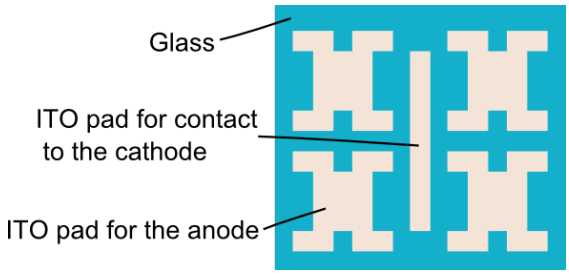

Figure 7.6: OLED grade, patterned ITO on glass substrate. This design yields 4 devices. The ITO strip located at the middle of the substrate is for contacting the cathode.

Four devices can be fabricated simultaneously from this type of substrate. The design of the substrate could possibly resolve some issues posed by the unpatterned ITO substrate. One disadvantage with the unpatterned ITO glass substrate is that the sheet resistance of ITO would imply that not all devices on the substrate are at the same potentials so that the actual voltage drop across the devices is not well-defined. The patterning of the ITO is such that each device is contacted separately and with the same geometry, so that the potential drop across the four devices on the substrate is identical. Another disadvantage of the unpatterned ITO is in the two-point electrical measurement technique where one of the probe needles comes into direct contact at a singular point on the cathode pad. This could result to a strong electric field at the point of contact right on top of the active area of the device. With an isolated point of contact to the cathode in a patterned ITO substrate, a homogenous electrical field across the entire device active area can be achieved.

After a rigorous cleaning of the substrates, the same semiconductor layers as in the initial phase were sequentially deposited. The ITO anode was contacted after scratching away some of the semiconductor layers covering the pad. Prior to the deposition of the cathode materials, the semiconductor layers covering top of the ITO pad for contact to the cathode were scratched away as well. Through a shadow mask, a 70 nm Ca layer was deposited followed by a 100 nm Al layer. A Ca/Al bilayer cathode had actually been found to exhibit improved electron injection against bare Al cathode.[310] Figure 7.7(b) and

Figure 7.9(b) represent a top-view schematic picture of the final device configuration. The dashed rectangles define the active regions for the four devices in this configuration.

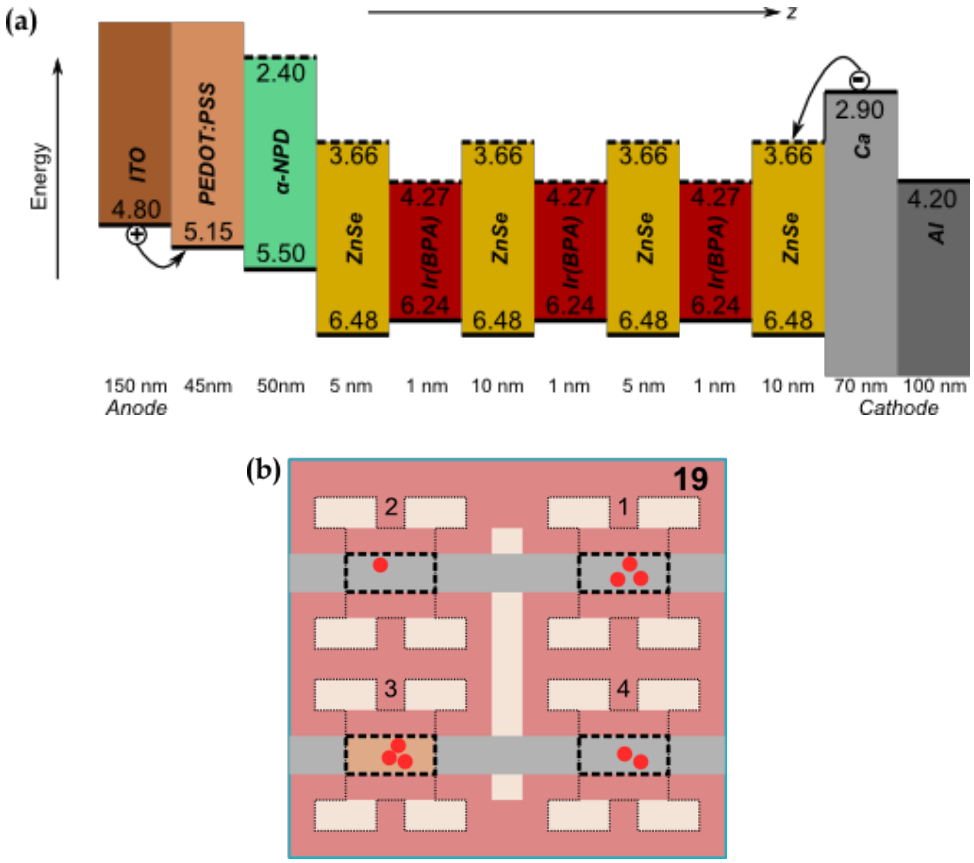

Figure 7.7: (a) Schematic diagram of Device 19 structure together with a suggested energy-band diagram. The active layer is composed of alternating 4 ZnSe and 3 Ir(BPA) layers. (b) Top-view schematic picture showing 4 devices on one substrate. The active regions of the devices are defined by the dashed rectangles. All of the devices emitted several weak red sparks that lasted as long as the applied current did not finally burn up the devices. Device 19-3 actually exhibited a weak areal emission of pale orange tint. Note that the viewpoint for luminescence is through the transparent glass backside and not through the opaque cathode; the red dots on the figure are just for illustration of the observed red sparks.

Figure 7.7(a) shows the cross-section structure and suggested energy-band diagram of a device, namely, Device 19, whose 33 nm thick EML is comprised of 4 alternating ZnSe layers that sandwich 3 Ir(BPA) layers. The thickness of the Ir(BPA) layers was set to 1 nm this time in order to ensure that approximately only a monolayer of dye is deposited. Having only a monolayer (or less) of dye would increase the physical contact of each individual dye molecule to ZnSe, which could lead to improved charge carrier injection from ZnSe to the dye as well as Förster energy transfer. The device would also benefit from the presence of pinholes within the Ir(BPA) layers since it will ensure the flow of charge carriers throughout the length of the EML.

All four devices of Device 19 emitted scattered red sparks upon current injection, as roughly depicted in Figure 7.7(b). Device 19-3, in particular, exhibited a very dim (but still distinguishable by the naked eye in a darkroom) areal emission of a pale orange tint. The

intensity of the emission was, apparently, not enough to be able to measure a reliable EL spectrum. However, evidence of the emission is found from the photocurrent generated by a silicon photodiode placed underneath the device during the recording of the device's current-voltage characteristics by a HP4155A semiconductor parameter analyzer. The *J*-V characteristics of the device, together with the corresponding photocurrent generated in the photodiode, are depicted in Figure 7.8. From the trend of the *J*-V curve, the device does not exhibit a highly rectifying behavior.

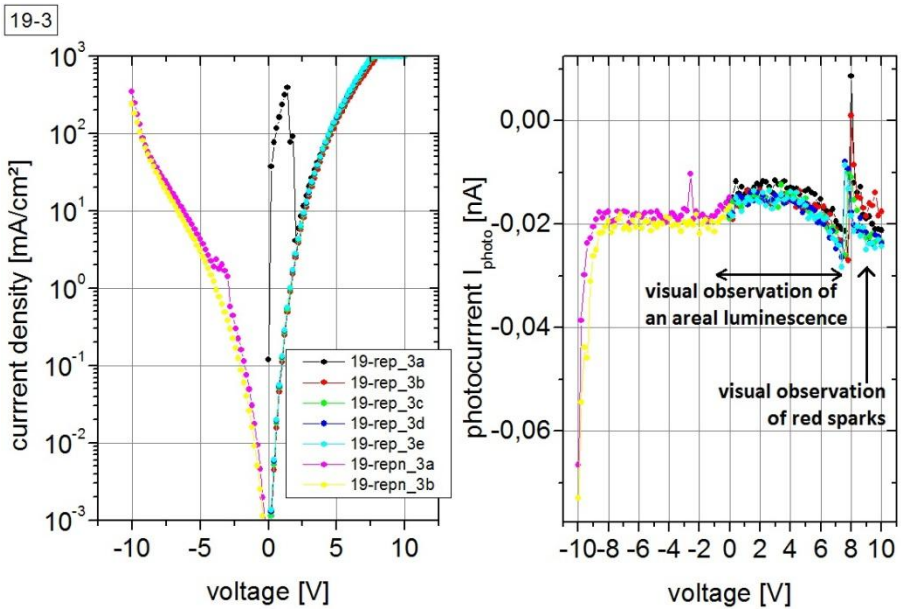

Figure 7.8: Current density versus applied (reverse and forward) voltage for Device 19-3. The photocurrents generated on a silicon photodiode against the applied voltage on the device are plotted here as well.

The areal luminescence was observed visually at low applied forward biases. Correlating this actual observation to the trend found in the generated photocurrent, this corresponds well to the broad feature found at the low forward voltage region of the spectra. When the voltage was increased further, the areal luminescence vanished and red sparks started to appear. The red sparks most likely correspond to the erratic peaks at the high voltage end of the spectra. Similarly for devices 19-1, 19-2 and 19-4, erratic photocurrent peaks were observed as well together with the red sparks. The current-voltage characteristics of these devices and the corresponding generated photocurrents at the photodiodes are itemized in Appendix D.

A device with a 34 nm thick EML consisting of 5 ZnSe layers that sandwich 4 Ir(BPA) layers was also fabricated. Figure 7.9(a) gives an illustration of the cross-section structure of this device, namely, Device 21. The EML thickness of Device 21 negligibly differs from that of Device 19; however, it has an additional layer of ZnSe and of Ir(BPA).

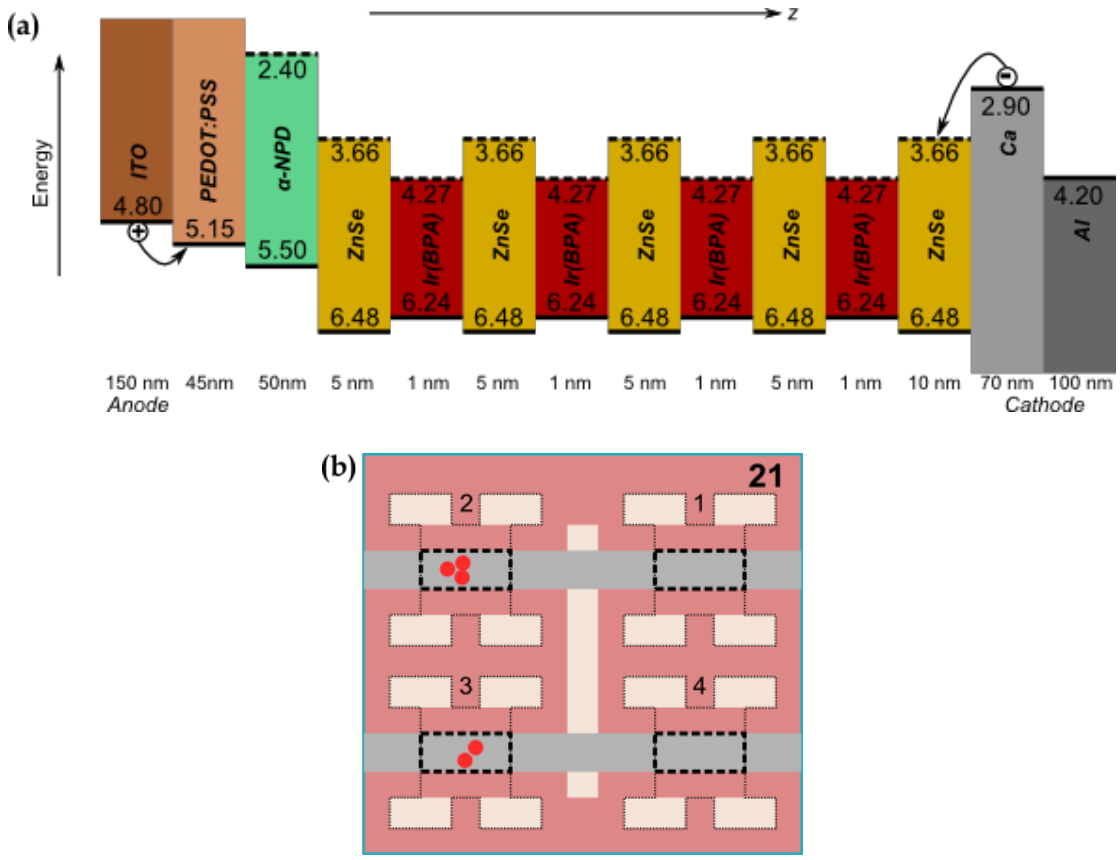

Figure 7.9: (a) Schematic diagram of Device 21 structure together with a suggested energy-band diagram. The active layer is composed of alternating 5 ZnSe and 4 Ir(BPA) layers. (b) Top-view schematic picture showing the 4 devices for this substrate. Two of the devices emitted several weak red sparks that lasted as long as the applied current did not finally burn up the devices.

Two devices of Device 21 emitted red sparks when voltage was applied, as depicted in Figure 7.9(b). The current-voltage characteristics of Device 21-3, together with the generated photocurrent on a silicon photodiode positioned under it, are shown in Figure 7.10. The rectifying behavior of the device is also not remarkable. Correlating the visual observations to the measured photocurrent, the red sparks would likely correspond to the photocurrent peaks. Such a correlation could be quite sensible since devices 21-1 and 21-4, where red sparks were not seen, did not result at all to photocurrent peaks at the photodiode (Appendix D). The presence of the sharp photocurrent peaks for devices 21-2 (Appendix D) and 21-3 in both the reverse and forward biased conditions is another indication of the non-remarkable rectifying property of these devices.

From the visual observations made on Device 19 and Device 21, the former appears to perform better than the latter. In terms of the EML thickness, the two devices are practically similar. The discrepancy in their performances could be accounted, therefore, only to the increase in the number of Ir(BPA) layers and Ir(BPA)/ZnSe interfaces.

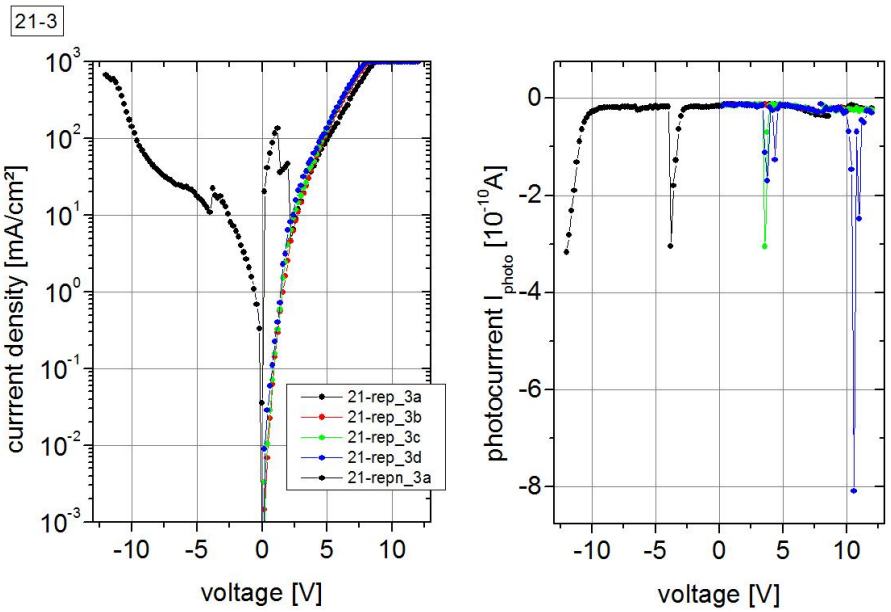

Figure 7.10: Current density versus applied (reverse and forward) voltage for Device 21-3. The photocurrent generated on a silicon photodiode against the applied voltage on the device are plotted here as well.

Practically, the roughness of the resulting layers probably is one factor which contributed greatly to the performance demise of our fabricated devices. Specifically, the high roughness could have originated from the ZnSe layers. Its surface roughness is made obvious in the AFM image shown in Figure 7.11 of an as-deposited 300 nm thick ZnSe film on ITO. A rough ZnSe surface leads to imbalanced internal electric field distributions in the device. The red sparks exhibited by Devices 19 and 21 could have been from parts where the electric fields were the highest.

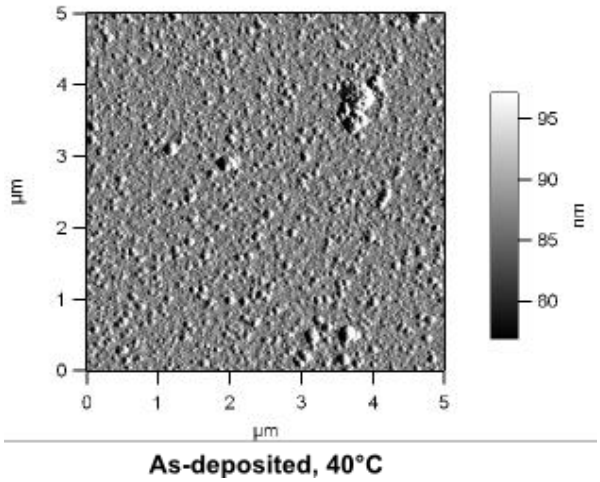

Figure 7.11: AFM image of the surface of a ~300 nm thick ZnSe film grown on an ITO glass substrate revealing a high roughness of the surface.

As far as this study could possibly go, no steadily working device has been achieved. Nevertheless, the proposed hybrid concept have been proven to be feasible as evidenced by

the red sparks of emission that were visually observed from the devices. A working device might be achieved by improving the quality of the EML. A composite structure for the EML by co-deposition of ZnSe and Ir(BPA) could eliminate the high surface roughness that is generated by ZnSe layers in an alternating layer structure. Furthermore, there remains the need to identify inorganic semiconductor - organic dye combinations that are less reactive at the interfaces in vacuum processing or that may be deposited by less reactive conditions such as wet chemical processing.

Chapter 8 ZnO - Ir(BPA) system

The material combination comprising of zinc oxide (ZnO) and the organic light emitter Ir(BPA) was also investigated. For a Förster energy transfer to Ir(BPA) from ZnO, this material combination definitely has promising potential because the emission spectrum of ZnO [44, 45, 47, 311, 312] overlaps significantly with the absorption spectrum of Ir(BPA). However, for a possible compatibility of this material combination to our proposed inorganic-organic emissive layer design, the alignment of the energy levels of ZnO and Ir(BPA) has to be determined whether it adapts or not to the scheme presented in Figure 1.5(b). For a charge transfer from ZnO to an embedded dye molecule in the emissive layer of a device, the alignment of the valence and conduction bands of ZnO to the HOMO and LUMO of Ir(BPA) must be able to provide the necessary driving forces. PES measurements on the ZnO/Ir(BPA) interface were performed, and the results are presented in this chapter.

8.1 ZnO

Transparent conducting oxides (TCOs) have for long been a subject of various investigations due to their unique physical properties and applications in commercial devices. Amongst the popular TCOs is zinc oxide (ZnO), which belongs to the II-VI semiconductor group as ZnSe. It is an environmentally friendly material and it is produced at low temperatures. ZnO is attractive for UV light emission because it has both a wide direct band gap of 3.37 eV and a very large free-exciton binding energy of 60 meV, which makes excitonic emission processes persist at or even above room temperature.[313] Due to an abundance of intrinsic defects in its lattice (e.g., O vacancies and Zn interstitials) and the presence of unintentionally incorporated impurities (e.g., substitutional and interstitial H, as hydrogen is present in almost all growth and processing environments [313, 314]), ZnO is natively strongly *n*-type doped. Up to now, there is still the lack of control over its electrical conductivity, which hinders the full potential of ZnO for use in electronic devices.

ZnO has several other favorable properties like good optical transparency to visible light, high electron mobility, and strong room-temperature (RT) luminescence. The typically observed PL emission of ZnO has two significant peaks: a strong, narrow UV peak (around 380 nm) due to near band-edge (NBE) excitonic emission and a broad visible peak (in the range 450 to 750 nm) associated with deep level emissions (DLEs).[44, 45, 47, 311, 312] This emission range of ZnO clearly overlaps with the absorption of the Ir(BPA) dye (Figure 4.16), making Förster energy transfer from ZnO to Ir(BPA) viable. In line with this, energy transfers from ZnO to organic semiconductors at RT have already been observed.[57, 80]

The integration of ZnO and organic semiconductors into hybrid structures for light emission is actually popular in many studies because of the difficulty of *p*-type doping of

ZnO to obtain a ZnO *p*-*n* homojunction LED. As alternative approaches to ZnO-based LEDs, the *n*-type ZnO has been combined with organic semiconductors with *p*-type conductivity to substitute for *p*-type ZnO.[42-47]

8.1.1 Deposition of ZnO thin films

ZnO films were obtained through the low-pressure chemical vapor deposition (CVD) technique. The deposition chamber that was utilized is part of the DAISY-SOL integrated system. CVD is known for its capability for growth of high-quality epitaxial thin films in the semiconductor industry. It is considered to be a suitable technique to grow high-quality ZnO and to realize the full potential of ZnO materials.

In the technique that was followed, the deposition of ZnO occurred as a result of chemical reactions of vapor phase precursors on a heated 120 nm thick ITO glass substrate. H_2O and dimethyl zinc (DMZ) were used as the oxygenic and zinc precursors, respectively. DMZ is a favored zinc precursor because it has a low decomposition temperature and a high metal organic vapor pressure. DMZ reacts readily with H_2O through the following mechanism:

$$Zn(CH_3)_2* + H_2O(g) \rightarrow ZnO* + 2CH_4(g),$$

Equation 8-1

where * denotes a surface species. The reaction of DMZ with water is quite exothermic such that it can be exploited to deposit ZnO thin films at low temperatures (80 - 150°C).[315, 316] In the performed depositions, vapors of DMZ (0.0015 mbar) and H_2O (0.0030 mbar) were simultaneously introduced into the chamber. The deposition rate was found to be dependent on the substrate temperature; and for the set substrate temperature range of 130 - 140°C, the deposition rate was ~10 nm/min.

8.1.2 Crystal structure of the ZnO film

The compound ZnO can crystallize in the wurtzite, zincblende or rocksalt structure. But the wurtzite structure is the most common because it is thermodynamically more stable under ambient conditions.[317] This structure has a hexagonal unit cell with two lattice parameters *a* and *c*. A schematic representation of the wurtzitic ZnO structure is shown in Figure 8.1.

The crystal structure and orientation of our as-deposited ZnO film on ITO glass substrate were determined from the XRD pattern shown in Figure 8.2. It can be seen that several peaks – (002), (101), (110) and (201) – appear together with the preferential (100) orientation peak, indicating a polycrystalline nature.[318] All these reflection peaks coincide well with the hexagonal wurtzite structure, revealing a ZnO that is single-phased.[319] Aside from the peaks coming from the ITO substrate and the gold coating[54] on top of the ZnO film, there are no other peaks to indicate impurities. The appearance of the (111) and

[54] The ZnO film was sputter-coated with a thin layer of gold for the SEM measurement.

(200) planes of the face-centered cubic gold proves the formation of a crystalline Au on the ZnO film.

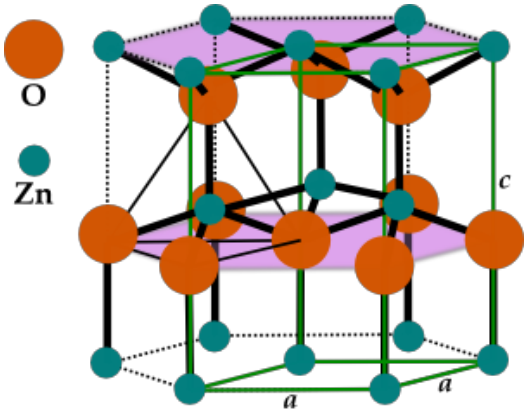

Figure 8.1: Hexagonal wurtzite structure of a ZnO crystal.

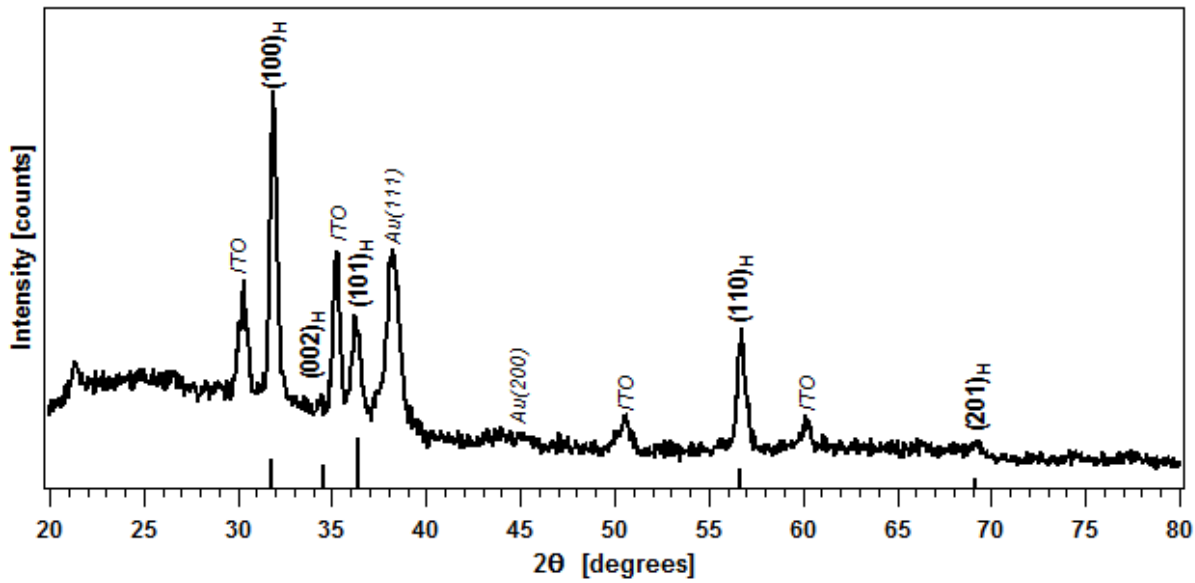

Figure 8.2: XRD spectra of a ZnO film deposited on ITO glass substrate along with bar markings on the *x*-axis for ZnO reflection peaks from the JCPDS [55] database.

8.1.3 Surface morphology of the ZnO film

Surface topology images, which were obtained by a scanning electron microscope, of the as-deposited ZnO film are shown in Figure 8.3. A uniformly rough surface is obtained with grain sizes (considering the longest dimension) that range from 70 – 300 nm. The rough surface is actually desirable for a solar energy application because it allows the light that enters into the solar cell through the oxide layer to scatter efficiently in order to enhance the absorption. However, such a rough surface could be detrimental for a HLED application. The high, non-uniform electric fields that are created by a rough surface can cause electrical

[55] JCPDS: Joint Committee on Powder Diffraction Standards

shorts, as well as degradation and dark spot (i.e. the non-emissive portion of the organic layer in the case of layered device design) formation [320]. Therefore, if the roughness is low and the surface is flat, then it is possible to incorporate it to an HLED device.[45, 52, 53]

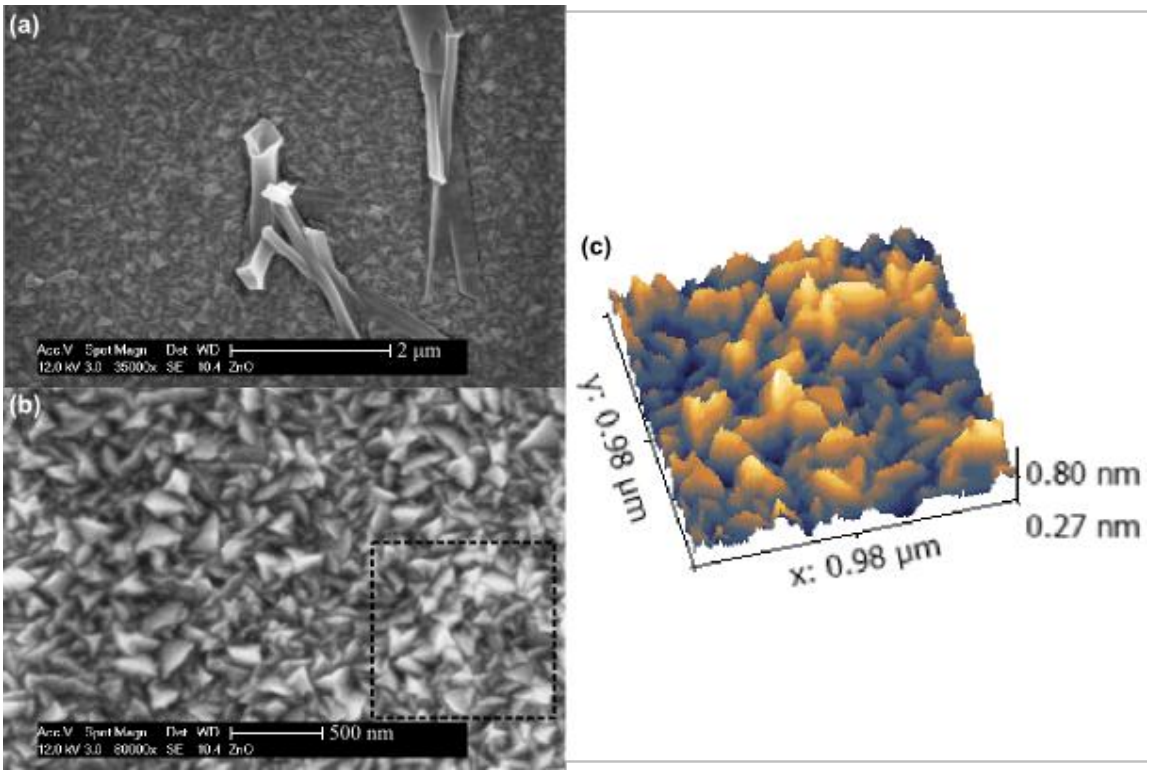

Figure 8.3: SEM images of the surface of the ZnO film with low (a) and high (b) magnifications, together with a pseudo 3D representation (c) of the area within the box in (b).

From the 3D version[56] (Figure 8.3(c)) of a portion of the SEM image shown in Figure 8.3(b), the majority of the grains seen on the surface are polygon-shaped which looks similar to other reports in literature.[318, 321-324] The polygon shape of the grains as observed on the SEM image confirms the (100)-preferred orientation seen on the XRD pattern.

Figure 8.4 gives an illustration of some of the crystal orientations for the hexagonal wurtzite ZnO and their relationship to the microstructures that can be observed from top-surface images. Correlating the surface morphology to the obtained X-ray diffraction pattern, the upright columnar *c*-plane crystal orientation (which is the most clearly distinguishable orientation for ZnO) is in fact barely observable in both the SEM image of the surface and the diffractogram.

[56] To obtain a 3D version of SEM images, it is possible to utilize the Gwyddion software which is a free platform for visualization and analysis of data from the different scanning probe microscopy techniques. However, recorded values on the z-axis would lack accuracy and precision. A roughness estimate would, thereby, be not reliable.

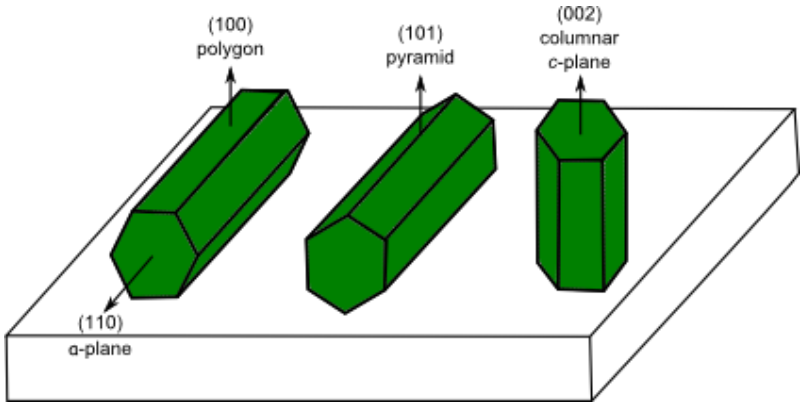

Figure 8.4: The hexagonal wurtzite microstructures of ZnO on a substrate together with their corresponding crystal growth orientations.

8.1.4 Absorption spectrum and the optical bandgap of the ZnO film

The optical property of an as-deposited ZnO film was studied by transmission measurement at room temperature in the spectral range from 300 to 800 nm. The transmission spectrum is shown in Figure 8.5.

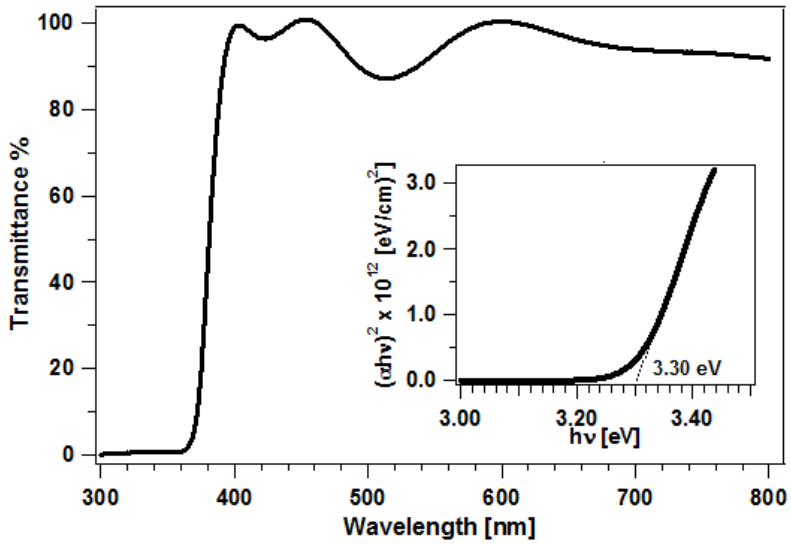

Figure 8.5: Transmission spectrum of the ZnO film deposited on an ITO glass substrate that exhibits a sharp optical absorption edge. Inset: An optical bandgap of 3.30 eV is derived from the plot of $(\alpha h\nu)^2$ versus $h\nu$ of the ZnO film.

The sharp optical absorption edge indicates a high degree of crystallinity for the ZnO film. Due to thin film interference, an oscillatory pattern is seen below the bandgap (i.e. at longer wavelengths) of ZnO. From the pattern, a film thickness of 270 nm (nominal value is 250 nm) is calculated using the method described in Chapter 3.2. Above the bandgap, no interference occurs due to the high absorption coefficient of ZnO in this region.

Absorption coefficients have been evaluated using the transmittance data and the ZnO film thickness. The plot of $(\alpha h\nu)^2$ versus $h\nu$ is then obtained and shown in the inset of Figure 8.5. Through a linear extrapolation to the x-intercept in the graph, the optical band

gap of the ZnO film is obtained to be 3.30 eV. This energy gap value is the same as the value reported from IPES and PES measurements.[325]

8.1.5 Electronic structure of ZnO investigated by PES

A nominal 100 nm thick ZnO film was deposited on ITO glass substrate. Visually, the film was clear, smooth, and transparent; and at certain angles, the film gives off a green color. The green color of ZnO is associated with certain concentration levels of oxygen vacancies.[326] PES measurements were then performed on this as-deposited film to obtain its electronic structure. The deposition and PES measurements were performed *in situ* using the DAISY-SOL in Darmstadt.

PES of the as-deposited ZnO film on ITO glass substrate

The XPS survey and detailed core level spectra together with the UPS SE cutoff and valence band spectra taken from the film are shown in Figure 8.6.

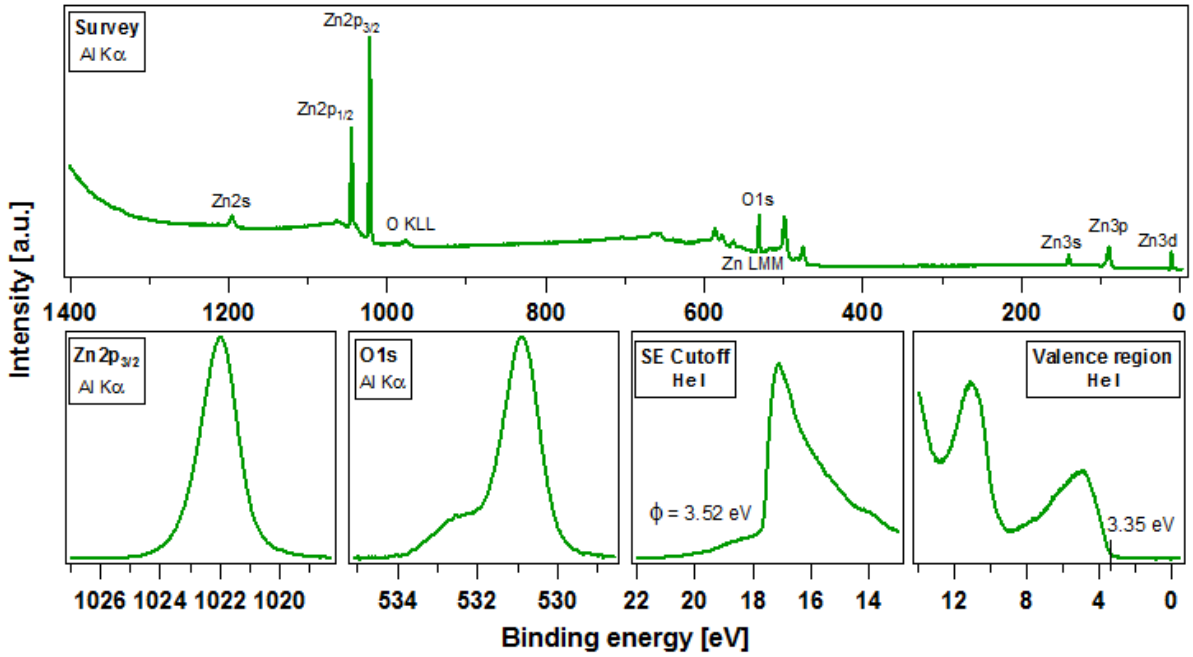

Figure 8.6: A survey spectrum showing all the peak photoemissions that are representative of the elemental composition of the as-deposited ZnO film on ITO glass substrate, together with the detailed spectra of $Zn2p_{3/2}$, O1s, SE cutoff region and the valence band. From the SE cutoff, ϕ is determined to be 3.52 eV. The VBM is located at 3.35 eV from the Fermi level.

In the XPS survey spectrum, all the ZnO characteristic photoemissions are designated. With no traces of contamination and substrate photoemissions found, a clean deposition and a thick enough film with the absence of pinholes are indicated, respectively. The most intense photoemission lines which are representative of the elements present in the compound (i.e. Zn and O) originate from the $Zn2p_{3/2}$ and O1s core levels. The detailed spectra of these core levels are also shown in Figure 8.6. After performing Shirley background subtraction and spectral fitting, the binding energy of $Zn2p_{3/2}$ is determined to

be ~1022 eV and the O1s peak binding energy to be ~530.9 eV, both corresponding well to literature values.[85, 312, 327-329] The asymmetric shape of the O1s emission spectrum reveals oxygen species at higher binding energies.[85, 312, 328-331] This is not unexpected because of the O vacancy native defect of ZnO, OH adsorbates and the deposition process-related unintentional H impurities that are bonded to the O of ZnO.

With a He I excitation (UV, $h\nu = 21.22$ eV), the SE cutoff and valence region spectra are obtained and also displayed in Figure 8.6. The lineshape of the valence region is confirmed in correspondence to literature.[80, 85, 328, 332] From the SE cutoff, the work function (ϕ) of the as-deposited ZnO film is derived to be 3.52 eV. This work function is smaller than reported values.[80, 85, 328, 332] From the valence region spectrum, (E_{VBM}-E_F) is derived, which is the position of the VBM from the Fermi level position at 0 eV, as 3.35 eV.

PES of the annealed ZnO film on ITO glass substrate

The as-deposited ZnO film sample was taken out of the DAISY-SOL and quickly transferred to the DAISY-MAT UHV system. The film was then subjected to annealing at 400°C in an O_2 atmosphere for 1 hour [85] in an oxide sample preparation chamber. PES measurements were performed and the obtained photoemission spectra are displayed in Figure 8.7.

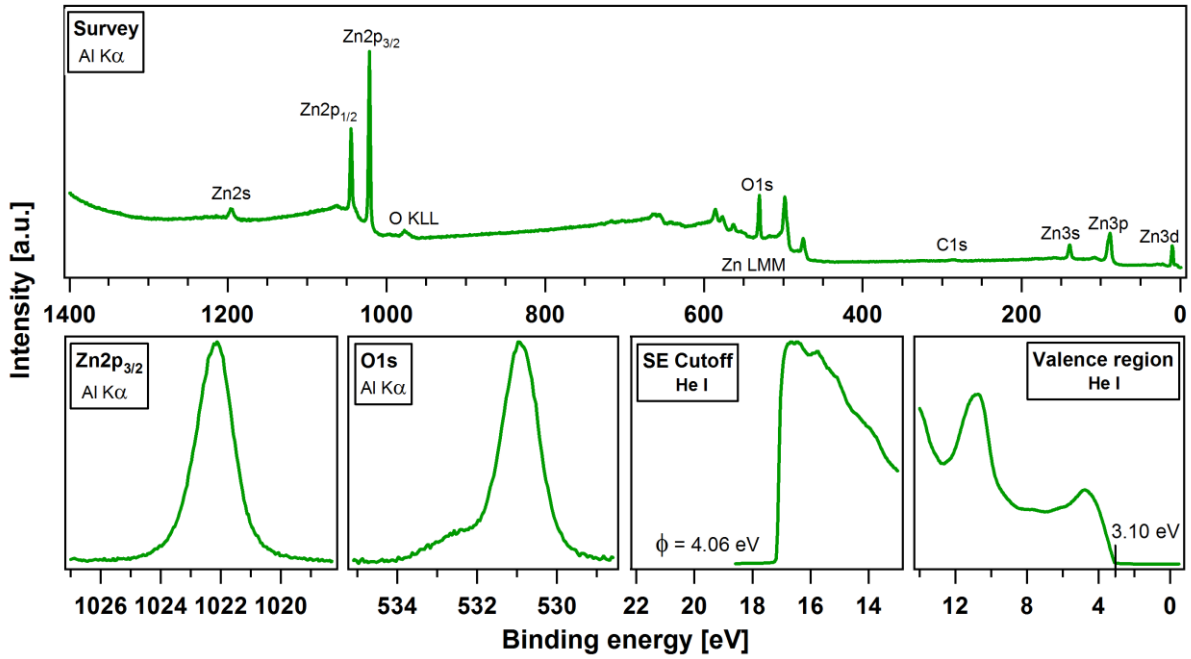

Figure 8.7: A survey spectrum showing all the peak photoemissions that are representative of the elemental composition of the annealed ZnO film deposited on ITO glass substrate, together with the detailed spectra of $Zn2p_{3/2}$, O1s, SE cutoff region and the valence region. From the SE cutoff, ϕ is determined to be 4.06 eV. The VBM is at 3.10 eV from the Fermi level.

From the XPS survey spectrum, it can be seen that there is a slight degree of carbon contamination afterwards. This most likely came from the exposure of the sample to ambient environment during the sample transfer, and was not completely removed by the

annealing. The rest of the peaks which can be found in the spectrum correspond to the photoemission peaks that are characteristic to ZnO.

The XPS detailed spectra of the $Zn2p_{3/2}$ and O1s emissions are also shown in Figure 8.7. No change in the $Zn2p_{3/2}$ emission of the annealed film was observed. However, the annealing does have a clear influence on oxygen as observed from the reduced intensity of the high binding energy oxygen species in the O1s spectrum.

From the SE cutoff spectra shown in Figure 8.7, the work function of the annealed ZnO film increased to 4.06 eV. At the same time, the VBM of the film shifted to 3.10 eV from the Fermi level.

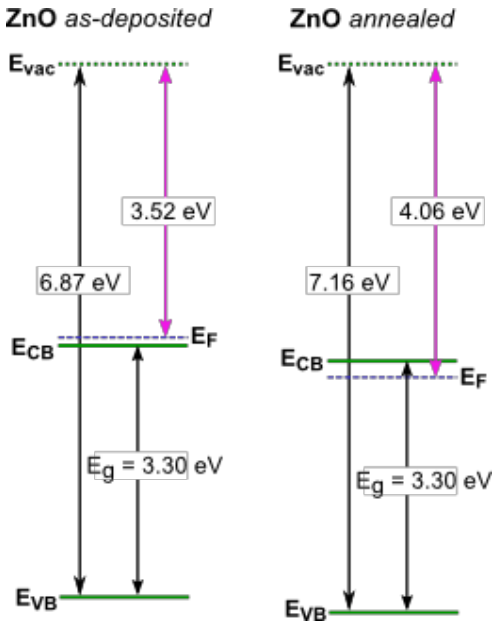

Figure 8.8: Energy levels of the as-deposited and annealed ZnO as deduced from the UPS measurements. The 3.30 eV energy gap is taken from the optical transmission measurement. The ionization potential and the work function of ZnO increased when annealed, approaching literature values.

From the UPS derived values for ϕ and (E_{VBM}-E_F), the electronic structure of the as-deposited ZnO film is drawn in Figure 8.8, together with its electronic structure after annealing. Several changes are observed: the ionization potential and ϕ increased, and the Fermi level shifted. Compared to other semiconductors, ZnO has a very high ionization potential. The ionization potential of our ZnO film after the annealing step approaches the typical values reported in literature for ZnO (7.15 - 7.9 eV).[204] In undoped ZnO crystals (which are natively *n*-type), the Fermi level generally lies 0.2 eV below the conduction band minimum (CBM).[332] From our results, the annealing process shifted the Fermi level from 0.05 eV above the CBM to 0.2 eV below the CBM in agreement with literature. This shift could be associated with a redistribution of oxygen-derived states at the valence band maximum [332] and the reduction of impurities (e.g. substitutional and interstitial H) that act as shallow donors [313, 314, 333]. The annealing step performed here definitely improved the quality of our as-deposited film.

Peak fitting analysis was performed on the O1s spectra of the ZnO film. The spectral fits are shown in Figure 8.9. A good fit is obtained using the three Voigt profiles labeled as O_I, O_{II} and O_{III} species. The binding energy positions of these three species approximate well the results reported in literature.[334-336] The O_I species at the low binding energy of 530.9 eV are the O^{2-} ions on the wurtzite structure of the hexagonal Zn^{2+} ion array, which are surrounded by zinc atoms with the full supplement of nearest-neighbor O^{2-} ions. In other words, the O_I species is attributed to the Zn-O bonds. The O_{II} species with a medium binding energy centered at around 531.4 eV are the O^{2-} ions that are in oxygen-deficient regions within the ZnO matrix. As a result, changes in the intensity of this component may be in connection with the variations of the concentration of oxygen vacancies (V_O). The high binding energy species, O_{III}, centered at 532.5 eV are usually attributed to chemisorbed or dissociated oxygen or OH species on the surface of the ZnO film, such as -CO_3, adsorbed H_2O or adsorbed O_2.[330, 331, 334-340]

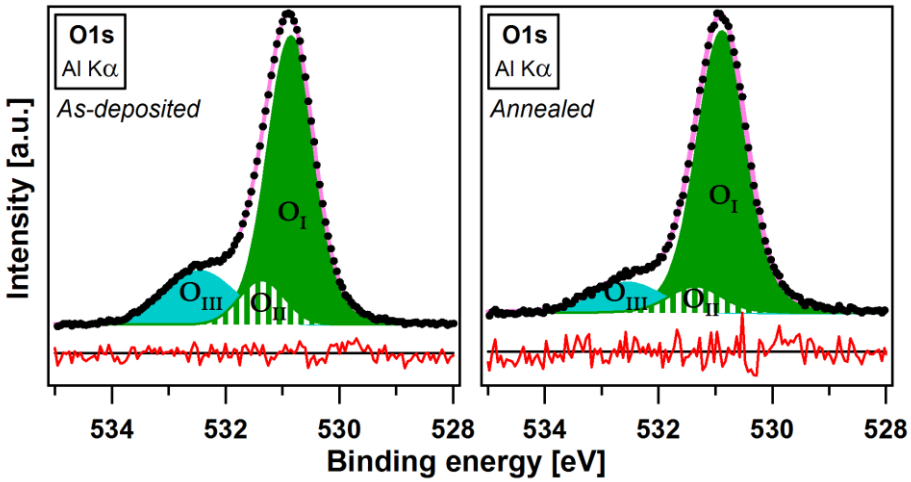

Figure 8.9: Spectral fits of the O1s emissions of the as-deposited and annealed ZnO films showing three oxygen species. The photoemission contributions of the higher binding energy O_{II} and O_{III} species are reduced upon annealing.

Comparing the O1s emission spectral fits of the as-deposited and annealed film, the annealed film exhibits a decrease in the photoemission intensity of O_{II} and O_{III} species. At the same time, the intensity ratio of the O_I species O1s emission to the $Zn2p_{3/2}$ emission (both normalized to their respective atomic sensitivity factors (ASF)) improved from 0.89 to 0.91, approaching a better stoichiometry. This O:Zn ratio for ZnO is actually quite good in reference to literature reports.[312, 329-331, 334, 335, 340]

Additionally, the 1-hour annealing at 400°C did not fully eliminate the O_{III} species since not all -OH species are generally found on the immediate surface. The unintentionally incorporated substitutional and interstitial H can also be strongly bound to O in ZnO within the lattice, thereby, making its elimination more demanding (but not impossible since interstitial H is highly mobile and can easily diffuse out of the samples).[341, 342]

Additionally, according to other theoretical and experimental works, the partial -OH termination of ZnO surfaces at RT is thermodynamically stable.[343-346] Thus, all the O_{III} species cannot be fully eliminated in native ZnO. The decrease in the emission intensity of the O_{III} species, however, presents evidence for the observed shift in the Fermi level due to reduced shallow donor states provided by the H impurities.

8.2 ZnO/Ir(BPA) interface characterization

Two interfaces were studied for this material combination by considering two ZnO films: as-deposited and annealed films. For each interface experiment, Ir(BPA) was step-wise deposited on top of the ZnO films. Subsequent PES measurements were performed at each deposition step to obtain the spectra of the core line emissions of the materials, valence band region and secondary electron (SE) cutoff.

8.2.1 As-deposited ZnO/Ir(BPA) interface

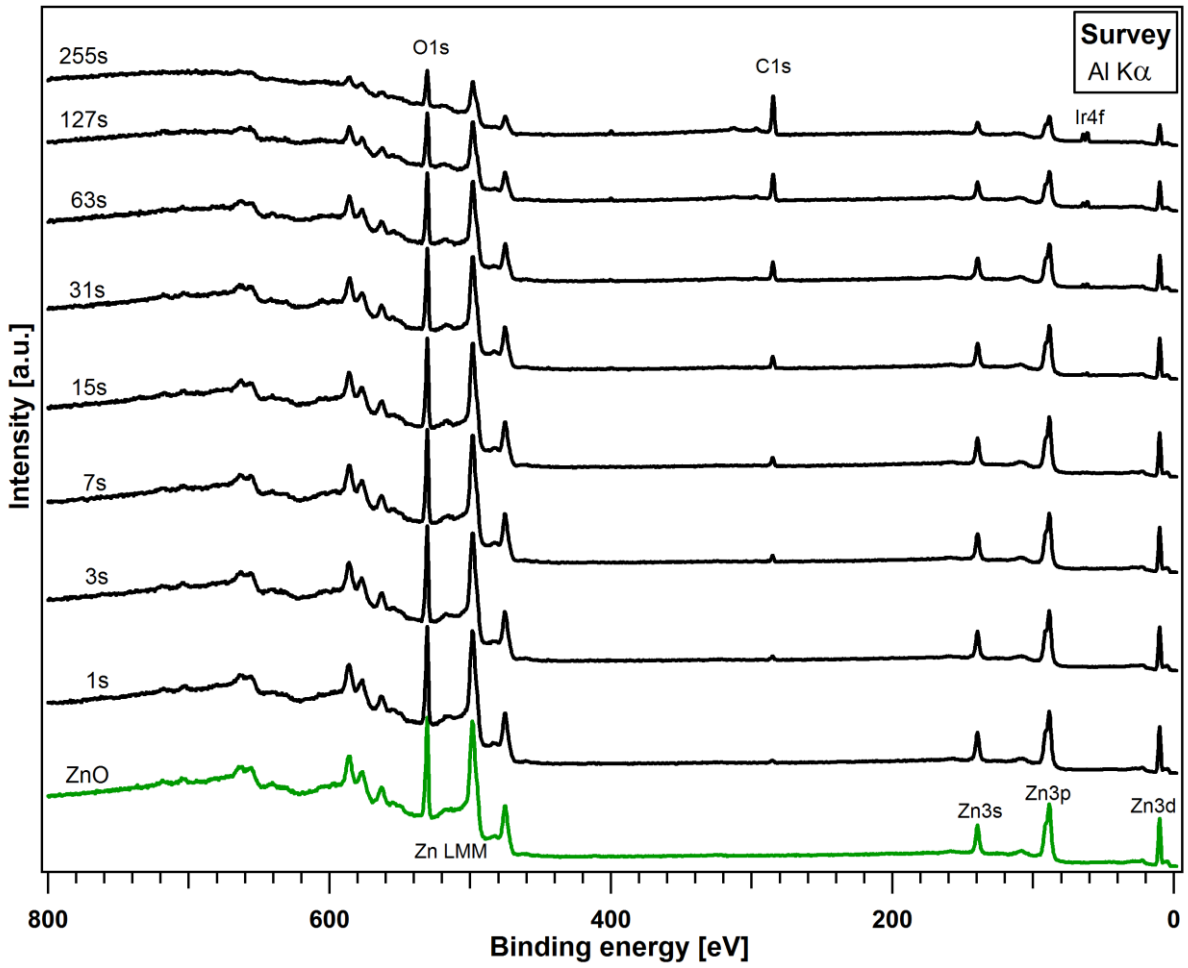

Figure 8.10: Survey spectra obtained at each deposition step in the ZnO/Ir(BPA) interface experiment. The total times for each of the Ir(BPA) deposition steps are indicated.

For this interface experiment, a freshly prepared, nominally 100 nm thick ZnO film deposited on an ITO glass substrate was used. The interface experiment was performed using the DAISY-SOL. The measured XPS survey spectra starting from the bare as-deposited ZnO film followed by the Ir(BPA) overlayer in sequential deposition steps are shown in Figure 8.10. The binding energy scale is shortened because including the highly intense $Zn2p_{3/2}$ emission at 1022 eV (which has a large ASF) obscures the observation of the evolution of the other core line emissions of O, Ir, C, and N. No photoelectron emissions from other elements are present in the survey spectra, indicating that the surfaces are free of contaminations. The survey spectrum for each deposition step is a superposition of the emissions coming from ZnO and the Ir(BPA) overlayer. It can be seen that the intensity of the ZnO lines are attenuated with increased overlayer depositions. At the same time, the intensity of the Ir(BPA) lines are increased. At the final deposition step that was performed, the Ir(BPA) layer was not completely closed as strong emissions from ZnO are still evident.

Figure 8.11 shows the XPS core level spectra of the most intense photoemission lines from ZnO ($Zn2p_{3/2}$ and O1s) and Ir(BPA) (Ir4f and C1s) for increasing Ir(BPA) deposition time. There are no changes in the lineshapes of the core line emissions of the dye overlayer and of the $Zn2p_{3/2}$ emission of the as-deposited ZnO. The changes in the lineshape of the O1s emission spectra are due to the overlapping and varied contributions coming from the oxygen atoms of ZnO and of Ir(BPA) with increasing Ir(BPA) overlayer.

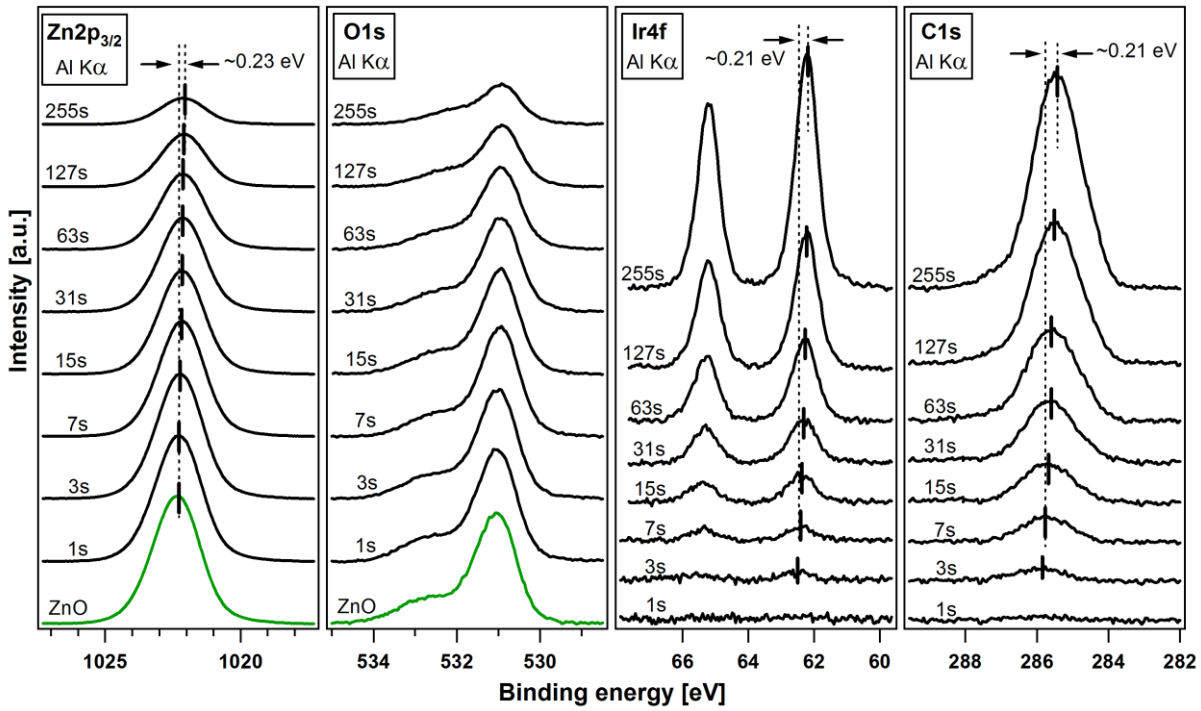

Figure 8.11: The $Zn2p_{3/2}$, O1s, Ir4f and C1s core level emission spectra of the as-deposited ZnO film substrate and the Ir(BPA) dye deposited stepwise onto ZnO by thermal evaporation. All spectra were recorded with Al Kα excitation. The Ir(BPA) deposition times are indicated. The ZnO $Zn2p_{3/2}$ emission shifts by ~0.23 eV to lower binding energies, while the Ir(BPA) Ir4f and C1s emissions shift by ~0.21 eV to lower binding energies from the 7 s to 255 s deposition steps.

The intensities of the $Zn2p_{3/2}$ and O1s emissions are damped with increased Ir(BPA) overlayer. Looking only at the $Zn2p_{3/2}$ emission, the attenuation of its intensity with increasing Ir(BPA) deposition time is plotted in Figure 8.12 on a logarithmic scale. Two regions are distinguished: below and above ~7 s with a linear and an exponential damping, respectively. Similar to the ZnSe/Ir(BPA) interface, a dye monolayer is formed initially on top of the ZnO film. It takes ~7 s of Ir(BPA) deposition to form the monolayer. The thickness of this dye monolayer is only 4 Å as compared to the 7 Å dye monolayer in the ZnSe/Ir(BPA) interface. Since the structure of the 3-dimensional dye is asymmetric, the orientation of the individual dye molecules in direct contact with the surface of the as-deposited ZnO could be different to that of ZnSe, explaining the difference in the monolayer thickness. Above the 7 s deposition, the damping increases exponentially. Assuming a constant sticking coefficient for Ir(BPA), this measured exponential damping of the substrate $Zn2p_{3/2}$ emission is too slow to account for a layer-by-layer dye growth when compared to the calculated damping of the $Zn2p_{3/2}$ emission (also shown in Figure 8.12) (where an escape depth (λ) of 13 Å and a nominal Ir(BPA) deposition rate of 21 Å/min were considered). The slower damping indicates that dye islands are formed instead. Thus, the dye first grows in a monolayer with a molecular thickness of approximately 4 Å, and then proceeds to grow in islands.

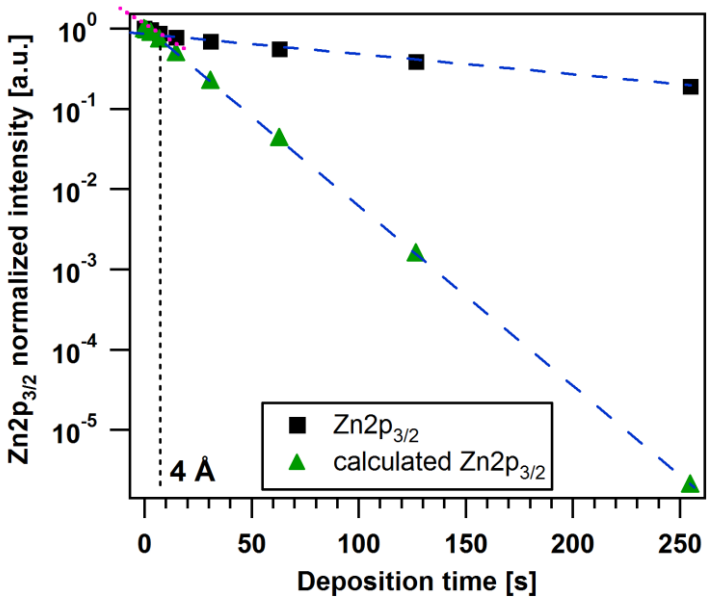

Figure 8.12: Normalized integrated $Zn2p_{3/2}$ emission intensity versus Ir(BPA) deposition time. Below 7 s the damping increases linearly, indicating a growth of a 4 Å thick monolayer. Above 7 s the damping is exponential, which could suggest a layer-by-layer or island growth. The calculated damping of the $Zn2p_{3/2}$ emission is also shown for a layer-by-layer growth considering the nominal Ir(BPA) deposition rate of 21 Å/min and a photoelectron escape depth of 13 Å.

Another noticeable trend for both ZnO and Ir(BPA) core line emission spectra shown in Figure 8.11 are the binding energy shifts of 0.23 eV and 0.21 eV to lower binding energies, respectively. These shifts were obtained from the 7 s to the 255 s deposition step. This shifts

are associated to the formation of a space charge region within the growing Ir(BPA) overlayer. This shifts are, thus, interpreted as band bending in the 3-dimensional dye islands.

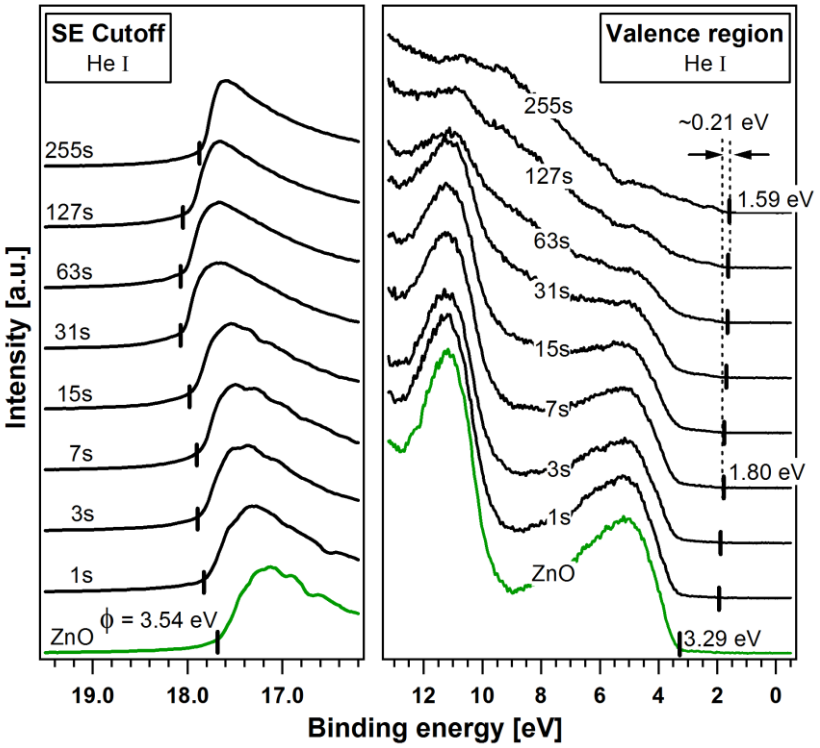

Figure 8.13: Secondary electron cutoff and valence region spectra during the step-wise deposition of Ir(BPA) on an as-deposited ZnO film. The Ir(BPA) deposition times are indicated. The $HOMO_{onset}$ of Ir(BPA) shifts from 1.80 eV at the 7 s deposition step to 1.59 eV by the last deposition step.

The UP spectra of the interface for the SE cutoff and valence region are shown in Figure 8.13. A similar shift of 0.21 eV is also observed for the HOMO of the dye starting from the 7 s deposition step to the final deposition step at 255 s. From the SE cutoff spectrum of the ZnO film, the work function is obtained to be 3.54 eV. At the same time, a (E_F - E_{VBM}) of 3.29 eV for the position of the VBM from the Fermi level is obtained from the valence band spectrum of this ZnO film. Since the Ir(BPA) overlayer was not closed after the 255 s deposition step, information for the pristine Ir(BPA) in this interface experiment is lacking. The Ir(BPA) electronic structure shown in Figure 5.3(b) is adapted here instead; and together with the electronic structure obtained for the as-deposited ZnO, the Anderson lineup of the energy levels of ZnO and Ir(BPA) before contact is drawn in Figure 8.14(a). Ir(BPA) has the larger work function than the as-deposited ZnO. This explains why there is no conclusive trend for the SE cutoff in Figure 8.13 which can be associated to the growing dye overlayer, as the material with the smaller work function is the one that is detected by UPS.

Considering the binding energy shifts of the core line emissions, the position of the dye HOMO during the 7 s deposition step (where a dye monolayer is already formed), the electronic structure of the pristine ZnO, and the adapted ionization potential of Ir(BPA), the

energy level alignment at the as-deposited ZnO/Ir(BPA) interface is finally drawn in Figure 8.14(b).

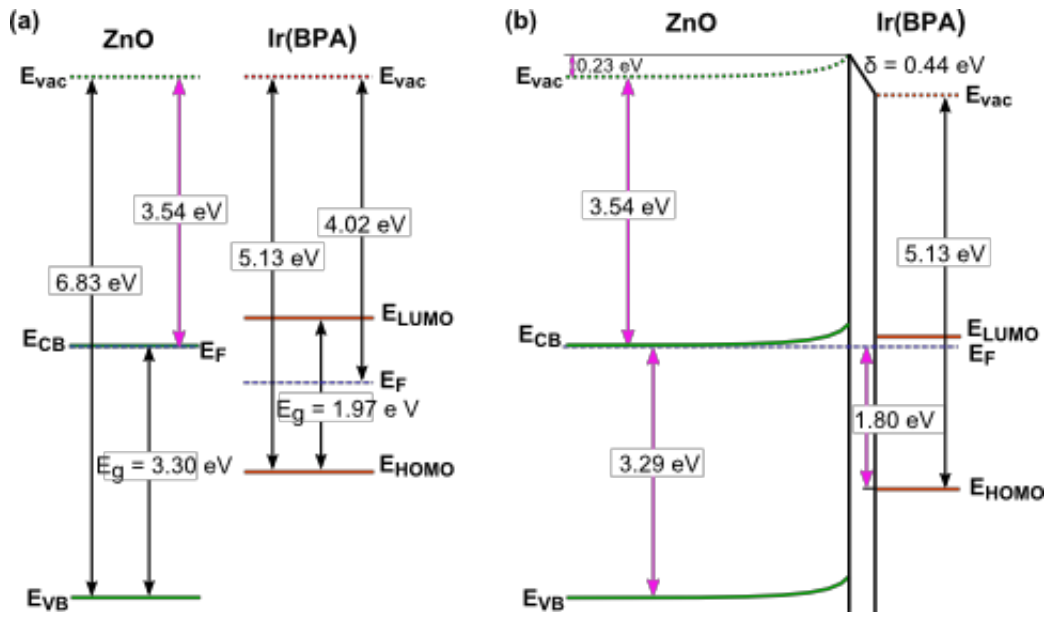

Figure 8.14: (a) Anderson lineup of the energy levels of the pristine as-deposited ZnO (left) and pristine Ir(BPA) (right) (adapted from Figure 5.3 b) before contact. (b) Interface band diagram of the as-deposited ZnO/Ir(BPA) bilayer that includes an interface dipole of 0.44 eV and ZnO band bending of 0.23 eV. The energy levels for Ir(BPA) drawn in the diagram is representative only of the formed dye monolayer (i.e. at the 7 s deposition step).

In this interface lineup, only the dye monolayer that is immediate to the interface is taken into consideration. The observed shift of the dye core line emissions to a lower binding energy in the non-closed overlayer is due to the dye overlayer reflecting the band bending it induced in the as-deposited ZnO substrate. A complete energy band diagram for the entire heterojunction would require a fully closed Ir(BPA) film. Satisfactorily enough though, the energy level alignment of the as-deposited ZnO and Ir(BPA) right at the interface is already fully represented by the band diagram drawn in the figure with only a dye monolayer. An interface dipole of 0.44 eV is derived. The energy lineup can provide a strong driving force for hole transfer from the ZnO to the Ir(BPA); however, this does not hold true for electron transfer.

8.2.2 Annealed ZnO/Ir(BPA) interface

The 100 nm thick, annealed ZnO film (which was presented in the above section 8.1.5) was then utilized as the substrate in another interface experiment with the Ir(BPA) light emitter. The interface experiment was performed at the DAISY-MAT. Successive depositions of the Ir(BPA) with subsequent PES measurements were performed until a fully-closed Ir(BPA) final overlayer was obtained.

The UP spectra of the pristine annealed ZnO film and fully-closed Ir(BPA) overlayer are shown Figure 8.15(a). The left graph shows the SE cutoffs where work functions of

4.06 eV and 3.78 eV are derived for the ZnO and Ir(BPA), respectively. The right graph shows the valence states regions where linear extrapolations of the low binding energy emission onset give 3.10 eV and 1.47 eV for the VBM and HOMO positions of ZnO and Ir(BPA), respectively. The corresponding electronic structures of the two materials before contact are depicted in the energy level diagrams shown in Figure 8.15(b). With the vacuum levels aligned (so called Anderson lineup), the LUMO of the dye is around 0.58 eV above the conduction band of the annealed ZnO. Thus, considering the isolated materials, the electron transfer from the conduction band of ZnO to the dye LUMO would not be energetically favorable.

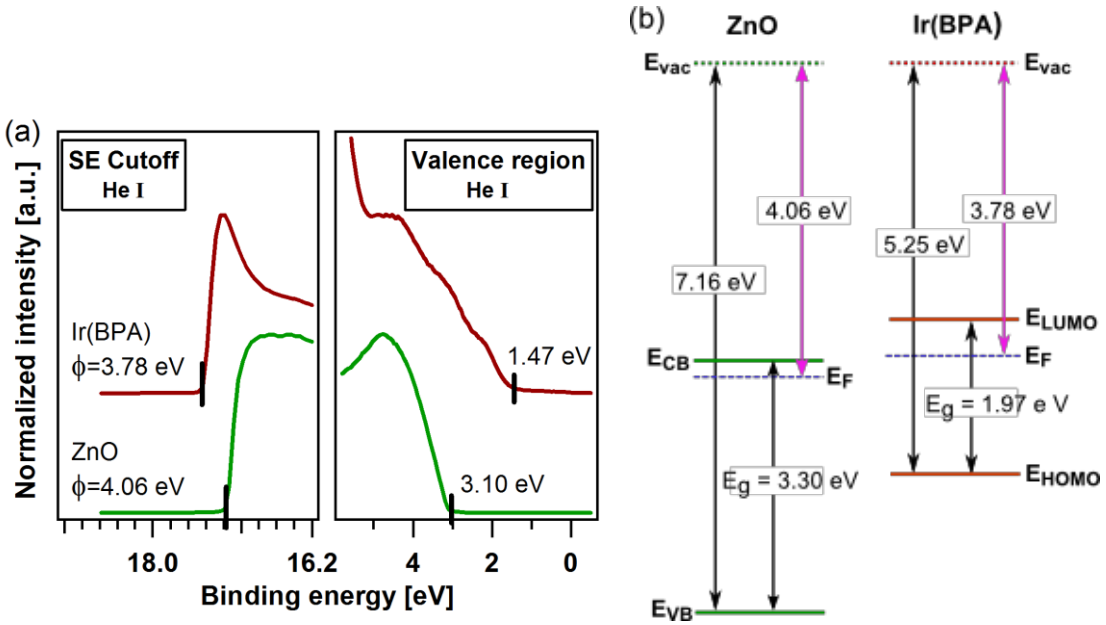

Figure 8.15: (a) Secondary electron cutoff and valence region spectra of the annealed ZnO film and fully-closed Ir(BPA) overlayer (a). The work functions (ϕ) and VBM/HOMO onset values are indicated. (b) An Anderson lineup of the energy levels of these two pristine materials before contact.

The core level spectra of the most intense photoemission lines are shown in Figure 8.16 for increasing Ir(BPA) deposition time. No changes in the lineshapes of the core line emissions of both the ZnO substrate and Ir (BPA) overlayer are observed. The $Zn2p_{3/2}$ and O1s emissions of ZnO exhibited no shifts of the binding energy positions indicating a Fermi level pinning in ZnO. Because of the slight carbon contamination at the surface of the annealed ZnO, difference spectra were obtained for the C1s emission of the dye.

Figure 8.17 plots the attenuation of the $Znp_{3/2}$ intensity with increasing Ir(BPA) deposition time on a logarithmic scale. Two regions are also distinguished: below and above ~70 s. Similar to the as-deposited ZnO/Ir(BPA) interface, a dye monolayer is formed initially on top of the annealed ZnO film. It takes ~70 s of Ir(BPA) deposition to form the monolayer, which has a thickness of ~8Å. This dye monolayer thickness coincides with that found for the ZnSe/Ir(BPA) interface. The orientation of the monolayer molecules that are in direct contact to the ZnSe and annealed ZnO surfaces are then probably the same.

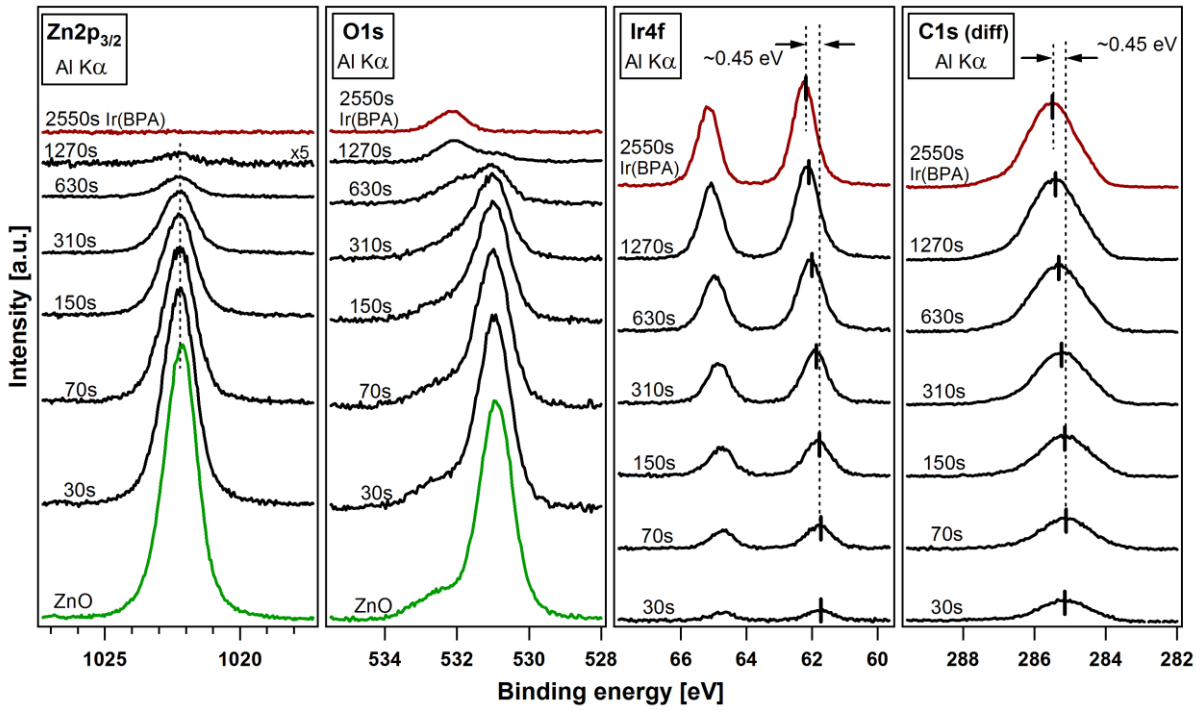

Figure 8.16: The $Zn2p_{3/2}$, O1s, Ir4f and C1s core level emission spectra of the annealed ZnO film substrate and the Ir(BPA) dye deposited stepwise on ZnO by thermal evaporation. All spectra were recorded under an Al Kα excitation. The Ir(BPA) deposition times are indicated. With the increase in coverage, the Ir4f and C1s emissions shift to higher binding energies by 0.45 eV from the 70 s to 2550 s deposition steps. The $Zn2p_{3/2}$ and ZnO O1s binding energies remain constant.

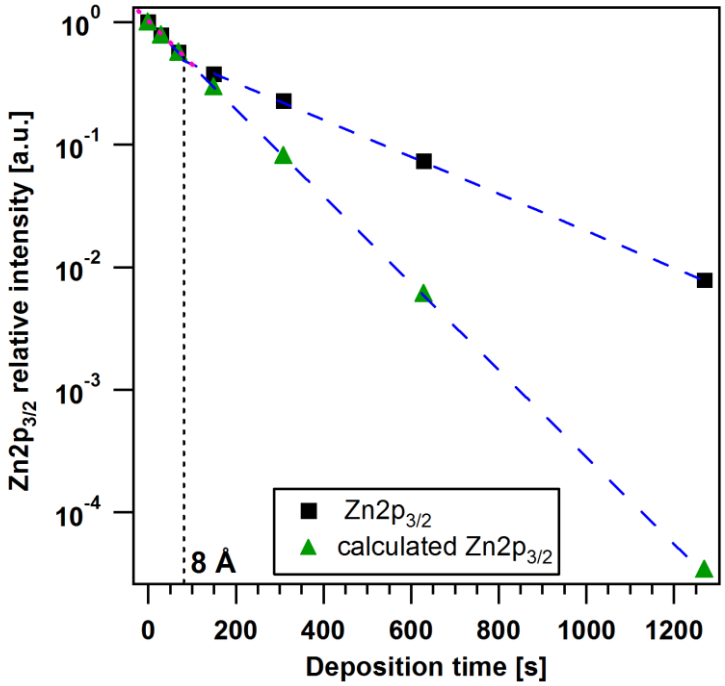

Figure 8.17: Normalized integrated $Zn2p_{3/2}$ emission intensity versus Ir(BPA) deposition time. Below 70 s the damping increases linearly (shown in the inset), indicating growth of a 8 Å thick monolayer. Above 70 s the damping is exponential, which could suggest a layer-by-layer or island growth. The calculated damping of the $Zn2p_{3/2}$ emission is also shown for a layer-by-layer growth considering the nominal Ir(BPA) deposition rate of 6.5 Å/min and a photoelectron escape depth of 13 Å.

After the 70 s deposition, the damping increases exponentially. This damping is too slow to account to a layer-by-layer dye growth when compared to the calculated damping of the $Zn2p_{3/2}$ emission (where an escape depth (λ) of 13 Å and a nominal Ir(BPA) deposition rate of 6.5 Å/min were considered). For the deposition on the annealed ZnO, the dye first grows a monolayer with a molecular thickness of approximately 8 Å, and then proceeds to grow in islands.

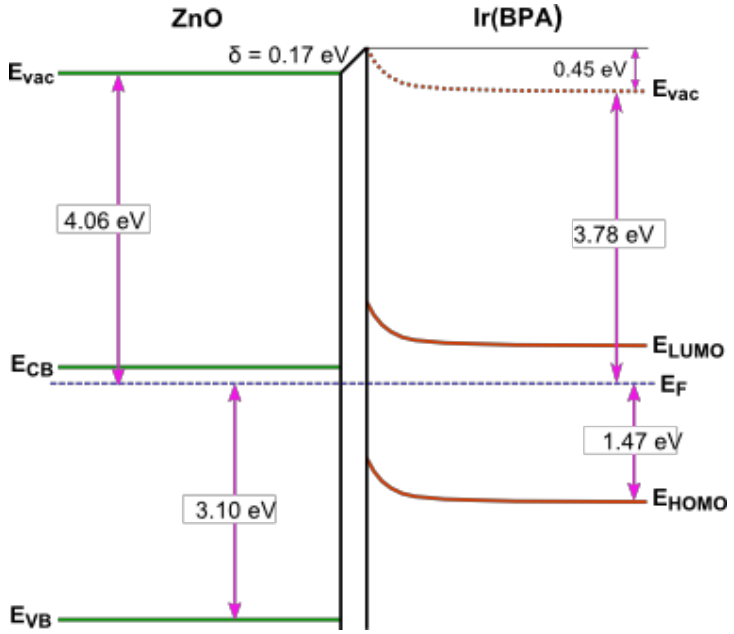

Figure 8.18: Interface band diagram of the annealed ZnO/Ir(BPA) heterojunction including a 0.17 eV interface dipole and 0.37 eV band bending in the emitter.

The electronic characteristics of the annealed ZnO/Ir(BPA) heterojunction derived from the interface experiment, which include a constant Fermi level in ZnO, an interface dipole, and a band bending in the Ir(BPA) layer, are summarized in the energy band diagram shown in Figure 8.18. The 0.28 eV difference in the Fermi level position represented by ϕ of ZnSe and Ir(BPA) (Figure 8.15(b)) is adjusted by a 0.17 eV interface dipole and a 0.45 eV band bending in the Ir(BPA) overlayer.

For the ZnO/Ir(BPA) interface, whether the ZnO substrate is heat treated or not, the alignment of the energy levels of ZnO to the HOMO and LUMO of Ir(BPA) do not match well to the proposed design in this study. Electron injection from the conduction band of the ZnO to the LUMO of Ir(BPA) is blocked by a potential barrier at the interface of the two materials. An intrinsic ZnO (in such a case, doping would be necessary) could be a good combination with the organic dye.

Chapter 9 nc-TiO_2 - TSQT system

The material combination consisting of a porous anatase nanocrystalline titanium dioxide (nc-TiO_2) and a monomeric squaraine molecule (labeled as TSQT) was investigated. A solution-based deposition (specifically, drop-casting method) was followed for the TSQT molecule in the investigation of the alignment of its energy levels against that of the nc-TiO_2. The porous nc-TiO_2 was specifically selected because its pore architecture can accommodate the drop-casted guest TSQT molecules, thereby, acting as a matrix. This chapter presents the results of our PES investigation on the interface of the nc-TiO_2 + TSQT composite as well as its photoluminescence (PL) properties.

9.1 nc-TiO_2

Titanium dioxide is an indirect, wide-bandgap semiconductor. Like ZnO, TiO_2 is normally *n*-type due to the formations of intrinsic *n*-type defects in the lattice such as oxygen vacancies and titanium interstitials. These defects give rise to states in the band gap, corresponding to electrons localized at Ti^{3+} centers. O vacancy in anatase results in two excess electrons occupying two Ti 3d orbitals, with one of these Ti sites neighboring the vacancy, and the second at a next-nearest Ti position. The formation of Ti interstitials donates four electrons to the Ti lattice. In anatase TiO_2, one of these electrons is located at the interstitial Ti site, and three occupied defect states are hybridized between three nearest neighbor Ti sites.

Nanocrystalline titanium dioxide represents one of the most successful modern functional nanomaterials with a broad spectrum of applications. The number of possible applications have expanded beyond photocatalysis due to the invention of nc-TiO_2 - based hybrid nanosystems such as the dye-sensitized solar cell [347-349] and the multicolor photochromic material (Ag-TiO_2 nanocomposite) [350]. For this study, a nc-TiO_2 layer was selected as the inorganic matrix material because its mesoporous and nanocrystalline structure can be loaded with guest dye molecules and can provide an optimal dye uptake due to a large surface area.

9.1.1 nc-TiO_2 film preparation

The porous nc-TiO_2 anatase films deposited on FTO glass substrates were provided by the research group of Prof. Dr. Theirry Toupance from the Institute of Molecular Sciences - UB. The films were prepared by sintering at 450°C screen printed layers of anatase nanoparticle paste (DSL 90T, Dyesol, average particles size 20 nm) on FTO (fluorine-doped tin oxide) with additional treatment in 40 mM $TiCl_4$ aqueous solution at 70°C for 30 min and sintered at 500°C for 30 min. The layer thickness is approximately 2 µm.

9.1.2 Crystal structure of anatase nc-TiO_2

TiO_2 exists in many polymorphs. Among them, rutile, anatase and brookite are well-known minerals in nature. The anatase crystal structure is shown in Figure 9.1.

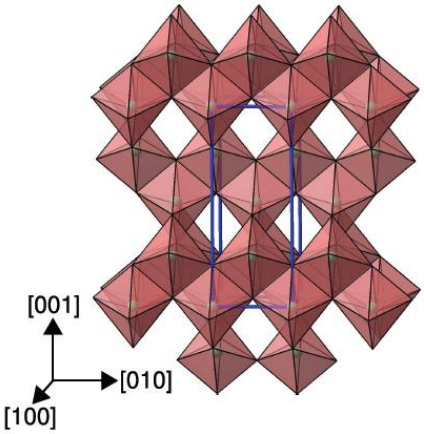

Figure 9.1: $[TiO_6]^{2-}$ octahedra building block representation for the anatase phase of TiO_2.

Anatase TiO_2 has a tetragonal unit cell within which each Ti atom is unequally coordinated to six O atoms. Its lattice is built up by this distorted $[TiO_6]^{2-}$ octahedra, with each octahedra sharing four of its edges.[351, 352]

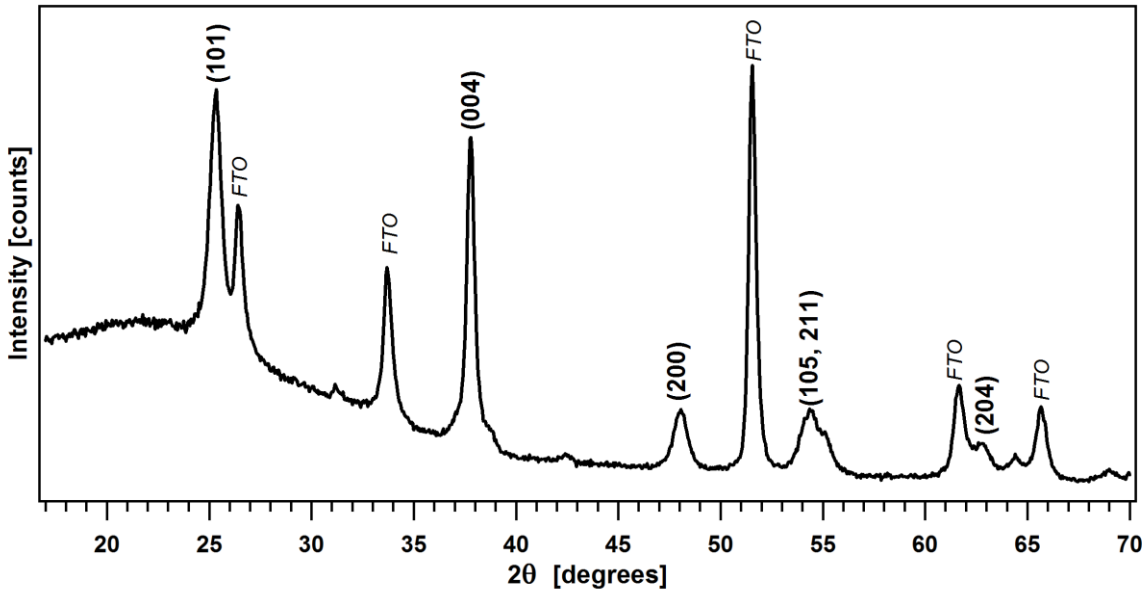

Figure 9.2: XRD spectrum of the nc-TiO_2 film on FTO glass substrate showing reflections of the anatase form.

An X-ray diffraction experiment with grazing incidence (GIXRD) was performed on the nc-TiO_2 to confirm its phase purity. From the characteristic reflections found on the XRD pattern shown in Figure 9.2, the crystalline phase could be clearly established as being

purely anatase. Sharp reflections originating from the SnO_2:F layer and a broad background from the glass substrate are additionally present in the pattern.

9.1.3 Surface morphology of the nc-TiO_2 film

Figure 9.3 shows an AFM image of the nc-TiO_2 over an area of 1 µm x 1 µm taken in non-contact mode using a phosphorus-doped silicon tip (radius: 8 ± 2 nm). The image confirms the porous morphology and the ~20 nm globular TiO_2 nanocrystals. The height profile (figure on the right) reveals a surface that is not uniformly flat, with an average height difference of about 30 nm.

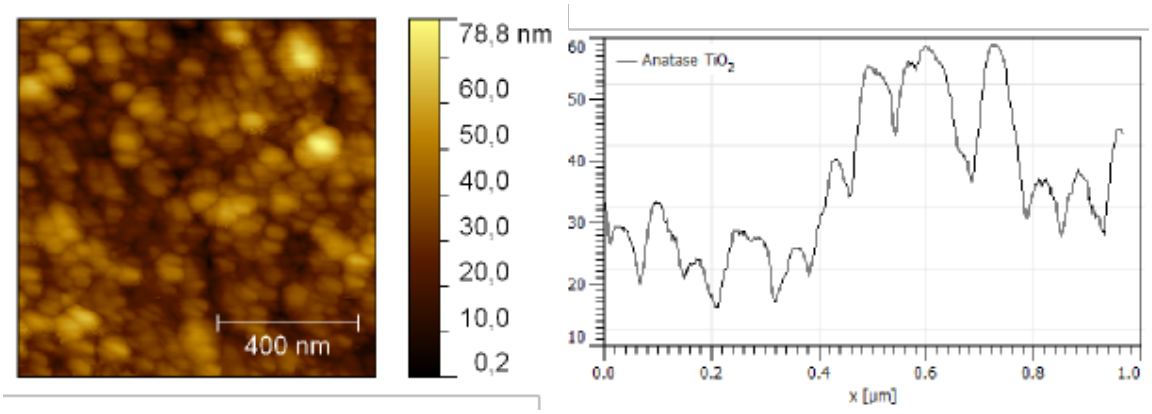

Figure 9.3: AFM image of the anatase nc-TiO_2 film with an average particle size of ~20 nm. The height profile reveals a surface that is not flat.

9.1.4 Absorption spectra and the optical bandgap of nc-TiO_2

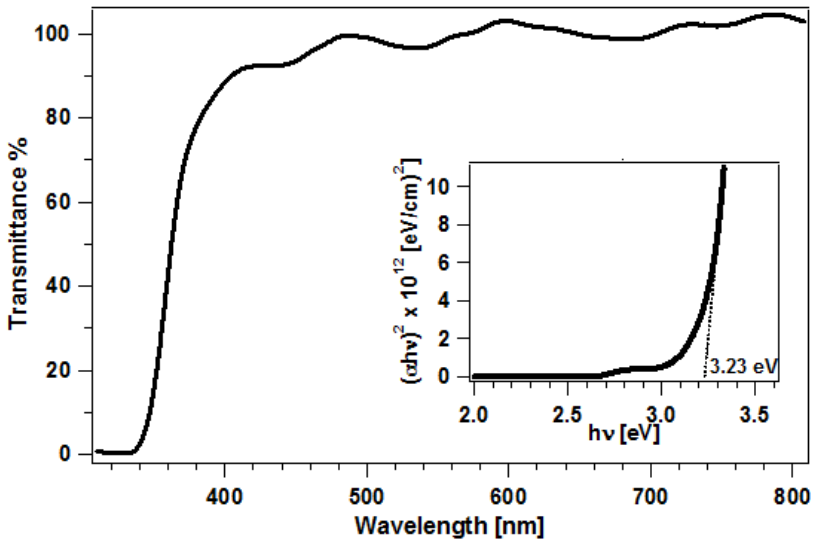

Figure 9.4: Optical transmission of the 2 µm thick anatase nc-TiO_2 film deposited on FTO glass substrate. Inset: An optical bandgap of 3.23 eV is derived from the plot, $(\alpha h\nu)^2$ versus $h\nu$.

The optical property of the nc-TiO_2 film was studied by transmission measurement at room temperature in the spectral range from 300 nm to 800 nm. The transmission spectrum

is shown in Figure 9.4. The spectrum includes a sharp optical absorption edge which is normally designated to a high degree of crystallinity. The $(\alpha h\nu)^2$ versus $h\nu$ graph was obtained and is shown in the inset of the figure. From the graph, the optical band gap is derived to be 3.23 eV.

9.2 TSQT: monomeric squaraine-derived molecule

Squaraine (SQ) dyes were first synthesized in the 1960s. The compounds are 1,3-disubstituted squaric acid derivatives containing an electron-deficient central four-membered ring and two electron-donating groups in a donor-acceptor-donor configuration in which a π-conjugated resonance structure helps stabilize the molecule.[353] The symmetric " $D^+ \rightarrow A^- \leftarrow D^+$ (donor-acceptor-donor) " configuration is expected to lead to the formation of intramolecular charge-transfer[57] states and to considerable intramolecular charge-transfer character in both the ground and excited states.[354-356]

The very dense electron distribution on the central ring imparts a very high absorption coefficient to these molecules.[353] Owing to this strong light harvesting property of SQ molecules, SQ dyes have been used to sensitize large band gap semiconductors and extend their photoresponse into the visible.[355, 357-359]

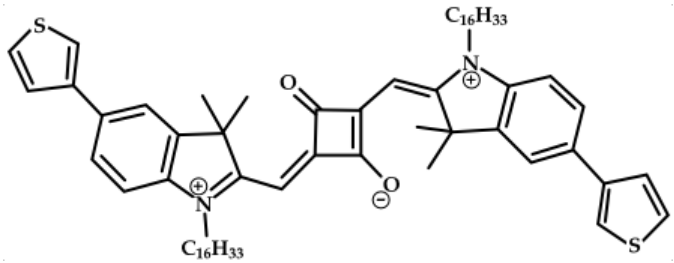

Figure 9.5: Chemical structure of the TSQT molecule. Central to the TSQT's structure is a squaraine dye moiety. It is end-capped with a thiophene.

A squaraine-derived molecule, whose chemical structure is shown in Figure 9.5, was synthesized and provided by the Polymer Electronic Materials and Devices research group of the Laboratoire de Chimie des Polymères Organiques - UB. Synthesis details for the polymeric form of this dye is found in [360]. The TSQT was used as received and had a microcrystalline powder solid-state structure. The molecule contains a highly polar and electron withdrawing central squaraine (C_4O_2) moiety disubstituted with strong electron donating groups and is end-capped with thiophene.

[57] Intramolecular charge transfer: A process that changes the overall charge distribution in a molecule.

9.2.1 TSQT sample preparation

Solution-based methods at ambient pressure and temperature were employed for the deposition of TSQT. These methods included spin-coating and drop-casting the dissolved TSQT on different substrates.

For the PES measurements, the glass cell was specifically utilized for the solution-based (drop-casting) deposition of the TSQT molecules into the porous nc-TiO_2 and on ITO glass substrates. Tetrahydrofuran (THF) was used as the solvent for TSQT. The glass cell is basically a KF50 glass double cross with two ports for sample transfers and tailored flanges for continuous inert gas flow and material (in solution) deposition, as shown in Figure 9.6. The constant rinsing of the cell with inert gas (argon 5.0 or 6.0) is the crucial parameter that makes the process contamination-free.

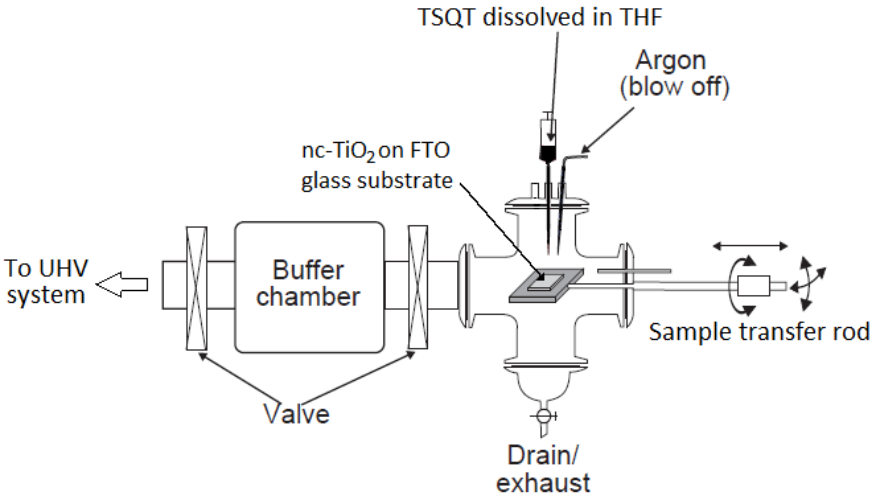

Figure 9.6: Glass cell for solution-based deposition of TSQT on nc-TiO_2.

The glass cell is connected to the UHV system via a buffer chamber which is designed to bridge the gap between ambient pressure solution-based depositions and UHV characterization conditions without exposing samples to air. The possibility to vent the buffer chamber with the inert gas and, at the same time, control the gas pressure within the chamber enables the transfer of samples from the UHV system to the glass cell, and vice-versa, without introducing contaminants into the chamber and the UHV system. The glass cell has been found to provide a much better control than a glovebox in terms of environmental contamination sources.[105, 361, 362]

9.2.2 Optical properties of the TSQT molecule

In solution, SQ dyes exhibit sharp and intense absorption in the visible region (λ_{max} ranging from 550-670 nm), depending on the substituent in the phenyl ring or at the nitrogen.[355, 356, 359] In a theoretical study, it was reported that for a certain SQ dye type, both the S_0 and S_1 states are intramolecular D-A-D charge transfer states. Furthermore, it was

shown that there is a charge transfer during the $S_0 \rightarrow S_1$ electronic excitation, with the charge transfer being primarily confined in the central C_4O_2 unit (~80%). They attributed the narrow absorption band of the SQ dye to the localization of this electronic transition.[354]

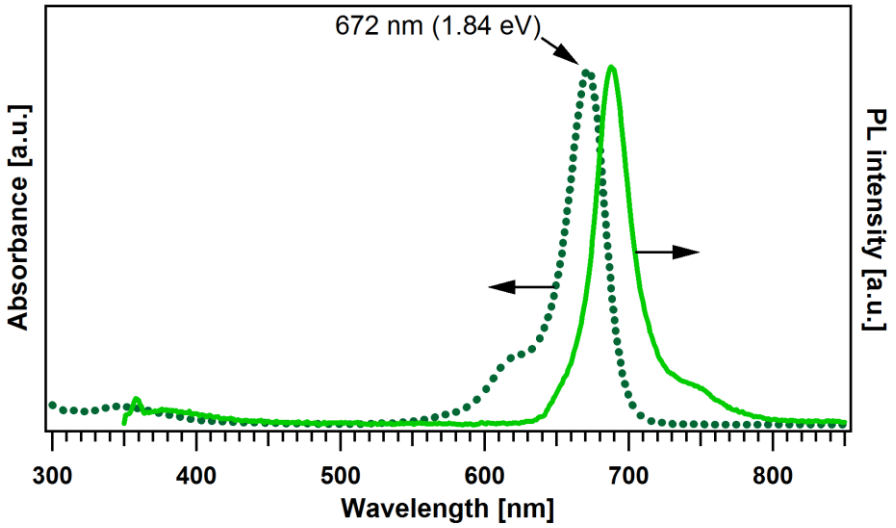

Figure 9.7: Room-temperature UV-Vis absorption and emission spectrum of TSQT molecules dispersed in tetrahydrofuran (THF). The emission spectrum is a mirror image of the absorption spectrum. The absorption of the molecule peaks at 672 nm (1.84 eV), while the PL peaks at 688 nm (1.80 eV).

Figure 9.7 shows the absorption and PL spectra of the TSQT molecule. The absorption band, as expected, is narrow and intense, peaking at ~672 nm (1.84 eV). The PL spectrum strongly resembles the mirror image of the absorption spectrum.[356] This behavior is usually exhibited by many common fluorophores, and is due to the fact that the same transitions are most favorable for both absorption and emission. A Stokes shift of ~16 nm is evident.

9.3 nc-TiO_2 + TSQT composite

As mentioned in Chapter 1.2.1, the addition of metallic, semiconducting, and dielectric nanocrystals into polymer matrices is known to enhance the efficiency and lifetime of devices. Several studies have already looked into hybrids comprising of embedded TiO_2 nanoparticles in polymer matrices for light emission.[38-40, 363, 364] In this study, the nc-TiO_2 + TSQT composite was obtained by embedding (e.g. solution drop-casting) TSQT dye molecules into the porous nc-TiO_2 matrix.

PES and PL measurements were performed on pristine layers of nc-TiO_2 and TSQT and on nc-TiO_2 + TSQT composites. The initial PES measurements were performed using the SOLIAS at BESSY II. And after some experimental method refinements and verifications, the final measurements were performed at the HEISY-ORG. Additional details on the PES of measurements of the samples are found in Appendix E. The PL measurements were similarly performed as description presented in Chapter 6.5.

9.3.1 Energy level alignment at the internal interfaces of the nc-TiO_2 + TSQT composite

To draw the energy band diagram for the interface of the nc-TiO_2 matrix and the TSQT guests within the composite, the relevant energy levels of the pristine nc-TiO_2, pristine TSQT and nc-TiO2+TSQT composite are obtained and compared. This is accomplished by, first, characterizing a cleaned pristine nc-TiO_2 layer[58]. A solution of TSQT is then drop-casted onto this characterized nc-TiO_2 layer, followed immediately by in-situ PES measurements of the resulting composite layer. As a final step in order to be able to complete the lineup, TSQT is drop-casted on a cleaned and ozone-treated ITO glass substrate (i.e. a highly conductive substrate is necessary to avoid charging effects) to obtain its pristine electronic characteristics.

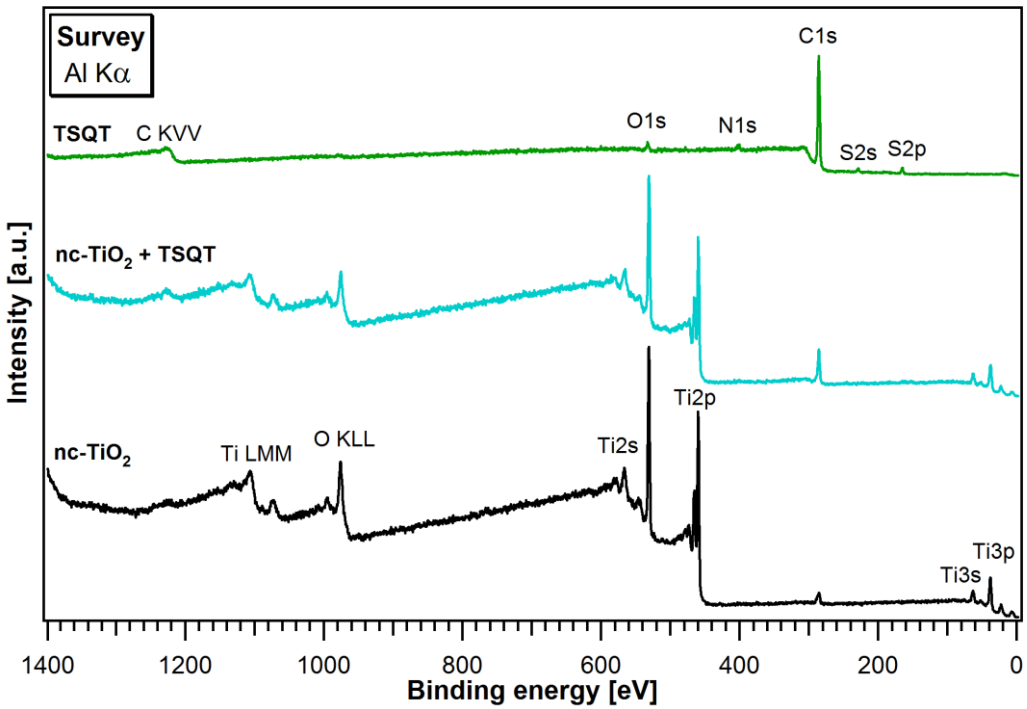

Figure 9.8: Survey spectra of pristine nc-TiO_2, drop-casted TSQT on the nc-TiO_2, and pristine TSQT. The C1s peak in the spectrum of the nc-TiO_2 indicates the presence of residual carbon contamination that was not fully eliminated by the cleaning procedure.

The XPS survey spectra of the pristine nc-TiO_2 and TSQT layers together with that of the nc-TiO_2 + TSQT composite are shown in Figure 9.8. The carbon contamination on the pristine nc-TiO_2 layer cannot be fully eliminated by the cleaning procedure. An Ar ion sputtering step to fully eliminate the contamination was avoided due to the preferential sputtering of oxygen which will change the surface characteristics of the layer (i.e. surface

[58] The mesoporous nc-TiO_2 layer was externally prepared. Prior to introducing it into the UHV system, it was rinsed with isopropanol and then with deionized water. Afterward, it was blow dried with N_2 gas, and mounted onto a clean metal sample holder. The whole assembly was heated to 100°C on a hot plate to further remove adsorbed water molecules in the nc-TiO_2 layer.

defects which lead to an increase in gap states that act as charge carrier traps).[362, 365-368] The survey spectrum for the pristine TSQT layer shows all the observable characteristic core line emissions in accordance to the elemental composition (carbon, oxygen, sulfur, nitrogen) of the dye. Photoelectron emissions from other elements are finally absent in the survey spectra, indicating a clean and homogeneous TSQT sample preparation. For the composite layer, its survey spectrum is a superposition of photoemissions coming from the nc-TiO_2 and from the embedded TSQT.

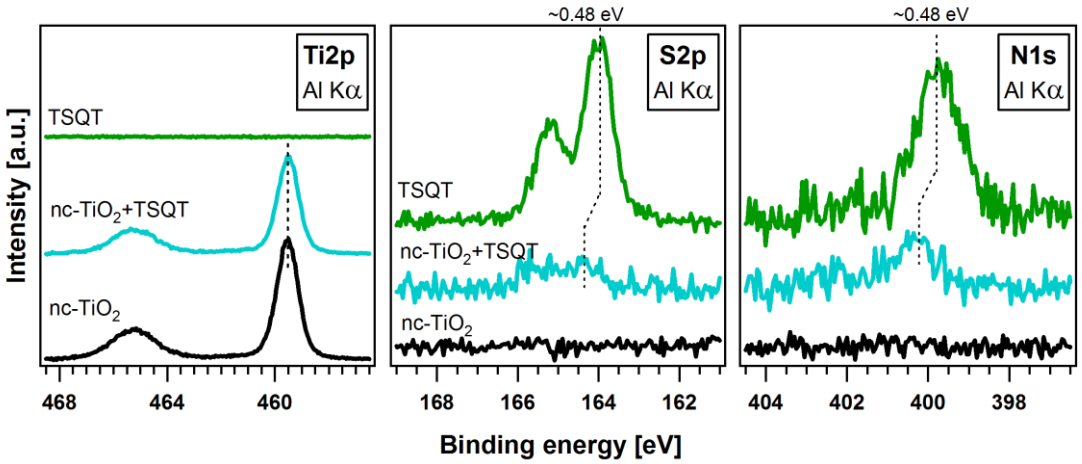

Figure 9.9: Photoemissions from Ti2p, S2p and N1s core levels. The binding energy position of the Ti2p emission does not change in the composite. A difference of ~0.48 eV is found for the binding energies of the S2p and N1s emissions of the composite from that of the pristine TSQT.

Figure 9.9 displays the Ti2p, S2p and N1s core line emissions. No difference in binding energy position was observed between the Ti2p emissions of the pristine nc-TiO_2 and the composite. This is interpreted as a Fermi level pinning in the nc-TiO_2. However, between the pristine TSQT and the composite, binding energy differences amounting to approximately 0.48 eV are observed in the S2p and N1s emissions. If this is projected to the case of a nc-TiO_2/TSQT bilayer heterojunction, this could be a sign of a band bending in the TSQT layer or of a dipole at the interface.

The SE cutoff and valence region spectra of the pristine and composite layers are shown in Figure 9.10. The measured work function of TSQT (4.63 eV) is larger than that of the nc-TiO_2 (3.74 eV). Therefore, the work function that is measured for the composite (3.61 eV) cannot be exclusively assigned to the embedded TSQT molecules. It also cannot be exclusively assigned to the nc-TiO_2 matrix of the composite because the work function is sensitive to changes in surface properties. It can be noted, though, that its value is near the measured work function for nc-TiO_2. The spectral lineshape of the valence region of the pristine nc-TiO_2 coincides with other reports.[361, 369] The valence band maximum is located at 3.25 eV from the Fermi level position. Taking a bandgap of 3.23 eV, the Fermi level of the nc-TiO_2 would then be located just a little above its conduction band (Figure 9.11(a)). The TSQT HOMO position is found to be at 1.06 eV from the Fermi level in the composite,

while it is at 0.59 eV in the pristine TSQT layer. This translates to a difference of 0.47 eV in the HOMO binding energy positions between the composite and pristine TSQT. The value agrees with the measured difference in the S2p and N1s core levels. This would confirm a parallel shift of the dye HOMO and core levels in the TSQT if a nc-TiO_2/TSQT bilayer heterojunction is considered.

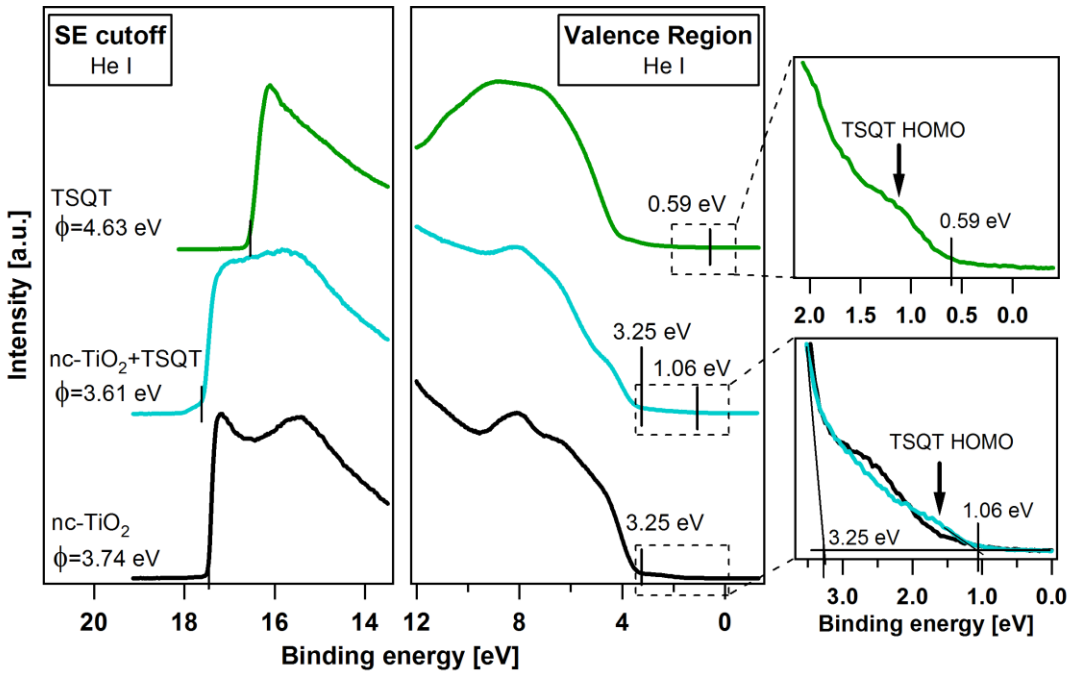

Figure 9.10: SE cutoff and valence region spectra of the pristine nc-TiO_2, nc-TiO_2 + TSQT composite and pristine TSQT layers. The spectra on the right side are enlarged versions of the boxed regions in the valence region spectra.

Considering a bandgap of 1.84 eV (from the absorption spectrum, Figure 9.7) for the TSQT, a HOMO position of 0.59 eV from the Fermi level signifies the TSQT dye as *p*-type. An illustration of the energetic levels of the pristine nc-TiO_2 and TSQT layers in an Anderson lineup is given by Figure 9.11(a). The Fermi level position in the TSQT is lower than in the nc-TiO_2. If these two materials are brought in contact to form a bilayer, an upward band bending could be expected in the TSQT layer.

Since no changes on the core level emissions and VBM position are observed for the nc-TiO_2 of the composite layer from that of the pristine layer, the ionization potential of nc-TiO_2 is then taken to be constant. This allows us to draw an energy level alignment at the internal interfaces of the nc-TiO_2 matrix and TSQT guest molecules of the composite as shown in Figure 9.11(b), where the HOMO-LUMO gap of the TSQT is not situated in between the energy gap of the nc-TiO_2. An interface dipole of 0.42 eV and an electron potential barrier of 0.80 eV are formed at the interface. The position of the Fermi level is shifted upward in the bandgap of the TSQT when it is embedded into the nc-TiO_2 matrix. This indicates an electron transfer from the nc-TiO_2 to the TSQT during the interface

formation in the composite, which is expected since the pristine nc-TiO_2 has a smaller work function than the pristine TSQT.

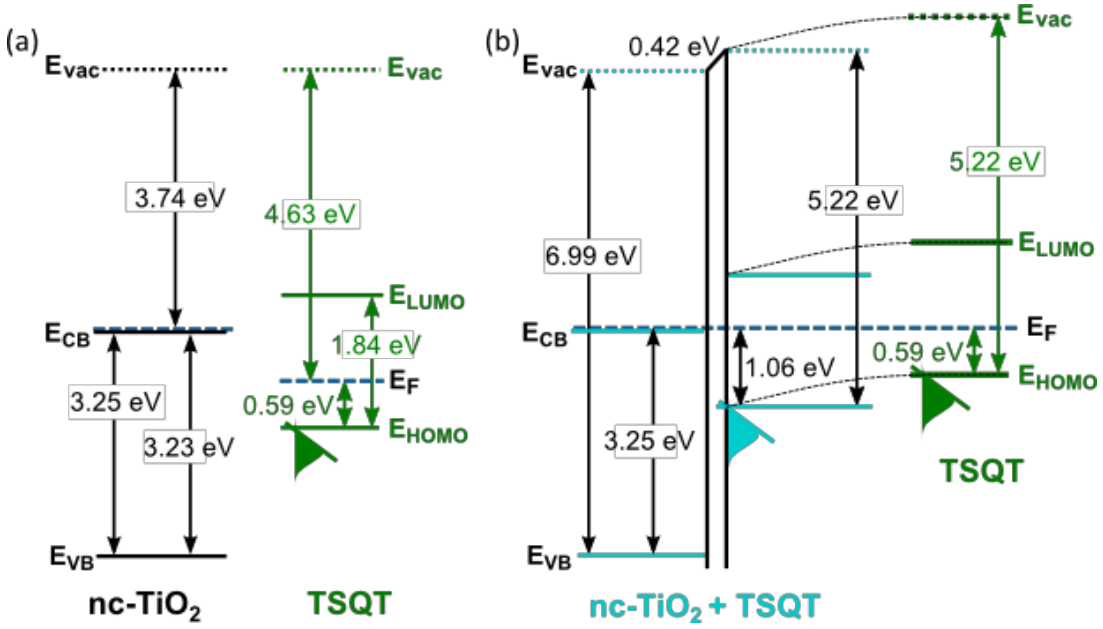

Figure 9.11: (a) Anderson lineup of the nc-TiO_2 and TSQT before contact. (b) Energy level alignment at the interfaces of the drop-casted TSQT guest molecules on the nc-TiO_2 matrix, together with the energy levels of the pristine TSQT. An extrapolated complete energy diagram for the nc-TiO_2/TSQT interface would include a Fermi level pinning in the nc-TiO_2, a band bending in the TSQT, and a large electron potential barrier at the interface.

9.3.2 Photoluminescence of nc-TiO_2+TSQT composites

TiO_2 exhibits a UV bandgap emission along with its well-known green emission that is associated with self-trapped [59] exciton (STE) recombination.[370-374] As TiO_2 is an indirect semiconductor, the band edge luminescence is difficult to observe.[375] The main features generally observed are the broad visible to near-infrared luminescence bands. In rutile TiO_2, free exciton states are present; while in anatase, exciton-phonon coupling leads to self-trapping of excitons. These STEs are found to be stable in anatase TiO_2. The broad luminescence band that peaks at around 2.3 eV are assigned to radiative recombination of STE localized on $[TiO_6]^{2-}$ octahedra.

With a decreased size for TiO_2 nanocrystals, the influence of the surface states and adsorbates becomes more significant and dominant. Similar to the STE emission, the surface-related PL of the nc-TiO_2 is also a broad band with a maximum that is in the green spectral region.[376-381] In the anatase nc-TiO_2 (particle size: 20 - 120 nm), the PL has been assigned to intrinsic STE and to radiative phonon-assisted recombination of excitons bound to oxygen vacancies or Ti^{3+} states.[377] In this study, the PL of the nc-TiO_2 layer shown in

[59] Self-trapped exciton state: When an electron or a hole is inserted, it can get "self-trapped" by deforming the local lattice structure. This permits a localized bound state to form with a lower energy than simple insertion of an electron or hole into the conduction or valence band.

Figure 9.12 agrees with literature. As expected, a broad surface-related PL, which peaks in the green region at around 2.3 eV, and no excitonic bandgap PL, are found.

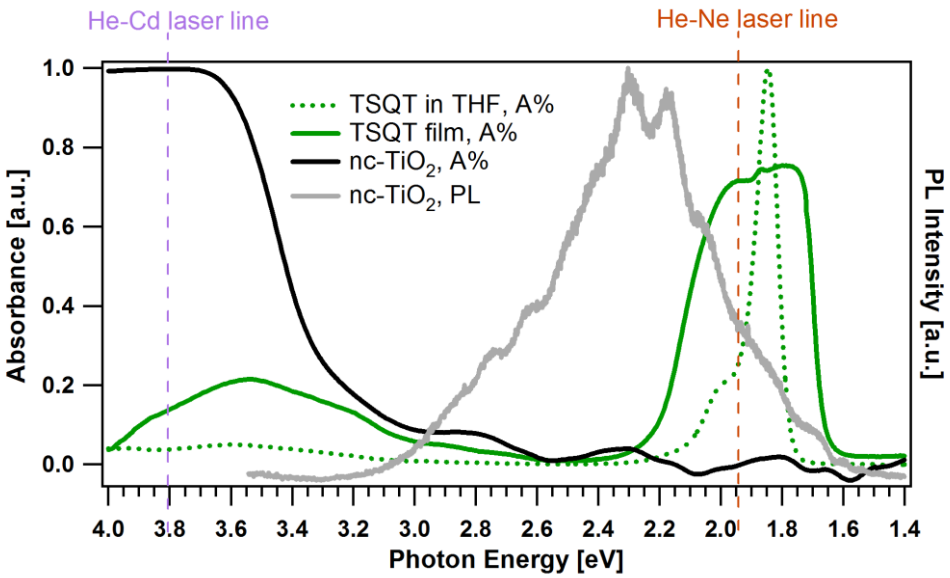

Figure 9.12: PL spectrum of the nc-TiO_2 layer (gray curve) shown together with the absorption spectra of TSQT molecules dispersed in THF and spin-coated on a quartz glass substrate (green curves) to demonstrate the spectral overlap, which indicates the likelihood of resonant exciton energy transfer from nc-TiO_2 to TSQT.

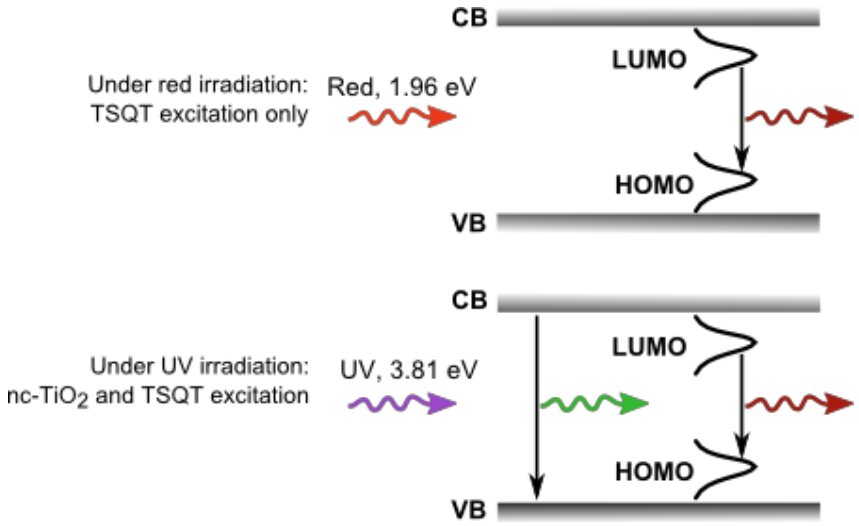

Figure 9.13: PL measurement technique employed in this study. Using a red laser for excitation, only the TSQT molecules in the composites are excited; thereby, only the emission of TSQT would then be observed. Under UV laser irradiation, the porous nc-TiO_2 matrix is excited. At this high energy excitation, the absorption of TSQT is very low while that of the nc-TiO_2 is high.

For the device operation of the composite design proposed by this study, light emission by direct electron injection from the conduction band of the nc-TiO_2 matrix to the LUMO of the TSQT guest molecules is not possible due to a large potential barrier at the interface. However, an emission due to Förster energy transfer is still possible due to the

spectral overlap of the nc-TiO_2 emission at the low photon energy end to the TSQT absorption. This spectral overlap is shown in Figure 9.12.

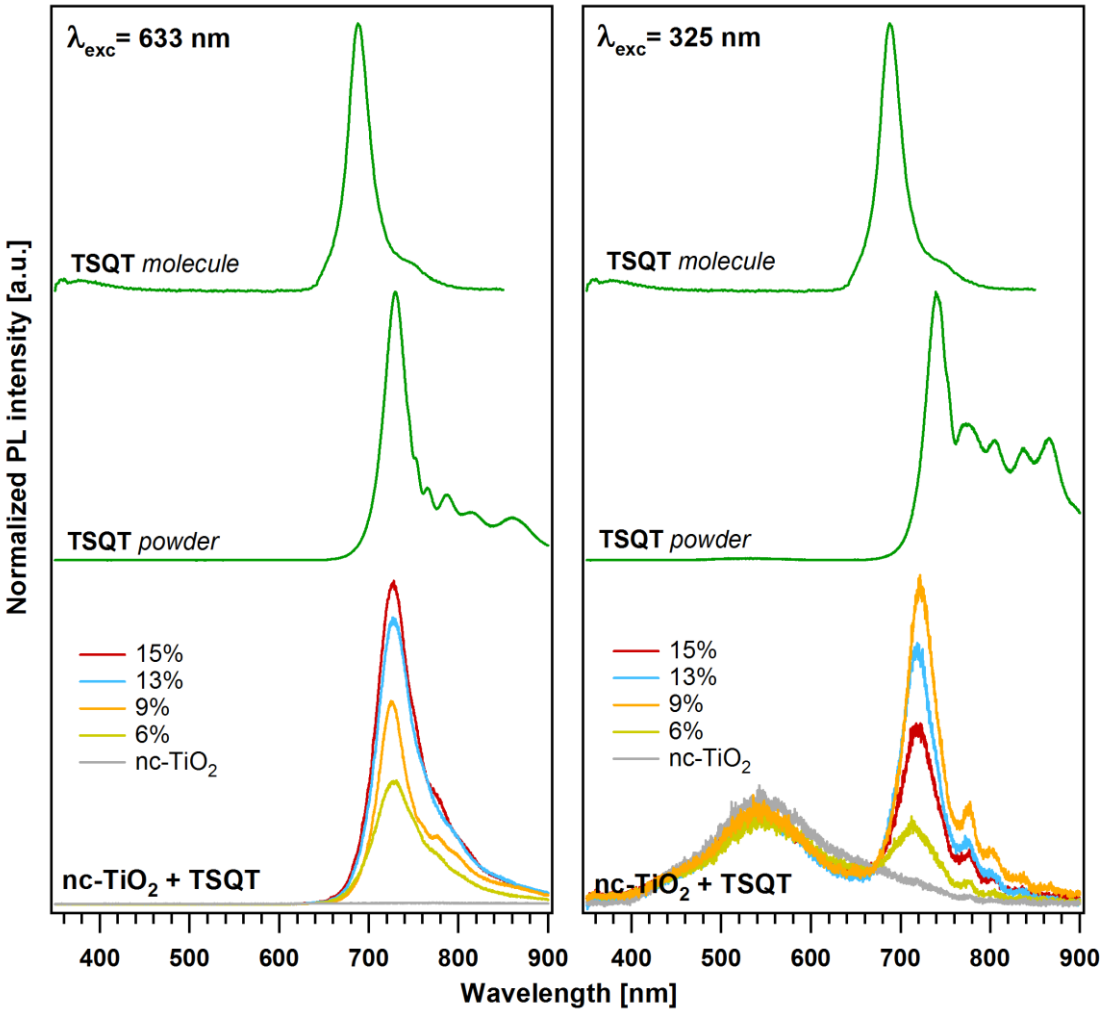

Figure 9.14: Superimposed PL spectra of nc-TiO_2 + TSQT composites under the red and UV laser irradiation. The PL spectra of the TSQT microcrystalline powder and molecule is included. The TSQT concentrations as indicated are obtained from the integrated TSQT PL intensities of the composites relative to that of the pristine TSQT powder all under the 633 nm excitation. Under UV excitation, dual luminescence is observed coming from both nc-TiO_2 and TSQT. However, the ~720 nm peak luminescence coming from the TSQT in the 9% composite (represented by the orange curve) is enhanced relative to the luminescence of the 13% and 15% composites (represented by the blue and red curves) that contain more TSQT.

For the direct measurement of the PL of nc-TiO_2 + TSQT composites at RT, two excitation laser sources (He-Ne and He-Cd lasers) were utilized. The measurement technique is illustrated in Figure 9.13. The He-Ne laser would be able to excite only the TSQT dye, while the He-Cd laser would excite both the nc-TiO_2 and TSQT. However, as can be seen from Figure 9.12, the excitation of the dye by the He-Cd laser would be weak because its absorption in the UV range is small. On top of this weak dye absorption, the nc-TiO_2 matrix of the composite would highly absorb most of the incident UV photons, in

competition against the embedded TSQT molecules. Any clear PL coming from the TSQT dye in the composite could, therefore, also be accounted to an energy transfer from the more excited nc-TiO_2 matrix.

Figure 9.14 shows the PL spectra obtained from four composite films of varying TSQT concentrations. The PL spectra of the TSQT microcrystalline powder and molecule (i.e. TSQT dispersed in THF) are included. The luminescence of the TSQT dye at the red end of the visible spectrum is observed from all of the composite samples indicating that the dye remains intact within the nc-TiO_2 matrix. Differences in the spectral lineshapes and peak positions are attributed to aggregations of the molecules, optophysical and chemical interactions with the matrix and modifications in the structures in the solid composite.[294, 296, 297] From the superimposed PL spectra of the four composites, the increased PL intensity of the 9% composite relative to the PL intensities of the 13% and 15% composites upon UV irradiation could be accounted to enhanced luminescence due to energy transfer from the highly excited nc-TiO_2 matrix. This is the same as the enhancement trend that was observed for the ZnSe + Ir(BPA) composites (Figure 6.14).

Chapter 10 Perspectives and outlook

The inorganic-organic hybrid system conceptualized in this study for active layers in light-emitting devices envisions an inorganic semiconductor matrix whose valence and conduction bands sandwich the HOMO and LUMO of an organic light-emitting dopant for an efficient transfer of electrons and holes from the matrix to the dopant during device operation. In the device configuration, the embedded organic dye acts as the radiative recombination sites for the charge carriers that are injected into the inorganic matrix.

Several challenges in realizing such a hybrid design were uncovered during the course of the research, which can be categorized basically into three major considerations: (1) energy level alignment between inorganic semiconductors and organic light-emitters, (2) chemical interactions at the interface of these two types of materials and (3) available deposition techniques for growing inorganic-organic sequential and composite layers.

From the results of our PES interface experiments, only the ZnSe - Ir(BPA) combination was feasible in implementing the energy level alignment of our proposed hybrid active layer design. Both the ZnO - Ir(BPA) and nc-TiO_2 - TSQT combinations exhibited an alignment where the organic dyes' HOMOs and LUMOs are offset higher relative to the valence and conduction bands of the inorganic semiconductors. This type of lineup is able to provide ample driving forces for hole transfer from the valence bands of the inorganic semiconductors to the HOMO of the organic dyes. Yet, on the other hand, the lineup does not encourage electron transfer from the conduction bands of the inorganic semiconductors to the LUMOs of the dyes due to the potential barriers for electrons at the interfaces.

Based on the derived energy band diagrams for the different inorganic-organic material combinations, we have experimentally observed that the position of the Fermi energy level in the pristine materials dictates on the resulting alignment of the energy levels. Both ZnO and nc-TiO_2 are highly *n*-type semiconductors. This could have led to the offset position of the HOMO and LUMO of Ir(BPA) and TSQT against the energy bands of ZnO and nc-TiO_2. So in conclusion, a more intrinsic type of inorganic semiconductor coupled with a large interface dipole would give a higher probability of an energy alignment with an organic dye as proposed by this study.

On a side note, the electroluminescence of a hybrid device could be speculated to be driven by direct charge injection, energy transfer, or both. In the case of a direct charge injection, the proposed energy level alignment for the inorganic and organic phases is necessary to the eventual radiative recombination at the organic dopant phases after charge transfer from the inorganic matrix. However, the alignment is not necessary for energy transfer. Generally, the relative sizes of the optical energy gaps are the ones which are relevant together with the specific requirements (as discussed in Chapter 2.3.1) for Förster

and Dexter energy transfer. In the photoluminescence experiments performed in this study to elucidate a possible energy transfer taking place in our hybrid (ZnSe+Ir(BPA) and nc-TiO_2+TSQT) material systems, the alignment of the energy levels is irrelevant.

In the derivation of energy band diagrams from PES experiments, it is common to discuss in terms of the energy gap together with the VBM (HOMO) and CBM (LUMO) energy positions of inorganic (organic) semiconductors. PES measures directly the energy level position of the VBM (HOMO) but not the CBM (LUMO) (which can be probed by the inverse photoemission spectroscopy (IPES)[60] technique). And in order to estimate the position of the CBM (LUMO) relative to the PES measured VBM (HOMO) position when IPES is unavailable, reported values of the transport gap or of the optically measured energy gap are used. This leads to minor offsets in the drawn energy band diagram, specifically at the energy levels of the unoccupied states (CBM and LUMO), because different energy gaps are obtained by different measurement techniques (Figure 2.8). Despite that only approximations can be drawn, the derived energy band diagrams, nevertheless, could still give valuable insight into the alignment of the materials' energy levels.

Even though the ZnSe-Ir(BPA) material system implements well the proposed design for the energy lineup as derived for the ZnSe/Ir(BPA) heterojunction and ZnSe+Ir(BPA) composite, it is not without any predicament. As was measured by UPS in the ZnSe/Ir(BPA) interface experiment, the lineshapes of the HOMO region spectra of the Ir(BPA) submonolayer during the initial Ir(BPA) depositions steps, where spatially-distributed Ir(BPA) molecules are in immediate contact to the ZnSe surface, are modified. This HOMO region modification hints at a chemical interaction between ZnSe and Ir(BPA), which cannot be quantified within the scope of this study. The effects of this chemical interaction is observed outstandingly once the deposition sequence is reversed -- that is, ZnSe is deposited[61] on top of an Ir(BPA) layer. The PES spectra of the initial ZnSe deposition steps reveals the intercalation of Zn atoms into the immediate Ir(BPA) layer at the interface and the formation of amorphous Se^0 phases that strongly compete against the formation of ZnSe. Together with these mixed phases at the interface, reduced selenium species and oxidized dye species are found as well. The reason for the existence of these additional two species may possibly be traced to the electronegativity of the oxygen[62] atoms that are in the structure of the dye and/or to the strong attraction of selenium to iridium. In any case, these

[60] Inverse photoemission spectroscopy (IPES) is a surface science technique that probes the unoccupied electronic structure of a sample by directing a collimated beam of electrons with a well-defined energy (<20 eV) onto the sample and then detecting the emitted photons in order to generate an energy spectrum (photon counts versus incident electron energy). The principle of IPES is that electrons can be absorbed by a material into unoccupied states above the Fermi level and that the photons emitted in the decay process can be detected to give information about the unoccupied states.
[61] As noted in Chapter 4, the thermal evaporation of ZnSe leads to a congruent vaporization that produces Zn and Se_2 fluxes.
[62] Oxygen is more electronegative than selenium.

are just scientific speculations, which remain unsubstantiated within the limitations of this study.

In the co-deposition of ZnSe and Ir(BPA) to obtain the composite matrix-dopant structure, similar observations as the Ir(BPA)/ZnSe bilayer are drawn. However, the amount of extra phases (i.e. intercalated Zn, amorphous Se^0, reduced Se, oxidized dye molecules) is much more reduced at the internal interfaces of the Ir(BPA) dopants and ZnSe matrix for composites with a low dye concentration as compared to the immediate interface region of the Ir(BPA)/ZnSe bilayer. Because of this, clear cut photoemission spectra for each of the ZnSe matrix and the Ir(BPA) dopant could still be obtained and an energy band diagram be estimated. And similar to the ZnSe/Ir(BPA) bilayer, this composite implements the proposed energy level alignment for the hybrid active layer design. On the other hand, for composites with a large Ir(BPA) dopant concentration, the contributions of the "extra" phases become significant, similar to the behavior found at the Ir(BPA)/ZnSe interface. For this case, no energy band diagram can be drawn for such a highly phase-mixed composite.

The disadvantage of the chemical interaction between ZnSe and Ir(BPA) is that the resulting reactive interface formed between these two materials could hinder efficient energy and charge transfer, impede charge carrier conduction, and instigate non-radiative recombination. If there is a possibility for a less chemically-reactive deposition method for ZnSe coupled with the possibility for a layered sequence and composite deposition with an organic semiconductor, then this would be worthwhile to look further into. As an additional note which is in line with this, chemical bath deposition (CBD) of ZnSe was actually attempted in this study. However, the experiment was unsuccessful as there was barely any ZnSe film formed on the ITO glass substrate; and all the more there was nothing formed when a solution of an organic solvent and organic molecules was added in order to possibly achieve a composite film by CBD.

Appendix A

Vocabulary for describing the quality of solid-state lighting devices

There are two main factors that have to be considered in assessing the quality of an SSL device: (1) how efficiently the electrical power supplied to the device is converted in to radiative power and (2) how that radiative power affects the eye.

Power conversion efficiency (PCE): This is the radiative power emitted by an SSL device divided by the electrical power input. Even if every electron and hole injected into an SSL device combine to create photons that eventually exit the device, the PCE will see be less than 100%. Due to ohmic losses, the electrical energy supplied to the electrons and holes is always greater than the energy released when electrons combine with holes.

Internal quantum efficiency (IQE): Not every injected electron-hole pair can yield an emitted photon. The IQE is the fraction of injected electrons that combines with holes to produce photons.

Light-extraction efficiency: LED chips in a SSL device typically have high refractive indices so that some of the photons produced are internally reflected within the device. The light-extraction efficiency is the fraction of photons that actually escape from the device.

External quantum efficiency (EQE): This is the product of the internal quantum efficiency and the light-extraction efficiency. The EQE multiplied by the ratio of the photon energy to the electrical energy supplied to the combining electron-hole pair yields the PCE.

Luminosity coefficient: Since the sensitivity of the human eye varies with color, a device emitting a watt of yellow light will be perceived as brighter than a device emitting a watt of blue light. The luminosity coefficient gives a relative scale of color visibility. It peaks at 680 for light with a wavelength of about 555 nm (yellow-green) and drops to 30 at 450 nm (blue) and to 70 at 650 nm (red).

Luminous flux: This is a measure of visual impact and is the radiated power multiplied by the luminosity coefficient.

Lumen (lm): This is the unit associated with the luminous flux when the radiated power is measured in watts.

Overall luminous efficiency or efficacy or performance: This is the luminous flux divided by the power input. It is expressed in units of lumens per watt. Equivalently, this is also the PCE multiplied by the luminosity coefficient.

Appendix B

Evaporation source calibration for determining deposition rates

In a source calibration experiment, a material is stepwise deposited on a clean, smooth, conductive substrate. The temperature of the source is nominally set at each deposition step by resistive heating using a power supply where the applied current and voltage can be varied. The temperature is monitored through a thermocouple that is attached to the crucible. The deposition time has to be considered carefully so as not to fully close the overlayer during the intermediate deposition steps so that photoemissions from the substrate can still be obtained. As presented in Chapter 3.1.5, the thickness of the overlayer at each deposition step can be determined from measured substrate and overlayer core line photoemissions. With the defined deposition times, the deposition rate for each step can then be established.

Figure B.1(a) is a diagram of a layer B, which has a thickness d_B, deposited on top of a substrate layer A. If the overlayer B is thin enough, then the x-ray radiation can reach layer A as well. In such a case, the core line photoemissions from both layers can be observed. From the integrated intensities of these photoemissions, the overlayer thickness (d_B) can be calculated in two ways:

(1) by considering the damping of a core line photoemission of the substrate layer A

$$I'_A = I^0_A exp\left(-\frac{\mathrm{d_B}}{\lambda(E_A)}\right)$$

$$\mathrm{d_B} = -\lambda(E_A)\ \ln\frac{I'_A}{I^0_A}$$

Equation B-1

where I^0_A and I'_A are the integrated intensities of a core line from the substrate layer A before and after the deposition of the overlayer B, respectively, and $\lambda(E_A)$ is the inelastic mean free path (IMFP) of the core line photoelectron from substrate layer A in the overlayer B,

(2) by considering the increase of a core line photoemission of the overlayer B

$$I'_B = I^\infty_B\left(1 - exp\left(-\frac{\mathrm{d_B}}{\lambda(E_B)}\right)\right)$$

$$\mathrm{d_B} = -\lambda(E_B)\ln\left(1 - \frac{I'_B}{I^\infty_B}\right)$$

Equation B-2

where I'_B is the corresponding integrated intensity of a core line from the deposited overlayer B, I^∞_B is the integrated intensity of the core line when the overlayer B is finally completely closed, and $\lambda(E_B)$ is the IMFP of the core line photoelectron from overlayer B within the overlayer B.

The IMFP of a photoelectron in a layer of a given material is obtained using the NIST database [382] and the respective kinetic energy of the photoelectron. In the database

calculations, the Gries (G1) equation is implemented to obtain the IMFP from predictive chemical formulas, which requires the stoichiometric chemical formula of the material and its density. The IMFP of In3d photoelectrons in ZnSe is 27.92 Å.

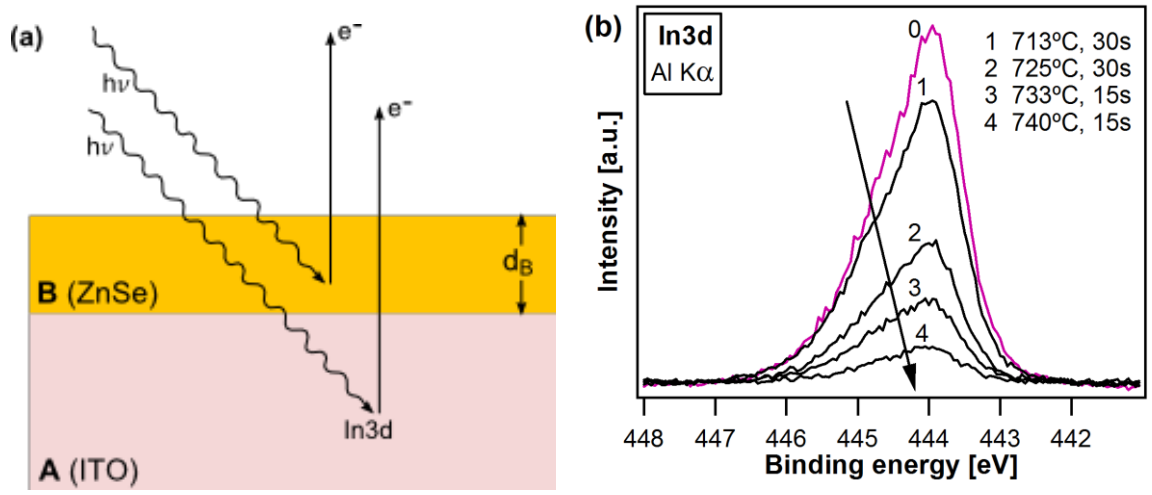

Figure B.1: (a) Schematic geometry for a layer model in obtaining layer thickness. The substrate is ITO on glass and the overlayer is ZnSe with a thickness of d_B. (b) Attenuation of the ITO In3d emission upon the step-wise deposition of ZnSe.

Figure B.1(b) is a sample spectra for the attenuation of the ITO substrate's In3d emission when ZnSe is stepwise deposited on the top. Using the integrated intensities of the In3d emissions and the ZnSe deposition times, the ZnSe layer thicknesses and deposition rates for all the steps can be calculated by using Equation B-1. By taking the source temperature (T_D) in Kelvin units and plotting on a logarithmic scale the deposition rate against ($1/T_D$), a linear equation can then be obtained from a linear fit. This equation then allows for the determination of the deposition rate from a given source temperature.

Appendix C

Calculations for the dopant volume percentage in a composite sample

Two models were developed in this study to obtain the amount of dye in the ZnSe+Ir(BPA) composites in terms of volume percentages.

C.1 Model I: Photoemission intensities of the measured core lines give the atom fractions for the composition of a homogeneous sample

The intensity of a photoemission line gives the number of detected photoelectrons per second, and is a product of several factors:

$$I = nf\sigma\theta y\lambda AT$$

Equation C-1

where n is the number of atoms of the element per cm^3 of the sample, f is the x-ray flux in photons/cm^2 s, σ is the photoelectric cross-section for the atomic orbital of interest in cm^2, θ is an angular efficiency factor for the instrumental arrangement based on the angle between the photon path and detected electron, y is the efficiency in the photoelectric process for formation of photoelectrons of the normal photoelectron energy, λ is the mean free path of the photoelectrons in the sample, A is the area of the sample from which photoelectrons are detected, and T is the detection efficiency for electrons emitted from the sample. Rearranging Equation C-1,

$$n = \frac{I}{f\sigma\theta y\lambda AT} = \frac{I}{ASF}$$

Equation C-2

where the denominator is condensed into a single definition- the atomic sensitivity factor[63], ASF.[164]

For the ZnSe+Ir(BPA) composite, its composition is obtained by calculating n from the integrated intensities of the Zn2p$_{3/2}$, Se3d, and Ir4f photoemissions (shown in Figures C.1 and C.2) and then considering the volumes of the Ir(BPA) dye and the unit cells of ZnSe and Se. By taking into account that there are 4 Zn and 4 Se atoms in a unit cell, which has a volume of ~182 Å^3, the total ZnSe volume in the composite can be derived from n. Since it is observed that there is an excess in selenium in the composites, its volume is also considered by taking its stable form, the trigonal Se.[383] The trigonal Se unit cell contains 3 Se atoms and has a volume of ~84 Å^3.[384] Meanwhile for the Ir(BPA) dye, since no experimental evidence points to dye degradation, then it is taken that each Ir atom represents a singular intact dye entity. Approximating a spherical volume of 542 Å (r ≈ 5 Å) for the asymmetric dye, the total volume of the dye in the composites is derived. Adding up the individual volumes of the ZnSe, Se and Ir(BPA) dye in the composite gives the total

[63] Calculating atomic fractions assumes that the ratio of ASFs for different elements is matrix-independent for all materials. For any spectrometer, it is possible to develop a set of relative values of ASFs for all of the elements.

analysis volume. The volume percentages as indicated in the figures below are of the dye molecules in the composite.

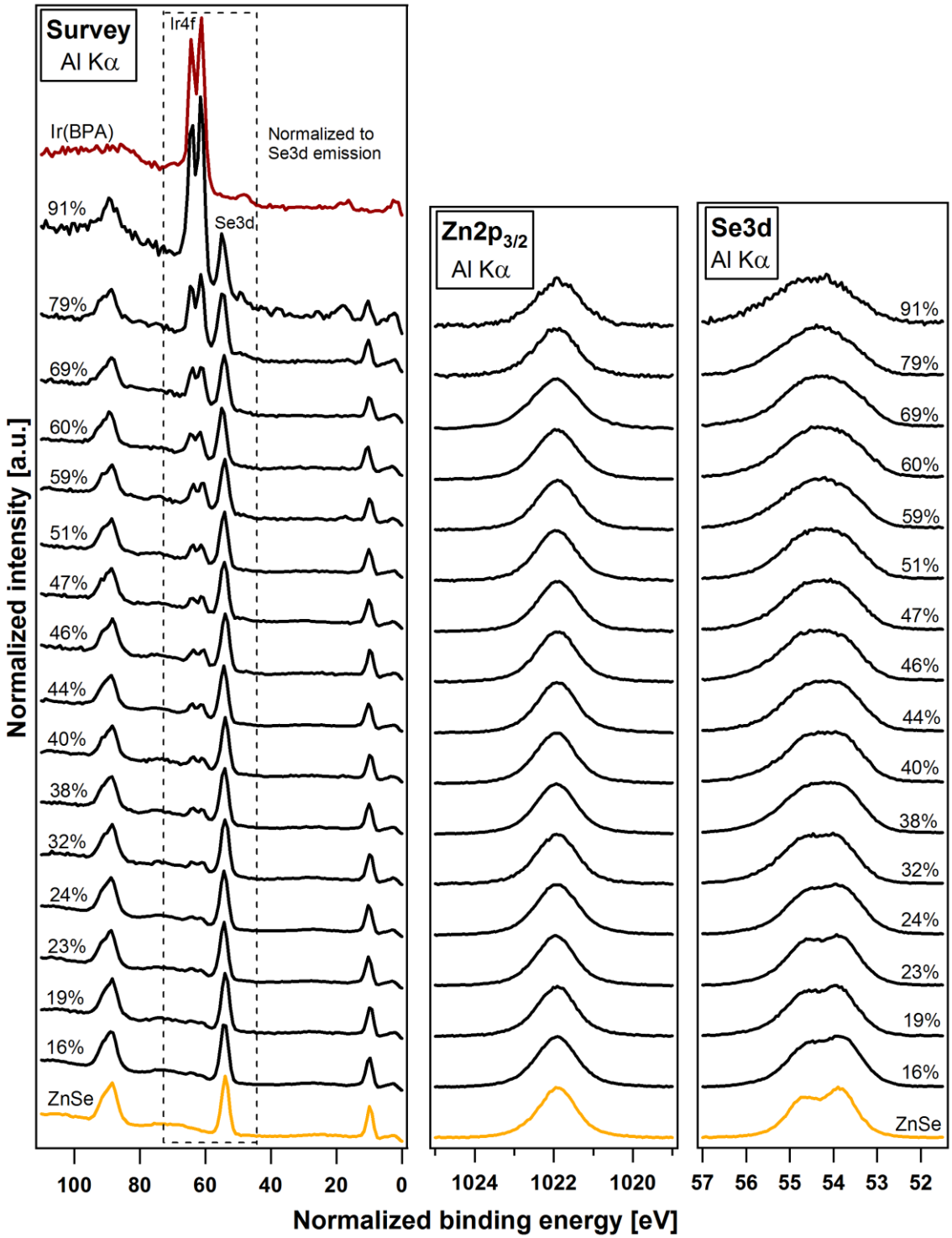

Figure C.1: Survey spectra, $Zn2p_{3/2}$ and Se3d detailed spectra of several composites. The survey spectra are normalized to the peak of the Se3d emission in order to obtain a rough visualization of the dye to ZnSe+Se ratio. The dye volume percentages are indicated.

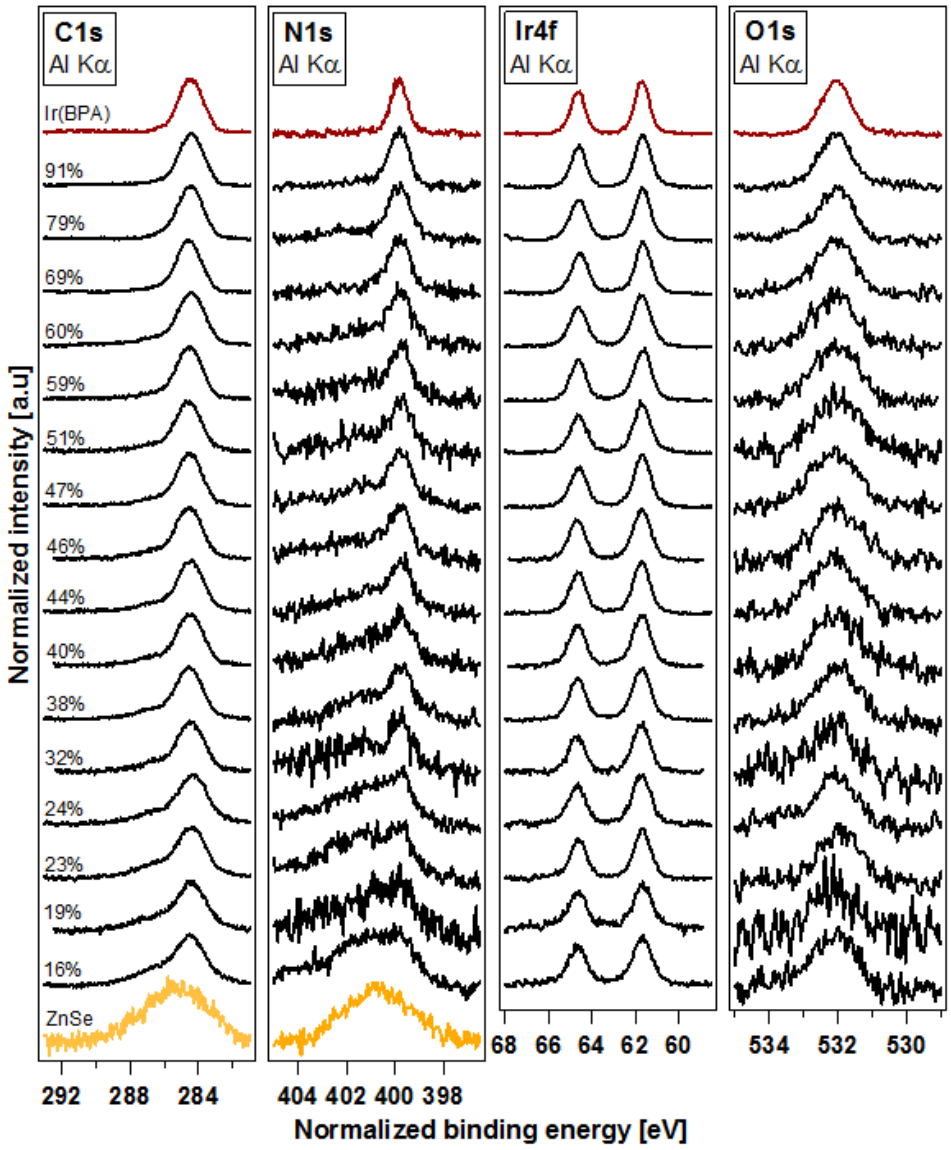

Figure C.2: Core line (C1s, N1s, Ir4f, O1s) emissions of the Ir(BPA) dye in several composites. The C1s and N1s emissions of the dye superimpose with broad Auger emissions coming from the ZnSe. The dye volume percentages are indicated.

A second approach (as presented in the succeeding section), based on the calibration of the composite emissions using the pristine material emissions, was derived in order to verify this first model. We found that the first model, where certain degrees of approximations were made in obtaining volume percentages, agrees with the second model.

C.2 Model II: Assuming a constant PES analysis volume and using the pure materials for calibrating the composite material

This model assumes that upon irradiation, the PES analysis volume is constant, as shown in Figure C.3 for pure samples, X and Y, and composite sample, X+Y.

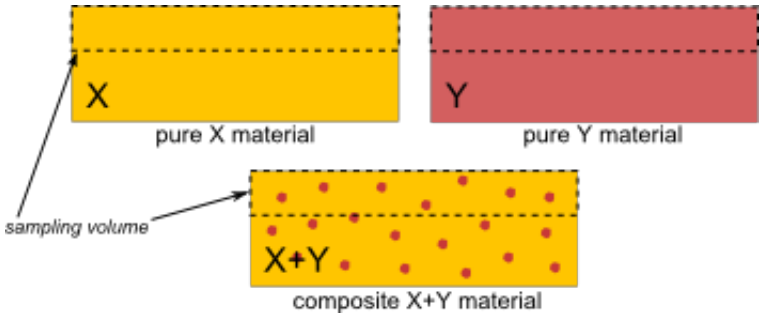

Figure C.3: Pure X and Y samples together with an X+Y composite sample. The PES analysis volume is constant in all three.

The analysis volume ratio for the pure X and Y samples is, therefore, equal to 1, that is:

$$\frac{vol\ \mathrm{X}\ (pure)}{vol\ \mathrm{Y}\ (pure)} = 1$$

Equation C-3

Considering that the intensity[64] of a core line emission from the X material ($I_{CL,X}$) and the intensity of a core line emission from the Y material ($I_{CL,Y}$) are produced only by atoms which are all within the analysis volumes of materials X and Y, respectively, then the following relation can hold:

$$\frac{vol\ \mathrm{X}\ (pure)}{vol\ \mathrm{Y}\ (pure)} = \frac{\mathrm{I_{CL,X}}\ (pure)}{\mathrm{I_{CL,Y}}\ (pure)}$$

Equation C-4

Now, when doping the X material to get the composite X+Y material, a certain proportion of the analysis volume is replaced by the Y material. The total volume consisting of the volume fractions of materials X and Y in the composite is equal to 1.

$$vol\ \mathrm{X}\ (composite) + vol\ \mathrm{Y}\ (composite) = 1$$

Equation C-5

Rewriting Equation C-5 yields,

$$vol\ \mathrm{Y}\ (composite) = \frac{1}{\frac{vol\ \mathrm{X}\ (composite)}{vol\ \mathrm{Y}\ (composite)} + 1}$$

Equation C-6

Similar to Equation C-4,

$$\frac{vol\ \mathrm{X}\ (composite)}{vol\ \mathrm{Y}\ (composite)} = \frac{\mathrm{I_{CL,X}}\ (composite)}{\mathrm{I_{CL,Y}}\ (composite)}$$

Equation C-7

[64] By "intensity" of a core line emission, what is always referred here is the core line's integrated intensity after background subtraction and atomic sensitivity factor normalization.

Using the core line intensities of the pure materials for calibrating the intensity ratio of the composite and relating them to the material volumes, we write

$$\frac{\frac{vol\ \mathrm{X}\ (composite)}{vol\ \mathrm{Y}\ (composite)}}{\frac{vol\ \mathrm{X}\ (pure)}{vol\ \mathrm{Y}\ (pure)}} = \frac{\frac{\mathrm{I}_{\mathrm{CL,X}}\ (composite)}{\mathrm{I}_{\mathrm{CL,Y}}\ (composite)}}{\frac{\mathrm{I}_{\mathrm{CL,X}}\ (pure)}{\mathrm{I}_{\mathrm{CL,Y}}\ (pure)}}$$

Equation C-8

Combining Equations C-3, C-6 and C-8, an expression for the volume fraction of the dopant material Y is obtained:

$$vol\ \mathrm{Y}\ (composite) = \frac{1}{\frac{\frac{\mathrm{I}_{\mathrm{CL,X}}\ (composite)}{\mathrm{I}_{\mathrm{CL,Y}}\ (composite)}}{\frac{\mathrm{I}_{\mathrm{CL,X}}\ (pure)}{\mathrm{I}_{\mathrm{CL,Y}}\ (pure)}} + 1}$$

Equation C-9

If the composite is homogeneous, then this composition within the analysis volume would be representative of the whole sample.

Appendix D

Additional J-V and I_{photo}-V data for Devices 19 and 21

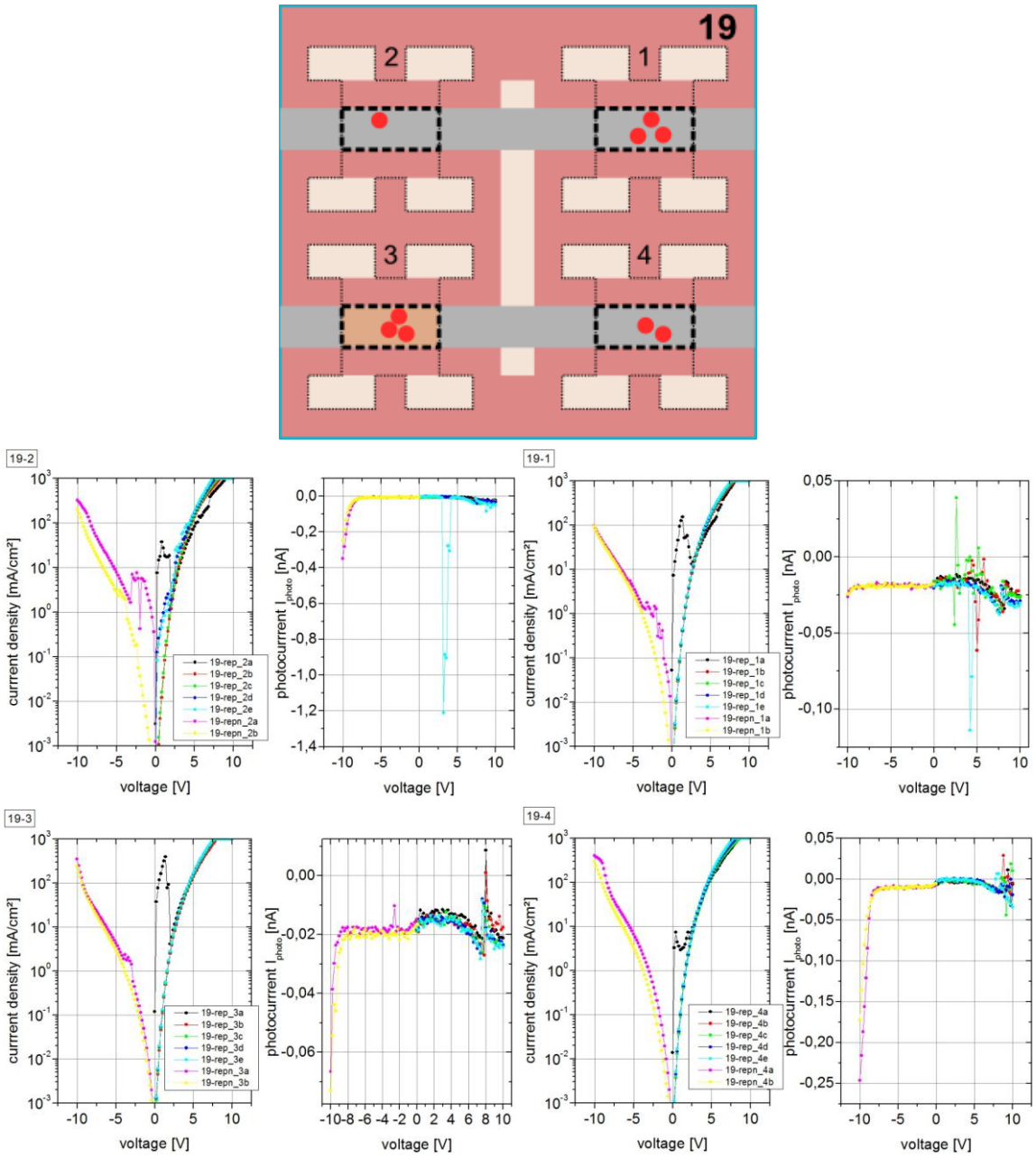

Figure D.1: Top-view schematic of Device 19 with its 4 devices (namely: 19-1, 19-2, 19-3 and 19-4). The current density versus applied voltage characteristics of the devices and the photocurrent generated on a silicon photodiode against the applied voltage on the devices are shown.

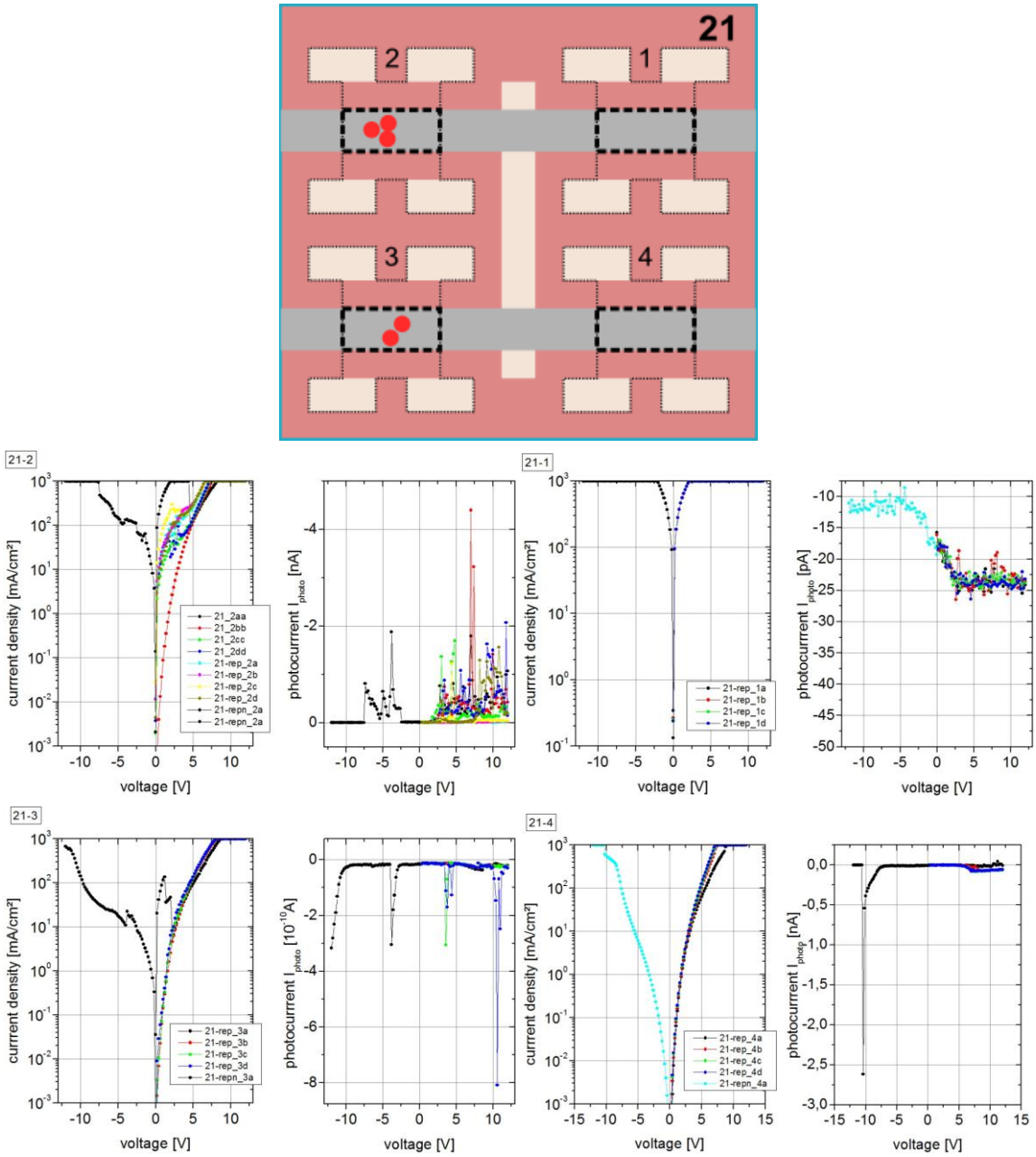

Figure D.2: Top-view schematic of Device 21 with its 4 devices (namely: 21-1, 21-2, 21-3 and 21-4). The current density versus applied voltage characteristics of the devices and the photocurrent generated on a silicon photodiode against the applied voltage on the devices are shown.

Appendix E

Additional photoelectron spectroscopy data for the nc-TiO_2 - TSQT system

E.1 The nc-TiO_2 film

The photoemission spectra shown in Figure E.1 were taken using a monochromatized Al Kα (hν=1486.6 eV) radiation source. The C1s emission present in the survey spectra may also demonstrate a contribution from residuals of the organic binder of the anatase nc-TiO_2 slurry used in the screen-printing deposition process.

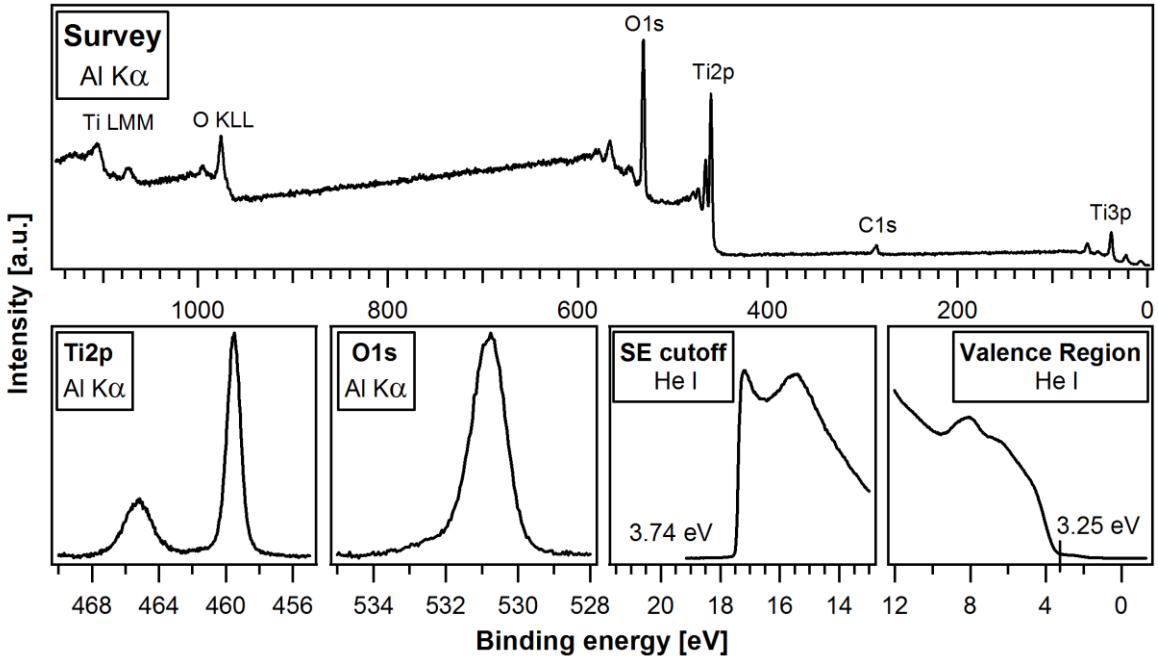

Figure E.1: Survey spectrum and detailed spectra of the Ti2p and O1s emissions from the pristine nc-TiO_2 layer, together with the spectra of the SE cutoff and valence region.

The Ti2p core line emission is a doublet: $Ti2p_{3/2}$ at 459.54 eV and $Ti2p_{1/2}$ at 465.21 eV. This gives a spin-orbit splitting of 5.67 eV. These emissions are unambiguously assigned to the Ti^{4+} oxidation state.

The O1s emission spectra contains a high binding energy shoulder with respect to the main emission. The main emission is accounted to bulk oxygen, while the shoulder to chemisorbed OH-groups or alternatively to oxygen attached to hydrogen atoms.[385-387]

E.2 The TSQT film

Figure E.2 shows the X-ray photoemission spectra of the pristine TSQT film drop-casted on an ITO glass substrate. The survey spectrum does not show emissions other than those from the elemental composition ($C_{66}H_{92}O_2S_2N_2$) of the dye. This additionally affirms the integrity of the deposition processed that was developed by the Surface Science group.

From calculations of the atom fractions using Equation 3-9, the stoichiometric composition of the dye is confirmed. The detailed spectra of the S2p and N1s emissions display only a single chemical species for S and N. This agrees with the dye composition. Peculiarly, the O1s emission seem to be a contribution of several O species.

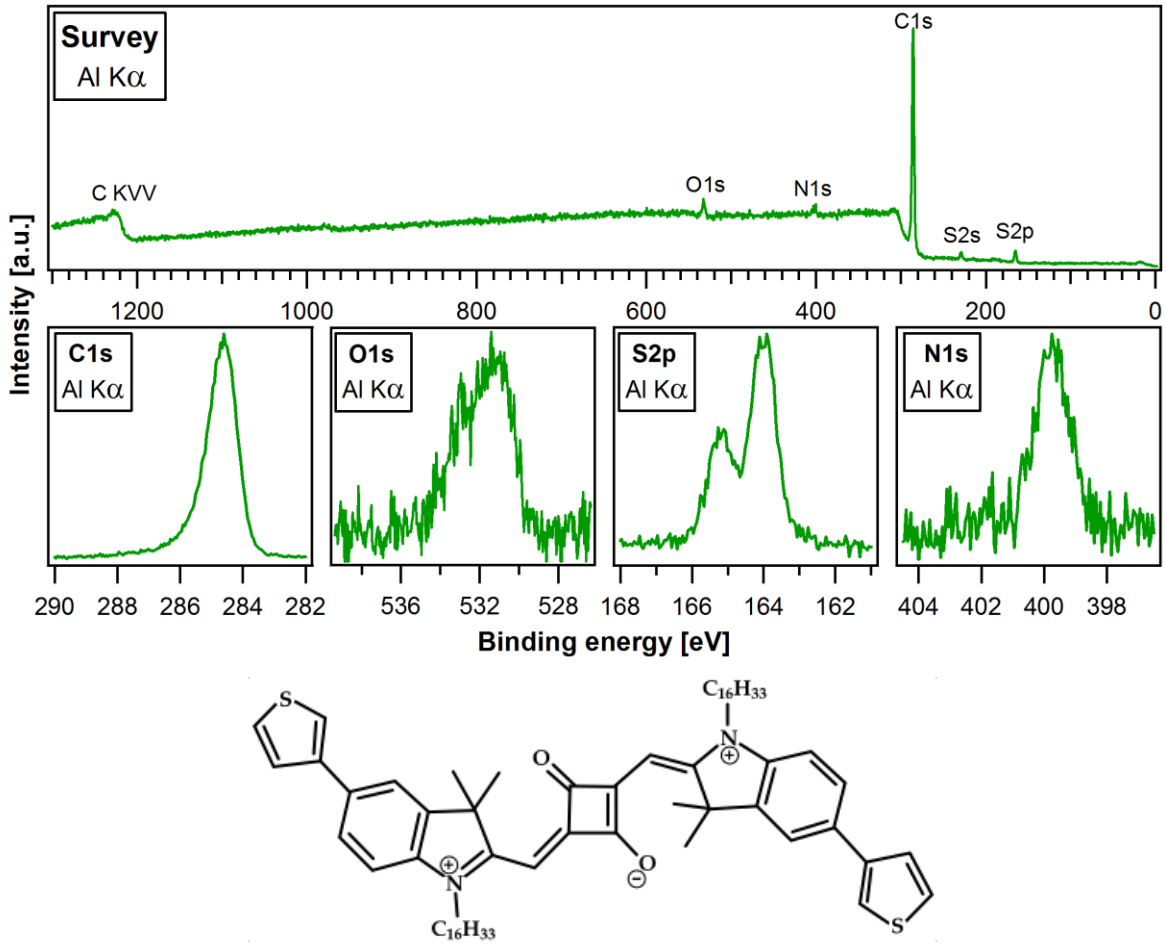

Figure E.2: Survey spectrum and detailed spectra of the C1s, O1s, S2p and N1s core line emissions from the pristine TSQT film drop-casted on an ITO glass substrate. The chemical structure of the dye is also shown.

E.3 The nc-TiO_2 + TSQT composite

The X-ray photoemission spectra from the composite are shown in Figure E.3. The dye concentration is too low to get a good signal-to-noise ratio for the emissions coming from the embedded TSQT molecules. The survey spectrum shows no traces of contaminations from the deposition of the TSQT into the porous nc-TiO_2 layer. The He I photoemission spectra display more the characteristics of the nc-TiO_2 matrix.

The He I valence region spectra of the pristine and composite layers are compiled in Figure E.4(a). The dip in the spectrum of the composite as point out by the arrow seems to hint at a possible chemical interaction between the nc-TiO_2 matrix and the TSQT guests. The surface sensitivity of XPS and UPS, however, cannot clearly show this interaction.

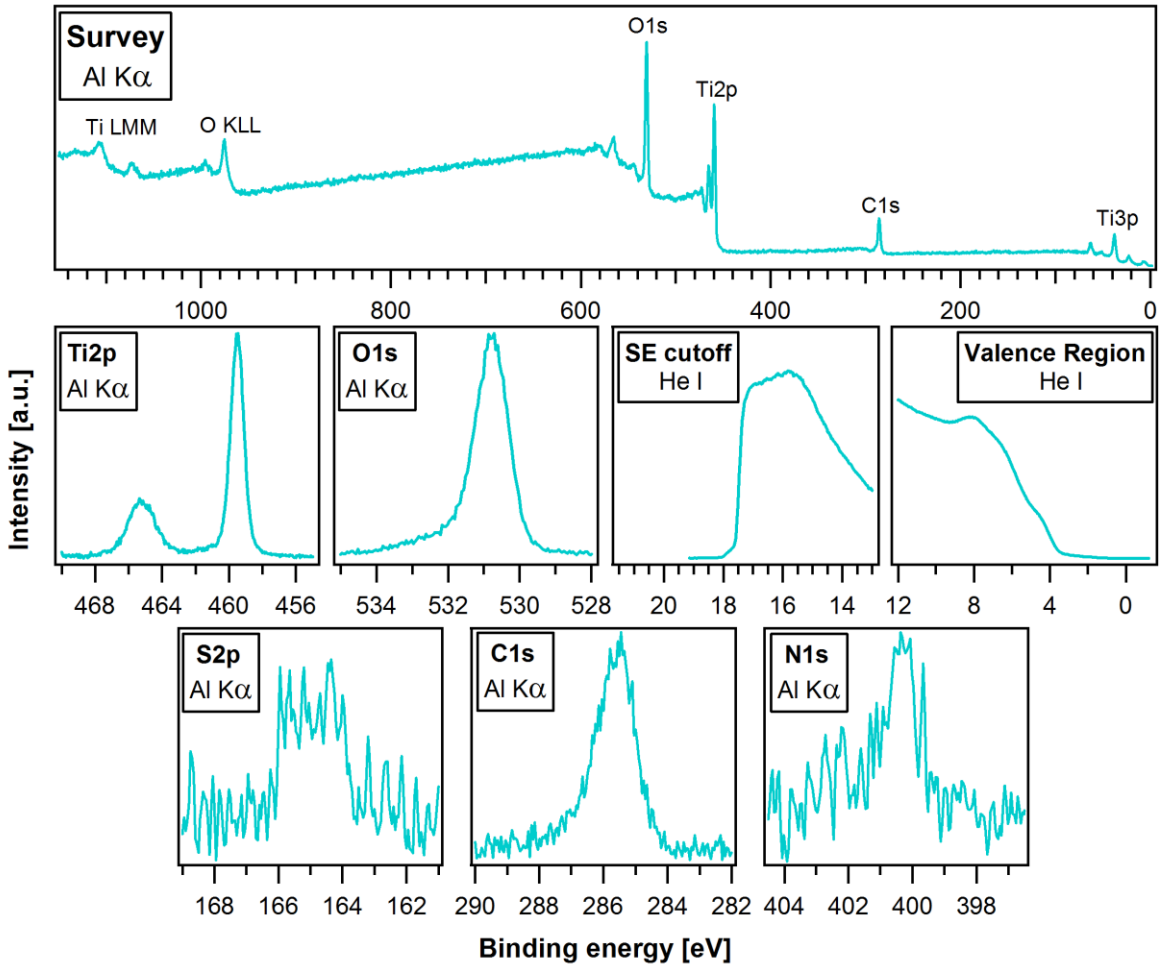

Figure E.3: Survey spectrum and detailed spectra of the Ti2p, O1s, S2p, C1s and N1s core line emissions from the nc-TiO_2 + TSQT composite, together with the spectra for the SE cutoff and valence region.

The valence band of anatase is made up predominantly of O2p states, with some Ti3d and Ti4sp character acquired through hybridization with the empty Ti 3d/4sp conduction band states. Figure E.4(b) shows the He II valence region spectra of the pristine and composite layers. The most prominent structure of the pristine nc-TiO_2 valence spectra is located within the 10 - 3.5 eV binding energy range. The emission in this region is mainly attributed to the O2p states.

In addition to the pristine and composite He II valence region spectra, the difference spectra that are obtained by subtracting the TSQT signal from the composite emission (given by the gray curve) and by subtracting the nc-TiO_2 signal from the composite emission (given by the light green curve) are shown. From the looks of it, subtracting the TSQT signal from the composite emission leads to a spectrum that closely resembles that of the pristine nc-TiO_2. On the other hand, subtracting the nc-TiO_2 signal from the composite emission leads to a spectrum that resembles that of the pristine TSQT.

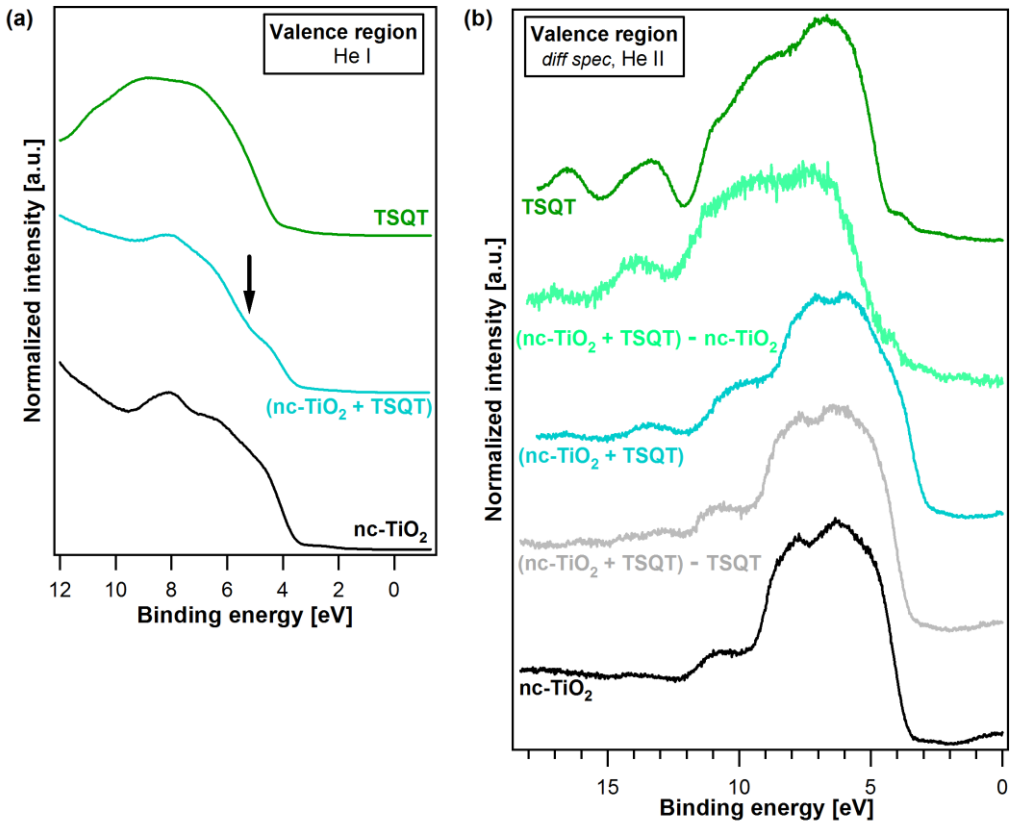

Figure E.4: Valence region emission spectra from the pristine nc-TiO_2 and TSQT layers and the nc-TiO_2 + TSQT composite under (a) He I and (b) He II photoexcitations. The gray and light green curves in (b) give the difference spectra of the He II valence region.

Because the observation of weak surface states is unlikely to be possible with XPS and UPS, some data from the initial PES measurements done using the SOLIAS at BESSY II are reviewed. The most fundamental problems (as there were many) encountered during the measurements were the fast degradation of the TSQT dye and some reactions of the nc-TiO_2 layer upon exposure to the synchrotron light that made the complete process of alignment, optimization and then spectral measurement at the same sample spot impossible. It has to be noted that a measurement at a singular spot is critical as deposition by drop-casting does not lead to a homogenous film due to the coffee ring effect. The spectra presented in Figure E.5 for the pristine nc-TiO_2 and composite nc-TiO_2 + TSQT were all taken from different, but adjacent, spots.

As hinted by the He I UPS measurement of the valence region, a chemical interaction between nc-TiO_2 and TSQT at their interface might be observed from the more surface-sensitive SXPS measurements. Spectral analyses were performed, and the resulting curve fits are shown in Figure E.5. As shown in the figure, the analysis for the pristine nc-TiO_2 layer reveals a state at the low binding energy shoulder of the main Ti2p emission spectrum coming from the Ti^{4+} state. This additional state is located at a binding energy that is lower by 1.58 eV from the Ti^{4+} emission peak and is assigned as the Ti^{3+} state that is associated to the oxygen vacancies on the surface.[388-391] Analysis of the gap region emission spectra of

the pristine nc-TiO_2 layer confirms the presence of deep (due to oxygen vacancies, V_O) and shallow (Ti3d states below the Fermi level, Ti3d<E_F) gap states.[392] Note that the V_O, Ti3d<E_F, and Ti^{3+} states are not observable from the less surface-sensitive XPS and UPS measurements (Figure E.1). Their presence in the SXPS measurements implies that they are states located at the surface.

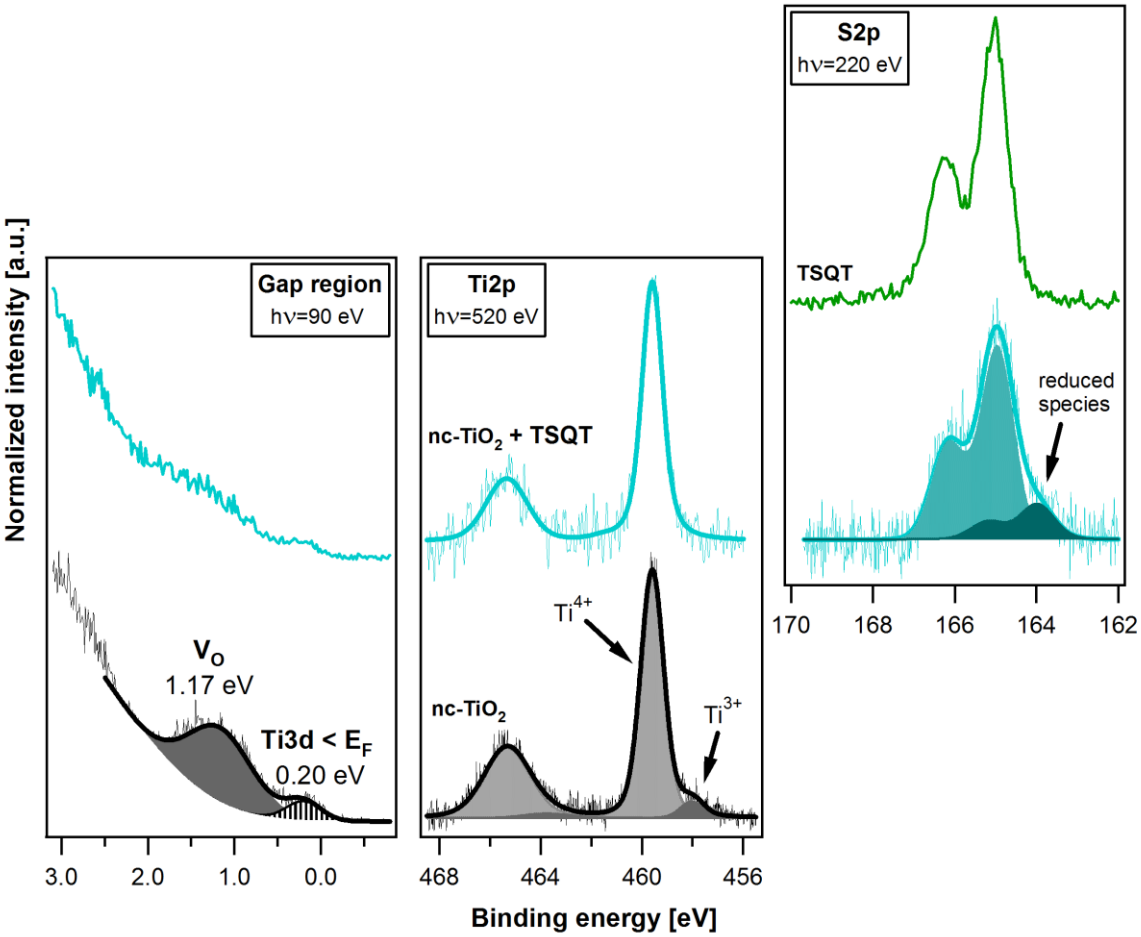

Figure E.5: Curve fitting analyses for the gap region, Ti2p and S2p emission spectra under synchrotron light irradation. Due to higher surface sensitivity, the V_O and Ti3d<E_F gap states, Ti^{3+} Ti2p and reduced S2p emissions are clearly resolved. The quenching of the V_O gap and Ti^{3+} species in the nc-TiO_2 + TSQT composite layer is accompanied by the reduction of guest TSQT molecules as evidenced by the presence of S2p species with a smaller binding energy.

After the drop-casting of TSQT into the nc-TiO_2 layer, the gap region and Ti2p emission spectra of the resulting composite layer reveals a "quenching" of the V_O and Ti^{3+} states. At the same time, a reduced S species appears in the S2p emission of the composite. This indicates a chemical reaction of the two materials where electrons are transferred from the nc-TiO_2 to the TSQT at their internal interfaces within the composite.

Bibliography

[1] W. Schivelbusch, Disenchanted Night: The Industrialization of Light in the Nineteenth Century, University of California Press, Berkeley, CA, 1988.
[2] R. Haitz, J.Y. Tsao, Solid-state lighting: 'The case' 10 years after and future prospects, Physica Status Solidi (a), 208 (2011) 17-29.
[3] J.Y. Tsao, M.H. Crawford, M.E. Coltrin, A.J. Fischer, D.D. Koleske, G.S. Subramania, G.T. Wang, J.J. Wierer, R.F. Karlicek, Toward Smart and Ultra-efficient Solid-State Lighting, Advanced Optical Materials, 2 (2014) 809-836.
[4] The Nobel Prize in Physics 2014.
http://www.nobelprize.org/nobel_prizes/physics/laureates/2014/press.html, in,
http://www.nobelprize.org/nobel_prizes/physics/laureates/2014/press.html.
[5] R. Wiley, OLED TV vs. AMOLED TV vs. LED TV: What's the difference? Definitions and Comparisons, in, http://oled.lcdtvbuyingguide.com/oled-tv-articles/oled-vs-amoled.html.
[6] IEA, Fact Sheet: Light's Labour's Lost, in, International Energy Agency, 2006.
[7] U.S. EIA, Commercial Buildings Energy Consumption Survey (CBECS), in: EIA (Ed.), 2008.
[8] IEA, OECD, Light's Labour's Lost: Policies for Energy-efficient Lighting, International Energy Agency, 2006.
[9] R. Haitz, F. Kish, J. Tsao, J. Nelson, The Case for a National Research Program on Semiconducor Lighting, in, Annual Forum of the Optoelectronics Industry Development Association, Washington DC, 1999.
[10] S.T. Tan, X.W. Sun, H.V. Demir, S.P. DenBaars, Advances in the LED Materials and Architectures for Energy-Saving Solid-State Lighting Toward Lighting Revolution, Photonics Journal, IEEE, 4 (2012) 613-619.
[11] I.L. Azevedo, M.G. Morgan, F. Morgan, The Transition to Solid-State Lighting, Proceedings of the IEEE, 97 (2009) 481-510.
[12] U.S. Government, Solid-State Lighting Research and Development Multi-Year Program Plan, in: D.o. Energy (Ed.), DOE, U.S.A., 2014.
[13] H.J. Round, A note on carborundum, Electrical World, 49 (1907) 309.
33 O.V. Lossev, CII. Luminous carborundum detector and detection effect and oscillations with crystals, The London, Edinburgh, and Dublin Philosophical Magazine and Journal of Science, 6 (1928) 1024-1044.
[15] N. Zheludev, The life and times of the LED - a 100-year history, Nature Photonics, 1 (2007) 189-192.
[16] N. Holonyak, S.F. Bevacqua, COHERENT (VISIBLE) LIGHT EMISSION FROM Ga(As1−xPx) JUNCTIONS, Applied Physics Letters, 1 (1962) 82-83.
[17] R.N. Hall, G.E. Fenner, J.D. Kingsley, T.J. Soltys, R.O. Carlson, Coherent Light Emission From GaAs Junctions, Physical Review Letters, 9 (1962) 366-368.
[18] M.I. Nathan, W.P. Dumke, G. Burns, F.H. Dill, G. Lasher, STIMULATED EMISSION OF RADIATION FROM GaAs p-n JUNCTIONS, Applied Physics Letters, 1 (1962) 62-64.
[19] T.M. Quist, R.H. Rediker, R.J. Keyes, W.E. Krag, B. Lax, A.L. McWhorter, H.J. Zeigler, SEMICONDUCTOR MASER OF GaAs, Applied Physics Letters, 1 (1962) 91-92.
[20] S. Nakamura, T. Mukai, M. Senoh, Candela-class high-brightness InGaN/AlGaN double-heterostructure blue-light-emitting diodes, Applied Physics Letters, 64 (1994) 1687-1689.
[21] H. Amano, N. Sawaki, I. Akasaki, Y. Toyoda, Metalorganic vapor phase epitaxial growth of a high quality GaN film using an AlN buffer layer, Applied Physics Letters, 48 (1986) 353-355.
[22] H. Amano, M. Kito, K. Hiramatsu, I. Akasaki, P-Type Conduction in Mg-Doped GaN Treated with Low-Energy Electron Beam Irradiation (LEEBI), Japanese Journal of Applied Physics, 28 (1989) L2112.
[23] A. Bergh, G. Craford, A. Duggal, R. Haitz, The promise and challenge of solid-state lighting, in: Physics Today, AIP Publishing, 2001, pp. 42-47.
[24] A. Bernanose, M. Comte, P. Vouaux, A New Method of Emission of Light by Certain Organic Compounds, J. Chim. Phys., 50 (1953) 64-68.
[25] H. Kallmann, M. Pope, Bulk Conductivity in Organic Crystals, Nature, 186 (1960) 31-33.
[26] M. Pope, H.P. Kallmann, P. Magnante, Electroluminescence in Organic Crystals, The Journal of Chemical Physics, 38 (1963) 2042-2043.
[27] W. Helfrich, W.G. Schneider, Recombination Radiation in Anthracene Crystals, Physical Review Letters, 14 (1965) 229-231.
[28] P.S. Vincett, W.A. Barlow, R.A. Hann, G.G. Roberts, Electrical conduction and low voltage blue electroluminescence in vacuum-deposited organic films, Thin Solid Films, 94 (1982) 171-183.

[29] C.W. Tang, S.A. VanSlyke, Organic electroluminescent diodes, Applied Physics Letters, 51 (1987) 913-915.
[30] J.H. Burroughes, D.D.C. Bradley, A.R. Brown, R.N. Marks, K. Mackay, R.H. Friend, P.L. Burns, A.B. Holmes, Light-emitting diodes based on conjugated polymers, Nature, 347 (1990) 539-541.
[31] M.A. Baldo, D.F. O'Brien, Y. You, A. Shoustikov, S. Sibley, M.E. Thompson, S.R. Forrest, Highly efficient phosphorescent emission from organic electroluminescent devices, Nature, 395 (1998) 151-154.
[32] C. Adachi, M.A. Baldo, M.E. Thompson, S.R. Forrest, Nearly 100% internal phosphorescence efficiency in an organic light-emitting device, Journal of Applied Physics, 90 (2001) 5048-5051.
[33] P.-W. Wang, Y.-J. Liu, C. Devadoss, P. Bharathi, J.S. Moore, Electroluminescent diodes from a single component emitting layer of dendritic macromolecules, Advanced Materials, 8 (1996) 237-241.
[34] P.L. Burn, S.C. Lo, I.D.W. Samuel, The Development of Light-Emitting Dendrimers for Displays, Advanced Materials, 19 (2007) 1675-1688.
[35] S.C. Lo, N.A.H. Male, J.P.J. Markham, S.W. Magennis, P.L. Burn, O.V. Salata, I.D.W. Samuel, Green Phosphorescent Dendrimer for Light-Emitting Diodes, Advanced Materials, 14 (2002) 975-979.
[36] V.L. Colvin, M.C. Schlamp, A.P. Alivisatos, Light-emitting diodes made from cadmium selenide nanocrystals and a semiconducting polymer, Nature, 370 (1994) 354-357.
[37] B.O. Dabbousi, M.G. Bawendi, O. Onitsuka, M.F. Rubner, Electroluminescence from CdSe quantum-dot/polymer composites, Applied Physics Letters, 66 (1995) 1316-1318.
[38] W.L. Sha, C.H. Liu, R.R. Alfano, Spectral and temporal measurements of laser action of Rhodamine 640 dye in strongly scattering media, Optics Letters, 19 (1994) 1922-1924.
[39] F. Hide, B.J. Schwartz, M.A. Díaz-García, A.J. Heeger, Laser emission from solutions and films containing semiconducting polymer and titanium dioxide nanocrystals, Chemical Physics Letters, 256 (1996) 424-430.
[40] S.A. Carter, J.C. Scott, P.J. Brock, Enhanced luminance in polymer composite light emitting devices, Applied Physics Letters, 71 (1997) 1145-1147.
[41] W. Rieß, H. Riel, P.F. Seidler, H. Vestweber, Organic–inorganic multilayer structures: a novel route to highly efficient organic light-emitting diodes, Synthetic Metals, 99 (1999) 213-218.
[42] C.-Y. Chang, F.-C. Tsao, C.-J. Pan, G.-C. Chi, H.-T. Wang, J.-J. Chen, F. Ren, D.P. Norton, S.J. Pearton, K.-H. Chen, L.-C. Chen, Electroluminescence from ZnO nanowire/polymer composite p-n junction, Applied Physics Letters, 88 (2006) 173503.
[43] R. Könenkamp, R.C. Word, M. Godinez, Ultraviolet Electroluminescence from ZnO/Polymer Heterojunction Light-Emitting Diodes, Nano Letters, 5 (2005) 2005-2008.
[44] S.-L. Zhao, P.-Z. Kan, Z. Xu, C. Kong, D.-W. Wang, Y. Yan, Y.-S. Wang, Electroluminescence of ZnO nanorods/MEH-PPV heterostructure devices, Organic Electronics, 11 (2010) 789-793.
[45] J.H. Na, M. Kitamura, M. Arita, Y. Arakawa, Hybrid p-n junction light-emitting diodes based on sputtered ZnO and organic semiconductors, Applied Physics Letters, 95 (2009) 253303.
[46] C.-Y. Lee, Y.-T. Haung, W.-F. Su, C.-F. Lin, Electroluminescence from ZnO nanoparticles/organic nanocomposites, Applied Physics Letters, 89 (2006) 231116.
[47] N. Bano, S. Zaman, A. Zainelabdin, S. Hussain, I. Hussain, O. Nur, M. Willander, ZnO-organic hybrid white light emitting diodes grown on flexible plastic using low temperature aqueous chemical method, Journal of Applied Physics, 108 (2010) 043103.
[48] M. Willander, Y.E. Lozovik, A. Wadeasa, O. Nur, A.G. Semenov, N.S. Vonorova, Light emission from different ZnO junctions and nanostructures, physica status solidi (a), 206 (2009) 853-859.
[49] A. Wadeasa, O. Nur, M. Willander, The effect of the interlayer design on the electroluminescence and electrical properties of n-ZnO nanorod/p-type blended polymer hybrid light emitting diodes, Nanotechnology, 20 (2009) 065710.
[50] J.H. Na, M. Kitamura, M. Arita, Y. Arakawa, Dual luminescence from organic/inorganic hybrid p-n junction light-emitting diodes, Applied Physics Letters, 94 (2009) 213302.
[51] S. Chanyawadee, P.G. Lagoudakis, R.T. Harley, D.G. Lidzey, M. Henini, Nonradiative exciton energy transfer in hybrid organic-inorganic heterostructures, Physical Review B, 77 (2008) 193402.
[52] H.J. Bolink, E. Coronado, D. Repetto, M. Sessolo, Air stable hybrid organic-inorganic light emitting diodes using ZnO as the cathode, Applied Physics Letters, 91 (2007) -.
[53] H.J. Bolink, E. Coronado, M. Sessolo, White Hybrid Organic–Inorganic Light-Emitting Diode Using ZnO as the Air-Stable Cathode, Chemistry of Materials, 21 (2009) 439-441.
[54] H.J. Bolink, H. Brine, E. Coronado, M. Sessolo, Phosphorescent Hybrid Organic–Inorganic Light-Emitting Diodes, Advanced Materials, 22 (2010) 2198-2201.
[55] M. Sessolo, H.J. Bolink, Hybrid Organic–Inorganic Light-Emitting Diodes, Advanced Materials, 23 (2011) 1829-1845.

[56] B.R. Lee, W. Lee, T.L. Nguyen, J.S. Park, J.-S. Kim, J.Y. Kim, H.Y. Woo, M.H. Song, Highly Efficient Red-Emitting Hybrid Polymer Light-Emitting Diodes via Förster Resonance Energy Transfer Based on Homogeneous Polymer Blends with the Same Polyfluorene Backbone, ACS Applied Materials & Interfaces, 5 (2013) 5690-5695.
[57] J.P. Zou, P. Le Rendu, I. Musa, S.H. Yang, Y. Dan, C.T. That, T.P. Nguyen, Investigation of the optical properties of polyfluorene/ZnO nanocomposites, Thin Solid Films, 519 (2011) 3997-4003.
[58] N. Mastour, Z. Ben Hamed, A. Benchaabane, M.A. Sanhoury, F. Kouki, Effect of ZnSe quantum dot concentration on the fluorescence enhancement of polymer P3HT film, Organic Electronics, 14 (2013) 2093-2100.
[59] D.K. Sinha, Y.N. Mohapatra, Charge trapping and electroluminescence at quantum dots embedded in a polymer matrix, Organic Electronics, 13 (2012) 1456-1462.
[60] M.C. Schlamp, X. Peng, A.P. Alivisatos, Improved efficiencies in light emitting diodes made with CdSe(CdS) core/shell type nanocrystals and a semiconducting polymer, Journal of Applied Physics, 82 (1997) 5837-5842.
[61] S. Coe, W.-K. Woo, M. Bawendi, V. Bulovic, Electroluminescence from single monolayers of nanocrystals in molecular organic devices, Nature, 420 (2002) 800-803.
[62] A.H. Mueller, M.A. Petruska, M. Achermann, D.J. Werder, E.A. Akhadov, D.D. Koleske, M.A. Hoffbauer, V.I. Klimov, Multicolor Light-Emitting Diodes Based on Semiconductor Nanocrystals Encapsulated in GaN Charge Injection Layers, Nano Letters, 5 (2005) 1039-1044.
[63] P.O. Anikeeva, J.E. Halpert, M.G. Bawendi, V. Bulović, Quantum Dot Light-Emitting Devices with Electroluminescence Tunable over the Entire Visible Spectrum, Nano Letters, 9 (2009) 2532-2536.
[64] P.O. Anikeeva, C.F. Madigan, J.E. Halpert, M.G. Bawendi, V. Bulović, Electronic and excitonic processes in light-emitting devices based on organic materials and colloidal quantum dots, Physical Review B, 78 (2008) 085434.
[65] P.O. Anikeeva, J.E. Halpert, M.G. Bawendi, V. Bulović, Electroluminescence from a Mixed Red−Green−Blue Colloidal Quantum Dot Monolayer, Nano Letters, 7 (2007) 2196-2200.
[66] J.W. Stouwdam, R.A.J. Janssen, Red, green, and blue quantum dot LEDs with solution processable ZnO nanocrystal electron injection layers, Journal of Materials Chemistry, 18 (2008) 1889-1894.
[67] L. Qian, Y. Zheng, J. Xue, P.H. Holloway, Stable and efficient quantum-dot light-emitting diodes based on solution-processed multilayer structures, Nat Photon, 5 (2011) 543-548.
[68] T.-H. Kim, K.-S. Cho, E.K. Lee, S.J. Lee, J. Chae, J.W. Kim, D.H. Kim, J.-Y. Kwon, G. Amaratunga, S.Y. Lee, B.L. Choi, Y. Kuk, J.M. Kim, K. Kim, Full-colour quantum dot displays fabricated by transfer printing, Nat Photon, 5 (2011) 176-182.
[69] S. Coe-Sullivan, Nanotechnology for displays: A potential breakthrough for OLED displays and LCDs, in: SID Display Week 2012, Society for Information Display, 2012.
[70] Y. Shirasaki, G.J. Supran, M.G. Bawendi, V. Bulovic, Emergence of colloidal quantum-dot light-emitting technologies, Nat Photon, 7 (2013) 13-23.
[71] N.C. Greenham, X. Peng, A.P. Alivisatos, Charge separation and transport in conjugated-polymer/semiconductor-nanocrystal composites studied by photoluminescence quenching and photoconductivity, Physical Review B, 54 (1996) 17628-17637.
[72] J.J.M. Halls, C.A. Walsh, N.C. Greenham, E.A. Marseglia, R.H. Friend, S.C. Moratti, A.B. Holmes, Efficient photodiodes from interpenetrating polymer networks, Nature, 376 (1995) 498-500.
[73] G. Yu, J. Gao, J.C. Hummelen, F. Wudl, A.J. Heeger, Polymer Photovoltaic Cells: Enhanced Efficiencies via a Network of Internal Donor-Acceptor Heterojunctions, Science, 270 (1995) 1789-1791.
[74] T. Mayer, U. Weiler, C. Kelting, D. Schlettwein, S. Makarov, D. Wöhrle, O. Abdallah, M. Kunst, W. Jaegermann, Silicon–organic pigment material hybrids for photovoltaic application, Solar Energy Materials and Solar Cells, 91 (2007) 1873-1886.
[75] A. Decker, S.-L. Suraru, O. Rubio-Pons, E. Mankel, M. Bockstedte, M. Thoss, F. Würthner, T. Mayer, W. Jaegermann, Toward Functional Inorganic/Organic Hybrids: Phenoxy-allyl-PTCDI Synthesis, Experimentally and Theoretically Determined Properties of the Isolated Molecule, Layer Characteristics, and the Interface Formation of Phenoxy-allyl-PTCDI on Si(111):H Determined by SXPS and DFT, The Journal of Physical Chemistry C, 115 (2011) 21139-21150.
[76] T. Mayer, U. Weiler, E. Mankel, W. Jaegermann, C. Kelting, D. Schlettwein, N. Baziakina, D. Wöhrle, Organic–inorganic hybrid composites for photovoltaics: Organic guest molecules embedded in μc-Si and ZnSe host matrices, Renewable Energy, 33 (2008) 262-266.
[77] S. Kappaun, C. Slugovc, E. List, Phosphorescent Organic Light-Emitting Devices: Working Principle and Iridium Based Emitter Materials, International Journal of Molecular Sciences, 9 (2008) 1527-1547.

[78] D.S. Ginger, N.C. Greenham, Photoinduced electron transfer from conjugated polymers to CdSe nanocrystals, Physical Review B, 59 (1999) 10622-10629.
[79] W. Jaegermann, Prof. Dr. (64823, Groß-Umstadt, DE), Mayer, Thomas, Dr. (64287, Darmstadt, DE), Arrangement for a composite made of inorganic matrix and embedded organic phase as optoelectronic active medium in light-emitting diode or other e.g. light emitting transistors, where an organic dye is embedded in an inorganic material, in, TU Darmstadt, 64289 (DE), 2012.
[80] S. Blumstengel, S. Sadofev, C. Xu, J. Puls, R.L. Johnson, H. Glowatzki, N. Koch, F. Henneberger, Electronic coupling in organic-inorganic semiconductor hybrid structures with type-II energy level alignment, Physical Review B, 77 (2008) 085323.
[81] I.G. Hill, A.J. Mäkinen, Z.H. Kafafi, Initial stages of metal/organic semiconductor interface formation, Journal of Applied Physics, 88 (2000) 889-895.
[82] I.G. Hill, A.J. Mäkinen, Z.H. Kafafi, Distinguishing between interface dipoles and band bending at metal/tris-(8-hydroxyquinoline) aluminum interfaces, Applied Physics Letters, 77 (2000) 1825-1827.
[83] S.T. Lee, Y.M. Wang, X.Y. Hou, C.W. Tang, Interfacial electronic structures in an organic light-emitting diode, Applied Physics Letters, 74 (1999) 670-672.
[84] S. Olthof, R. Meerheim, M. Schober, K. Leo, Energy level alignment at the interfaces in a multilayer organic light-emitting diode structure, Physical Review B, 79 (2009) 245308.
[85] R. Schlesinger, Y. Xu, O.T. Hofmann, S. Winkler, J. Frisch, J. Niederhausen, A. Vollmer, S. Blumstengel, F. Henneberger, P. Rinke, M. Scheffler, N. Koch, Controlling the work function of ZnO and the energy-level alignment at the interface to organic semiconductors with a molecular electron acceptor, Physical Review B, 87 (2013) 155311.
[86] S.Y. Kim, J.-L. Lee, In situ determination of interface dipole energy in organic light emitting diodes with iridium interfacial layer using synchrotron radiation photoemission spectroscopy, Applied Physics Letters, 89 (2006) 223515.
[87] A. Klein, T. Mayer, A. Thissen, W. Jaegermann, Photoelectron Spectroscopy in Materials Science and Physical Chemistry: Analysis of Composition, Chemical Bonding and Electronic Structure of Surfaces and Interfaces, Bunsen Magazin, 10 (2008) 124-139.
[88] J.R. Waldrop, R.W. Grant, S.P. Kowalczyk, E.A. Kraut, Measurement of semiconductor heterojunction band discontinuities by x-ray photoemission spectroscopy, Journal of Vacuum Science & Technology A, 3 (1985) 835-841.
[89] S. Reineke, F. Lindner, G. Schwartz, N. Seidler, K. Walzer, B. Lussem, K. Leo, White organic light-emitting diodes with fluorescent tube efficiency, Nature, 459 (2009) 234-238.
[90] Y. Sun, N.C. Giebink, H. Kanno, B. Ma, M.E. Thompson, S.R. Forrest, Management of singlet and triplet excitons for efficient white organic light-emitting devices, Nature, 440 (2006) 908-912.
[91] S. Lamansky, P. Djurovich, D. Murphy, F. Abdel-Razzaq, H.-E. Lee, C. Adachi, P.E. Burrows, S.R. Forrest, M.E. Thompson, Highly Phosphorescent Bis-Cyclometalated Iridium Complexes: Synthesis, Photophysical Characterization, and Use in Organic Light Emitting Diodes, Journal of the American Chemical Society, 123 (2001) 4304-4312.
[92] Y. Chi, P.-T. Chou, Transition-metal phosphors with cyclometalating ligands: fundamentals and applications, Chemical Society Reviews, 39 (2010) 638-655.
[93] M.A. Baldo, S. Lamansky, P.E. Burrows, M.E. Thompson, S.R. Forrest, Very high-efficiency green organic light-emitting devices based on electrophosphorescence, Applied Physics Letters, 75 (1999) 4-6.
[94] P.I. Djurovich, M.E. Thompson, Chapter 3, in: Highly Efficient OLEDs with Phosphorescent Materials; Yersin, H., Wiley-VCH, Berlin, 2007, pp. 131-161.
[95] M.E. Thompson, P.I. Djurovich, S. Barlow, S.R. Marder, Comprehensive Organmetallic Chemistry, in: Comprehensive Organometallic Chemistry; O'Hare, D., Elsevier, Oxford, 2007, pp. 101−194.
[96] H. Yersin, A.F. Rausch, R. Czerwieniec, T. Hofbeck, T. Fischer, The triplet state of organo-transition metal compounds. Triplet harvesting and singlet harvesting for efficient OLEDs, Coordination Chemistry Reviews, 255 (2011) 2622-2652.
[97] A.C. Jacko, R.H. McKenzie, B.J. Powell, Models of organometallic complexes for optoelectronic applications, Journal of Materials Chemistry, 20 (2010) 10301-10307.
[98] J. Koenigsberger , K. Schilling On electrical conductivity in fixed elements and compounds I. Minimum resistance, testing on electron behaviour, use of dissociation formula, Ann. Phys., 32 (1910) 179-230.
[99] M. Volmer, The different photoelectrical occurrences on anthracene, their connections to each other, to fluorescence and dianthracene formation, Ann. Phys., 40 (1913) 775-796.
[100] H. Naarmann, Electrically Conducting Polymers, in: Ullmann's Encyclopedia of Industrial Chemistry, Wiley-VCH Verlag GmbH & Co. KGaA Weinheim, 2000.

[101] H. Ishii, K. Sugiyama, E. Ito, K. Seki, Energy Level Alignment and Interfacial Electronic Structures at Organic/Metal and Organic/Organic Interfaces, Advanced Materials, 11 (1999) 605-625.
[102] D. Schlettwein, K. Hesse, N.E. Gruhn, P.A. Lee, K.W. Nebesny, N.R. Armstrong, Electronic Energy Levels in Individual Molecules, Thin Films, and Organic Heterojunctions of Substituted Phthalocyanines, The Journal of Physical Chemistry B, 105 (2001) 4791-4800.
[103] A. Gassmann, C. Melzer, Organic Semiconductors and Devices, in: T.U. Darmstadt (Ed.) Lecture Script, 2011.
[104] W. Brütting, Introduction to the Physics of Organic Semiconductors, in: W. Brütting (Ed.) Physics of Organic Semiconductors, WILEY-VCH Verlag GmbH & Co. KGaA, Weinheim, Germany, 2005.
[105] J. Maibach, Preparation and characterization of solution-processed organic semiconductor interfaces: Electronic properties of thiophene-fullerence based donor-acceptor systems, in: T.U. Darmstadt (Ed.) Ph.D. Thesis, Technische Universität Darmstadt, Darmstadt, 2014.
[106] I.G. Hill, A. Kahn, Z.G. Soos, J.R.A. Pascal, Charge-separation energy in films of π-conjugated organic molecules, Chemical Physics Letters, 327 (2000) 181-188.
[107] E.A. Silinsh, V.A. Kolesnikov, I.J. Muzikante, D.R. Balode, On Charge Carrier Photogeneration Mechanisms in Organic Molecular Crystals, Physica Status Solidi (b), 113 (1982) 379-393.
[108] S. Krause, M.B. Casu, A. Schöll, E. Umbach, Determination of transport levels of organic semiconductors by UPS and IPS, New Journal of Physics, 10 (2008) 085001.
[109] B.A. Gregg, Bilayer molecular solar cells on spin-coated TiO2 substrates, Chemical Physics Letters, 258 (1996) 376-380.
[110] B.A. Gregg, M.A. Fox, A.J. Bard, Photovoltaic effect in symmetrical cells of a liquid crystal porphyrin, The Journal of Physical Chemistry, 94 (1990) 1586-1598.
[111] I.H. Campbell, T.W. Hagler, D.L. Smith, J.P. Ferraris, Direct Measurement of Conjugated Polymer Electronic Excitation Energies Using Metal/Polymer/Metal Structures, Physical Review Letters, 76 (1996) 1900-1903.
[112] M. Pope, C.E. Swenberg, Electronic Processes in Organic Crystals and Polymers, Oxford University Press, New York, 1999.
[113] H. Yersin, Triplet Emitters for OLED Applications. Mechanisms of Exciton Trapping and Control of Emission Properties, in: Transition Metal and Rare Earth Compounds, Springer Berlin Heidelberg, 2004, pp. 1-26.
[114] S. Lamansky, R.C. Kwong, M. Nugent, P.I. Djurovich, M.E. Thompson, Molecularly doped polymer light emitting diodes utilizing phosphorescent Pt(II) and Ir(III) dopants, Organic Electronics, 2 (2001) 53-62.
[115] S. Braun, W.R. Salaneck, M. Fahlman, Energy-Level Alignment at Organic/Metal and Organic/Organic Interfaces, Advanced Materials, 21 (2009) 1450-1472.
[116] N.D. Lang, W. Kohn, Theory of Metal Surfaces: Work Function, Physical Review B, 3 (1971) 1215-1223.
[117] N.D. Lang, W. Kohn, Theory of Metal Surfaces: Charge Density and Surface Energy, Physical Review B, 1 (1970) 4555-4568.
[118] N.D. Lang, Interaction between Closed-Shell Systems and Metal Surfaces, Physical Review Letters, 46 (1981) 842-845.
[119] P.S. Bagus, V. Staemmler, C. Wöll, Exchangelike Effects for Closed-Shell Adsorbates: Interface Dipole and Work Function, Physical Review Letters, 89 (2002) 096104.
[120] Y. Morikawa, H. Ishii, K. Seki, Theoretical study of \textbf{ \textit{n} } -alkane adsorption on metal surfaces, Physical Review B, 69 (2004) 041403.
[121] P.S. Bagus, D. Käfer, G. Witte, C. Wöll, Work Function Changes Induced by Charged Adsorbates: Origin of the Polarity Asymmetry, Physical Review Letters, 100 (2008) 126101.
[122] W. Osikowicz, X. Crispin, C. Tengstedt, L. Lindell, T. Kugler, W.R. Salaneck, Transparent low-work-function indium tin oxide electrode obtainedby molecular scale interface engineering, Applied Physics Letters, 85 (2004) 1616-1618.
[123] L. Lindell, M. Unge, W. Osikowicz, S. Stafström, W.R. Salaneck, X. Crispin, M.P. de Jong, Integer charge transfer at the tetrakis(dimethylamino)ethylene/Au interface, Applied Physics Letters, 92 (2008) 163302.
[124] H. Vázquez, Y.J. Dappe, J. Ortega, F. Flores, Energy level alignment at metal/organic semiconductor interfaces: “Pillow” effect, induced density of interface states, and charge neutrality level, The Journal of Chemical Physics, 126 (2007) 144703.
[125] X. Crispin, V. Geskin, A. Crispin, J. Cornil, R. Lazzaroni, W.R. Salaneck, J.-L. Brédas, Characterization of the Interface Dipole at Organic/ Metal Interfaces, Journal of the American Chemical Society, 124 (2002) 8131-8141.

[126] X. Crispin, Interface dipole at organic/metal interfaces and organic solar cells, Solar Energy Materials and Solar Cells, 83 (2004) 147-168.
[127] H. Yamane, D. Yoshimura, E. Kawabe, R. Sumii, K. Kanai, Y. Ouchi, N. Ueno, K. Seki, Electronic structure at highly ordered organic/metal interfaces: Pentacene on Cu(110), Physical Review B, 76 (2007) 165436.
[128] R. Dudde, B. Reihl, Complete electronic structure of oriented films of hexatriacontane, Chemical Physics Letters, 196 (1992) 91-96.
[129] D. Yoshimura, H. Ishii, Y. Ouchi, E. Ito, T. Miyamae, S. Hasegawa, K.K. Okudaira, N. Ueno, K. Seki, Angle-resolved ultraviolet photoelectron spectroscopy and theoretical simulation of a well-ordered ultrathin film of tetratetracontane on Cu(100): Molecular orientation and intramolecular energy-band dispersion, Physical Review B, 60 (1999) 9046-9060.
[130] E. Ito, H. Oji, H. Ishii, K. Oichi, Y. Ouchi, K. Seki, Interfacial electronic structure of long-chain alkane/metal systems studied by UV-photoelectron and metastable atom electron spectroscopies, Chemical Physics Letters, 287 (1998) 137-142.
[131] A. Kahn, N. Koch, W. Gao, Electronic structure and electrical properties of interfaces between metals and π-conjugated molecular films, Journal of Polymer Science Part B: Polymer Physics, 41 (2003) 2529-2548.
[132] R.L. Anderson, Germanium-Gallium Arsenide Heterojunctions [Letter to the Editor], IBM Journal of Research and Development, 4 (1960) 283-287.
[133] R.L. Anderson, Experiments on Ge-GaAs heterojunctions, Solid-State Electronics, 5 (1962) 341-351.
[134] N. Debbar, D. Biswas, P. Bhattacharya, Conduction-band offsets in pseudomorphic InGaAs/AlGaAs quantum wells measured by deep-level transient spectroscopy, Physical Review B, 40 (1989) 1058-1063.
[135] J. Bardeen, Surface States and Rectification at a Metal Semi-Conductor Contact, Physical Review, 71 (1947) 717-727.
[136] C. Hein, Anpassung der elektronischen struktur an organischen heterokontakten, in: T.U. Darmstadt (Ed.) Ph.D. Thesis, Technische Universität Darmstadt, Darmstadt, 2012.
[137] M. Fahlman, A. Crispin, X. Crispin, S.K.M. Henze, M.P.d. Jong, W. Osikowicz, C. Tengstedt, W.R. Salaneck, Electronic structure of hybrid interfaces for polymer-based electronics, Journal of Physics: Condensed Matter, 19 (2007) 183202.
[138] J. Hwang, A. Wan, A. Kahn, Energetics of metal–organic interfaces: New experiments and assessment of the field, Materials Science and Engineering: R: Reports, 64 (2009) 1-31.
[139] J. Hwang, E.-G. Kim, J. Liu, J.-L. Brédas, A. Duggal, A. Kahn, Photoelectron Spectroscopic Study of the Electronic Band Structure of Polyfluorene and Fluorene-Arylamine Copolymers at Interfaces, The Journal of Physical Chemistry C, 111 (2007) 1378-1384.
[140] Y. Zou, L. Kilian, A. Schöll, T. Schmidt, R. Fink, E. Umbach, Chemical bonding of PTCDA on Ag surfaces and the formation of interface states, Surface Science, 600 (2006) 1240-1251.
[141] L. Romaner, G. Heimel, J.-L. Brédas, A. Gerlach, F. Schreiber, R.L. Johnson, J. Zegenhagen, S. Duhm, N. Koch, E. Zojer, Impact of Bidirectional Charge Transfer and Molecular Distortions on the Electronic Structure of a Metal-Organic Interface, Physical Review Letters, 99 (2007) 256801.
[142] H. Vázquez, R. Oszwaldowski, P. Pou, J. Ortega, R. Pérez, F. Flores, A. Kahn, Dipole formation at metal/PTCDA interfaces: Role of the Charge Neutrality Level, EPL (Europhysics Letters), 65 (2004) 802.
[143] H. Vázquez, F. Flores, R. Oszwaldowski, J. Ortega, R. Pérez, A. Kahn, Barrier formation at metal–organic interfaces: dipole formation and the charge neutrality level, Applied Surface Science, 234 (2004) 107-112.
[144] H. Vázquez, F. Flores, A. Kahn, Induced Density of States model for weakly-interacting organic semiconductor interfaces, Organic Electronics, 8 (2007) 241-248.
[145] F. Flores, C. Tejedor, On the formation of semiconductor interfaces, Journal of Physics C: Solid State Physics, 20 (1987) 145.
[146] T. Mayer, C. Hein, E. Mankel, W. Jaegermann, M.M. Müller, H.-J. Kleebe, Fermi level positioning in organic semiconductor phase mixed composites: The internal interface charge transfer doping model, Organic Electronics, 13 (2012) 1356-1364.
[147] C. Hein, E. Mankel, T. Mayer, W. Jaegermann, Engineering the electronic structure of the CuPc/BPE-PTCDI interface by WO3 doping of CuPc, physica status solidi (a), 206 (2009) 2757-2762.
[148] S. Hüfner, Photoelectron Spectroscopy: Principles and Applications. 2nd Edition., Springer, Berlin/Heidelberg, 1996.
[149] M. Kibel, Chapter 7, in: X-ray Photoelectron Spectroscopy, Springer, 1992, pp. 165-187.
[150] W. Schattke, M. Van Hove, F. Garcia de Abajo, M. Diez, R., N. Mannella, Chapter 2, in: Overview of Core and Valence Photoemission, Wiley-VCH, 2003, pp. 50-116.
[151] L. Hedin, Chapter 3, in: General Theory of Core Electron Photoemission, Wiley-VCH, 2003, pp. 116-141.

[152] J. Vickerman, G. I., Surface Analysis: The Principal Techniques, in, Johny Wiley & Sons Ltd., United Kingdom, 2009.
[153] M. Cardona, L. Ley, Photoemission in Solids I: General Principles, in, Springer Berlin Heidelberg, 1978.
[154] G. Borstel, Theoretical aspects of photoemission, Applied Physics A, 38 (1985) 193-204.
[155] G. Ertl, J. Küppers, Low Energy Electrons and Surface Chemistry, 2nd Revised Edition, (1986).
[156] D. Willock, Molecular Symmetry, John Wiley & Sons, Ltd, 2009.
[157] A. Thorne, U. Litzen, S. Johansson, Spectrophysics: Principles and Applications, Springer, (1999).
[158] H. Lüth, Solid surfaces, interfaces and thin films, Springer 2001.
[159] T. Rhodin, G. Ertl, The nature of the surface chemical bond, North-Holland Pub Co., Amsterdam (1979).
[160] M.P. Seah, W.A. Dench, Quantitative electron spectroscopy of surfaces: A standard data base for electron inelastic mean free paths in solids, Surface and Interface Analysis, 1 (1979) 2-11.
[161] H. Hertz, Ueber einen Einfluss des ultravioletten Lichtes auf die electrische Entladung, Annalen der Physik, 267 (1887) 983-1000.
[162] A. Einstein, Über einen die Erzeugung und Verwandlung des Lichtes betreffenden heuristischen Gesichtspunkt, Annalen der Physik, 322 (1905) 132-148.
[163] D. Cahen, A. Kahn, Electron Energetics at Surfaces and Interfaces: Concepts and Experiments, Advanced Materials, 15 (2003) 271-277.
[164] J.F. Moulder, W.F. Stickle, P.E. Sobol, K.D. Bomben, Handbook of X-ray Photoelectron Spectroscopy, Physical Electronics, Inc., 1992.
[165] N. Koch, D. Pop, R.L. Weber, N. Böwering, B. Winter, M. Wick, G. Leising, I.V. Hertel, W. Braun, Radiation induced degradation and surface charging of organic thin films in ultraviolet photoemission spectroscopy, Thin Solid Films, 391 (2001) 81-87.
[166] E.-E. Koch, Photoemission from Organic Molecular Solids and Organometallic Compounds, Physica Scripta, 1987 (1987) 120.
[167] N. Koch, A.C. Dürr, J. Ghijsen, R.L. Johnson, J.J. Pireaux, J. Schwartz, F. Schreiber, H. Dosch, A. Kahn, Optically induced electron transfer from conjugated organic molecules to charged metal clusters, Thin Solid Films, 441 (2003) 145-149.
[168] Y. Gassenbauer, R. Schafranek, A. Klein, S. Zafeiratos, M. Hävecker, A. Knop-Gericke, R. Schlögl, Surface states, surface potentials, and segregation at surfaces of tin-doped ${\mathrm{In}}_{2}{\mathrm{O}}_{3}$, Physical Review B, 73 (2006) 245312.
[169] W. Göpel, G. Rocker, R. Feierabend, Intrinsic defects of Ti${\mathrm{O}}_{2}$(110): Interaction with chemisorbed ${\mathrm{O}}_{2}$, ${\mathrm{H}}_{2}$, CO, and C${\mathrm{O}}_{2}$, Physical Review B, 28 (1983) 3427-3438.
[170] W. Song, M. Yoshitake, Effects of surface cleaning on oxidation of NiAl(1 1 0), Applied Surface Science, 241 (2005) 164-168.
[171] M. de Ridder, R.G. van Welzenis, H.H. Brongersma, Surface cleaning and characterization of yttria-stabilized zirconia, Surface and Interface Analysis, 33 (2002) 309-317.
[172] J.I. Pankove, Optical Processes in Semiconductors, Dover Publications, Inc., Mineola, N.Y. USA, 1971.
[173] M. Ashraf, S.M.J. Akhtar, A.F. Khan, Z. Ali, A. Qayyum, Effect of annealing on structural and optoelectronic properties of nanostructured ZnSe thin films, Journal of Alloys and Compounds, 509 (2011) 2414-2419.
[174] T.M. Khan, M.F. Mehmood, A. Mahmood, A. Shah, Q. Raza, A. Iqbal, U. Aziz, Synthesis of thermally evaporated ZnSe thin film at room temperature, Thin Solid Films, 519 (2011) 5971-5977.
[175] M. El Sherif, F.S. Terra, S.A. Khodier, Optical characteristics of thin ZnSe films of different thicknesses, Journal of Materials Science: Materials in Electronics, 7 (1996) 391-395.
[176] G.M. Lohar, S.K. Shinde, V.J. Fulari, Structural, morphological, optical and photoluminescent properties of spray-deposited ZnSe thin film, Journal of Semiconductors, 35 (2014) 113001.
[177] S. Venkatachalam, Y.L. Jeyachandran, P. Sureshkumar, A. Dhayalraj, D. Mangalaraj, S.K. Narayandass, S. Velumani, Characterization of vacuum-evaporated ZnSe thin films, Materials Characterization, 58 (2007) 794-799.
[178] R. Swanepoel, Determination of the thickness and optical constants of amorphous silicon, Journal of Physics E: Scientific Instruments, 16 (1983) 1214.
[179] E.R. Shaaban, I.S. Yahia, E.G. El-Metwally, Validity of Swanepoel's Method for Calculating the Optical Constants of Thick Films, Acta Physica Polonica A, 121 (2012) 628-635.
[180] B.D. Cullity, Elements of X-ray Diffraction, Third Edition ed., Addison-Wesley Publishing Company, Inc., London, 1978.

[181] S. Guha, R.A. Haight, J.M. Karasinski, R.R. Troutman, Light emitting diodes, in, International Business Machines Corporation, NY 10504 (US), 1998.
[182] H. Riel, S. Karg, T. Beierlein, W. Rieß, K. Neyts, Tuning the emission characteristics of top-emitting organic light-emitting devices by means of a dielectric capping layer: An experimental and theoretical study, Journal of Applied Physics, 94 (2003) 5290-5296.
[183] S. Guha, V. J. Leppert, S.H. Risbud, Identification of the electronic states of Se2− molecules embedded in borosilicate glasses and in Se-based nanometer sized crystals, Journal of Non-Crystalline Solids, 240 (1998) 43-49.
[184] J.J. Andrade, A.G. Brasil Jr, P.M.A. Farias, A. Fontes, B.S. Santos, Synthesis and characterization of blue emitting ZnSe quantum dots, Microelectronics Journal, 40 (2009) 641-643.
[185] H. Jeon, J. Ding, W. Patterson, A.V. Nurmikko, W. Xie, D.C. Grillo, M. Kobayashi, R.L. Gunshor, Blue-green injection laser diodes in (Zn,Cd)Se/ZnSe quantum wells, Applied Physics Letters, 59 (1991) 3619-3621.
[186] W.W. Jiang, S.L. Zhao, F.J. Zhang, Z. Xu, Electroluminescence of ZnSe enhanced by improved layered optimization structure, Materials Science in Semiconductor Processing, 13 (2010) 360-363.
[187] N. Kayunkid, A. Keawprajak, A. Jaruwanawat, J. Nukeaw, Blue Emission Mechanism of NPB/ZnSe Hybrid Structure, in: Nano/Micro Engineered and Molecular Systems, 2007. NEMS '07. 2nd IEEE International Conference on, 2007, pp. 643-646.
[188] M. Drechsler, B.K. Meyer, D.M. Hofmann, P. Ruppert, D. Hommel, Optically detected cyclotron resonance properties of high purity ZnSe epitaxial layers grown on GaAs, Applied Physics Letters, 71 (1997) 1116-1117.
[189] T. Yasuda, I. Mitsuishi, H. Kukimoto, Metalorganic vapor phase epitaxy of low-resistivity p-type ZnSe, Applied Physics Letters, 52 (1988) 57-59.
[190] X.W. Fan, J. Woods, Blue electroluminescence in forward-biased ZnSe diodes, Electron Devices, IEEE Transactions on, 28 (1981) 428-433.
[191] X.W. Fan, J. Woods, Free exciton emission in forward biased ZnSe MIS diodes, Journal of Physics C: Solid State Physics, 14 (1981) 1863.
[192] J. Nishizawa, K. Itoh, Y. Okuno, F. Sakurai, Blue light emission from ZnSe p-n junctions, Journal of Applied Physics, 57 (1985) 2210-2216.
[193] M.A. Haase, J. Qiu, J.M. DePuydt, H. Cheng, Blue-green laser diodes, Applied Physics Letters, 59 (1991) 1272-1274.
[194] G. Mueller, R. Willardson, E. Weber, Electroluminescence I, 1st Edition ed., Academic Press, San Diego, U.S.A., 2000.
[195] M. Aven, High Electron Mobility in Zinc Selenide Through Low-Temperature Annealing, Journal of Applied Physics, 42 (1971) 1204-1208.
[196] A.M. Goodman, Electrically Conducting Photoluminescent ZnSe Films, Journal of The Electrochemical Society, 116 (1969) 364-368.
[197] J. Aranovich, A.L. Fahrenbruch, R.H. Bube, High conductivity ZnSe films, Journal of Applied Physics, 49 (1978) 2584-2585.
[198] S.P. Kowalczyk, E.A. Kraut, J.R. Waldrop, R.W. Grant, Measurement of ZnSe–GaAs(110) and ZnSe–Ge(110) heterojunction band discontinuities by x-ray photoelectron spectroscopy (XPS), Journal of Vacuum Science and Technology, 21 (1982) 482-485.
[199] E. Bacaksiz, S. Aksu, I. Polat, S. Yılmaz, M. Altunbaş, The influence of substrate temperature on the morphology, optical and electrical properties of thermal-evaporated ZnSe thin films, Journal of Alloys and Compounds, 487 (2009) 280-285.
[200] I.A. Davydov, S.I. Spasskaya, L.P. Strakhov, I.R. Tagirov, S.L. Tselishchev, V.N. Shchemelev, Spectroscopy of surface electron states in thin zinc selenide layers, J Appl Spectrosc, 50 (1989) 193-197.
[201] U. Khairnar, S. Behere, P. Pawar, Optical Properties of Polycrystalline Zinc Selenide Thin Films, Materials Sciences and Applications, (2012) 36-40.
[202] K. Navaphun, K. Anusit, J. Anuchit, J. Nukeaw, Blue Emission Mechanism of NPB/ZnSe Hybrid Structure, in: Nano/Micro Engineered and Molecular Systems, 2007. NEMS '07. 2nd IEEE International Conference on, 2007, pp. 643-646.
[203] K. Onlaor, B. Tunhoo, T. Thiwawong, J. Nukeaw, Electrical bistability of tris-(8-hydroxyquinoline) aluminum (Alq3)/ZnSe organic-inorganic bistable device, Current Applied Physics, 12 (2012) 331-336.
[204] A. Hofmann, C. Pettenkofer, Surface orientation dependent band alignment for CuInSe2–ZnSe–ZnO, Applied Physics Letters, 98 (2011).
[205] Y.P. Venkata Subbaiah, P. Prathap, M. Devika, K.T.R. Reddy, Close-spaced evaporated ZnSe films: Preparation and characterization, Physica B: Condensed Matter, 365 (2005) 240-246.

[206] A. Ohtake, S. Miwa, L.-H. Kuo, K. Kimura, T. Yasuda, C. Jin, T. Yao, Polar surface dependence of epitaxy processes: ZnSe on GaAs{111}A, B-(2×2), Applied Surface Science, 130–132 (1998) 398-402.
[207] W. Chen, A. Kahn, P. Soukiassian, P.S. Mangat, J. Gaines, C. Ponzoni, D. Olego, ZnSe(100) surface: Atomic configurations, composition, and surface dipole, Physical Review B, 49 (1994) 10790-10793.
[208] S. Ghosh, N.P. Stern, B. Maertz, D.D. Awschalom, G. Xiang, M. Zhu, N. Samarth, Internal magnetic field in thin ZnSe epilayers, Applied Physics Letters, 89 (2006) -.
[209] C.-W. Huang, H.-M. Weng, Y.-L. Jiang, H.-Y. Ueng, Optimum growth of ZnSe film by molecular beam deposition, Vacuum, 83 (2008) 313-318.
[210] C.-W. Huang, H.-M. Weng, Y.-L. Jiang, H.-Y. Ueng, Investigation on the properties of molecular beam deposited ZnSe films, Thin Solid Films, 517 (2009) 3667-3671.
[211] C. Kim, S. Sivananthan, Optical properties of ZnSe and its modeling, Physical Review B, 53 (1996) 1475-1484.
[212] Y. Koide, T. Kawakami, N. Teraguchi, Y. Tomomura, A. Suzuki, M. Murakami, Schottky barrier heights of metals contacting to p-ZnSe, Journal of Applied Physics, 82 (1997) 2393-2399.
[213] M. Moldovan, S.D. Setzler Zhonghaiyu, T.H. Myers, L.E. Halliburton, N.C. Giles, Photoluminescence of nitrogen-doped zinc selenide epilayers, Journal of Electronic Materials, 26 (1997) 732-737.
[214] H. Oniyama, S. Yamaga, A. Yoshikawa, H. Kasai, Metalorganic molecular beam epitaxy of ZnSe films using dimethylzinc and hydrogen selenide, Journal of Crystal Growth, 93 (1988) 679-685.
[215] M.R. Park, W.A. Anderson, M. Jeon, H. Luo, Ohmic contacts to n-type and p-type ZnSe, Solid-State Electronics, 43 (1999) 113-121.
[216] J. Qiu, Q.D. Qian, R.L. Gunshor, M. Kobayashi, D.R. Menke, D. Li, N. Otsuka, Influence of GaAs surface stoichiometry on the interface state density of as-grown epitaxial ZnSe/epitaxial GaAs heterostructures, Applied Physics Letters, 56 (1990) 1272-1274.
[217] R. Bertacco, M. Riva, M. Cantoni, F. Ciccacci, M. Portalupi, A. Brambilla, L. Duò, P. Vavassori, F. Gustavsson, J.M. George, M. Marangolo, M. Eddrief, V.H. Etgens, Electronic, magnetic, and structural properties of the Fe/ZnSe interface, Physical Review B, 69 (2004) 054421.
[218] H. Akinaga, K. Tanaka, Atomic layer epitaxy of ZnSe using reflectance difference spectroscopy, Applied Surface Science, 82–83 (1994) 298-304.
[219] C.D. Lee, S.I. Min, S.K. Chang, High purity ZnSe epilayers grown by atmospheric double zone metalorganic atomic layer epitaxy, Journal of Crystal Growth, 159 (1996) 108-111.
[220] A. Rizzo, M.A. Tagliente, L. Caneve, S. Scaglione, The influence of the momentum transfer on the structural and optical properties of ZnSe thin films prepared by r.f. magnetron sputtering, Thin Solid Films, 368 (2000) 8-14.
[221] A.M. Chaparro, C. Maffiotte, M.T. Gutiérrez, J. Herrero, Morphological and compositional study of CBD-ZnSe thin films by microscopy techniques and angle resolved XPS, Thin Solid Films, 358 (2000) 22-29.
[222] R.B. Kale, C.D. Lokhande, Influence of air annealing on the structural, morphological, optical and electrical properties of chemically deposited ZnSe thin films, Applied Surface Science, 252 (2005) 929-938.
[223] C.T. Hsu, Y.J. Lin, Y.K. Su, M. Yokoyama, Growth of ZnSe thin films on ITO/glass substrates by low pressure metalorganic chemical vapor deposition, Journal of Crystal Growth, 125 (1992) 420-424.
[224] E. Krause, H. Hartmann, J. Menninger, A. Hoffmann, C. Fricke, R. Heitz, B. Lummer, V. Kutzer, I. Broser, Influence of growth non-stoichiometry on optical properties of doped and non-doped ZnSe grown by chemical vapour deposition, Journal of Crystal Growth, 138 (1994) 75-80.
[225] A. Rumberg, C. Sommerhalter, M. Toplak, A. Jäger-Waldau, M.C. Lux-Steiner, ZnSe thin films grown by chemical vapour deposition for application as buffer layer in CIGSS solar cells, Thin Solid Films, 361–362 (2000) 172-176.
[226] A. Saidane, D.L. Kirk, The influence of the method of deposition on the microstructure and optical properties of junctions of ZnSe with indium tin oxide, Thin Solid Films, 144 (1986) 49-67.
[227] A.P. Samantilleke, M.H. Boyle, J. Young, I.M. Dharmadasa, Electrodeposition of n-type and p-type ZnSe thin films for applications in large area optoelectronic devices, Journal of Materials Science: Materials in Electronics, 9 (1998) 289-290.
[228] K. Ogata, D. Kawaguchi, T. Kera, S. Fujita, S. Fujita, Effects of annealing atmosphere and temperature on acceptor activation in ZnSe:N grown by photoassisted MOVPE, Journal of Crystal Growth, 159 (1996) 312-316.
[229] R.B. Kale, C.D. Lokhande, Room temperature deposition of ZnSe thin films by successive ionic layer adsorption and reaction (SILAR) method, Materials Research Bulletin, 39 (2004) 1829-1839.
[230] E. Wisotzki, A. Klein, W. Jaegermann, Quasi van der Waals epitaxy of ZnSe on the layered chalcogenides InSe and GaSe, Thin Solid Films, 380 (2000) 263-265.

[231] T.C. Chiang, F.J. Himpsel, ZnSe. Electronic Structure of Solids: Photoemission Spectra and Related Data, Landolt-Bornstein Group III,, Springer Verlang,, New York.
[232] F. Xu, M. Vos, J.H. Weaver, H. Cheng, Interface dipoles, surface work functions, and Schottky-barrier formation at Au/ZnSe(100) interfaces, Physical Review B, 38 (1988) 13418-13421.
[233] M. Cantoni, R. Bertacco, A. Brambilla, F. Ciccacci, Photon- and electron-induced surface voltage in electron spectroscopies on ZnSe(001), Journal of Electron Spectroscopy and Related Phenomena, 173 (2009) 84-87.
[234] M. Shenasa, S. Sainkar, D. Lichtman, XPS study of some selected selenium compounds, Journal of Electron Spectroscopy and Related Phenomena, 40 (1986) 329-337.
[235] S. Venkatachalam, D. Mangalaraj, S.K. Narayandass, K. Kim, J. Yi, Structure, optical and electrical properties of ZnSe thin films, in: Physica B: Condensed Matter, 2005, pp. 27-35.
[236] B. Xi, D. Xu, S. Xiong, C. Wang, X. Feng, H. Zhou, Y. Qian, Preparation and Characterization of Cubic and Hexagonal Polytypes of ZnSe:Cu2+ One-Dimensional Nanostructures, The Journal of Physical Chemistry C, 112 (2008) 5333-5338.
[237] E. Bacaksiz, B.M. Basol, M. Altunbaş, S. Yılmaz, M. Tomakin, B. Abay, Effect of substrate temperature and post-deposition annealing on the properties of evaporated CdSe thin films, physica status solidi (b), 244 (2007) 497-504.
[238] G.K.M. Thutupalli, S.G. Tomlin, The optical properties of thin films of cadmium and zinc selenides and tellurides, Journal of Physics D: Applied Physics, 9 (1976) 1639.
[239] B. Pejova, The higher excited electronic states and spin–orbit splitting of the valence band in three-dimensional assemblies of close-packed ZnSe and CdSe quantum dots in thin film form, Journal of Solid State Chemistry, 181 (2008) 1961-1969.
[240] N. Kumbhojkar, S. Mahamuni, V. Leppert, S.H. Risbud, Quantum confinement effects in chemically grown, stable ZnSe nanoclusters, Nanostructured Materials, 10 (1998) 117-129.
[241] D.F. O'Brien, A Study of Infrared Absorption in Zinc Selenide Thin Films, in: A.J. Glass, A.H. Guenther (Eds.) Laser Induced Damage in Optical Materials, 1977: Proceedings of the 9th Annual Symposium on Optical Materials for High Power Lasers, Department of Commerce, National Bureau of Standards, NBS Boulder, Colorado 80303, 1977, pp. 276--279.
[242] R.K. Beri, P. More, B.G. Bharate, P.K. Khanna, Band-gap engineering of ZnSe quantum dots via a non-TOP green synthesis by use of organometallic selenium compound, Current Applied Physics, 10 (2010) 553-556.
[243] G.Y. Park, J.-h. Seo, Y.K. Kim, Y.S. Kim, Y. Ha, Efficient Red Electrophosphorescent Devices Based on Iridium Complexes of Fluorinated 1-Phenylisoquinoline, Japanese Journal of Applied Physics, 46 (2007) 2735.
[244] X. Yang, D.C. Müller, D. Neher, K. Meerholz, Highly Efficient Polymeric Electrophosphorescent Diodes, Advanced Materials, 18 (2006) 948-954.
[245] Y.J. Su, H.L. Huang, C.L. Li, C.H. Chien, Y.T. Tao, P.T. Chou, S. Datta, R.S. Liu, Highly Efficient Red Electrophosphorescent Devices Based on Iridium Isoquinoline Complexes: Remarkable External Quantum Efficiency Over a Wide Range of Current, Advanced Materials, 15 (2003) 884-888.
[246] Z. Liu, M.G. Helander, Z. Wang, Z. Lu, Highly efficient two component phosphorescent organic light-emitting diodes based on direct hole injection into dopant and gradient doping, Organic Electronics, 14 (2013) 852-857.
[247] P.-C. Kao, S.-Y. Chu, C.-H. Chen, H.-H. Huang, C.-H. Yang, I.-W. Sun, White and Red Organic Light-Emitting Diodes Using a Phosphorescent Iridium Complex as a Red Dopant, Journal of The Electrochemical Society, 153 (2006) H228-H231.
[248] J.P. Duan, P.P. Sun, C.H. Cheng, New Iridium Complexes as Highly Efficient Orange–Red Emitters in Organic Light-Emitting Diodes, Advanced Materials, 15 (2003) 224-228.
[249] Y. Wang, N. Herron, V.V. Grushin, D. LeCloux, V. Petrov, Highly efficient electroluminescent materials based on fluorinated organometallic iridium compounds, Applied Physics Letters, 79 (2001) 449-451.
[250] Y.-Y. Noh, C.-L. Lee, J.-J. Kim, K. Yase, Energy transfer and device performance in phosphorescent dye doped polymer light emitting diodes, The Journal of Chemical Physics, 118 (2003) 2853-2864.
[251] H.Z. Xie, M.W. Liu, O.Y. Wang, X.H. Zhang, C.S. Lee, L.S. Hung, S.T. Lee, P.F. Teng, H.L. Kwong, H. Zheng, C.M. Che, Reduction of Self-Quenching Effect in Organic Electrophosphorescence Emitting Devices via the Use of Sterically Hindered Spacers in Phosphorescence Molecules, Advanced Materials, 13 (2001) 1245-1248.
[252] Y. Kawamura, K. Goushi, J. Brooks, J.J. Brown, H. Sasabe, C. Adachi, 100% phosphorescence quantum efficiency of Ir(III) complexes in organic semiconductor films, Applied Physics Letters, 86 (2005) 071104.
[253] D.-F. Huang, T.J. Chow, C.-Y. Wu, S.-S. Sun, S.-H. Tsai, Y.-S. Wen, S. Polosan, T. Tsuboi, The Preparation of (8-Hydroxyquinolinato)Bis(2-Phenylpyridyl)Iridium Complexes and Their Photophysical Properties, Journal of the Chinese Chemical Society, 55 (2008) 439-448.

[254] C.-H. Yang, C.-C. Tai, I.W. Sun, Synthesis of a high-efficiency red phosphorescent emitter for organic light-emitting diodes, Journal of Materials Chemistry, 14 (2004) 947-950.
[255] C.-L. Ho, W.-Y. Wong, Charge and energy transfers in functional metallophosphors and metallopolyynes, Coordination Chemistry Reviews, 257 (2013) 1614-1649.
[256] M. Ravaglia, M. Garavelli, M. Polson, F. Scandola, Iridium Complexes with Terdentate Ligands: Cyclometalated vs. Polypyridine Analogues; Hybrid vs. "Pure" DFT, AIP Conference Proceedings, 963 (2007) 659-662.
[257] A.F. Rausch, H.H.H. Homeier, H. Yersin, Organometallic Pt(II) and Ir(III) Triplet Emitters for OLED Applications and the Role of Spin–Orbit Coupling: A Study Based on High-Resolution Optical Spectroscopy, in: A.J. Lees (Ed.) Photophysics of Organometallics, Springer Berlin Heidelberg, Springer-Verlag Berlin Heidelberg, 2010, pp. 193-235.
[258] T. Saito, Inorganic Chemistry, Kanagawa University, 2004.
[259] T. Azumi, H. Miki, Spectroscopy of the spin sublevels of transition metal complexes, in: H. Yersin (Ed.) Electronic and Vibronic Spectra of Transition Metal Complexes II, Springer Berlin Heidelberg, 1997, pp. 1-40.
[260] H. Miki, M. Shimada, T. Azumi, J.A. Brozik, G.A. Crosby, Effect of the ligand-field strength on the radiative properties of the ligand-localized 3.pi..pi.* state of rhodium complexes with 1,10-phenanthroline: proposed role of dd states, The Journal of Physical Chemistry, 97 (1993) 11175-11179.
[261] S. Kimachi, R. Satomi, H. Miki, K. Maeda, T. Azumi, M. Onishi, Excited-State Properties of the Ligand-Localized 3ππ* State of Cyclometalated Ruthenium(II) Complexes, The Journal of Physical Chemistry A, 101 (1997) 345-349.
[262] C. Giesbergen, M. Glasbeek, Radiative properties and charge-transfer character of the phosphorescent triplet state in mixed rhodium chelates, The Journal of Physical Chemistry, 97 (1993) 9942-9946.
[263] A. Ruggi, Tuning brightness and oxygen sensitivity of Ru(II) and Ir(III) luminophores, in, University of Twente, Enschede, 2011, pp. 176.
[264] K. Soon-ki, T. Kuppusamy, K. Seul-Ong, Y. Kang, K. Yun-Hi, The Efficient Green Emitting Iridium(III) Complexes and Phosphorescent Organic Light Emitting Diode Characteristics, in: M. Mazzeo (Ed.) Organic Light Emitting Diode, Sciyo, InTech, 2010, pp. 25-42.
[265] K.D. Glusac, S. Jiang, K.S. Schanze, Photophysics of Ir(iii) complexes with oligo(arylene ethynylene) ligands, Chemical Communications, (2002) 2504-2505.
[266] A. Aboulaich, M. Geszke, L. Balan, J. Ghanbaja, G. Medjahdi, R.l. Schneider, Water-Based Route to Colloidal Mn-Doped ZnSe and Core/Shell ZnSe/ZnS Quantum Dots, Inorganic Chemistry, 49 (2010) 10940-10948.
[267] S.M. Park, H. Yu, M.G. Park, S.Y. Han, S.W. Kang, H.M. Park, J.W. Kim, Quantitative analysis of an organic thin film by XPS, AFM and FT-IR, Surface and Interface Analysis, 44 (2012) 156-161.
[268] R. Hock, T. Mayer, W. Jaegermann, p-Type Doping of Spiro-MeOTAD with WO3 and the Spiro-MeOTAD/WO3 Interface Investigated by Synchrotron-Induced Photoelectron Spectroscopy, The Journal of Physical Chemistry C, 116 (2012) 18146-18154.
[269] A.J. Mäkinen, I.G. Hill, Z.H. Kafafi, Vacuum level alignment in organic guest-host systems, Journal of Applied Physics, 92 (2002) 1598-1603.
[270] H. Ishii, K. Seki, Energy level alignment at organic/metal interfaces studied by UV photoemission: breakdown of traditional assumption of a common vacuum level at the interface, Electron Devices, IEEE Transactions on, 44 (1997) 1295-1301.
[271] S. Braun, W. Osikowicz, Y. Wang, W.R. Salaneck, Energy level alignment regimes at hybrid organic–organic and inorganic–organic interfaces, Organic Electronics, 8 (2007) 14-20.
[272] Z. Li, X. Zhang, G. Lu, Dipole-Assisted Charge Separation in Organic–Inorganic Hybrid Photovoltaic Heterojunctions: Insight from First-Principles Simulations, The Journal of Physical Chemistry C, 116 (2012) 9845-9851.
[273] Y. Liu, S.R. Scully, M.D. McGehee, J. Liu, C.K. Luscombe, J.M.J. Fréchet, S.E. Shaheen, D.S. Ginley, Dependence of Band Offset and Open-Circuit Voltage on the Interfacial Interaction between TiO2 and Carboxylated Polythiophenes, The Journal of Physical Chemistry B, 110 (2006) 3257-3261.
[274] N. Sai, K. Leung, J.R. Chelikowsky, Hybrid density functional study of oligothiophene/ZnO interface for photovoltaics, Physical Review B, 83 (2011) 121309.
[275] A. Chaieb, O. Halimi, A. Bensouici, B. Boudine, M. Sebais, B. Sahraoui, Optical properties of the ZnSe nanocrystals embedded in PMMA matrix, in: Mediterranean Winter, 2008. ICTON-MW 2008. 2nd ICTON, 2008, pp. 1-4.
[276] M. Sebais, A. Chaieb, B. Boudine, Z. Ouili, S. Halimi, Study of nanocomposite ZnSe/PMMA, in: Electronics, Communications and Photonics Conference (SIECPC), 2011 Saudi International, 2011, pp. 1-3.

[277] N.E. Schlotter, J.F. Rabolt, Measurements of the Optical Anisotropy of Trapped Molecules in Oriented Polymer Films by Waveguide Raman Spectroscopy (WRS), Appl. Spectrosc., 38 (1984) 208-211.
[278] H.-R. Tsai, K.-Y. Lu, S.-H. Lai, C.-H. Fan, C.-H. Cheng, I.C. Chen, Metal–Ligand Bonding Strength of Fluoro-Substituted Cyclometalated Iridium(III) Complexes from Raman and Infrared Spectra, The Journal of Physical Chemistry C, 115 (2011) 17163-17174.
[279] C.M. Dolan, The synthesis and characterisation of inorganic and organic luminophores suitable for biomolecule conjugation, in: School of Chemical Sciences, Dublin City University, Glasnevin, Dublin, 2011, pp. 382.
[280] A. Campion, J.E. Ivanecky, C.M. Child, M. Foster, On the Mechanism of Chemical Enhancement in Surface-Enhanced Raman Scattering, Journal of the American Chemical Society, 117 (1995) 11807-11808.
[281] A.T. Zayak, Y.S. Hu, H. Choo, J. Bokor, S. Cabrini, P.J. Schuck, J.B. Neaton, Chemical Raman Enhancement of Organic Adsorbates on Metal Surfaces, Physical Review Letters, 106 (2011) 083003.
[282] A.A. Baganich, V.I. Mikla, D.G. Semak, A.P. Sokolov, A.P. Shebanin, Raman Scattering in Amorphous Selenium Molecular Structure and Photoinduced Crystallization, physica status solidi (b), 166 (1991) 297-302.
[283] N. Ohta, W. Scheuermann, K. Nakamoto, Resonance Raman spectrum of selenium thin film, Solid State Communications, 27 (1978) 1325-1327.
[284] V.V. Poborchii, Raman spectra of sulfur, selenium or tellurium clusters confined in nano-cavities of zeolite A, Solid State Communications, 107 (1998) 513-518.
[285] S.N. Yannopoulos, K.S. Andrikopoulos, Raman scattering study on structural and dynamical features of noncrystalline selenium, The Journal of Chemical Physics, 121 (2004) 4747-4758.
[286] E. Han, Y.-Y. Lyu, T.-W. Lee, Y. Byun, O. Kwon, A. Tikhonovsky, Y. Kwon, G.-S. Park, R. Ragini Das, Solution-Processed High-Efficiency Organic Phosphorescent Devices Utilizing a Blue Ir(III) Complex, Journal of Nanoscience and Nanotechnology, 8 (2008) 2990-2995.
[287] R. Stevenson, R. Riehn, R.G. Milner, D. Richards, E. Moons, D.-J. Kang, M. Blamire, J. Morgado, F. Cacialli, Ultraviolet–visible near-field microscopy of phase-separated blends of polyfluorene-based conjugated semiconductors, Applied Physics Letters, 79 (2001) 833-835.
[288] L.M. Herz, C. Silva, R.H. Friend, R.T. Phillips, S. Setayesh, S. Becker, D. Marsitsky, K. Müllen, Effects of aggregation on the excitation transfer in perylene-end-capped polyindenofluorene studied by time-resolved photoluminescence spectroscopy, Physical Review B, 64 (2001) 195203.
[289] P. Wang, A. Abrusci, H.M.P. Wong, M. Svensson, M.R. Andersson, N.C. Greenham, Photoinduced Charge Transfer and Efficient Solar Energy Conversion in a Blend of a Red Polyfluorene Copolymer with CdSe Nanoparticles, Nano Letters, 6 (2006) 1789-1793.
[290] M.A. Baldo, S.R. Forrest, Transient analysis of organic electrophosphorescence: I. Transient analysis of triplet energy transfer, Physical Review B, 62 (2000) 10958-10966.
[291] V. Cleave, G. Yahioglu, P.L. Barny, R.H. Friend, N. Tessler, Harvesting Singlet and Triplet Energy in Polymer LEDs, Advanced Materials, 11 (1999) 285-288.
[292] V.Y. Degoda, N.Y. Pavlova, G.P. Podust, A.O. Sofiienko, Spectral structure of the X-ray stimulated phosphorescence of monocrystalline ZnSe, Physica B: Condensed Matter, 465 (2015) 1-6.
[293] N.K. Al-Rasbi, C. Sabatini, F. Barigelletti, M.D. Ward, Red-shifted luminescence from naphthalene-containing ligands due to [small pi]-stacking in self-assembled coordination cages, Dalton Transactions, (2006) 4769-4772.
[294] S.R. Forrest, Ultrathin Organic Films Grown by Organic Molecular Beam Deposition and Related Techniques, Chemical Reviews, 97 (1997) 1793-1896.
[295] A. Klein, N. Hurkes, A. Kaiser, W. Wielandt, π-Stacking Modulates the Luminescence of [(dppz)Ni(Mes)Br] (dppz = dipyrido[3,2-a:2′,3′-c]phenazine, Mes = 2,4,6-trimethylphenyl), Zeitschrift für anorganische und allgemeine Chemie, 633 (2007) 1659-1665.
[296] M. Levichkova, J. Assa, H. Fröb, K. Leo, Photoluminescence properties of vacuum-deposited organic molecule-oxide (MePTCDI–SiO2) mixed layers, Journal of Luminescence, 128 (2008) 1384-1388.
[297] D. Avnir, D. Levy, R. Reisfeld, The nature of the silica cage as reflected by spectral changes and enhanced photostability of trapped Rhodamine 6G, The Journal of Physical Chemistry, 88 (1984) 5956-5959.
[298] J.S. Wang, W.J. Chen, C.S. Yang, Y.H. Tsai, H.H. Wang, R.H. Chen, J.L. Shen, C.D. Tsai, Improving stability of photoluminescence of ZnSe thin films grown by molecular beam epitaxy by incorporating Cl dopant, Applied Physics Letters, 98 (2011) 021908.
[299] L. Chen, J.S. Lai, X.N. Fu, J. Sun, Z.F. Ying, J.D. Wu, H. Lu, N. Xu, Growth of ZnSe nano-needles by pulsed laser deposition and their application in polymer/inorganic hybrid solar cells, Thin Solid Films, 529 (2013) 76-79.

[300] J.S. Massa, G.S. Buller, A.C. Walker, J. Simpson, K.A. Prior, B.C. Cavenett, Photoluminescence decay measurements of n- and p-type doped ZnSe grown by molecular beam epitaxy, Applied Physics Letters, 64 (1994) 589-591.
[301] I.D. Parker, Carrier tunneling and device characteristics in polymer light-emitting diodes, Journal of Applied Physics, 75 (1994) 1656-1666.
[302] P.S. Davids, S.M. Kogan, I.D. Parker, D.L. Smith, Charge injection in organic light-emitting diodes: Tunneling into low mobility materials, Applied Physics Letters, 69 (1996) 2270-2272.
[303] A. Kohler, H. Bassler, Electronic Processes in Organic Semiconductors: An Introduction, Wiley-VCH Verlag GmbH & Co. KGaA, Weinheim, Germany, 2015.
[304] H.L. Gimaiel, G. Santos, E.A.T. Dirani, F.J. Fonseca, A.M. De Andrade, Charge Transport Layers in OC1C10-PPV PLEDs, ECS Transactions, 14 (2008) 547-551.
[305] S. Lee, C.-H. Chung, S.M. Cho, Effect of α-NPD film in electron transport layer on electroluminescence color change for organic light emitting devices, Synthetic Metals, 126 (2002) 269-273.
[306] S. Yang, Y. Jiang, F. Teng, Z. Xu, Y. Hou, X. Xu, The roles of zinc selenide sandwiched between organic layers and its applications in white light-emitting diodes, Solid State Communications, 139 (2006) 415-418.
[307] K.C. Tang, S.R. Tseng, W.S. Li, H.F. Meng, S.F. Horng, C.S. Hsu, Broad band and white phosphorescent polymer light-emitting diodes in multilayer structure, Synthetic Metals, 158 (2008) 287-291.
[308] O.P. Dimitriev, Y.P. Piryatinski, A.A. Pud, Evidence of the Controlled Interaction between PEDOT and PSS in the PEDOT:PSS Complex via Concentration Changes of the Complex Solution, The Journal of Physical Chemistry B, 115 (2011) 1357-1362.
[309] Y. Qi, P. Chen, T. Wang, X. Hu, S. Zhou, Fabrication of Self-Assembled PEDOT/PSS-ZnO Nanocables with Diverse Inner Core Sizes Facilitated by Vacuum Conditions, Macromolecular Rapid Communications, 27 (2006) 356-360.
[310] T.A. Papadopoulos, H. Li, E.-G. Kim, J. Liu, J.A. Cella, C.M. Heller, A. Shu, A. Kahn, A. Duggal, J.-L. Brédas, Impact of Functionalized Polystyrenes as the Electron Injection Layer on Gold and Aluminum Surfaces: A Combined Theoretical and Experimental Study, Israel Journal of Chemistry, 54 (2014) 779-788.
[311] Z. Chen, T. Salagaj, C. Jensen, K. Strobl, M. Nakarmi, K. Shum, ZnO thin film deposition on sapphire substrates by chemical vapor deposition, in: MRS Spring Meeting, San Francisco, California, 2009.
[312] J.D. Ye, S.L. Gu, F. Qin, S.M. Zhu, S.M. Liu, X. Zhou, W. Liu, L.Q. Hu, R. Zhang, Y. Shi, Y.D. Zheng, Y.D. Ye, MOCVD growth and properties of ZnO films using dimethylzinc and oxygen, Applied Physics A, 81 (2005) 809-812.
[313] A. Janotti, C.G. Van de Walle, Fundamentals of zinc oxide as a semiconductor, Reports on Progress in Physics, 72 (2009) 126501.
[314] A. Janotti, C.G. Van de Walle, Hydrogen multicentre bonds, Nat Mater, 6 (2007) 44-47.
[315] T. Tynell, M. Karppinen, Atomic layer deposition of ZnO: a review, Semiconductor Science and Technology, 29 (2014) 043001.
[316] J.T. Tanskanen, J.R. Bakke, T.A. Pakkanen, S.F. Bent, Influence of organozinc ligand design on growth and material properties of ZnS and ZnO deposited by atomic layer deposition, Journal of Vacuum Science & Technology A, 29 (2011) 031507.
[317] H. Morkoc, U. Ozgur, Zinc Oxide: Fundamentals, Materials and Device Technology, WILEY-VCH Verlag GmbH & Co. KGaA, Weinheim, 2009.
[318] Y.-H. Hu, Y.-C. Chen, H.-J. Xu, H. Gao, W.-H. Jiang, F. Hu, Y.-X. Wang, Texture ZnO Thin-Films and their Application as Front Electrode in Solar Cells, Engineering, Vol. 2 (2010) 4.
[319] M. Caglar, Y. Caglar, S. Ilican, The determination of the thickness and optical constants of the ZnO crystalline thin film by using envelope method, Journal of Optoelectronics and Advanced Materials, 8 (2006).
[320] L.-M. Do, D.-H. Hwang, H.-Y. Chu, S.H. Kim, J.-I. Lee, H. Park, T. Zyung, The initial state of dark spots in degradation of polymer lighting-emitting diodes, Synthetic Metals, 111–112 (2000) 249-251.
[321] C.H. Ahn, Y.Y. Kim, D.C. Kim, S.K. Mohanta, H.K. Cho, A comparative analysis of deep level emission in ZnO layers deposited by various methods, Journal of Applied Physics, 105 (2009) -.
[322] W. Zhang, T. Salagaj, J. Wei, C. Jensen, K. Strobl, Comparison of APCVD to LPCVD Processes in the Manufacturing of ZnO TCO for Solar Applications, in: MRS Fall Meeting, Boston, Massachusetts, 2009.
[323] R. Biswal, A. Maldonado, J. Vega-Pérez, D. Acosta, M. De La Luz Olvera, Indium Doped Zinc Oxide Thin Films Deposited by Ultrasonic Chemical Spray Technique, Starting from Zinc Acetylacetonate and Indium Chloride, Materials, 7 (2014) 5038-5046.
[324] S. Nicolay, M. Benkhaira, L. Ding, J. Escarre, G. Bugnon, F. Meillaud, C. Ballif, Control of CVD-deposited ZnO films properties through water/DEZ ratio: Decoupling of electrode morphology and electrical characteristics, Solar Energy Materials and Solar Cells, 105 (2012) 46-52.

[325] C.-L. Dong, J. Guo, Y.-Y. Chen, C. Ching-Lin, Soft-x-ray spectroscopy probes nanomaterial-based devices, in: SPIE Newsroom, SPIE, SPIE Europe, 2007.
[326] D. Schulz, S. Ganschow, D. Klimm, K. Struve, Inductively heated Bridgman method for the growth of zinc oxide single crystals, Journal of Crystal Growth, 310 (2008) 1832-1835.
[327] T. Nakano, Synthesis, structure and function of [pi]-stacked polymers, Polym J, 42 (0000) 103-123.
[328] P. Blumentrit, M. Yoshitake, S. Nemšák, T. Kim, T. Nagata, XPS and UPS study on band alignment at Pt–Zn-terminated ZnO(0 0 0 1) interface, Applied Surface Science, 258 (2011) 780-785.
[329] Y. Zhang, G. Du, X. Wang, W. Li, X. Yang, Y. Ma, B. Zhao, H. Yang, D. Liu, S. Yang, X-ray photoelectron spectroscopy study of ZnO films grown by metal-organic chemical vapor deposition, Journal of Crystal Growth, 252 (2003) 180-183.
[330] H.B. Fan, S.Y. Yang, P.F. Zhang, H.Y. Wei, X.L. Liu, C.M. Jiao, Q.S. Zhu, Y.H. Chen, Z.G. Wang, Investigation of Oxygen Vacancy and Interstitial Oxygen Defects in ZnO Films by Photoluminescence and X-Ray Photoelectron Spectroscopy, Chinese Physics Letters, 24 (2007) 2108.
[331] G. Atanasova, A.O. Dikovska, M. Stankova, P. Stefanov, P.A. Atanasov, XPS study of ZnO nanostructures prepared by laser ablation, Journal of Physics: Conference Series, 356 (2012) 012036.
[332] K. Jacobi, G. Zwicker, A. Gutmann, Work function, electron affinity and band bending of zinc oxide surfaces, Surface Science, 141 (1984) 109-125.
[333] C.G. Van de Walle, Hydrogen as a Cause of Doping in Zinc Oxide, Physical Review Letters, 85 (2000) 1012-1015.
[334] M. Chen, X. Wang, Y.H. Yu, Z.L. Pei, X.D. Bai, C. Sun, R.F. Huang, L.S. Wen, X-ray photoelectron spectroscopy and auger electron spectroscopy studies of Al-doped ZnO films, Applied Surface Science, 158 (2000) 134-140.
[335] Z.G. Wang, X.T. Zu, S. Zhu, L.M. Wang, Green luminescence originates from surface defects in ZnO nanoparticles, Physica E: Low-dimensional Systems and Nanostructures, 35 (2006) 199-202.
[336] P.T. Hsieh, Y.C. Chen, K.S. Kao, C.M. Wang, Luminescence mechanism of ZnO thin film investigated by XPS measurement, Applied Physics A, 90 (2008) 317-321.
[337] S. Major, S. Kumar, M. Bhatnagar, K.L. Chopra, Effect of hydrogen plasma treatment on transparent conducting oxides, Applied Physics Letters, 49 (1986) 394-396.
[338] T. Szörényi, L.D. Laude, I. Bertóti, Z. Kántor, Z. Geretovszky, Excimer laser processing of indium-tin-oxide films: An optical investigation, Journal of Applied Physics, 78 (1995) 6211-6219.
[339] K. Kotsis, V. Staemmler, Ab initio calculations of the O1s XPS spectra of ZnO and Zn oxo compounds, Physical Chemistry Chemical Physics, 8 (2006) 1490-1498.
[340] C. Liangyuan, L. Zhiyong, B. Shouli, Z. Kewei, L. Dianqing, C. Aifan, C.C. Liu, Synthesis of 1-dimensional ZnO and its sensing property for CO, Sensors and Actuators B: Chemical, 143 (2010) 620-628.
[341] D.G. Thomas, J.J. Lander, Hydrogen as a Donor in Zinc Oxide, The Journal of Chemical Physics, 25 (1956) 1136-1142.
[342] M.G. Wardle, J.P. Goss, P.R. Briddon, First-Principles Study of the Diffusion of Hydrogen in ZnO, Physical Review Letters, 96 (2006) 205504.
[343] O. Dulub, U. Diebold, G. Kresse, Novel Stabilization Mechanism on Polar Surfaces: ZnO(0001)-Zn, Physical Review Letters, 90 (2003) 016102.
[344] M. Valtiner, M. Todorova, G. Grundmeier, J. Neugebauer, Temperature Stabilized Surface Reconstructions at Polar ZnO(0001), Physical Review Letters, 103 (2009) 065502.
[345] B. Meyer, First-principles study of the polar O-terminated ZnO surface in thermodynamic equilibrium with oxygen and hydrogen, Physical Review B, 69 (2004) 045416.
[346] S.T. King, S.S. Parihar, K. Pradhan, H.T. Johnson-Steigelman, P.F. Lyman, Observation of a (√3 × √3)R30° reconstruction on O-polar ZnO surfaces, Surface Science, 602 (2008) L131-L134.
[347] B. O'Regan, M. Gratzel, A low-cost, high-efficiency solar cell based on dye-sensitized colloidal TiO2 films, Nature, 353 (1991) 737-740.
[348] M. Gratzel, Photoelectrochemical cells, Nature, 414 (2001) 338-344.
[349] M. Grätzel, Dye-sensitized solar cells, Journal of Photochemistry and Photobiology C: Photochemistry Reviews, 4 (2003) 145-153.
[350] Y. Ohko, T. Tatsuma, T. Fujii, K. Naoi, C. Niwa, Y. Kubota, A. Fujishima, Multicolour photochromism of TiO2 films loaded with silver nanoparticles, Nat Mater, 2 (2003) 29-31.
[351] M. Landmann, E. Rauls, W.G. Schmidt, The electronic structure and optical response of rutile, anatase and brookite TiO 2, Journal of Physics: Condensed Matter, 24 (2012) 195503.
[352] T. Zhu, S.-P. Gao, The Stability, Electronic Structure, and Optical Property of TiO2 Polymorphs, The Journal of Physical Chemistry C, 118 (2014) 11385-11396.

[353] G. Chen, H. Sasabe, T. Igarashi, Z. Hong, J. Kido, Squaraine dyes for organic photovoltaic cells, Journal of Materials Chemistry A, 3 (2015) 14517-14534.
[354] R.W. Bigelow, H.-J. Freund, An MNDO and CNDO / S(S + DES CI) study on the structural and electronic properties of a model squaraine dye and related cyanine, Chemical Physics, 107 (1986) 159-174.
[355] K.Y. Law, Organic photoconductive materials: recent trends and developments, Chemical Reviews, 93 (1993) 449-486.
[356] P.V. Kamat, S. Das, K.G. Thomas, M.V. George, Photochemistry of squaraine dyes. 1. Excited singlet, triplet, and redox states of bis[4-(dimethylamino)phenyl]squaraine and bis[4-(dimethylamino)-2-hydroxyphenyl]squaraine, The Journal of Physical Chemistry, 96 (1992) 195-199.
[357] P.V. Kamat, S. Hotchandani, M. de Lind, K.G. Thomas, S. Das, M.V. George, Excited-state properties and photosensitization behaviour of bis(2,4-dihydroxyphenyl)squaraine, Journal of the Chemical Society, Faraday Transactions, 89 (1993) 2397-2402.
[358] Y.S. Kim, K. Liang, K.Y. Law, D.G. Whitten, An investigation of photocurrent generation by squaraine aggregates in monolayer-modified tin oxide (SnO2) electrodes, The Journal of Physical Chemistry, 98 (1994) 984-988.
[359] B. Patrick, M.V. George, P.V. Kamat, S. Das, K.G. Thomas, Photochemistry of squaraine dyes: excited states and reduced and oxidized forms of 4-(4-acetyl-3,5-dimethylpyrrolium-2-ylidene)-2-(4-acetyl-3,5-dimethylpyrrol-2-yl)-3-oxocyclobut-1-en-1-olate, Journal of the Chemical Society, Faraday Transactions, 88 (1992) 671-676.
[360] J. Oriou, Synthesis and structure-properties relationship of alternated pi-conjugated copolymers, in: U.o. Bordeaux (Ed.) Ph.D. Thesis, University of Bordeaux, Bordeaux, 2013.
[361] K. Schwanitz, The TiO_2/Dye/Electrolyte Interface in the Dye Sensitized Solar Cell: A synchrotron induced photoelectron spectroscopy study, in: T.U. Darmstadt (Ed.) Ph.D. Thesis, Technische Universität Darmstadt, Darmstadt, 2008.
[362] R. Pekkola, Electronic structure of solid-state dye-sensitized solar cells: Synchrotron induced photoelectron spectroscopy on nanocrystalline TiO2, newly developed dyes and spiro-MeOTAD, in: T.U. Darmstadt (Ed.) Ph.D. Thesis, Technische Universität Darmstadt, Darmstadt, 2014.
[363] Y.-T. Lin, T.-W. Zeng, W.-Z. Lai, C.-W. Chen, Y.-Y. Lin, Y.-S. Chang, W.-F. Su, Efficient photoinduced charge transfer in TiO 2 nanorod/conjugated polymer hybrid materials, Nanotechnology, 17 (2006) 5781.
[364] P.H.N. Nguyen, N.D. Nguyen, Green light-emitting diodes based on a hybrid TiO 2 nanoparticle-conducting polymer blend, Advances in Natural Sciences: Nanoscience and Nanotechnology, 2 (2011) 035012.
[365] G. Liu, W. Jaegermann, J. He, V. Sundström, L. Sun, XPS and UPS Characterization of the TiO2/ZnPcGly Heterointerface: Alignment of Energy Levels, The Journal of Physical Chemistry B, 106 (2002) 5814-5819.
[366] G. Schlichthörl, S.Y. Huang, J. Sprague, A.J. Frank, Band Edge Movement and Recombination Kinetics in Dye-Sensitized Nanocrystalline TiO2 Solar Cells: A Study by Intensity Modulated Photovoltage Spectroscopy, The Journal of Physical Chemistry B, 101 (1997) 8141-8155.
[367] A.J. Frank, N. Kopidakis, J.v.d. Lagemaat, Electrons in nanostructured TiO2 solar cells: transport, recombination and photovoltaic properties, Coordination Chemistry Reviews, 248 (2004) 1165-1179.
[368] K. Zhu, N. Kopidakis, N.R. Neale, J. van de Lagemaat, A.J. Frank, Influence of Surface Area on Charge Transport and Recombination in Dye-Sensitized TiO2 Solar Cells†, The Journal of Physical Chemistry B, 110 (2006) 25174-25180.
[369] A. Orendorz, J. Wüsten, C. Ziegler, H. Gnaser, Photoelectron spectroscopy of nanocrystalline anatase TiO2 films, Applied Surface Science, 252 (2005) 85-88.
[370] N. Hikmat, T. Shuji, O. Shigeo, K. Ariyuki, S. Hidetoshi, Green and Ultraviolet Emissions From Anatase TiO2 Films Fabricated by Chemical Vapor Deposition, Japanese Journal of Applied Physics, 44 (2005) 245.
[371] N. Hosaka, T. Sekiya, S. Kurita, Excitonic state in anatase TiO2 single crystal, Journal of Luminescence, 72–74 (1997) 874-875.
[372] H. Tang, H. Berger, P.E. Schmid, F. Lévy, G. Burri, Photoluminescence in TiO2 anatase single crystals, Solid State Communications, 87 (1993) 847-850.
[373] I. Sildos, A. Suisalu, J. Aarik, T. Sekiya, S. Kurita, Self-trapped exciton emission in crystalline anatase, Journal of Luminescence, 87–89 (2000) 290-292.
[374] M. Watanabe, S. Sasaki, T. Hayashi, Time-resolved study of photoluminescence in anatase TiO2, Journal of Luminescence, 87–89 (2000) 1234-1236.
[375] A.V. Emeline, V.K. Ryabchuk, N. Serpone, Dogmas and Misconceptions in Heterogeneous Photocatalysis. Some Enlightened Reflections, The Journal of Physical Chemistry B, 109 (2005) 18515-18521.

[376] J. Preclíková, P. Galář, F. Trojánek, S. Daniš, B. Rezek, I. Gregora, Y. Němcová, P. Malý, Nanocrystalline titanium dioxide films: Influence of ambient conditions on surface- and volume-related photoluminescence, Journal of Applied Physics, 108 (2010) 113502.
[377] L. Cavigli, F. Bogani, A. Vinattieri, V. Faso, G. Baldi, Volume versus surface-mediated recombination in anatase TiO2 nanoparticles, Journal of Applied Physics, 106 (2009) 053516.
[378] W.F. Zhang, M.S. Zhang, Z. Yin, Microstructures and Visible Photoluminescence of TiO2 Nanocrystals, physica status solidi (a), 179 (2000) 319-327.
[379] M. Šćepanović, Z. Dohčević-Mitrović, I. Hinić, M. Grujić-Brojčin, G. Stanišić, Z.V. Popović, Photoluminescence of Laser-Synthesized Anatase Titanium Dioxide Nanopowders, Materials Science Forum, 494 (2005) 265-270.
[380] L. Forss, M. Schubnell, Temperature dependence of the luminescence of TiO2 powder, Appl. Phys. B, 56 (1993) 363-366.
[381] A. Suisalu, J. Aarik, H. Mändar, I. Sildos, Spectroscopic study of nanocrystalline TiO2 thin films grown by atomic layer deposition, Thin Solid Films, 336 (1998) 295-298.
[382] C.J. Powell, A. Jablonski, NIST Electron Inelastic Mean Free Path Database, in: Standard Reference Data Program, National Institute of Standards and Technology, Gainsburg, 1.1 Edition, 2000.
[383] Selenium (Se) crystal structure, lattice and cell parameters, monoclinic selenium (alpha, beta, gamma), in: O. Madelung, U. Rössler, M. Schulz (Eds.) Non-Tetrahedrally Bonded Elements and Binary Compounds I, Springer Berlin Heidelberg, 1998, pp. 1-5.
[384] Selenium (Se) crystal structure, lattice and cell parameters, trigonal Se, in: O. Madelung, U. Rössler, M. Schulz (Eds.) Non-Tetrahedrally Bonded Elements and Binary Compounds I, Springer Berlin Heidelberg, 1998, pp. 1-5.
[385] B. Xin, L. Jing, Z. Ren, B. Wang, H. Fu, Effects of Simultaneously Doped and Deposited Ag on the Photocatalytic Activity and Surface States of TiO2, The Journal of Physical Chemistry B, 109 (2005) 2805-2809.
[386] E.L. Bullock, L. Patthey, S.G. Steinemann, Clean and hydroxylated rutile TiO2(110) surfaces studied by X-ray photoelectron spectroscopy, Surface Science, 352–354 (1996) 504-510.
[387] T.K. Sham, M.S. Lazarus, X-ray photoelectron spectroscopy (XPS) studies of clean and hydrated TiO2 (rutile) surfaces, Chemical Physics Letters, 68 (1979) 426-432.
[388] A.N. Shultz, W. Jang, W.M. Hetherington Iii, D.R. Baer, L.-Q. Wang, M.H. Engelhard, Comparative second harmonic generation and X-ray photoelectron spectroscopy studies of the UV creation and O2 healing of Ti3+ defects on (110) rutile TiO2 surfaces, Surface Science, 339 (1995) 114-124.
[389] K. Schwanitz, U. Weiler, R. Hunger, T. Mayer, W. Jaegermann, Synchrotron-Induced Photoelectron Spectroscopy of the Dye-Sensitized Nanocrystalline TiO2/Electrolyte Interface: Band Gap States and Their Interaction with Dye and Solvent Molecules, The Journal of Physical Chemistry C, 111 (2007) 849-854.
[390] J.T. Mayer, U. Diebold, T.E. Madey, E. Garfunkel, Titanium and reduced titania overlayers on titanium dioxide(110), Journal of Electron Spectroscopy and Related Phenomena, 73 (1995) 1-11.
[391] R. Gouttebaron, D. Cornelissen, R. Snyders, J.P. Dauchot, M. Wautelet, M. Hecq, XPS study of TiOx thin films prepared by d.c. magnetron sputtering in Ar–O2 gas mixtures, Surface and Interface Analysis, 30 (2000) 527-530.
[392] P. Reckers, M. Dimamay, J. Klett, S. Trost, K. Zilberberg, T. Riedl, B.A. Parkinson, J. Brötz, W. Jaegermann, T. Mayer, Deep and Shallow TiO2 Gap States on Cleaved Anatase Single Crystal (101) Surfaces, Nanocrystalline Anatase Films, and ALD Titania Ante and Post Annealing, The Journal of Physical Chemistry C, 119 (2015) 9890-9898.

Acknowledgements

I would like to express my heartfelt gratitude to many people and institutions whose guidance, assistance, encouragement, provisions and support have been indispensable to the accomplishment of this endeavor. I made here a list to the best of my memory; and if I may have failed to mention some names, then it is but only a shortcoming.

- *Prof. Dr. Wolfram Jaegermann*, thank you, sir, for giving me the opportunity to work with you in your group and learn new scientific skills that would have been otherwise a slim chance for me to obtain elsewhere; for the support, guidance and time you gave, the valuable discussions as well as the scientific freedom in doing our research.
- *Prof. Dr. Georges Hadziioannou*, for giving me the opportunity to work with you in your group in Bordeaux and learn from the research that you do; thank you for the provisions that were made available to me; and for taking over the second report.
- *Dr. Thomas Mayer*, thank you for making the work exciting and challenging me to have a wider perspective and approach on the research we do, for the time (even through Skype, at different time zones) and expert eye you gave on highly valued discussions and detailed data analysis, and for all the support you gave me through these years.
- *Prof. Dr. Annemarie Pucci*, for your effort and time, and for taking over the pre-defense thesis report.
- *Dr. Christian Melzer*, for your effort and time, and for taking over the pre-defense thesis report
- *Hessisches Ministerium für Wissenschaft und Kunst*, for the funding of my Ph.D. scholarship.
- *IDS-FunMat and its organizers and staff*, for the platform you created to provide opportunities for striving individuals who wish to further their academic achievements and contributions, as well as for the continuous support and aid you offer to your scholars.
- *Ingenium*, for the STIBET scholarship you granted me during the last leg of this dissertation.
- *Ruben Precht*, for the support and the work we have done for the initial phase of this study, together facing the challenges of not knowing where and how to start.
- *Organic group members*, for the productive discussions during our meetings and for being considerate in terms of the language medium. Special mention to: *Philip Reckers*, for all

the technical, theoretical and moral support you gave me from DAISY to BESSY; *Julia Maibach*, for the introduction to the HEISY-ORG glass cell operation and the succeeding PES measurements; *Eric Mankel*, for general laboratory and theoretical support; and *Andreas Decker*, for the introduction to DAISY-MAT.

- *Surface Science group members*, for the many interesting experiences we all shared during this transient period of our academic lives as well as for the great camaraderie which makes our experiences together worthwhile. Special mention to: *Johannes Türck*, *André Schwöbel*, *Michael Wussler* and *Joachim Klett*, for helping me find my way through Inkscape, Igor, Origin and Word; *Anne Fuchs* and *Eduard Feldmeier*, for the introduction to DAISY-SOL; *Jürgen Ziegler*, for the shared technical knowledge lab-wise and thesis-wise; *Alexander Issanin*, for the introduction to ZnO CVD; *Thorsten Bayer*, for the assistance with my ZnO sample annealing; *Johannes Türck*, for the introduction to AFM measurements; *Dr. Lucangelo Dimesso*, for the theoretical and moral support; *Dr. Wolfram Calvet*, for the introduction to the SOLIAS glass cell operation and drop-casting experiments, and for the BESSY technical support; *Marga Lang*, for the endless administrative and moral support; and the girls -- *Natalia Schulz, Natascha Weidler*, *Mercedes Carillo*, *Shanting Zhang* and *Leslie Frotscher*, for the support, fun times and the ears we lent each other when we were up to our necks in work.

- *DAISY-MAT users*, for the efficient working atmosphere and considerations for each other given that there are so many of us sharing the system.

- *LCPO group members*, for the technical support you gave me when I needed them. Special mention to: *Jules Oriou*, for synthesizing the TSQT monomers for use in this study; *Deniz Beyazit*, for the introduction to the ATR-FTIR equipment; *Antoine Charbonnier*, for helping me manage my way through the lab and living in Bordeaux; and *Aude Manson,* for the administrative support.

- *David Talaga*, for assisting me with the Raman and photoluminescence measurements using your equipment at ISM-UB.

- *Dr. Thierry Toupance*, *Tamez Uddin* and *Céline Olivier*, for the nc-TiO_2 discussions and for supplying the anatase nc-TiO_2 substrates and powders.

- *Dr. Aina Quintilla* and *Abebe Tarekegne*, for assisting me with the initial photoluminescence measurements using your equipment at KIT.

- *Dr. Jörg Zimmermann*, for the introduction to E-MAT's optical characterization setups.

- *Dr. Andrea Gassmann*, for the introduction to E-MAT's device fabrication SOPs and the electro-optical measurements.

- *Eric Lebraud* and *Jean-Christophe Jaud*, for the XRD measurements.

- My lifelong friends, *Gwendolyne Pascua* and *Margie Olbinado*, for the constant and consistent support we have for each other, especially on our common pursuit for our doctorates at different parts of the globe.
- My in-laws, *Marian* and *Hedwig*, for your provisions, finances and moral support.
- My siblings, *Mark*, *Walter* and *Jessamyn*, for being there to remind me to be focused, calm, realistic and grounded so I can finally finish this dissertation.
- My parents, *Fred* and *Kit*, for your unceasing prayers, motivational conversations, finances, and your pride and joy of your daughter's accomplishments so far from home.
- My husband, *Bartosch*, of whom without I could have been in the worst of situations. Thank you for bearing with me, for going the extra mile and filling in for me during those stressful periods, and, most of all, for sharing with me the joy and relief I feel now that this is finally done.

Curriculum vitae

For reasons of data protection, the curriculum vitae is not included in the online version.

Erklärung zur Dissertation

Hiermit versichere ich, die vorliegende Dissertation ohne Hilfe Dritter nur mit den angegebenen Quellen und Hilfsmitteln angefertigt zu haben. Alle Stellen, die aus Quellen entnommen wurden, sind als solche kenntlich gemacht. Diese Arbeit hat in gleicher oder ähnlicher Form noch keiner Prüfungsbehörde vorgelegen.

Darmstadt, den 25.01.2016

(Mariel Grace Jama, geb. Dimamay)